LMSC-4-05-70-9 • MAY 1970

LMSC-4-05-70-9

ELASTIC AND PLASTIC ANALYSIS OF PRESSURE VESSEL WELD LANDS WITH MISMATCH

CONTRACT NAS 9-9726

Lockheed

PALO ALTO RESEARCH LABORATORY

LOCKHEED MISSILES & SPACE COMPANY • A GROUP DIVISION OF LOCKHEED AIRCRAFT CORPORATION
PALO ALTO, CALIFORNIA

NASA CR 108516

ELASTIC AND 'LASTIC ANALYSIS OF PRESSURE VESSEL WELD LANDS WITH MISMATCH

J. Skogh and A. M. C. Holmes

LMSC/4-05-70-9 May 1970

Lockheed Palo Alto Research Laboratory
Palo Alto, California

FOREWORD

The research described in the present report was performed under Contract NAS9-9726 with the NASA/Manned Spacecraft Center, Houston, Texas, with Mr. H. C. Kavanaugh as Contract Monitor.

The following persons made significant contributions to the work:

Mr. J. Skogh	-	Project Leader
Mr. A.M.C. Holmes	-	Experimental Program
Dr. C. R. Steele	-	Consultant, Asymptotic Solutions
Mr. P. Stern	-	Consultant, Elastic-Plastic Computer Programs

ABSTRACT

The problem of weld mismatch in pressure vessels is treated in detail. Design graphs are given for mismatch in cylinders joined to cylinders, and hemispheres joined to cylinders. These graphs, which are in nondimensional form, show elastic and plastic stresses for a wide range of weld land geometries. The material used in generating the data is titanium 6Al-4V, but the design graphs may also be used for other strain-hardening materials with a stress-strain curve that is virtually horizontal in the plastic region.

The data which form the basis for the design data have been almost entirely obtained from parametric computer solutions. These solutions were checked with a test program using cylinders and spheres with precisely controlled, simulated mismatch in a variety of weld land configurations. Excellent correlation between theory and test was achieved for static loadings.

In addition to static loadings the test program was also designed to provide information on the behavior of pressure vessels with mismatch under pressure cycling. Failure criteria for low cycle fatigue obtained from this work are also included.

The present program is a continuation of a previous, similar, NASA contract (NAS 9-8303) concerned with the elastic and plastic behavior of pressure vessels with weld sinkage type geometries.

CONTENTS

NOMENCLATURE

A_w	Weld Land Area (Fig. 6-4) - in^2
E	Modulus of Elasticity - lb/in^2
F	Inertia Force - lb
F_{PL}	Proportionate Limit - lb/in^2
F_{tu}	Ultimate Strength - lb/in^2
F_{ty}	Yield Strength - lb/in^2
G	Shear Modulus - lb/in^2
L	Weld Land Length (Fig. 3-10) - inch
L^*	$= L/\sqrt{Rt}$
m	Mismatch Parameter $m = \Delta R/t_w$
m_F	Equivalent Mismatch for Inertia Force
$\bar{m}$	Defined on Page 3-3
M_F	Inertia Moment - inlb/in
M_θ	Hoop Moment - inlb/in
M_φ	Meridional Moment - inlb/in
n	$= N_\theta/N_\varphi$
$n_1, n_2, n_3 \ldots$	Number of Applied Pressure Cycles at Pressure $p_1, p_2, p_3 \ldots$
$\bar{n}$	Defined by Eq. (3.6)
N_F	Inertia Stress Resultant - lb/in
N_x	Axial Stress Resultant - lb/in

N_φ	Meridional Stress Resultant - lb/in
N_θ	Hoop Stress Resultant - lb/in
N_1, N_2, N_3...	Number of Pressure Cycles that Cause Failure at Pressure P_1, P_2, P_3...
P	Internal Pressure - lb/in^2
P_m	Normalizing Pressure - lb/in^2
R	Cylinder Radius, Sphere Radius - inch
R_2	Hoop Radius (normal to shell meridian) - inch
ΔR	Mismatch - inch
s	Surface Coordinate - inch
t	Thickness - inch
t_w	Weld Land Thickness - inch
z	Thickness Coordinate - inch
$\alpha = \frac{\bar{\alpha}}{\bar{\alpha}_m}$	Reduced Stress Factor
$\bar{\alpha}$	Equivalent Stress Factor
$\bar{\alpha}_m$	Equivalent Stress Factor in Membrane Region
α_θ	Hoop Stress Factor
α_φ	Meridional Stress Factor
β	Defined by Eq. (3.5)
ϵ_1, ϵ_2, ϵ_3	Strains in Directions 1, 2, 3 - in/in
ϵ_θ	Hoop Strain - in/in

ϵ_φ	Meridional Strain - in/in
$\bar{\epsilon}$	Effective Strain - in/in
$\bar{\epsilon}_p$	Plastic Effective Strain - in/in
$\bar{\epsilon}_R$	Residual Effective Strain - in/in
$\bar{\epsilon}_t$	Total Effective Strain - in/in
$\bar{\epsilon}_y$	Normalizing Strain - in/in
ρ	$= \dfrac{p}{\frac{2}{\sqrt{3(1-\nu^2)}} E\left(\frac{t}{R_2}\right)^2}$ Nonlinearity Parameter
θ	Hoop Coordinate - radians
$\sigma_1, \sigma_2, \sigma_3$	Stresses in Directions 1, 2, 3 - lb/in^2
σ_θ	Hoop Stress - lb/in^2
σ_φ	Meridional Stress - lb/in^2
σ_{φ_m}	Membrane Meridional Stress - lb/in^2
$\bar{\sigma}$	Effective Stress - lb/in^2
ν	Poisson's Ratio
φ	Meridional Coordinate - radians

Section 1

INTRODUCTION

The present work is the second of a series of investigations into the behavior of pressure vessels with unintentional discontinuities. The first investigation [1]* dealt primarily with the effects of a slope discontinuity, such as a weld shrinkage, in cylinders and spheres; the present investigation concerns itself with the elastic and plastic behavior of cylinder and cylinder-hemisphere junctures with mismatch. The substance of the present work is presented in the design graphs of Section 6 which give solutions to the following problems:

- Mismatch in cylinder-cylinder joints with weld lands: elastic stresses, pressure versus strain in the plastic region.
- Mismatch in hemisphere-cylinder joints with weld lands: elastic stresses, pressure versus strain in the plastic region.
- Residual stress after one load into the plastic region for the above shell types.
- Low-cycle fatigue of the above shell types.

The design curves are given for a wide range of weld land geometries and mismatches up to 100 percent of the weld land thickness. The material used for the generation of the curves is titanium 6Al-4V. However, since the problem has been treated in a nondimensional way, pressure vessels made of other materials with a similar stress-strain curve may also be analyzed by the use of these curves, at least approximately.

The solutions given in this work reflect the current state-of-the-art. The discontinuity effects are treated as a problem of applied theory of thin shells. Thus, local stress concentrations in the sense of the theory

*Numbers in square brackets indicate references in Section 10

of elasticity are not being considered. This approach is in keeping with current praxis and does not introduce any serious limitations on the results given, as long as the pressure vessels are relatively thin. For long-term fatigue at relatively low stress levels elastic stress concentrations can be important. However, for the short-term, high stress level repeated loadings considered in the present investigation, the elastic stress concentrations are not of consequence.

The type of discontinuity under investigation here is referred to as "weld mismatch". This term is to be construed as one of convenience and does not imply that the complete problem, including residual stresses introduced during the machining and welding process, has been solved. Rather, only the geometric aspects are considered; the discontinuities are assumed to be free of residual stress and strain at the application of the first pressure load. However, residual stresses and strains which result from the first pressure cycle can be determined from the information given here.

The results given in this report have been obtained mainly by the application of the EPSOR (Elastic-Plastic Shells of Revolution) computer program [2]. In all, some 350 combinations of loads and parametrically varied geometries were required to produce the design graphs. Closed-form analytical solutions were ruled out as being impossible (or at least very impractical) for the quite complicated geometries involving variable thickness shells employed here. However, an effort to accomplish a closed-form solution for the residual-stress problem was made and is presented in Appendix A.

Thus, the work presented here may be considered almost entirely experimental with the experiments being performed on the computer. This experimentation is rather time-consuming, but less so than would have been the case if the experimentation had been carried out au naturel, i.e., with actual physical models. However, a small experimental program employing six titanium pressure vessels with carefully machined-in mismatches in a variety of weld land geometries was part of the present work. This experimental work served as a check on the numerical-analytical predictions (the agreement was excellent) and were used to investigate an area which

is beyond the current analytical capabilities, namely, low-cycle fatigue.

The main goal of the present investigation has been the development of the design curves in Section 6. Constructed mainly with the requirements of the practical engineer in mind, typical uses of these graphs would include

- Design of proper weld land geometry.
- Determination of acceptable drawing tolerances for weld mismatch.
- Determination of internal pressure capabilities (static and cyclic) for pressure vessels with weld mismatch.

Section 2

SOME FUNDAMENTAL CONSIDERATIONS

The most significant aspect of the analysis of shell structures with discontinuities is that it is concerned with only a narrow zone in which the stresses are very high and quickly damped out into the general, membrane, state of stress in the major part of the shell. The main deviation from the basic membrane state of stress is caused by a bending moment at the geometric discontinuity. Local changes in the membrane (middle surface) stress are generally of minor importance. Thus, an important factor in describing, or classifying, a discontinuity is to define the size of the resulting discontinuity moment.

The discontinuity moment may arise from two sources:

- o Induced moments, caused by rapid changes in geometry (thickness, and/or meridional geometry). Induced moments are statically indeterminate.

- o Applied moments, caused by externally applied forces. Applied moments are statically determinate.

An example of an induced moment is the weld sinkage problem dealt with in Ref. 1. An example of an applied moment is the couple created by a mismatch in two shells of equal, uniform, thickness. A shell with mismatched weld land develops both kinds of discontinuity moments, as discussed in detail in Sections 3 and 4.

The major difference between the two types of moments, and the reason for making a distinction between them, is that the induced moments are sensitive to the change in geometry which occurs as the shell is pressurized, while the applied moments are not. The change of geometry will, in general, have a beneficial effect on the induced moment in that it is lowered, and a complicating effect on the analysis in that it will be nonlinear, even in the elastic part of the material's stress-strain curve.

The EPSOR computer program [2] used to generate the data in the present work contains the proper pressure-coupling terms to account for the nonlinear elastic behavior. This nonlinear geometric behavior is also - of course - carried into the plastic range, coupling with the material nonlinear effects in that range. Other fundamental features of the program are as follows:

Shell Geometry - General shell of revolution, defined by two principal radii of curvature. The thickness is permitted to vary in the meridional direction. Thin-shell theory is used, i.e., the thickness is small in comparison to both radii of curvature.

Stress-Strain Relations - Because of axial symmetry, and the thin-shell assumption, the only non-zero stress components are the principl stresses σ_φ and σ_θ, which coincide with the meridional and hoop directions. The stress-strain relations used pertain to a temperature-dependent work-hardening material with the von Mises yield function. The loading possibilities are:

- For small initial changes in loads the shell response is elastic, provided that no previous plastic straining has taken place.
- As the loads are increased, stresses at certain points of the shell reach values corresponding to initial plastic yielding.
- Further increase in load results in the development of specified elastic and plastic regions.
- At some further time during load history, unloading from a plastic to an elastic state may take place. (Residual stresses upon unloading are computed.)
- Reloading from an elastic region which had been plastic constitutes the final possibility for formation of elastic and plastic regions.

Equilibrium Equations - The equilibrium equations are written in terms of the deformed shell, thus giving a nonlinear behavior in the elastic range.

Governing Differential Equations - The governing differential equations are analogous to those given in Ref. 3.

Methods of Solution - The governing differential equations and boundary conditions are transformed into a set of algebraic equations by finite difference approximations. At a given time in the load history the solution is advanced an increment in time Δt by solving these equations in conjunction with the flow rules associated with the loading function to determine the implicit plastic strain increment. This is accomplished by an iterative scheme. Finally, the complete solution for a specific load history is given by an integration with respect to time by a step-by-step procedure.

2.1 Stress Factors

In the present report the term stress factor is used to relate the stress at the point of the discontinuity (i.e., the point of maximum stress) to an easily determined reference stress, the meridional membrane stress.

The meridional membrane stress in the basic shell is

$$\sigma_{\varphi_m} = \frac{N_{\varphi_m}}{t} = \frac{pR_2}{2t} \tag{2.1}$$

This equation is valid for all axisymmetric, closed, shells with pressure loading. The uniaxial stress factors are defined in terms of the basic meridional stress:

$$\alpha_\varphi = \frac{\sigma_\varphi}{\sigma_{\varphi_m}} \tag{2.2a,b}$$

$$\alpha_\theta = \frac{\sigma_\theta}{\sigma_{\varphi_m}}$$

According to the von Mises yield criterion the equivalent stress $\bar{\sigma}$ is related to the uniaxial stresses by the equation

$$\bar{\sigma} = \sqrt{\sigma_\varphi^2 + \sigma_\theta^2 - \sigma_\varphi \sigma_\theta} \tag{2.3}$$

An equivalent, or effective, stress factor is defined similarly to the uniaxial stress factors

$$\bar{\alpha} = \frac{\bar{\sigma}}{\sigma_{\varphi_m}}$$

$$\text{or} \quad \bar{\alpha} = \sqrt{\alpha_\varphi^2 + \alpha_\theta^2 - \alpha_\varphi \alpha_\theta} \tag{2.4}$$

Further, a reduced stress factor is defined, as follows

$$\alpha = \frac{\bar{\sigma}}{\bar{\alpha}_m} \tag{2.5}$$

where $\bar{\alpha}_m$ is the equivalent stress factor in the membrane region of the shell.

2.2 Stress Factors and Normalizing Pressure for Uniform Thickness Shells with Mismatch

Fig. 2-1a shows a segment of the meridian of a uniform thickness shell with a mismatch ΔR. The shell is loaded by an (internal) pressure p resulting in the membrane stress resultants N_φ and N_θ. The meridional stress resultant creates at the discontinuity a moment of the magnitude

$$M = N_\varphi \Delta R \tag{2.6}$$

which may be thought of as an externally applied line moment for a shell without the abrupt step ΔR, as shown in Fig. 2-1b. Since the thickness

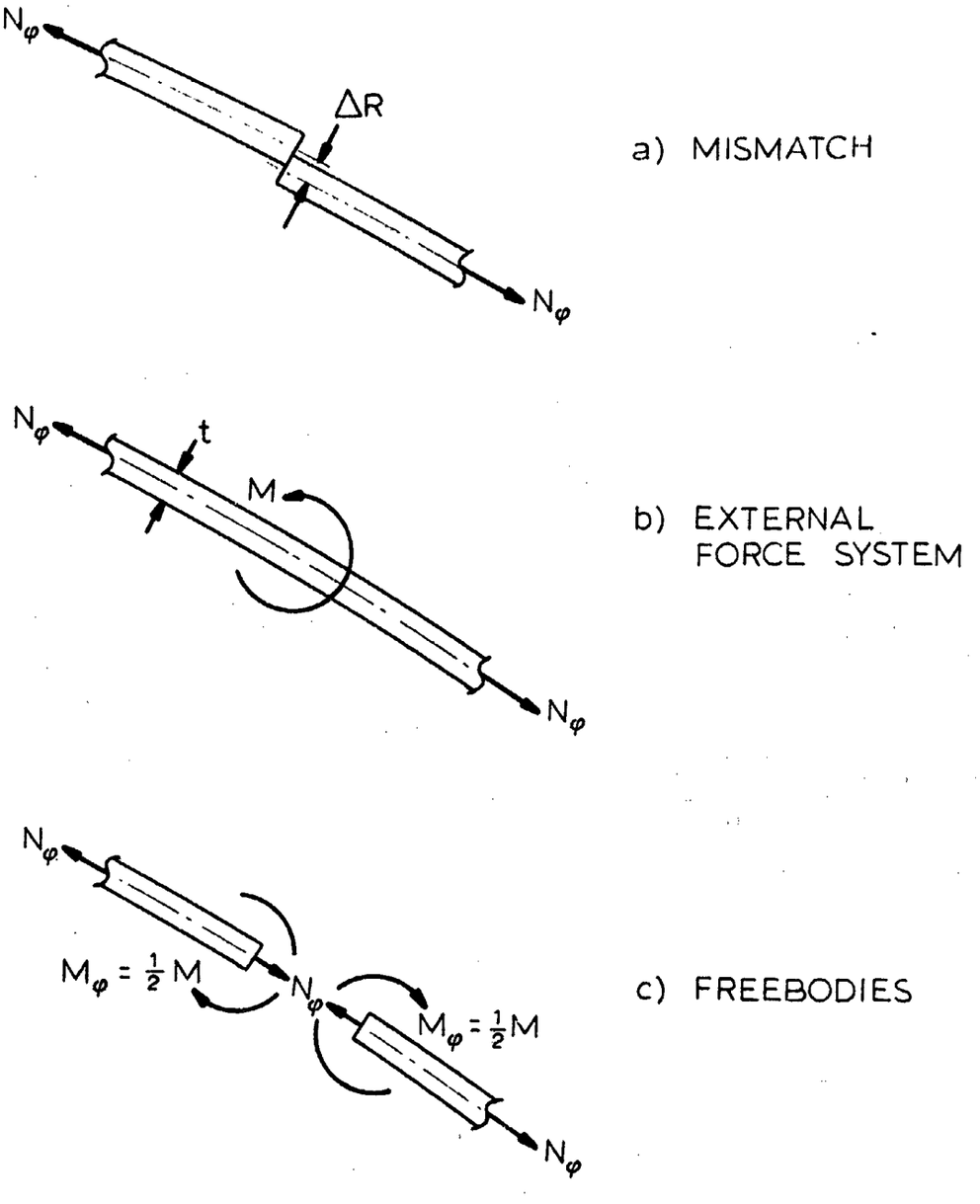

Fig. 2-1 Shell with Mismatch

(and therefore the shell stiffness) is the same on either side of the discontinuity, one-half of the applied moment will be absorbed by the left part and one-half by the right part of the shell, resulting in an antisymmetric stress and deformation situation. The maximum stress occurs at the discontinuity. Since the applied moment is of the nature of an externally applied line load, no nonlinear effects will occur at the discontinuity, however, the attenuation length*) will be slightly changed and the lower stresses at some distance from the discontinuity behave in a nonlinear way.

The meridional and the hoop stress at the discontinuity are

$$\sigma_\varphi = \frac{N_\varphi}{t} \pm \frac{6M_\varphi}{t^2}$$

$$\sigma_\theta = \frac{N_\theta}{t} \pm \nu \frac{6M_\varphi}{t^2}$$

or, since $M_\varphi = \frac{1}{2} N_\varphi \Delta R$

$$\sigma_\varphi = \frac{N_\varphi}{t} \left(1 \pm 3 \frac{\Delta R}{t}\right) \tag{2.7}$$

$$\sigma_\theta = \frac{N_\theta}{t} \left(1 \pm 3\nu \frac{N_\varphi}{N_\theta} \frac{\Delta R}{t}\right) \tag{2.8}$$

With these equations the maximum equivalent stress (Eq. 2.3) becomes

$$\bar{\sigma} = \frac{N_\varphi}{t} \sqrt{1 + n^2 - n} \sqrt{1 + 3m \frac{2 + 2\nu n - \nu - n}{1 + n^2 - n} + 9m^2 \frac{1 + \nu^2 - \nu}{1 + n^2 - n}} \tag{2.9}$$

where $$n = \frac{N_\theta}{N_\varphi} \tag{2.10}$$

$$m = \frac{\Delta R}{t} \tag{2.11}$$

*) See Section 6

The equivalent stress for no discontinuity is found by setting $m = 0$ in Eq. (2.9):

$$\bar{\sigma} = \frac{N_\varphi}{t} \sqrt{1 + n^2 - n} \tag{2.12}$$

Setting the equivalent stress $\bar{\sigma}$ equal to the ultimate tension strength of the material, F_{tu}, and using the definition according to Eq. (2.1), the following expression is obtained

$$p = p_m = F_{tu} \frac{t}{R_2} \frac{2}{\sqrt{1 + n^2 - n}} \tag{2.13}$$

This equation gives the pressure at which a shell without a discontinuity would collapse. For example, in a sphere under internal pressure $n = 1$, and Eq. (2.13) gives

$$p_m = 2 \frac{t}{R} F_{tu}$$

Similarly, for a cylinder $n = 2$ and the membrane collapse pressure is

$$p_m = \frac{2}{\sqrt{3}} \frac{t}{R} F_{tu}$$

It follows from the definition, Eq. (2.5), that the reduced stress factor is equal to the last term of Eq. (2.9):

$$\alpha = \sqrt{1 + 3m \frac{2 + 2\nu n - \nu - n}{1 + n^2 - n} + 9m^2 \frac{1 + \nu^2 - \nu}{1 + n^2 - n}} \tag{2.14}$$

This equation is plotted in Fig. 2-2.

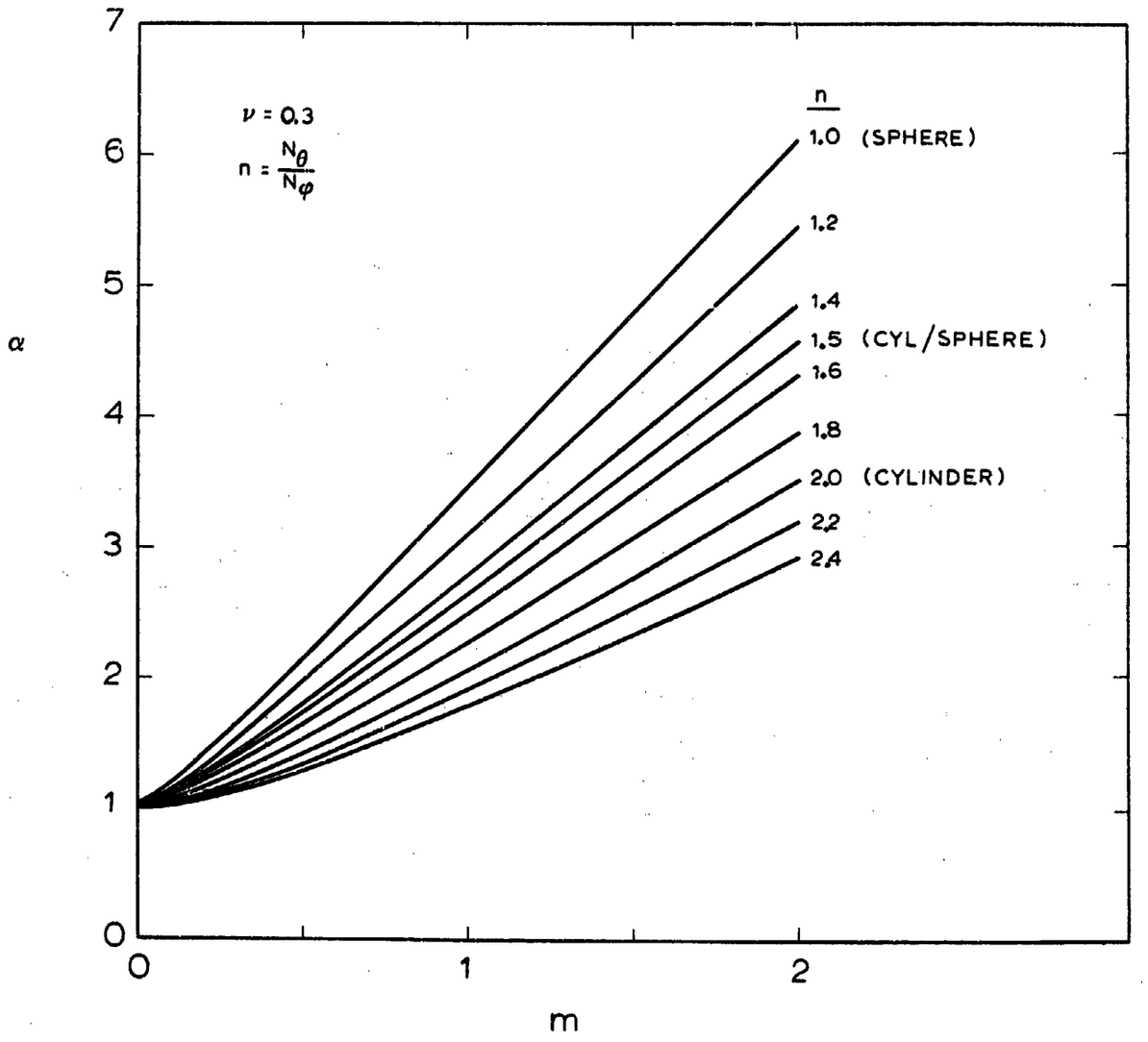

Fig. 2-2 Stress Factors for Uniform Thickness Shells with Mismatch

2.3 Stress-Strain Relations

The use of EPSOR for plastic analysis requires that stress-strain curves in terms of effective stresses and strains are available. The definitions are (see Ref. 4, p. 89)

$$\text{Effective Stress} \quad \bar{\sigma} = \frac{1}{\sqrt{2}} \sqrt{(\sigma_1 - \sigma_2)^2 + (\sigma_1 - \sigma_3)^2 + (\sigma_2 - \sigma_3)^2} \tag{2.15}$$

$$\text{Effective Strain} \quad \bar{\varepsilon} = \frac{\sqrt{2}}{3} \sqrt{(\varepsilon_1 - \varepsilon_2)^2 + (\varepsilon_1 - \varepsilon_3)^2 + (\varepsilon_2 - \varepsilon_3)^2} \tag{2.16}$$

where indices 1, 2, and 3 indicate the direction. Applying these equations to a uniaxial stress-strain curve (σ_1 vs. ε_1):

$$\left.\begin{aligned} \sigma_2 &= \sigma_3 = 0 \\ \varepsilon_2 &= \varepsilon_3 = \nu\varepsilon_1 \end{aligned}\right\} \text{Uniaxial}$$

Then

$$\left.\begin{aligned} \bar{\sigma} &= \frac{1}{\sqrt{2}} \sqrt{\sigma_1^2 + \sigma_1^2} = \sigma_1 \\ \bar{\varepsilon} &= \frac{\sqrt{2}}{3} \sqrt{\varepsilon_1^2(1+\nu)^2 + \varepsilon_1^2(1+\nu)^2 + 0} = \frac{2}{3}\varepsilon_1(1+\nu) \end{aligned}\right\} \text{Uniaxial} \tag{2.17}$$

Thus, given a uniaxial stress-strain curve (σ_1 vs. ε_1), the last two equations define an effective stress-strain curve.

The total effective strain is divided into a plastic and an elastic part (Ref. 4, p. 91)

$$\bar{\varepsilon} = \bar{\varepsilon}_p + \frac{2(1+\nu)}{3E}\,\bar{\sigma} \tag{2.18}$$

After some manipulation the following equations for effective strains result

$$\left.\begin{aligned} \bar{\varepsilon}_p &= \frac{2}{3}(1+\nu)\,\varepsilon_1 - \frac{\sigma_1}{E} \\ \bar{\varepsilon}_t &= \frac{2}{3}(1+\nu)\,\varepsilon_1 \\ \bar{\varepsilon}_t - \bar{\varepsilon}_p &= \frac{2}{3}(1+\nu)\,\frac{\sigma_1}{E} \\ &= \frac{\bar{\sigma}}{3G} \end{aligned}\right\} \tag{2.19}$$

where indices p and t stand for plastic and total, respectively. Plots of $\bar{\sigma}/3G$ vs. $\bar{\varepsilon}_p$ and $\bar{\varepsilon}_p$ vs. $\bar{\varepsilon}_t$ for titanium 6Al-4V STA are shown in Fig. 2-3. The curves labeled S-2 are typical values as obtained from coupon tests on the material used in the experimental part of the present study (see Section 7), while the curve labeled NASA was obtained from stress-strain curves used in the Apollo program. The curves are quite similar in their general and specific nature; the top figure shows that the NASA material has slightly lower ultimate strength, the bottom figure shows that the NASA material has slightly lower proportional limit. Adjusting the curves to the same ultimate strength would cause the curves to practically fall on top of each other; i.e., regarded in a non-dimensional way they are almost identical. Due to this similarity of the curves it was decided to use the NASA curve in the plasticity studies made in the program. This use extends only to the general shape of the curves and actual modulus and maximum strength values were used as required.

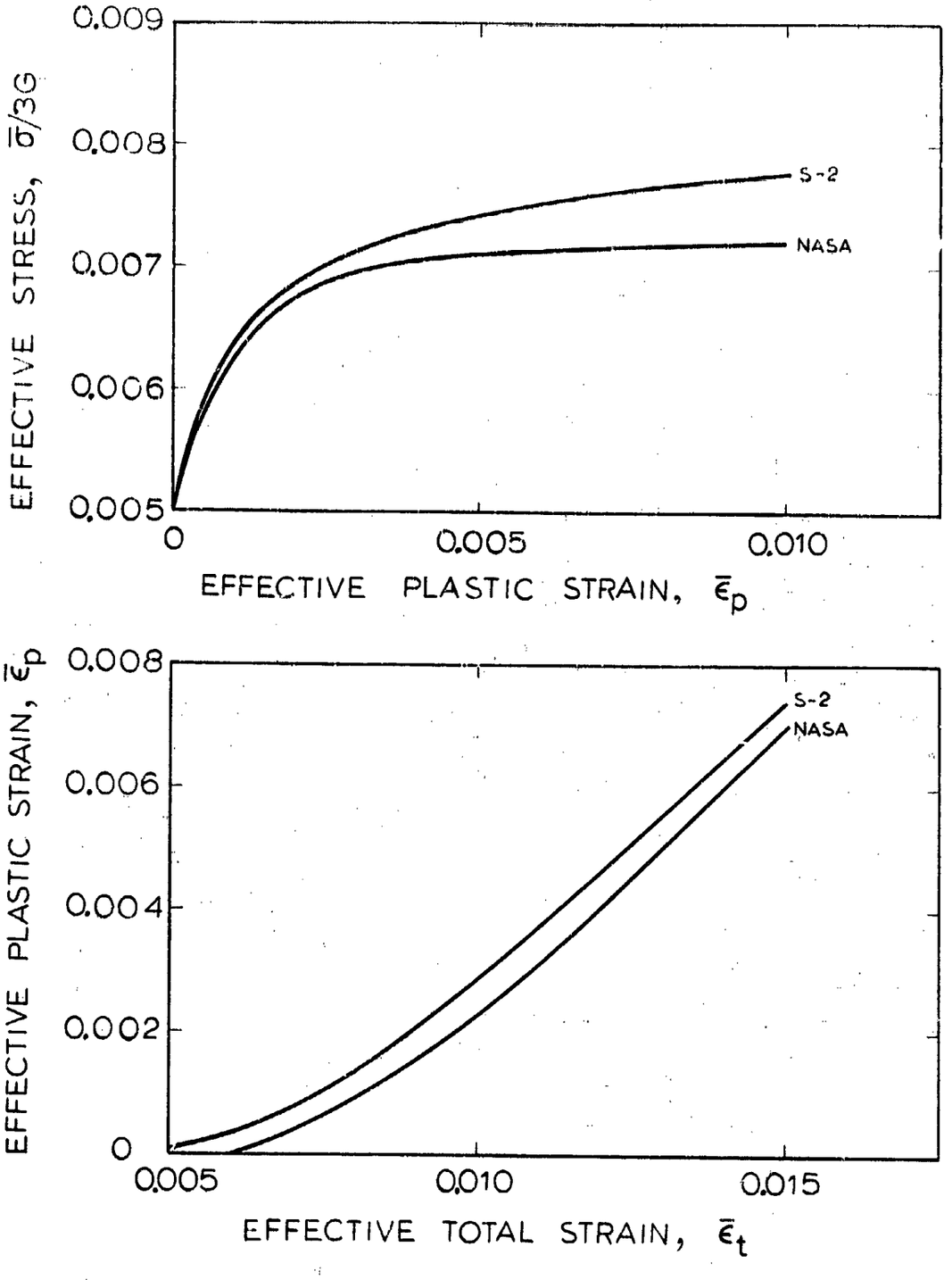

Fig. 2-3 Stress-Strain Curves for Titanium 6Al-4V STA

Section 3

MISMATCH IN CYLINDER-CYLINDER JUNCTURES

Elastic stresses in mismatched cylinders have been extensively investigated in the past.*) However, a thorough literature search [6] conducted in connection with the present program failed to indicate any satisfactory solutions to the plasticity and low-cycle fatigue aspects of the problem.

3.1 Uniform Thickness

Elastic stresses at the juncture of two mismatched cylinders are given by Equations (2.7) and (2.8). The calculation of the stress distributions away from the point of discontinuity is an elementary problem of shell analysis with tabulated solutions given in a number of standard works, such as [3]. Solutions for stresses and strain in the plastic areas are, however, not so easy to come by.

An approximate solution for the elastic/perfectly plastic case, based on the method given in [1] is offered here:

Consider a constant thickness cylinder with a discontinuity in radius, ΔR:

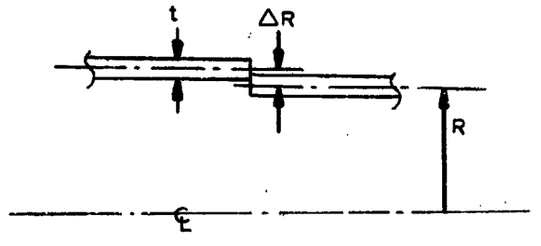

*) See, for example, Bizon [5].

Under internal pressure the stress resultants are, in all parts of the shell,

$$N_\varphi = \frac{pR}{2} \tag{3.1}$$

$$N_\theta = pR \tag{3.2}$$

At the discontinuity:

$$M_\varphi = \frac{1}{2}\Delta R N_\varphi \tag{3.3}$$

$$\epsilon_\theta = \frac{pR}{2Et}(2-\nu) \qquad \text{(Symmetry)} \tag{3.4}$$

Introduce the notation

$$\beta = \frac{6M_\varphi}{tN_\varphi} = \frac{3\Delta R}{t}, \quad \beta = 3m \tag{3.5}$$

$$\bar{n} = \frac{pR}{2tF_{tu}} \tag{3.6}$$

For a simplified analysis, assume that the dominant stress occurs meridionally, i.e., the problem is uniaxial. Then, for the elastic-perfectly plastic model the maximum edge moment (which gives infinite curvature) is obtained from page D-4 of [1]:

For yielding in tension and compression:

$$\bar{m} = \frac{3(1-\bar{n}^2)\bar{y}^2 - 1}{2\bar{y}^2}$$

For infinite curvature, $\bar{y} \to \infty$.

Thus

$$\bar{m} = \frac{3}{2}(1-\bar{n}^2) \tag{3.7}$$

But

$$\bar{m} = \frac{6M_\varphi}{Et^2\epsilon_y} \qquad \text{(definition)}$$

$$= \frac{6M_\varphi}{F_{tu}t^2}$$

$$= \beta\bar{n} \tag{3.8}$$

Thus

$$\beta\bar{n} = \frac{3}{2}(1-\bar{n}^2)$$

or

$$\bar{n} = \frac{\sqrt{\beta^2 + 9} - \beta}{3} \tag{3.9}$$

This gives an upper limit on the load when the dominant stress is in the axial direction. Collapse in circumferential tension occurs (uniaxially) when $\bar{n} = \frac{1}{2}$. Thus, the behavior is illustrated by the full curve of Figure 3-1. In this figure are also shown points from biaxial computer solutions, which by failure to converge indicate collapse. Quite good agreement is evident between the closed-form and the computer solutions.

Some details of computer solutions are shown in Figures 3-2 to 3-5. These solutions are for cylinders with a radius of 5 inch, a thickness of 0.05 inch, and material properties according to Fig. 2-3 (curves marked "NASA"). Fig. 3-2 shows stresses for the inside surface as a function of the surface coordinate s for a cylinder with 50% mismatch (m = 0.5). The discontinuity is at the extreme right of the graph, and the discontinuity moment is applied in such a manner that the tension on the inside surface is increased. Fig. 3-3 shows stresses through the thickness at the point of discontinuity.

Figures 3-4 and 3-5 are the counterparts of Figures 3-2 and 3-3, for m = 1. Note in both sets of figures that as the pressure is increased the meridional stress is readily penetrating the stress level equal to the ultimate strength of the material. The hoop stress does not exceed this

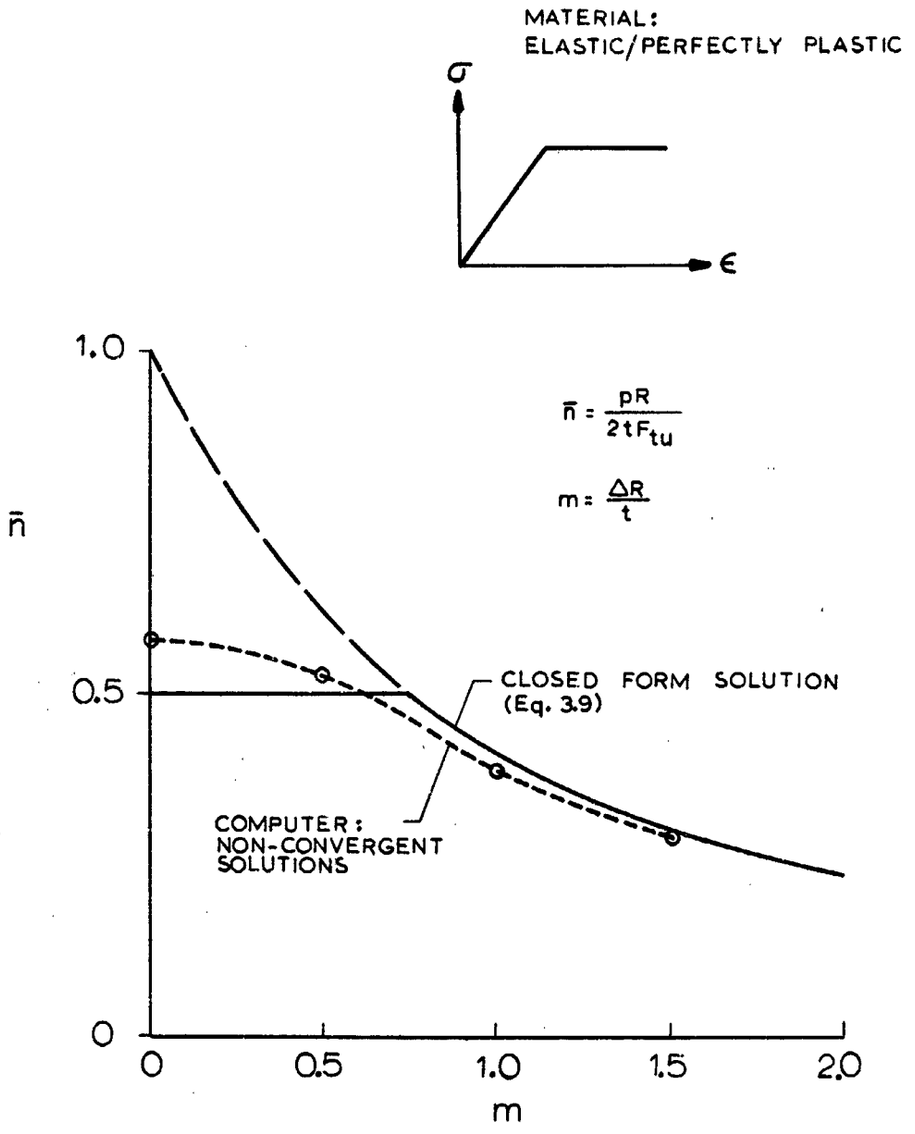

Fig. 3-1 Maximum Pressure in Cylinders with Mismatch

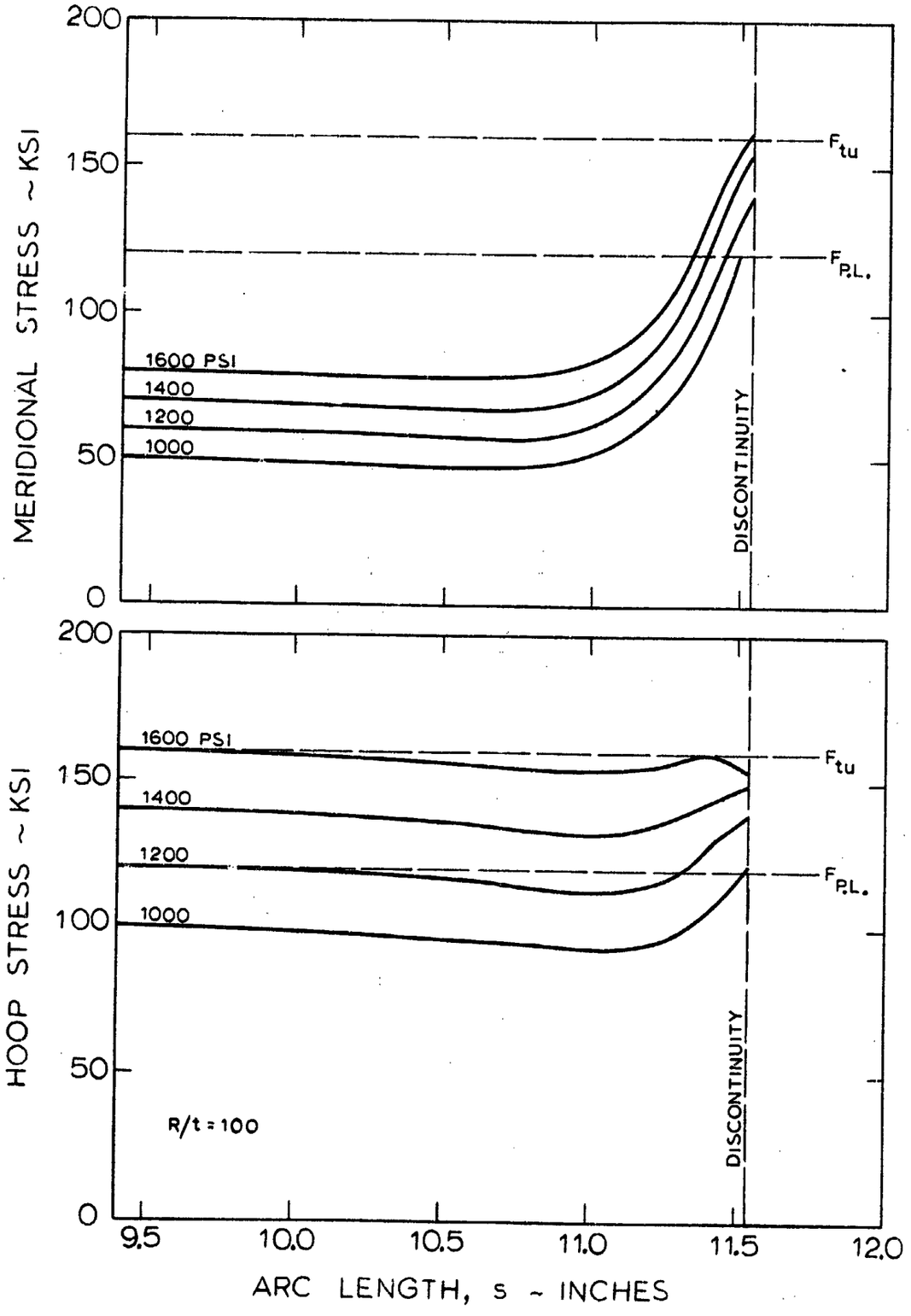

Fig. 3-2 Inside Surface Stresses in Cylinder with 50% Mismatch

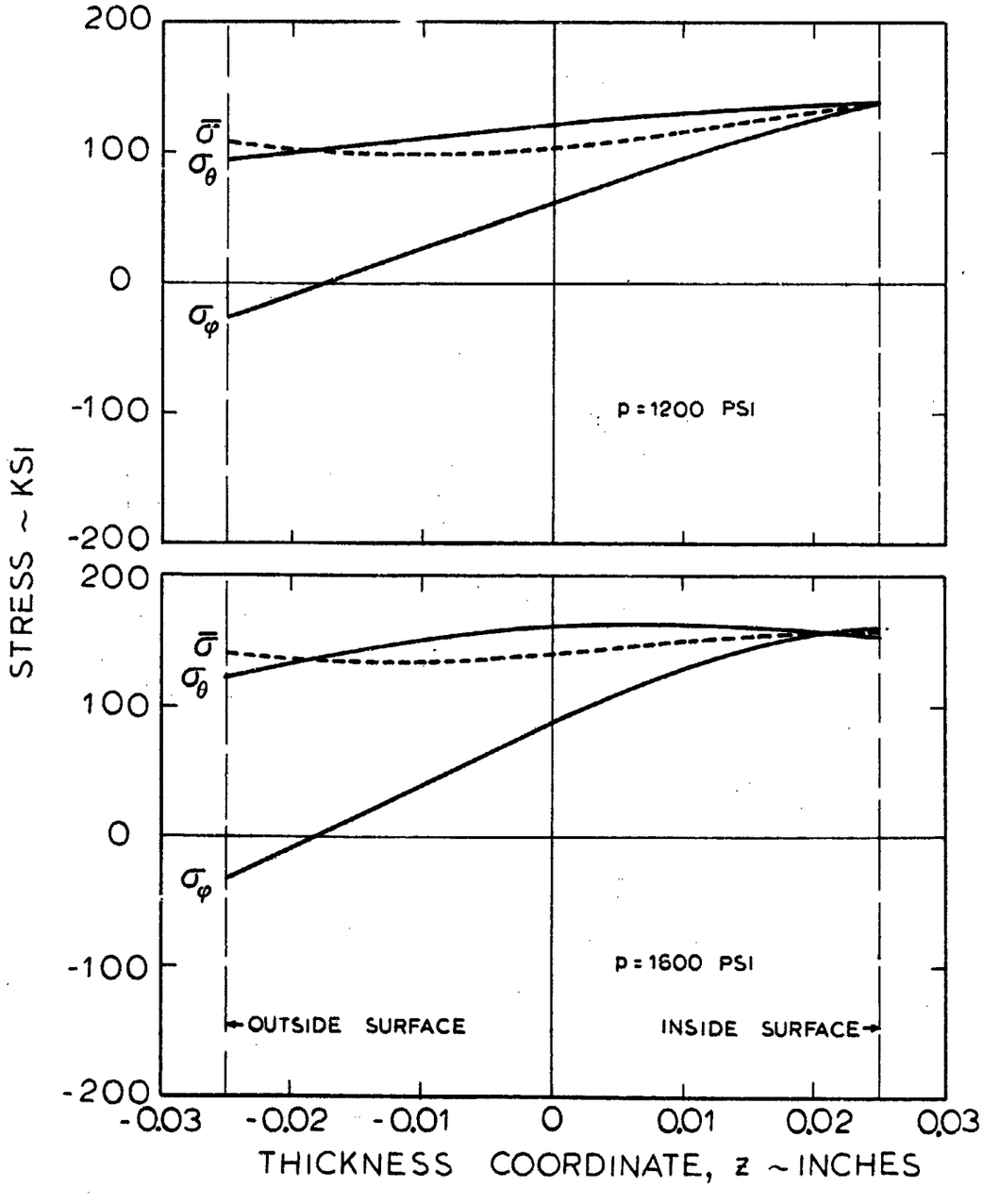

Fig. 3-3 Cylinder with 50% Mismatch: Stress at Discontinuity

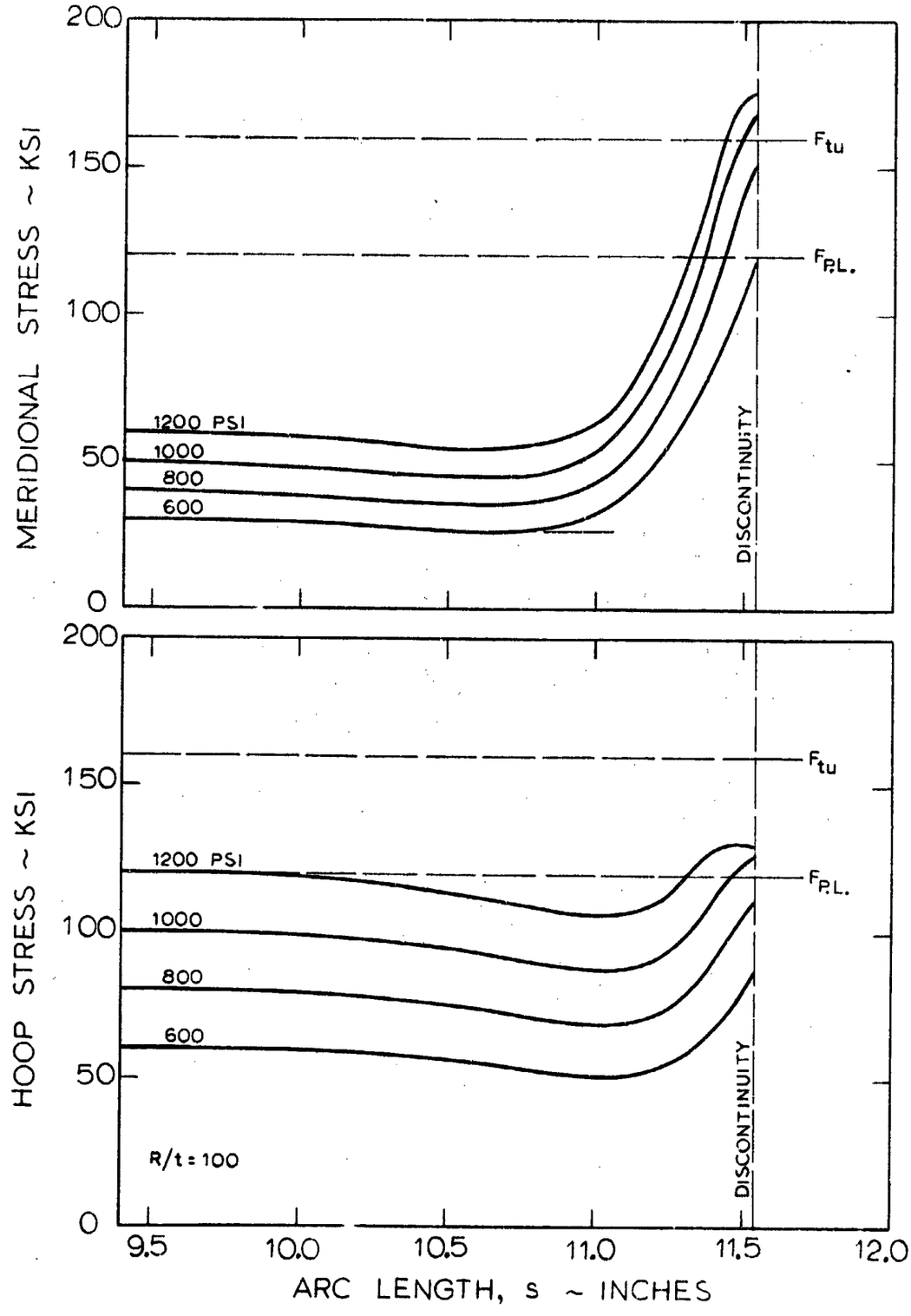

Fig. 3-4 Inside Surface Cylinder with 100% Mismatch

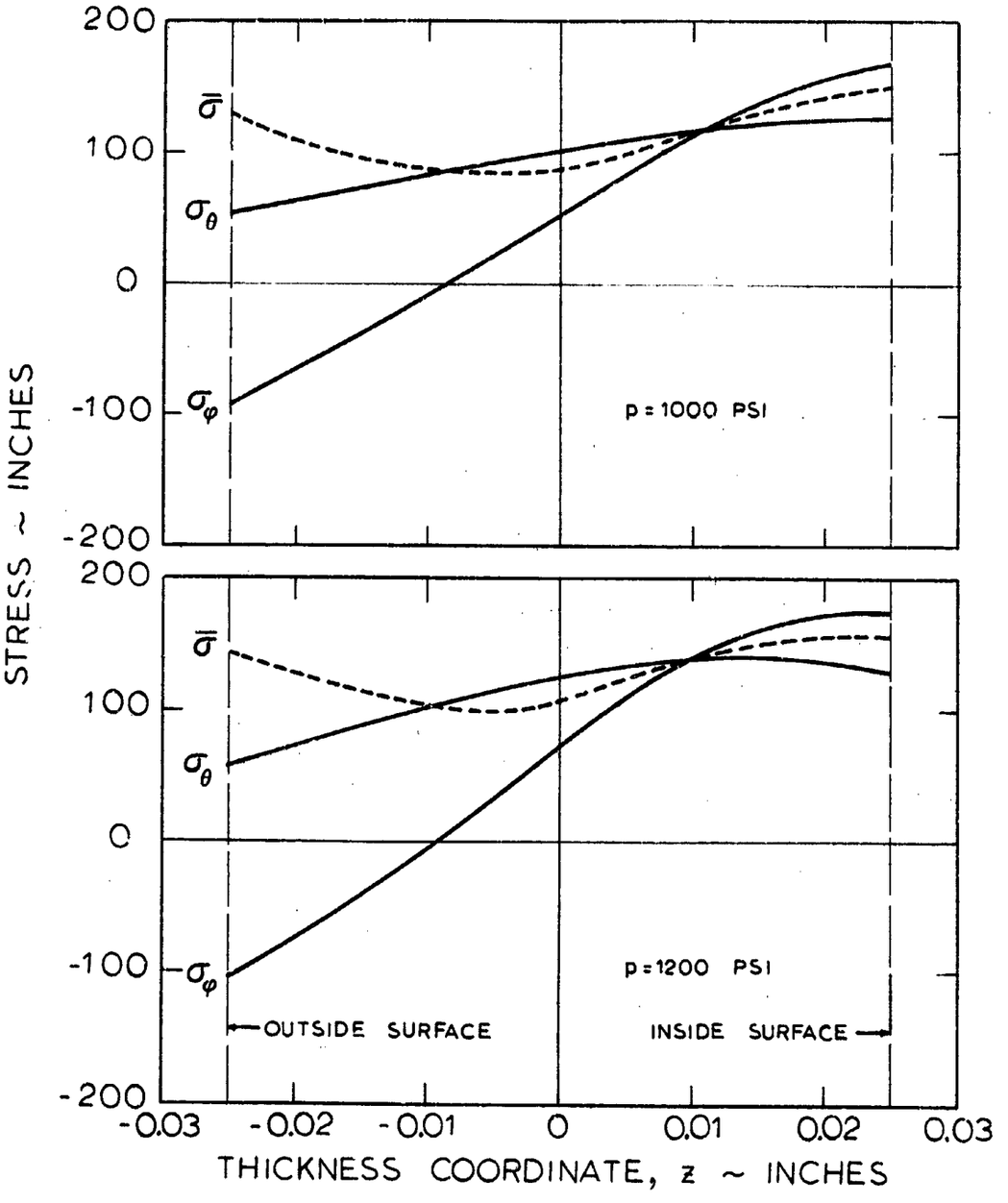

Fig. 3-5 Cylinder with 100% Mismatch: Stress at Discontinuity

level at the discontinuity. It appears that as the meridional stresses become large a compensatory effect takes place in the hoop direction; the point of maximum hoop stress is being pushed away from the discontinuity, thereby minimizing the growth of the equivalent von Mises stress (Eq. 2.3). The equivalent stress is, however, always maximum at the point of mismatch.

A further illustration of the development of stress as the pressure is increased is provided by Fig. 3-6. Meridional (σ_φ) and hoop (σ_θ) stresses at the inner and outer shell surfaces are shown for the cylinder with 50% mismatch (compare Figs. 3-2 and 3-3). As the pressure is increased the σ_φ vs. σ_θ curve approaches the final yield surface, bends over and follows it. The points shown along the initial loading path are for pressures of 0, 800, 1000, 1200, 1400, 1500, 1600, and 1650 psi, respectively. At the maximum load the effective*) strain is quite high: 0.0147, of which 0.0067 is plastic strain. Upon unloading from the maximum pressure to a point of zero pressure the shell will retain this plastic deformation, which results in the residual stresses indicated by the points "0" in the figure. Repeated loading and unloading from this point to the maximum pressure will take place elastically, with no plastic strains or residual stresses being added to the ones developed during the first load application.**)

The distribution of residual stress through the thickness at the point of mismatch is plotted in Fig. 3-7 and the residual stress variation along the meridian is plotted in Fig. 3-8. The maximum residual stress occurs at the surface, in this example. The possibility that the maximum residual

*) See definition, Eq. (2.16)

**) This pertains to the mathematical model used in the EPSOR [2] computer program, which does not recognize creep. Creep seems, to some extent, to have been present in the models in the test program. (See Section 8)

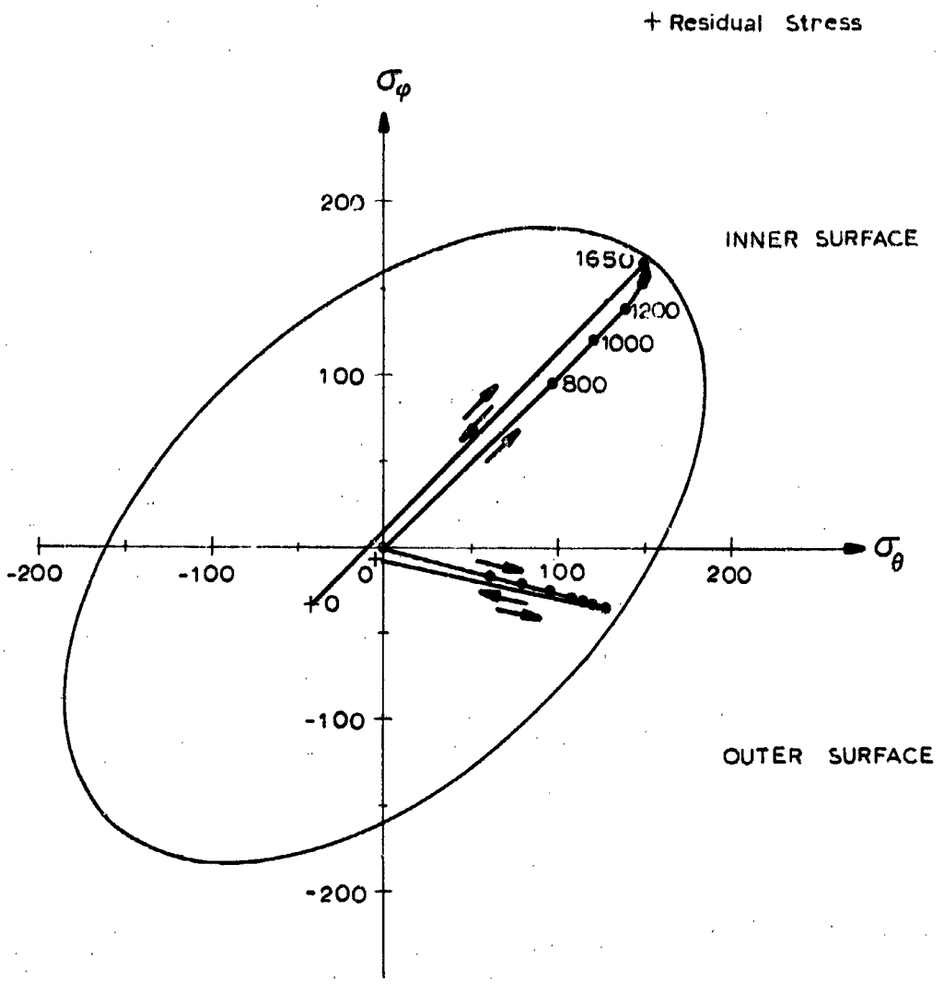

Fig. 3-6 Repeated Loading on Uniform Thickness Cylinder with 50% Mismatch. Computer Results.

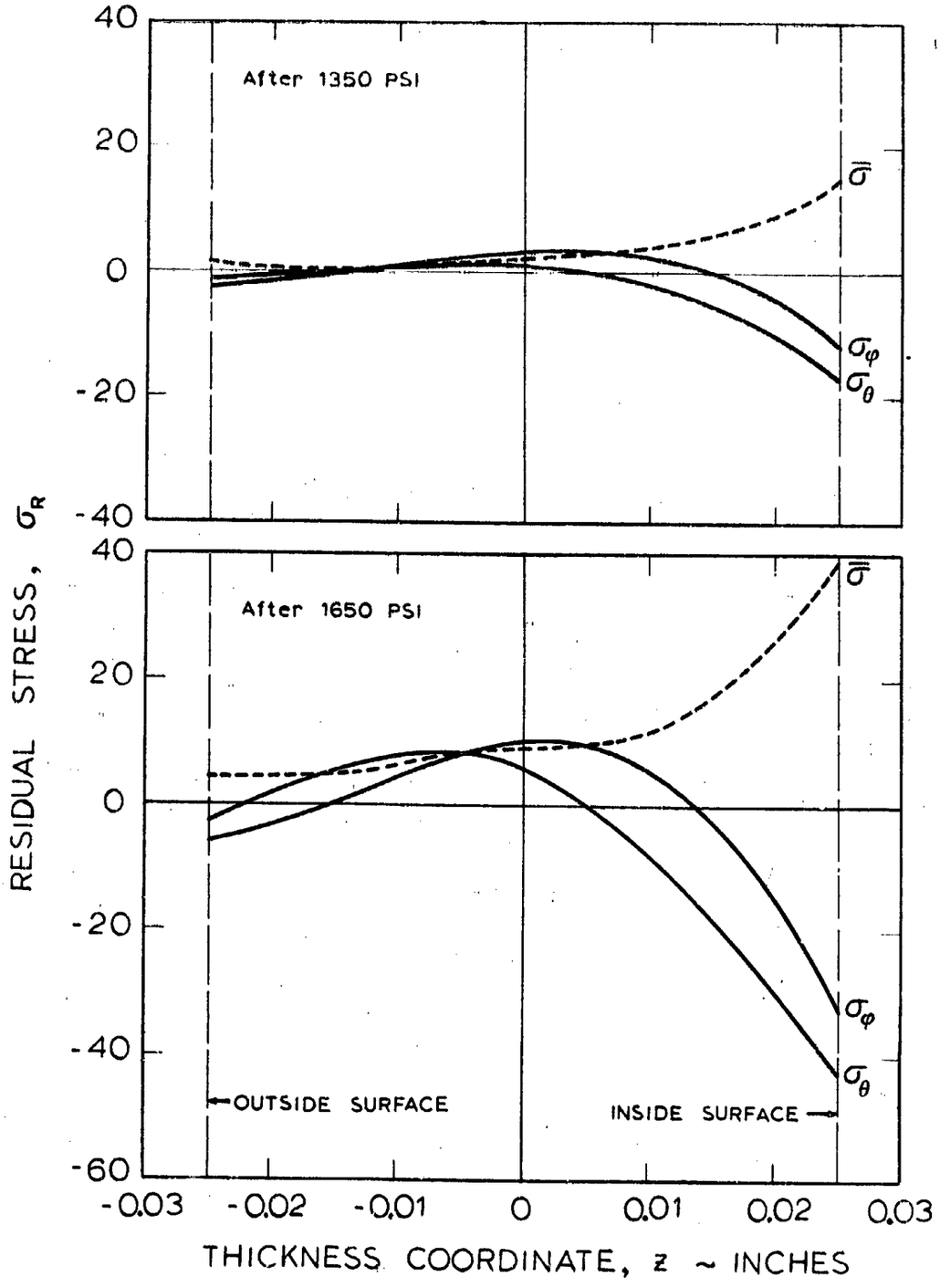

Fig. 3-7 Residual Stress in Cylinder with 50% Mismatch

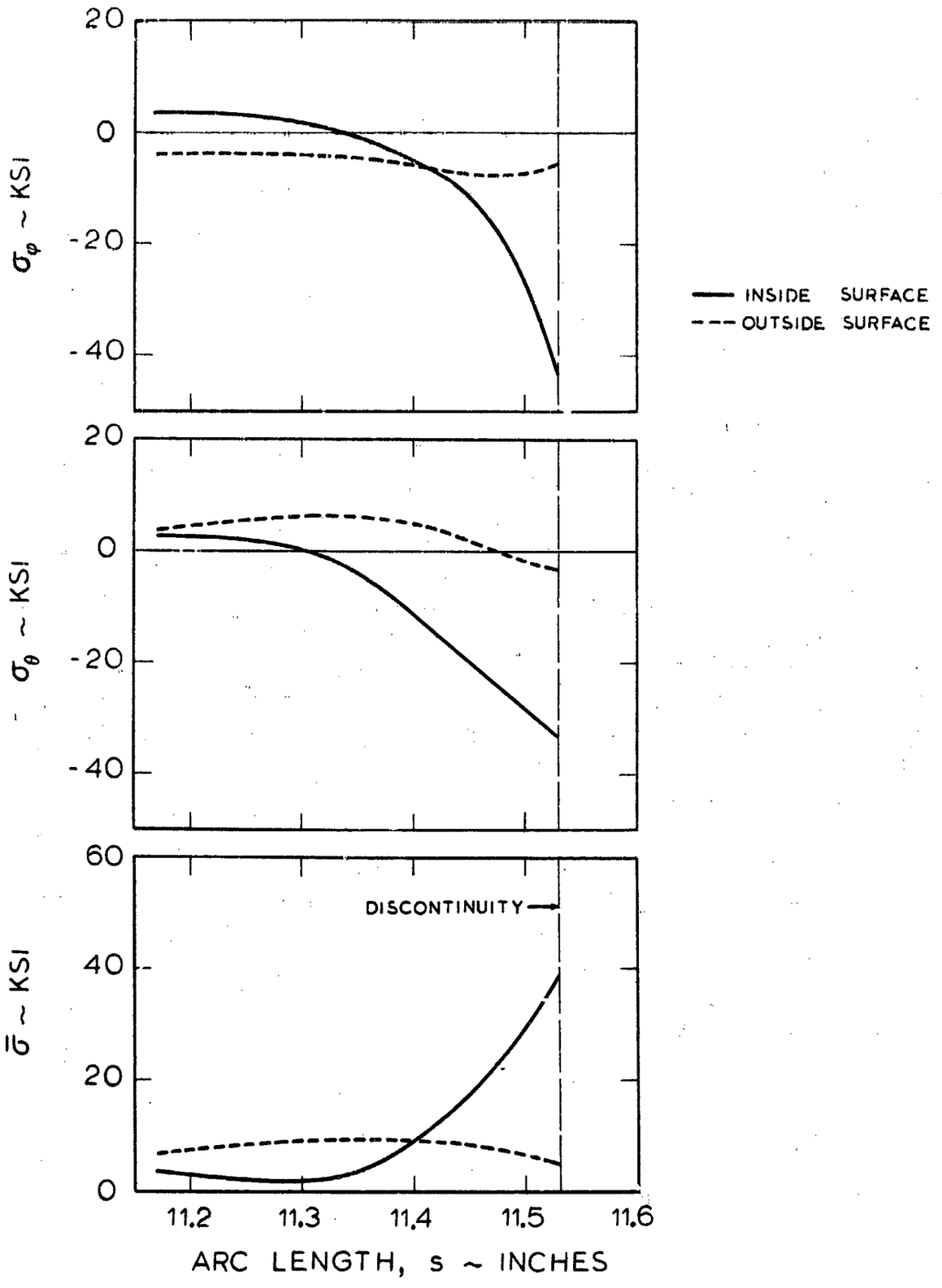

Fig. 3-8 Cylinder with 50% Mismatch: Residual Stress after Pressurizing to 1650 psi (p/p_m = .893)

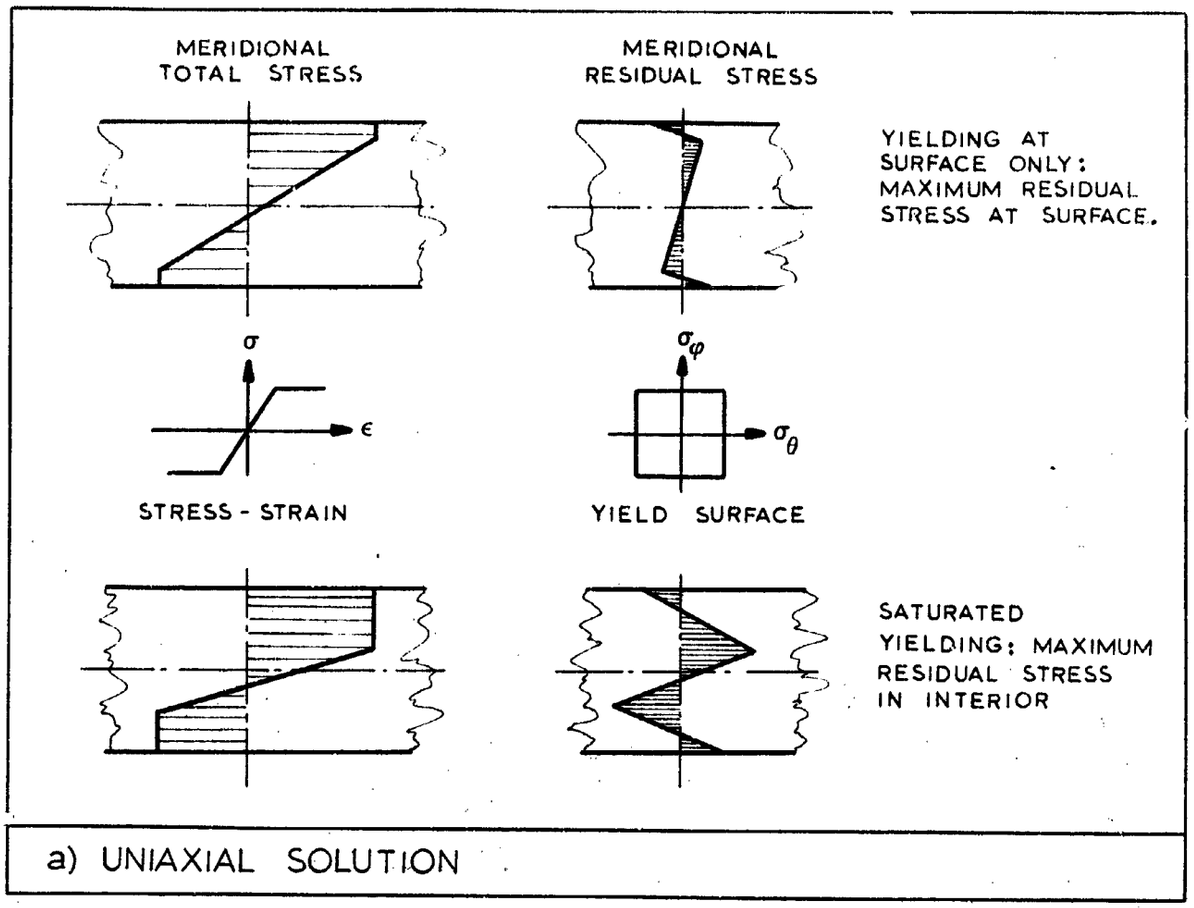

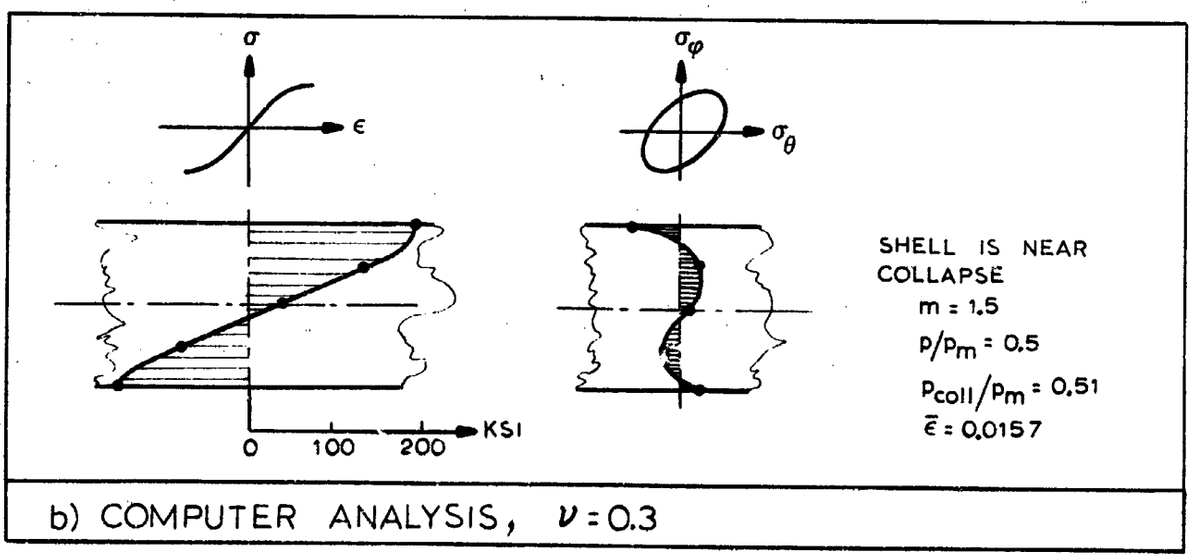

Fig. 3-9 Residual Stresses

stress occurs in the shell interior is not very large; this would require a very saturated yielding through the thickness. A qualitative example of this is shown in Fig. 3-9a, where by elementary uniaxial methods*) the residual stress has been calculated for an assumed through-the-thickness stress distribution. When the yielding becomes saturated, the maximum residual stress is shown to move from the surface to the interior. This does, however, require strains of a higher order than those developable in typical pressure vessel materials. Figure 3-9b illustrates this point: biaxial computer results obtained for a cylinder with a mismatch of m = 1.5 with a pressure very close (98%) to the collapse pressure are plotted there. The maximum stress is still on the surface. Note the principal similarity between the simple analysis and the computer solution; the differences that occur are due to the differences in stress-strain curves and yield surfaces.

3.2 Weld Land

The configuration of the weld lands studied in the present work is shown in Fig. 3-10. This particular geometry is arbitrarily chosen; it does, however, reflect the general practice in current pressure vessel design, i.e., a relatively short, uniform thickness region with a longer, smoothly varying transition zone between the weld land area and the basic membrane shell. All the thickening takes place on the outside surface, thus creating a shell centerline which is locally not a cylinder.

The thickness in the transition zone is described analytically as

$$t(s) = A_o + A_1 s^{m_1} + A_2 s^{m_2} + \ldots \qquad (3.10)$$

*) The shell is unloaded by elastic deformation in such a way that the applied bending moment vanishes. See Appendix A for a rigorous, closed-form solution for residual stresses.

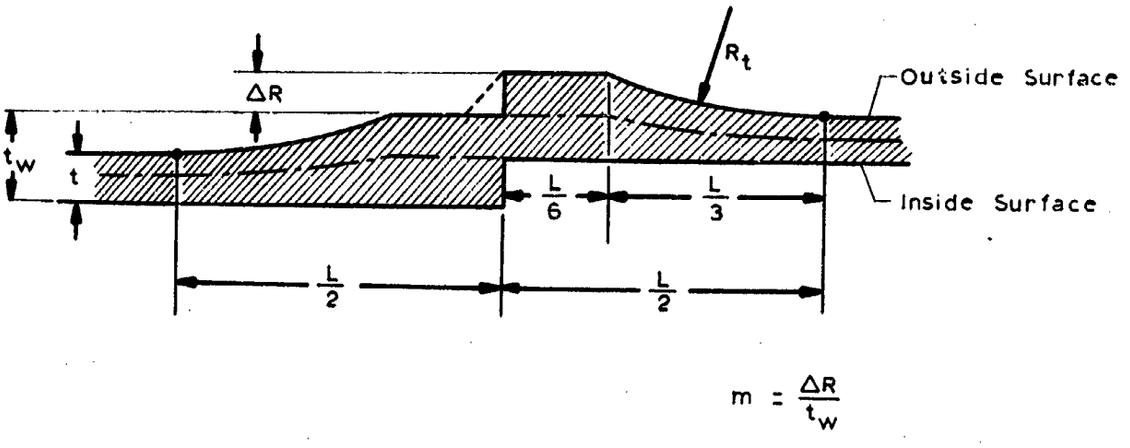

Fig. 3-10 Weld Land Configuration

where the A's and the m's are arbitrary constants. In the parametric runs that were performed on the BOSOR program only the first two terms in Eq. (3.10) were retained, and m_1 was set equal to 2. This results in a transition zone with a variable thickness very close to that which would be obtained by a constant value on the radius R_t, such as would be the case in an actual pressure vessel. The weld fillet (the dashed line in Fig. 3-10) was neglected in the analysis. This simplification results in a very slight conservatism in the analysis for mismatch values larger than about 0.5; when the mismatch approaches 1.0 the elastic stress overestimation is 2-3 percent for practical designs (see Fig. 2-5 of Ref. [1]).

It is usual in shell analysis to use the middle surface as a reference point, and to refer all forces to that surface. This means, among other things, that the pressure is acting on the middle surface, not the internal or external surface. It also means that in areas like the weld land transition zone the middle surface describes a complicated, curved, shell, and that problems regarding overlapping thicknesses and missing material arises, as illustrated by Fig. 3-11. This difficulty has been overcome in the EPSOR program by the use of an arbitrary surface as the

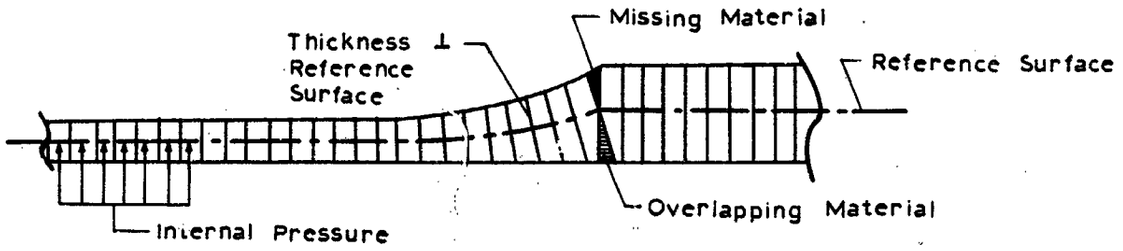

Fig. 3-11 Middle Surface as Reference Surface

reference surface. In the work described here the inside surface has been used as a reference, which accomplishes three things: a) the pressure is applied to the correct surface, b) no overlapping thickness problems arise (see Fig. 3-12), and c) description of meridional geometry is simplified.

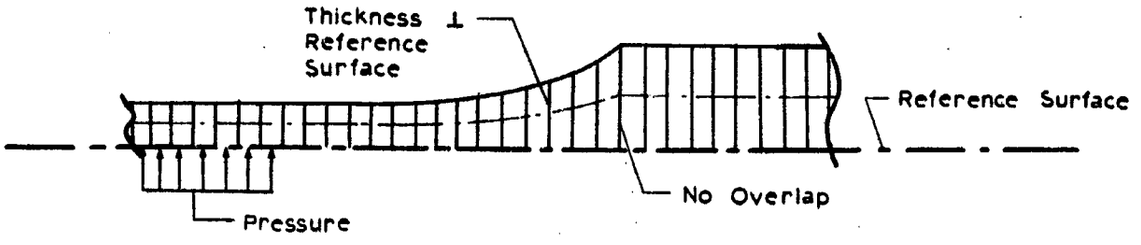

Fig. 3-12 Inside Surface as Reference Surface

The basic difference between the shells with a weld land and shells without one is the lack of moment symmetry for the former type of shell. Fig. 3-13 illustrates this: Due to the varying thickness a moment M_o

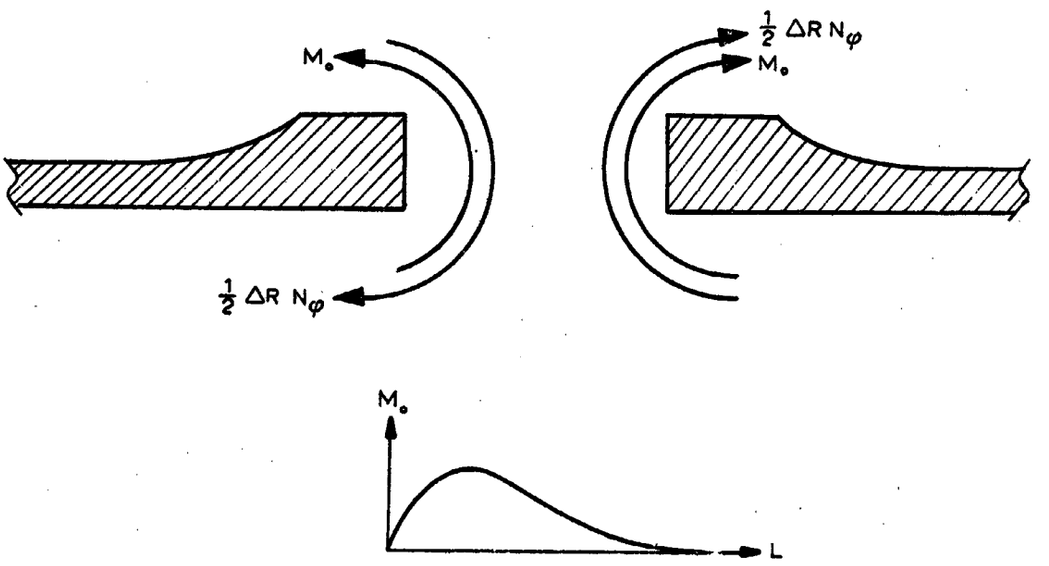

Fig. 3-13 Moments at a Weld Land with Mismatch

is created, which is independent of the mismatch. The mismatch itself also adds a moment, $\frac{1}{2}\Delta R N_\varphi$. The direction of the moments is shown in Fig. 3-13. Note that to the left the two moments are opposing each other, while to the right the two moments are added to each other. Thus, the critical region becomes the inside surface of the right shell, where the moment adds tension to the basic state of stress, which also is tension. The moment M_o is, obviously, a function of the land length L, being 0 when $L \to 0$ and $L \to \infty$, and a maximum for some intermediate value, as implied in the figure. Thus, for both very short and very long weld lands the behavior will resemble that of the uniform thickness shell. (There is a small

nonlinear effect on the induced moment M_o. The maximum deviation from linearity at the point of mismatch found in any of the computer runs made in the present work was less than one percent for nonlinearity parameter values up to 1.*) For most runs it was less. This nonlinearity is too small to be of any practical consequence.)

Typical stress distributions along the meridian are shown in Fig. 3-14. These figures are for a weld land configuration which is close to what might be considered a "best" configuration, i.e., it is sufficiently thickened (25% extra thickness) to prevent failure in weld for reasonable mismatch values, say up to 25% mismatch. The curves in Fig. 3-14 pertain to a 50 percent mismatch and are drawn for several pressure levels from the elastic and into the very high plastic region. In the elastic region (see the curve marked "600") both the meridional and the hoop stresses are maximum at inside fiber at the right-hand part of the mismatch. On the left part the stresses are lower, and reach their highest values at the outside surface. The absence of anti-symmetry, which would be expected from the discussion in connection with Fig. 3-13, is clearly indicated. For higher loads, into the plastic region, the maximum meridional stress remains at the inside of the right hand side part of the shell, while there is a shift of the maximum hoop stress to the outside of the left hand shell. (For pressures larger than 600 psi only the outer fiber stresses are shown for the left hand side, and the inner fiber stresses for the right hand side shell.) The effective stress does, however, remain at the inside of the right side for this case, as it was in all the cases run in the present investigation. The stress distributions through the thickness at the left and the right side of the mismatch are shown in Figures 3-15 and 3-16, and the residual stresses in Fig. 3-17. These results are quite similar to the ones given above for the uniform thickness case. In fact, it was

---

*) Nonlinearity parameter $\rho = \dfrac{p}{\dfrac{2}{\sqrt{3(1-\nu^2)}} E \left(\dfrac{t}{R_2}\right)^2}$, see [1]

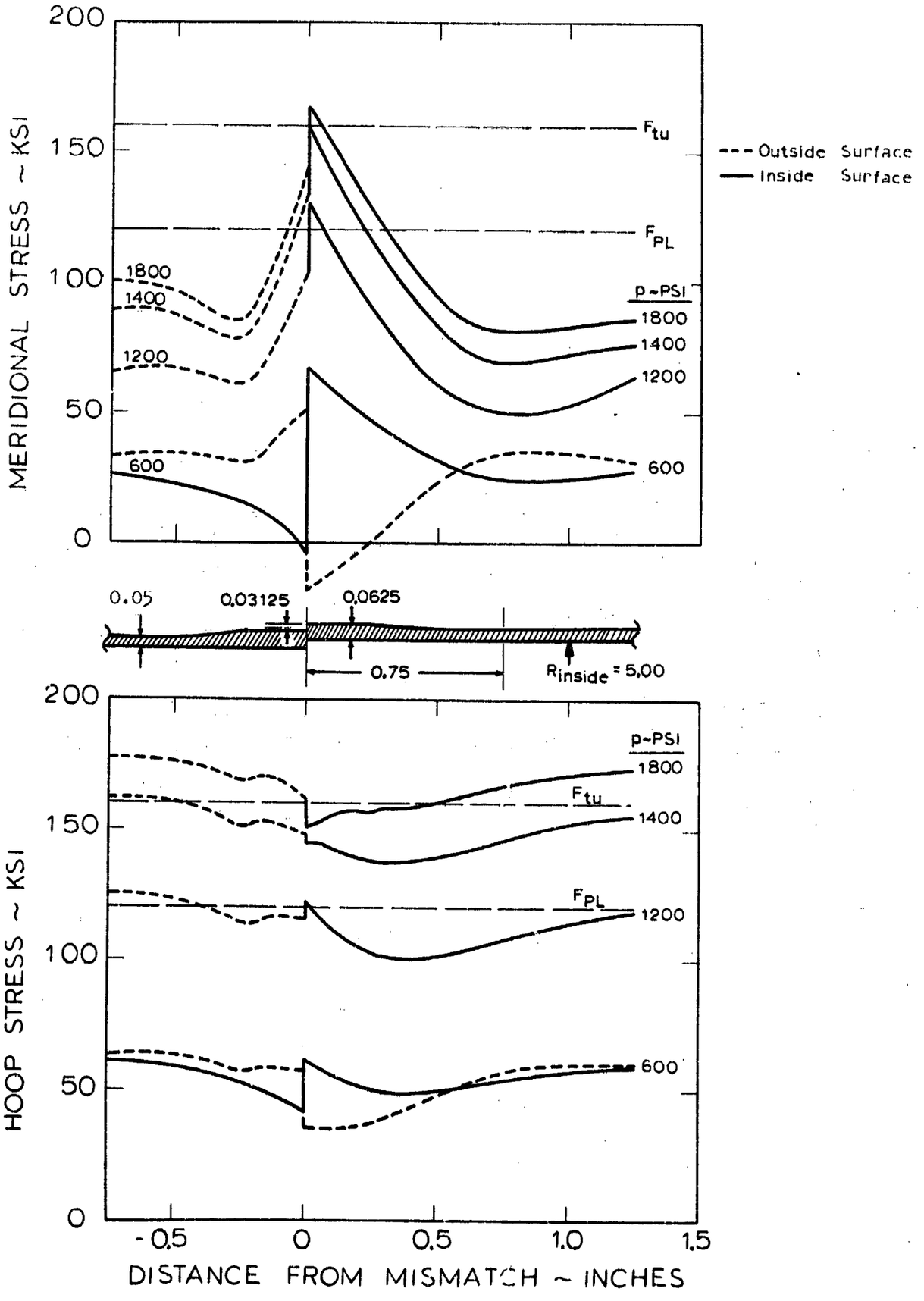

Fig. 3-14 Cylinder with Weld Land and 50% Mismatch

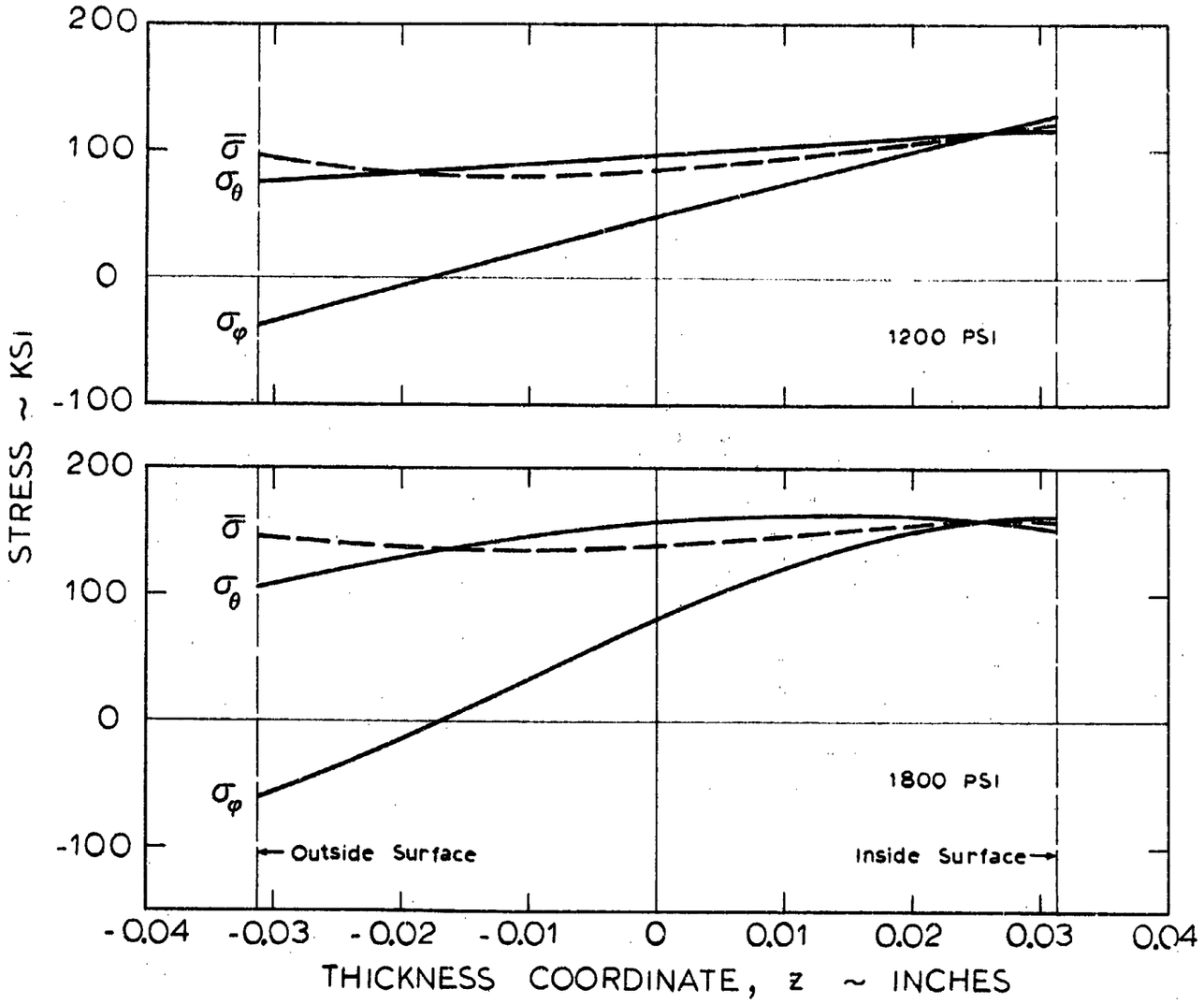

Fig. 3-15 Stress at Right-Hand Side of Discontinuity
(Same Configuration as in Fig. 3-14)

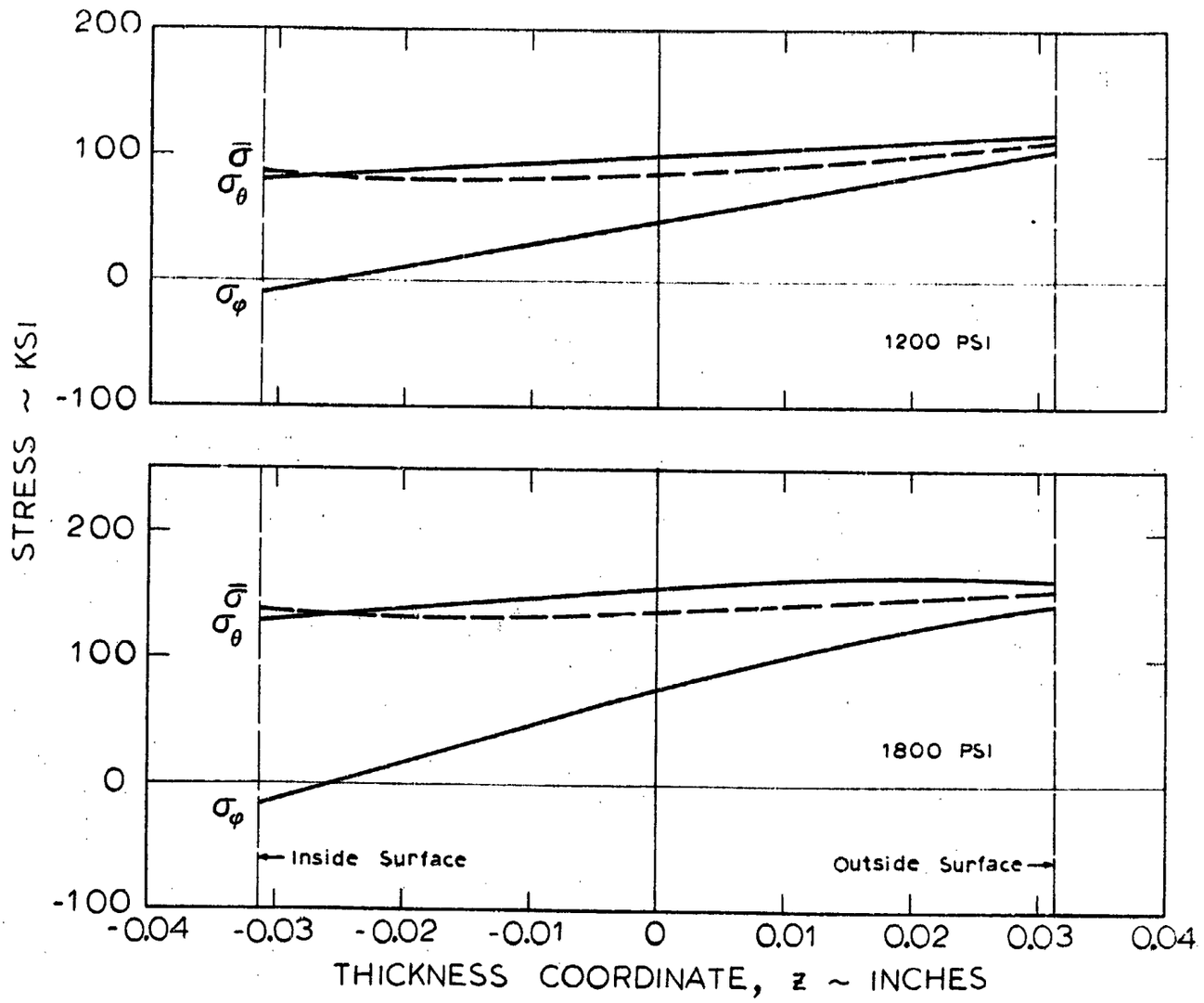

Fig. 3-16 Stress at Left-Hand Side of Discontinuity
(Same Configuration as in Fig. 3-14)

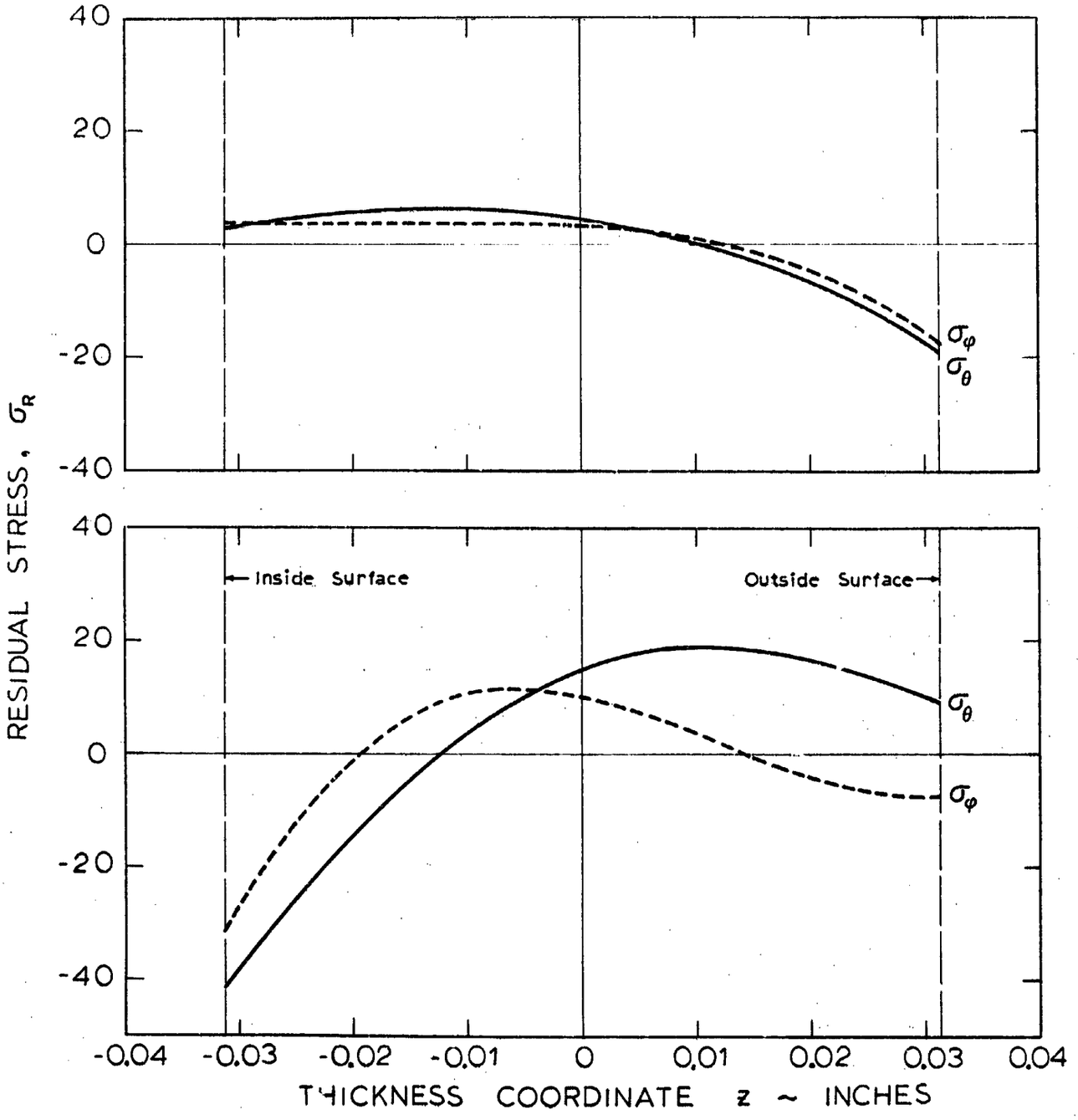

Fig. 3-17 Residual Stress After 1800 psi
(Same Configuration as in Fig. 3-14)

found that the residual stresses are the same for both uniform and non-uniform thickness shells, provided that the residual strain is the same.

Fig. 3-18 shows some results from computer runs investigating the effect of the weld land length L. Note, that as L is decreased (the top part of the figure) the stress at the beginning of the weld land transition ($s = -0.4$) is increasing, so that there is a tendency for the critical zone to move away from the weld land into the membrane region. The stress curves shown in the figure are drawn for a pressure which places the stresses in the knee region (between the limit of proportionality and ultimate strength) at the stress-strain curve. The maximum stresses are not influenced very much (154 vs. 146 ksi) by the change in weld land length, but the maximum strain figures (1.07 vs. 0.87%) are quite different. As the pressure is increased the difference in strains is slightly more accentuated (at 1800 psi the maximum strains are 1.49 and 1.13%, respectively), but as the horizontal part of the stress-strain curve is approached these differences tend to lose their importance and collapse occurs at 1970 psi and 1700 psi, respectively.

The weld land lengths of the shells shown in Fig. 3-18 are quite short when considered in the light of the commonly quoted figure of $3\sqrt{Rt}$ for the attenuation length of a shell. The larger of the weld land configurations is only about one half and the shorter only about one quarter of this figure, and still the effective stress in the transition and membrane areas is not much different from the membrane stress. Thus it is seen that the weld land can be quite short. In the present investigation the shortest weld land length was $0.75\sqrt{Rt}$, including the transition length, which is the configuration in the top part of Fig. 3-18. Shorter weld lands than this are probably not practical, at least for moderately thin shells.

3.3 Design Graphs

The design graphs in Section 6 were prepared from the results given by the application of the computer program EPSOR to a series of weld land configurations with parametrically varied dimensions. The material used

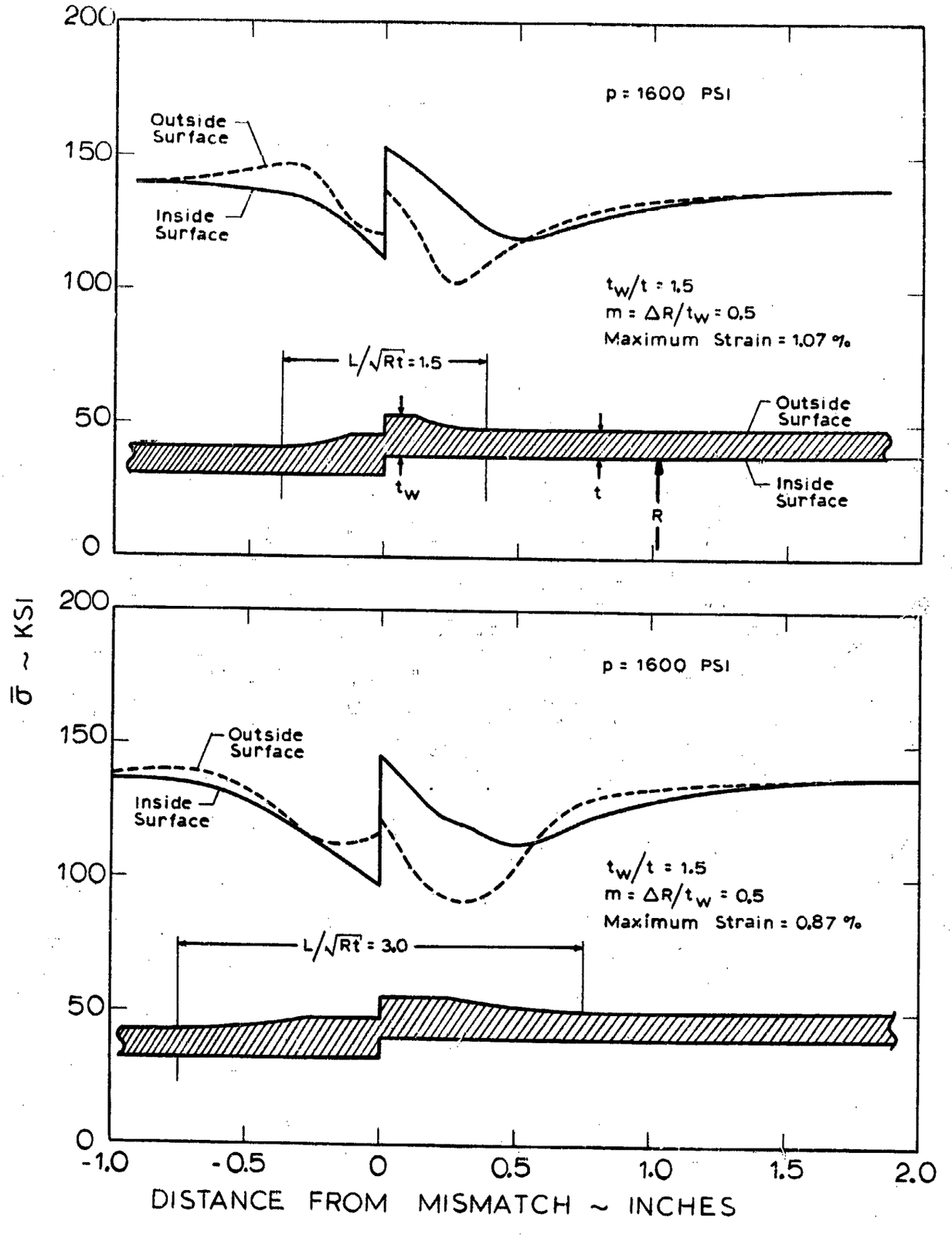

Fig. 3-18 Influence of Weld Land Length

in the computations is titanium 6Al-4V STA with properties as described by Fig. 2-3 (curve marked NASA). These properties extend throughout the shell; no degradation of material properties occur at the weld land. However, since the effects of the weld mismatch are very localized, the graphs may be used even when the material properties at the weld are lower than in the surrounding areas simply by using the actual material properties in the discontinuity area and assume that they pertain throughout the shell. Using the graphs in this way will be slightly conservative for the smaller (less than about 25%) mismatch, but will tend to become more and more accurate as the mismatch is increased.

In general the computer solutions converge relatively rapidly to the desired solution, but when the collapse pressure is approached it becomes more and more difficult to obtain convergent solutions. When the collapse pressure is exceeded no convergent solution is possible. A precise determination of the pressure at which the solution first becomes divergent is a quite difficult and lengthy process which had to be done by a trial-and-error approach. Due to this rather time-consuming process only a relatively few collapse pressures were determined, and the collapse pressures for other geometries were interpolated, three-dimensionally, from the computed values. An example of this is shown in Fig. 3-19, where collapse pressures for a weld land thickening of 50% ($t_w/t = 1.5$) are plotted versus weld land lengths. It was assumed (an assumption confirmed by the trends) that for values of the weld land length parameter $L/\sqrt{Rt}$ larger than 7, the weld land actually behaves as a shell of uniform thickness. For $L/\sqrt{Rt}$ values less than 7 there are 11 points shown in Fig. 3-19; these 11 points were used to define the entire surface of collapse pressures for this particular shell family.

The quantities used to normalize the design graphs are

- p_m, the collapse pressure for a uniform thickness pressure vessel without a discontinuity. p_m is defined for the thickness at the discontinuity, t_w, and is

$$p_m = \frac{2}{\sqrt{3}} \frac{t_w}{R} F_{tu}$$

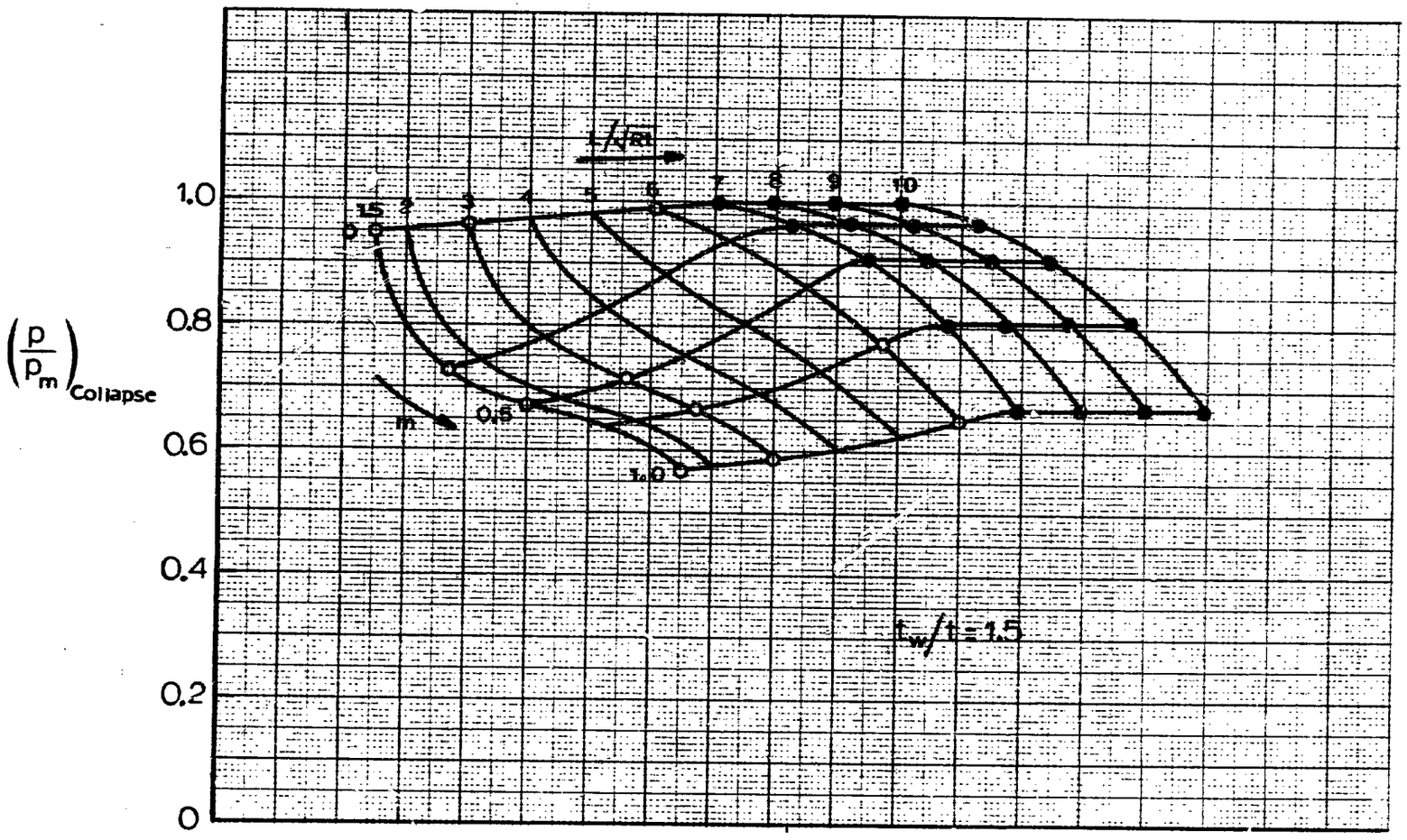

Fig. 3-19 Collapse Pressure for Weld Lands with Mismatch

(compare Eq. (2.13)). Note that the maximum weld land thickness, t_w, is used.

- The effective elastic strain $\bar{\epsilon}_y$ corresponding to p_m, defined by the sketch below

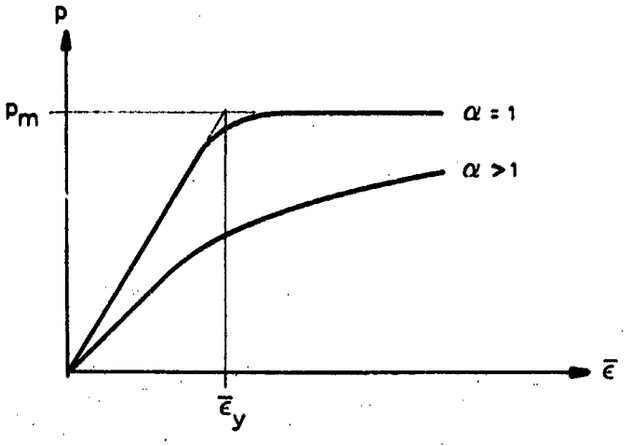

$$\bar{\epsilon}_y = \frac{2}{3}(1+\nu)\frac{F_{tu}}{E}$$

- The ratio $\tau = t_w/t$, where t_w is the thickness of the weld land (see Fig. 3-10) and t is the membrane thickness.

- The length ratio $L^* = \frac{L}{\sqrt{Rt}}$, where L is the combined length of the weld lands on either side of the discontinuity.

The design graphs were actually computed using the following material data (see also Fig. 2-3, curve marked NASA):

$$F_{ty} = 120{,}000 \text{ psi}$$
$$F_{tu} = 160{,}000 \text{ psi}$$
$$E = 17 \times 10^6 \text{ psi}$$

However, through the use of the normalizing parameter other materials with similar stress-strain curves may be used, at least for an approximate analysis.

The following technique was used to produce the design charts

1) Curves of p/p_m vs. $\bar{\epsilon}$ were computed for combinations of

$\tau = 1, 1.25, 1.5$

$L^* = 1.5, 3, 4.5, 6$

$m = 0, 0.25, 0.50, 0.75, 1$

2) Using the above curves three-dimensional crossplots for several values of $\bar{\epsilon}/\bar{\epsilon}_y$ were drawn.

3) Values from the three-dimensional crossplots were used to produce the series of two-dimensional design graphs in Section 6.

Examples of the three-dimensional graphs are shown in Figures 3-20a-e. In these figures the planes $L^* = 1.5$, 3, and 6 are fully defined for all combinations of τ and m. The plane $L^* = 4.5$ is defined only for ($\tau = 1$, $0 \leq m \leq 1$) and ($m = 0.5$, $\tau = 1.25$). All other values on the $L^* = 4.5$ plane are interpolated. A study of the plots in Fig. 3-20 indicates that linear interpolation between the parameter values selected in the set of design graphs in Section 6 is permissible without introducing any appreciable errors.

The residual stress graphs in Section 6 are based on computer runs for the uniform thickness case. The graphs have been checked for values computed for the weld land configurations. Fig. 3-21 shows this comparison. The points plotted there are for the entire range of parameters used in the investigation. No difference attributable to the geometry is evident, however, for the small mismatch of $m = .25$ there appears to be a tendency for the weld land configurations to have somewhat smaller residual stress than the uniform thickness shells. This difference, which is probably due to the softening of the shell due to plastic effects away from the thickened weld land area, has been ignored as far as the residual stress design graphs are concerned. This introduces a slight degree of conservatism for weld lands with mismatches of 25% or lower.

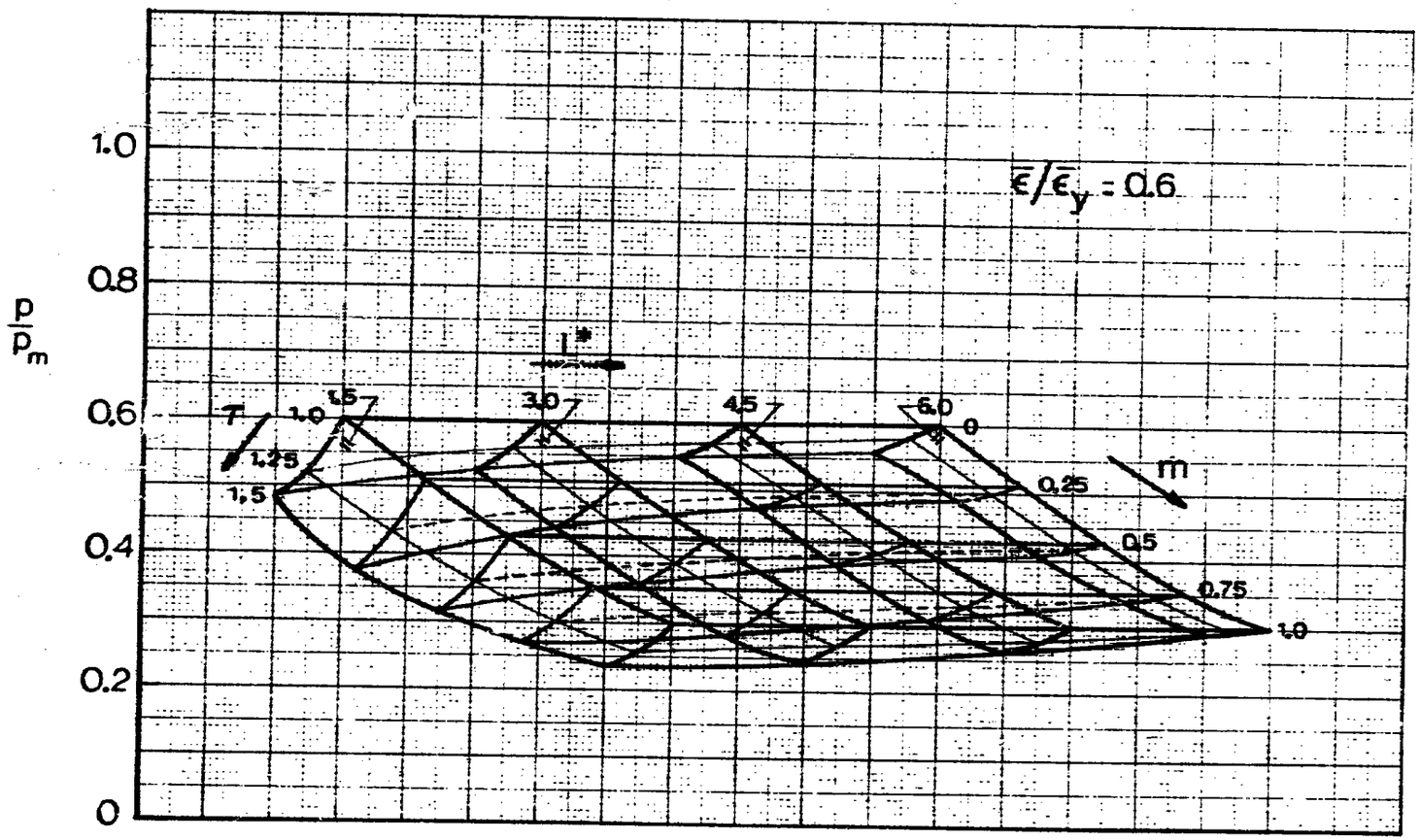

Fig. 3-20a Influence of Weld Land Geometry, Cylinder-Cylinder

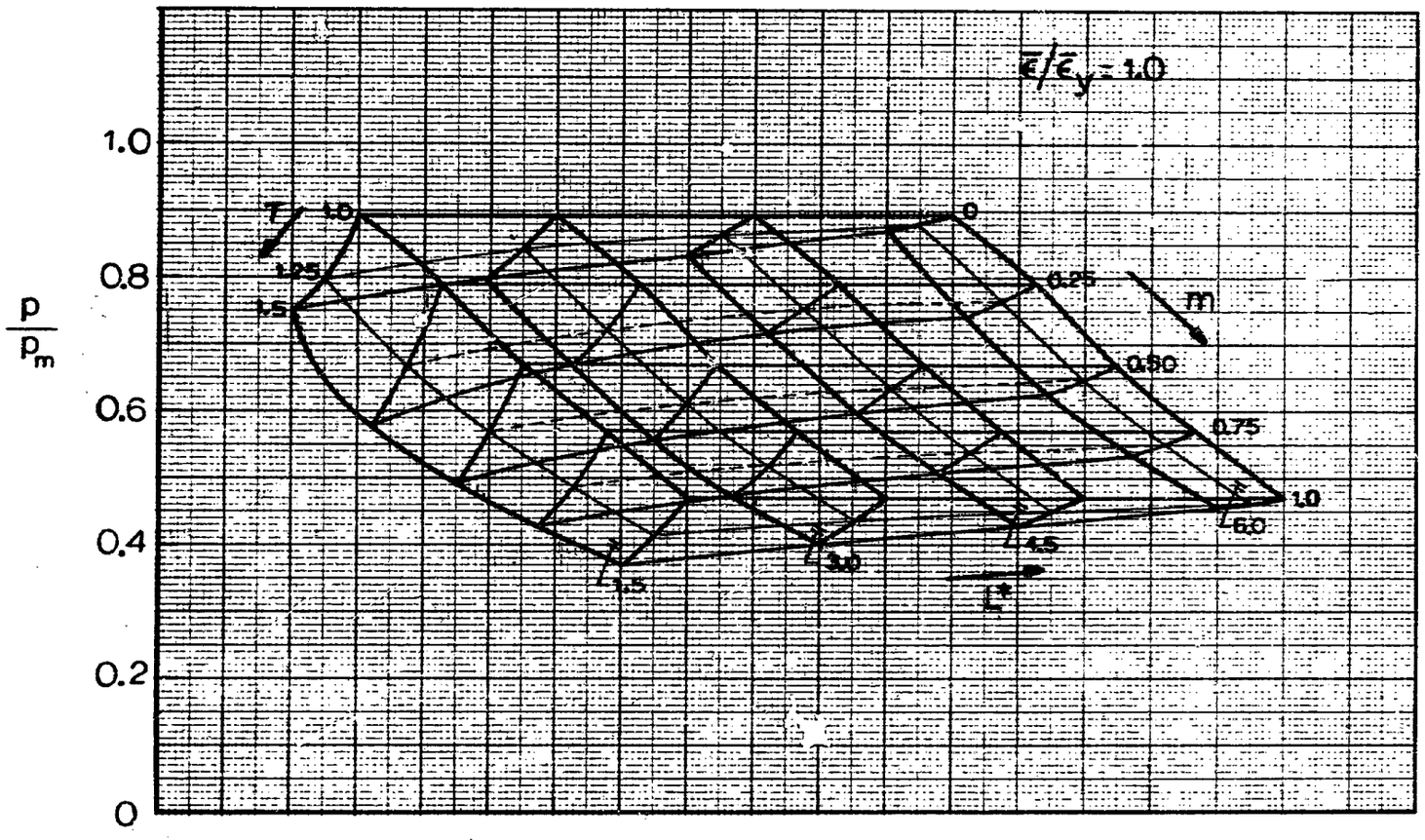

Fig. 3-20b Influence of Weld Land Geometry, Cylinder-Cylinder

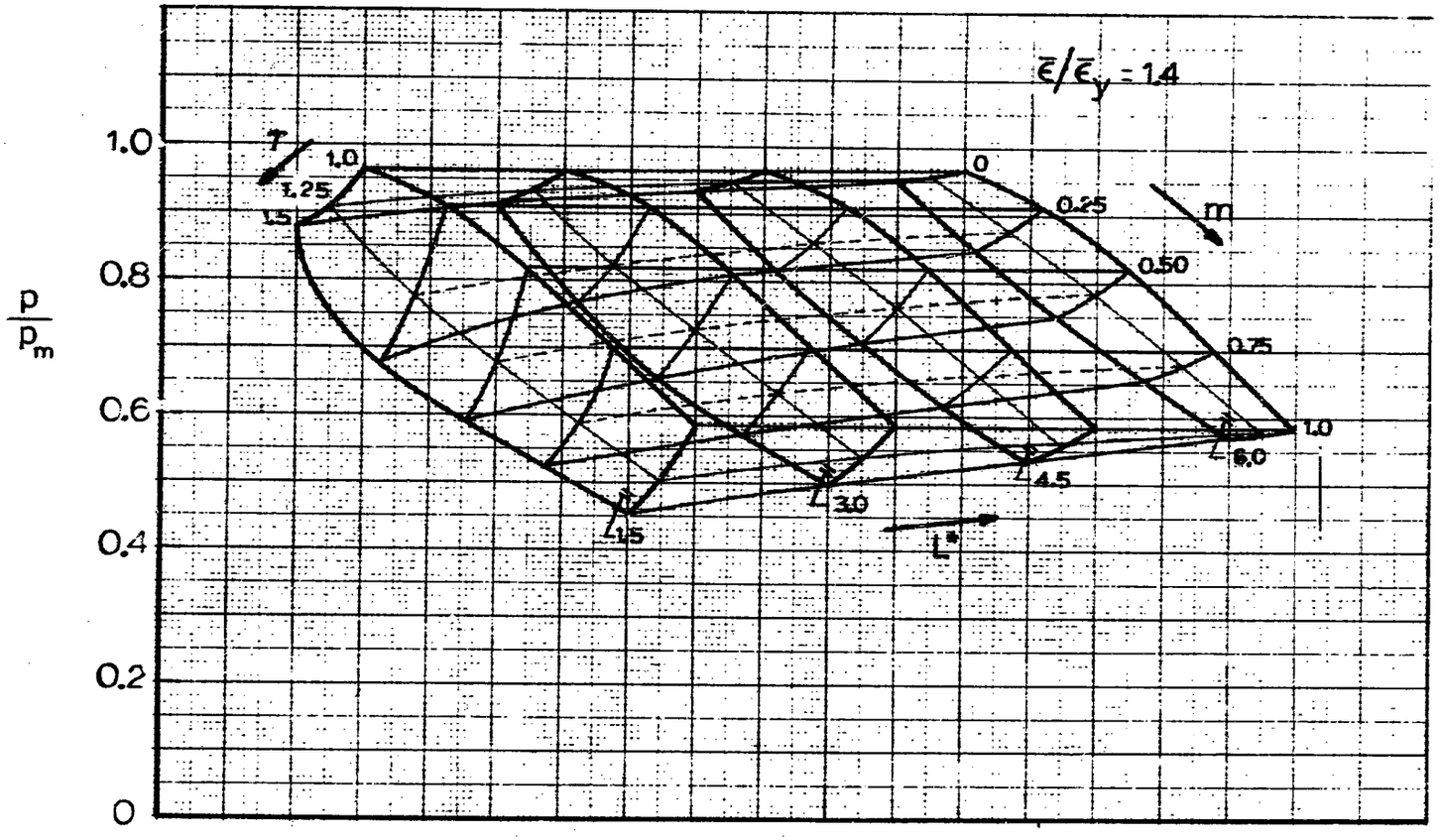

Fig. 3-20c Influence of Weld Land Geometry, Cylinder-Cylinder

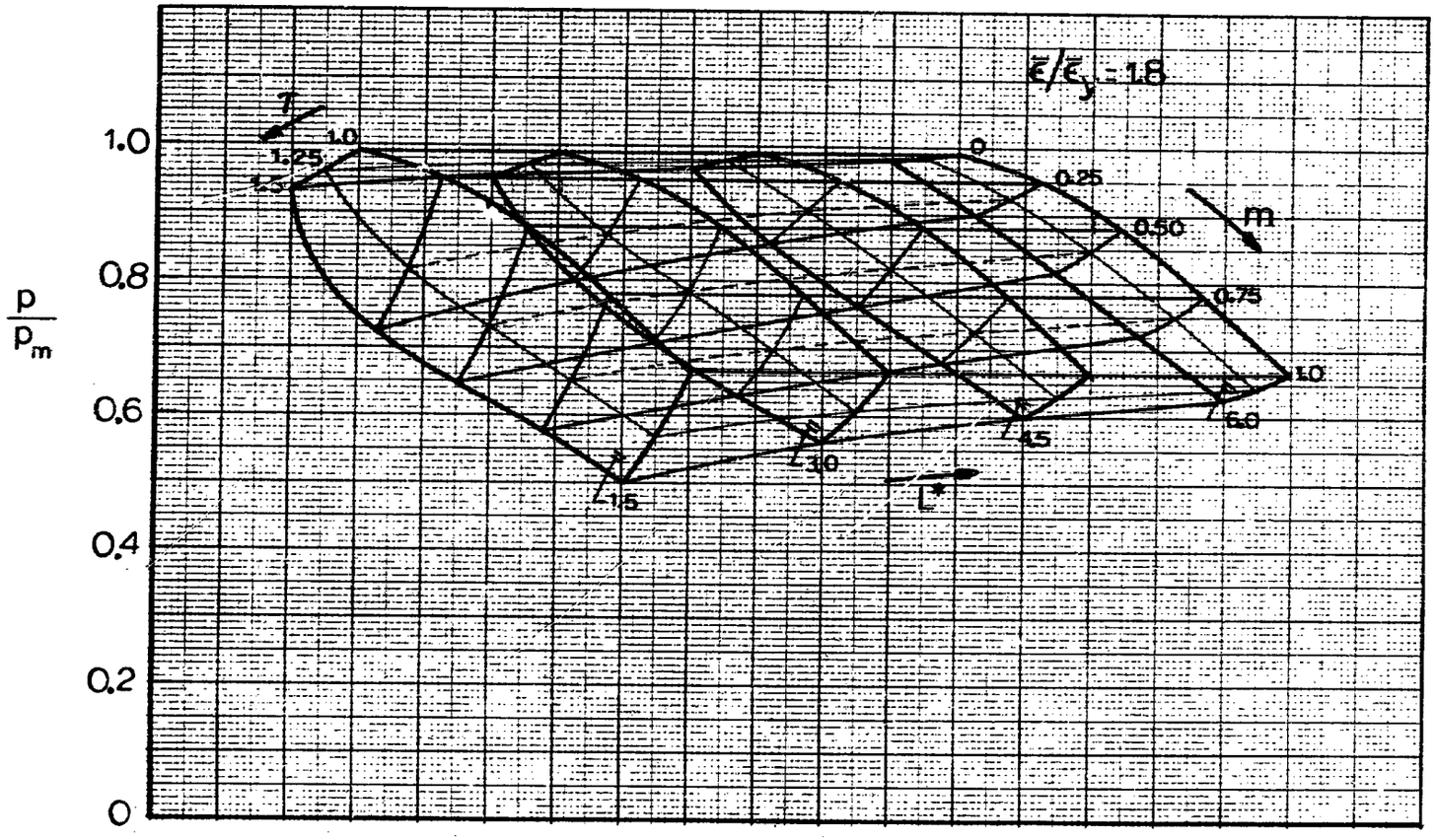

Fig. 3-20d Influence of Weld Land Geometry, Cylinder-Cylinder

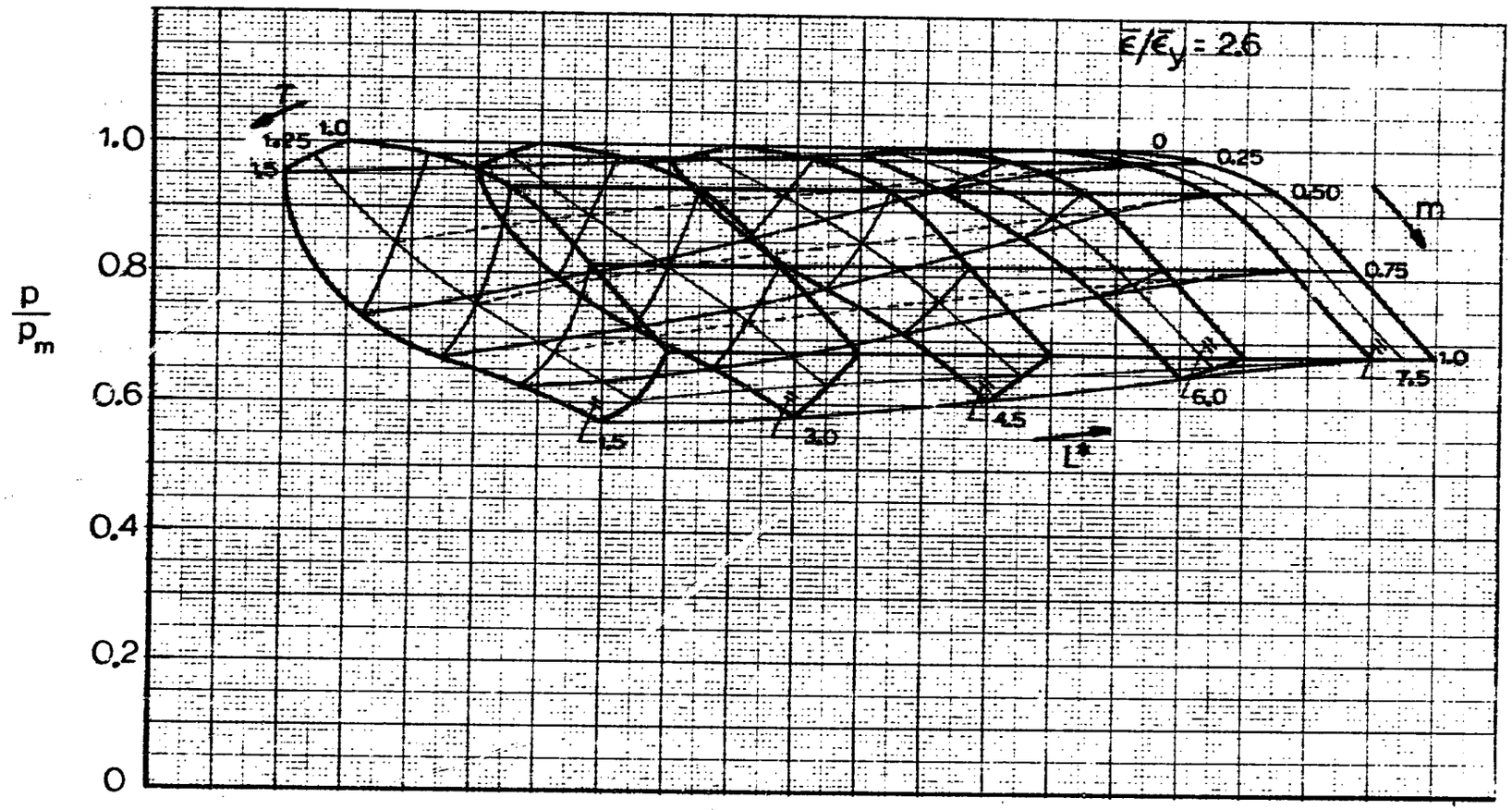

Fig. 3-20e Influence of Weld Land Geometry, Cylinder-Cylinder

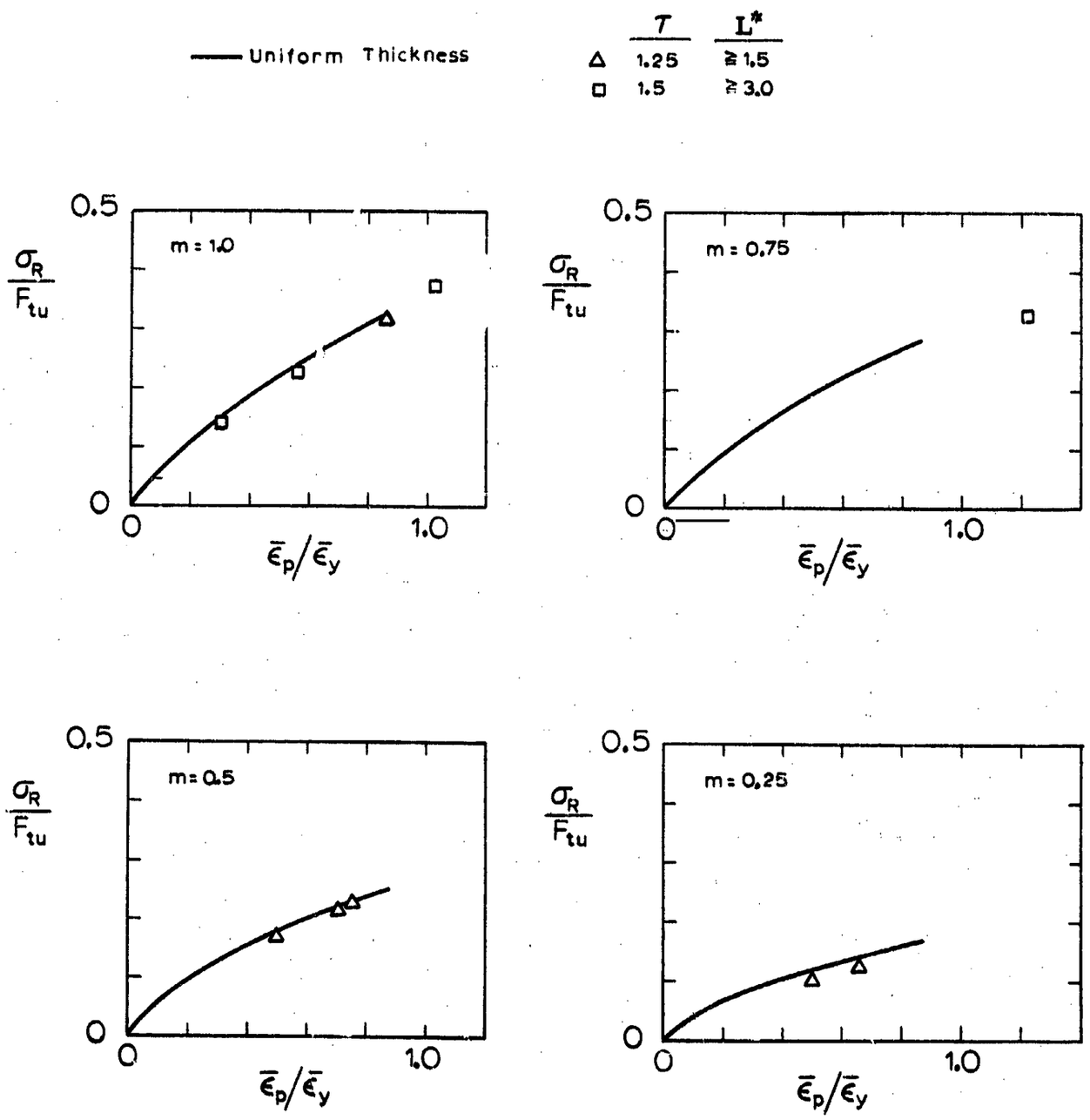

Fig. 3-21 Residual Stress in Cylinder-Cylinder Junctures: Comparison between Uniform Thickness and Weld Land Configurations

Section 4

MISMATCH IN SPHERE/CYLINDER JUNCTURES

The problem of a mismatch at the juncture between a hemispherical and cap and a cylinder is quite similar to that of a mismatch between two cylinders. However, there are differences, such as the different ratio of meridional to hoop stress, and the fact that the juncture itself is a discontinuity, which does not allow a pure membrane state of stress.

4.1 Uniform Thickness

The calculation of the stresses at a juncture of a hemisphere and a cylinder is an elementary problem of shell analysis. If the thicknesses of the hemisphere and the cylinder are equal, one finds (if the shells are thin) that the only redundant forces needed for compatibility of deformations are shear forces at the juncture, see Fig. 4-1. The magnitude of the

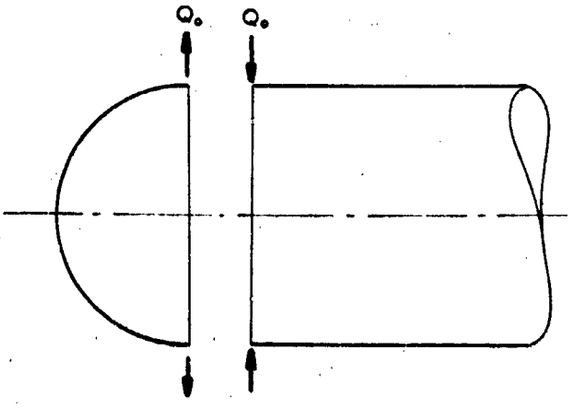

Fig. 4-1 Shear Forces at Hemisphere-Cylinder Juncture

shear stresses is small and the main effect of the shear forces is to modify the normal stress distribution in the vicinity of the juncture. Timoshenko [3] shows that the maximum meridional stress occurs in the cylinder at the distance $0.61\sqrt{Rt}$ from the juncture, and the maximum hoop stress occurs in the cylinder at a distance $1.44\sqrt{Rt}$ from the juncture. The stresses at these points are

$$\sigma_{\varphi_{max}} = 1.293 \frac{pR}{2t} \quad \text{at} \quad s = 0.61\sqrt{Rt} \tag{4.1}$$

$$\sigma_{\theta_{max}} = 1.032 \frac{pR}{t} \quad \text{at} \quad s = 1.44\sqrt{Rt} \tag{4.2}$$

At the juncture itself the stresses are

$$\left.\begin{aligned} \sigma_{\varphi} &= \frac{pR}{2t} \\ \sigma_{\theta} &= \frac{3}{4}\frac{pR}{t} \end{aligned}\right\} \text{at} \quad s = 0 \tag{4.3a,b}$$

Thus the uniaxial maximum stresses are significantly different from the membrane stresses. The maximum biaxial effective stress (Eq. 2.3) does not, however, exceed the membrane stress; results from the EPSOR computer program shows that the maximum effective membrane stress exceeds the effective membrane stress by only 0.5%, at a distance of about $2\sqrt{Rt}$ from the juncture. Fig. 4-2 shows the effective stress distribution in the vicinity of the juncture. It is quite clear that the juncture is not the critical area of this shell configuration, and that the strength of the pressure vessel is unaffected by the juncture. In fact, a mismatch may exist at the juncture without affecting the strength of the pressure vessel.

The existence of a bending moment in the vicinity of the juncture will have some influence on the stresses produced by a mismatch at the juncture. This effect is, however, quite small, and it is believed that the differences found in the behavior of the hemisphere-cylinder case

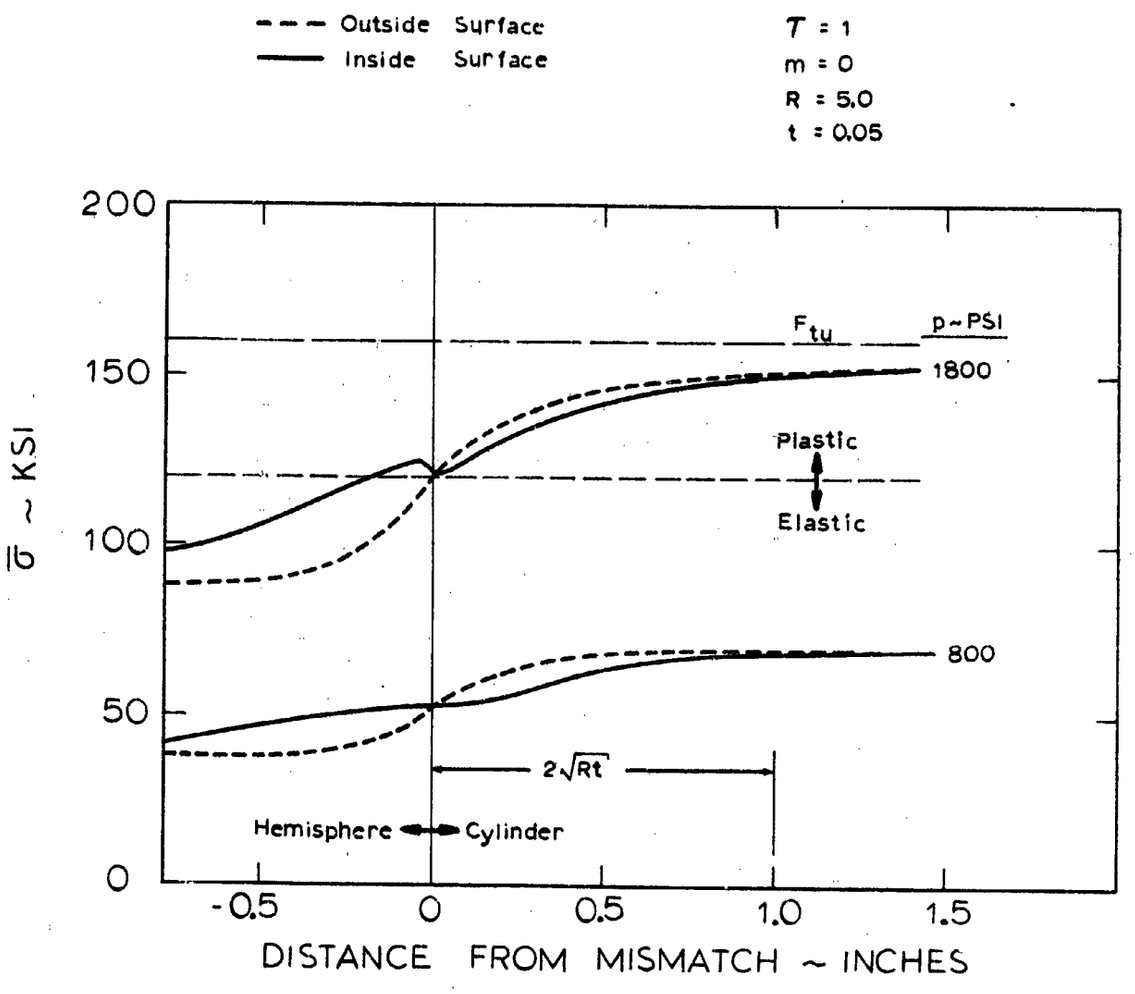

Fig. 4-2 Effective Stress, Cylinder with Hemispherical Cap

compared to the cylinder-cylinder case are mainly caused by the different ratios of meridional to hoop stress at the juncture. A rather complicated interrelationship must exist between the various discontinuities at the juncture (mismatch, change of curvature between hemisphere and cylinder, and variable thickness if a weld land is used). Even so, the gross behavior of the stress distributions is very similar to that of the cylinder-cylinder case, especially for larger values of the mismatch. This similarity of behavior suggests the idea of an equivalent mismatch, which is being pursued here briefly.

From Eq. (4.3) it is found that the quantity n, defined in Section 2, is

$$n = \frac{\sigma_\theta}{\sigma_\varphi} = \frac{3}{2}$$

which value upon substitution in Eqs. (2.9) and (2.13) gives

$$\bar{\sigma} = \frac{N_\varphi}{t} \frac{\sqrt{7}}{2} \left[1 \pm \frac{6}{7} (1+4\nu)m + \frac{36}{7} (1+\nu^2-\nu) m^2 \right]^{1/2} \tag{4.4}$$

and

$$p_m = \frac{4}{\sqrt{7}} \frac{t}{R} F_{tu} \tag{4.5}$$

The quantity $[\ ]^{1/2}$ in Eq. (4.4) is, as previously defined, the stress factor α. This factor is plotted in Fig. 4-3 (compare also Fig. 2-2) together with the similar factor for the cylinder-cylinder case ($n = 2$). Note, for example, that a mismatch of 1.0 in the sphere-cylinder case results in the same stress factor as a mismatch of 1.43 in the cylinder-cylinder. In the lower part of the figure this mismatch equivalence is plotted for the range of mismatches, and it is found that the cylinder-hemisphere juncture in general can take a mismatch which is 1.4-1.5 times as large as in the cylinder-cylinder juncture, for the same elastic equivalent stress factor α. As another example, take a mismatch of $n = 1$ and calculate the effective stress using values of α from Fig. 4-3:

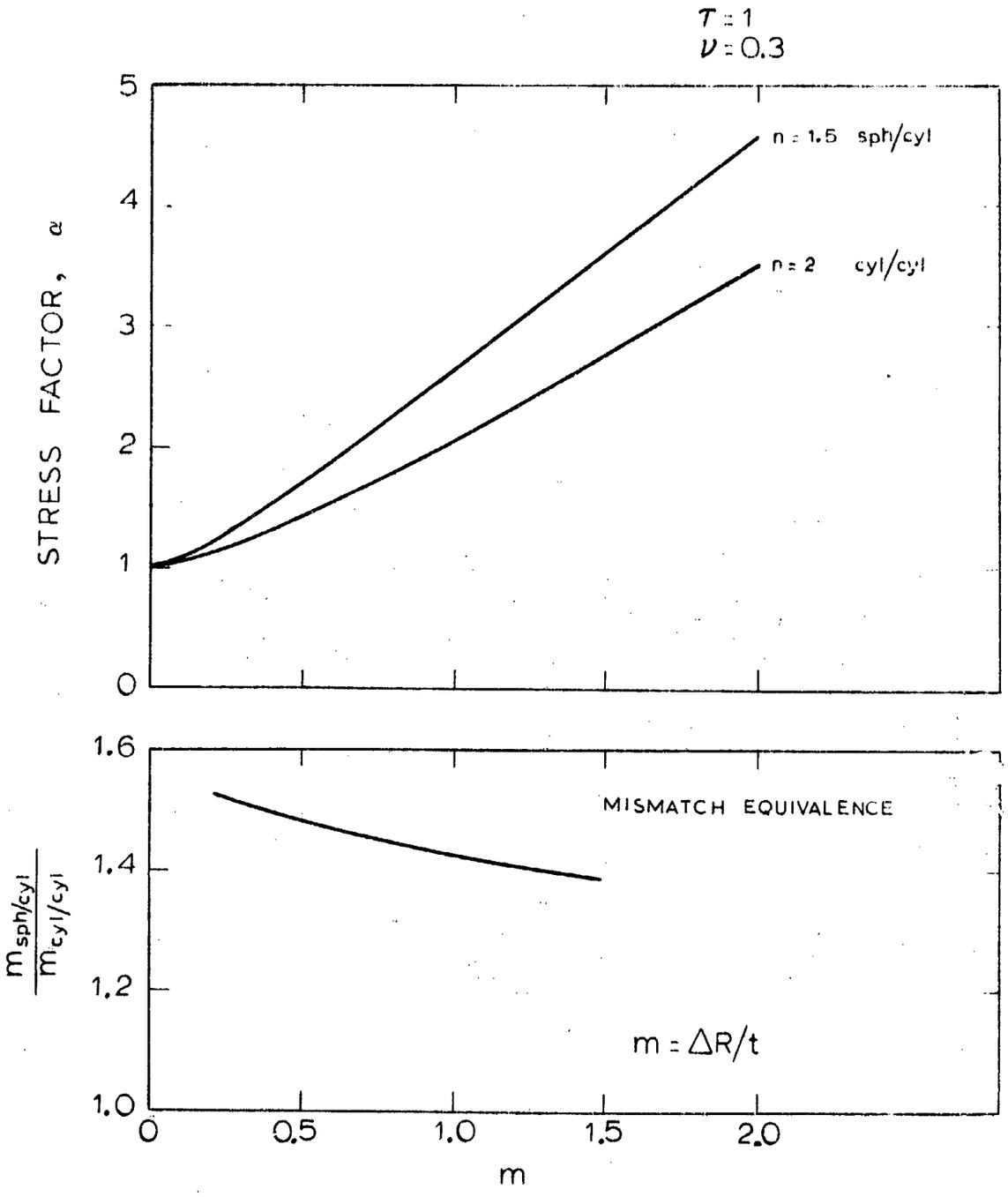

Fig. 4-3 Equivalence Between Cylinder/Cylinder and Spherical/Cylinder, $\tau = 1$

For the sphere-cylinder case

$$\bar{\sigma} = \frac{N_\varphi}{t} \frac{\sqrt{7}}{2} \times 2.64 = 3.49 \frac{N_\varphi}{t}$$

For the cylinder-cylinder case

$$\bar{\sigma} = \frac{N_\varphi}{t} \sqrt{3} \times 2.07 = 3.58 \frac{N_\varphi}{t}$$

Thus, since the meridional stress resultant N_φ is the same in both cases the sphere-cylinder case has a slightly lower effective elastic stress than the cylinder-cylinder case, for $m = 1$. Compare this with stresses at $m = 0$, i.e., no mismatch:

For the sphere-cylinder case

$$\bar{\sigma} = \frac{N_\varphi}{t} \frac{\sqrt{7}}{2} \times 1 = 1.32 \frac{N_\varphi}{t}$$

For the cylinder-cylinder case

$$\bar{\sigma} = \frac{N_\varphi}{t} \times \sqrt{3} = 1.73 \frac{N_\varphi}{t}$$

Here there is a 30% difference in the elastic stress in favor of the sphere-cylinder case.

A comparison between several uniform thickness cylinder-cylinder and hemisphere-cylinder junctures is shown in Fig. 4-4. The full-line grid represents the cylinder-cylinder junctures, and the points cylinder-hemisphere junctures, plotted versus the equivalent mismatch, as defined by Fig. 4-3. The dashed lines are cylinder-cylinder curves for the same effective mismatch as the hemisphere-cylinder points. For the larger values of mismatch ($m \approx 1.4$) the agreement is excellent, for the smaller ones ($m \approx .5$) there is a reduction of the pressure parameter for the hemisphere-cylinder configuration of some 10 percent in the high plastic strain range ($\bar{\epsilon}/\bar{\epsilon}_y \geq 1.5$). When the mismatch approaches zero

$$\frac{p}{p_m} = \begin{cases} \frac{2}{\sqrt{3}} \frac{t}{R} F_{tu} & \text{For Cylinder-Cylinder Juncture} \\ \frac{4}{\sqrt{7}} \frac{t}{R} F_{tu} & \text{For Hemisphere-Cylinder Juncture} \end{cases}$$

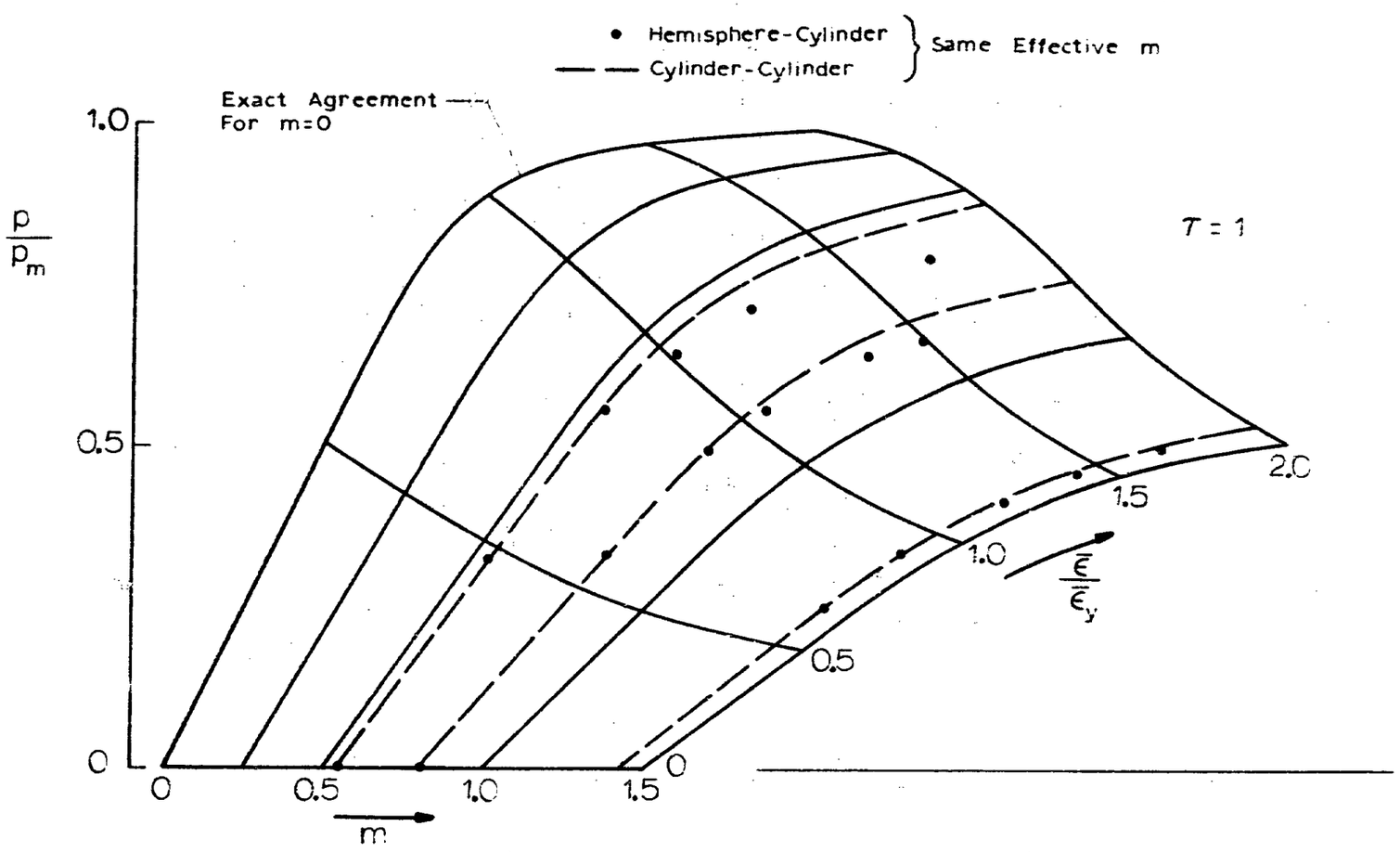

Fig. 4-4 Comparison of Junctures with the Same Equivalent Mismatch

the curves for the two configurations agree exactly, by definition of p_m. It is seen that, in general, the pressure which would cause collapse at the juncture of the hemisphere and the cylinder is somewhat lower than what would be expected from a knowledge of the stress factor α alone. The explanation of this is not clear; the phenomenon is simply noted here. (The possibility that early plasticity in the surrounding shell, which is higher stressed than the juncture for small mismatches, would influence conditions should be recognized. However, for mismatch values of the order 0.5 and higher this does not seem to be responsible for the relative lowering of the pressure).

As in the case of the cylinder-cylinder the maximum juncture stress occurs at the inside of the shell with the larger radius. Computer solutions with positive and negative mismatch (Fig. 4-5) failed to show any differences in the juncture stress.

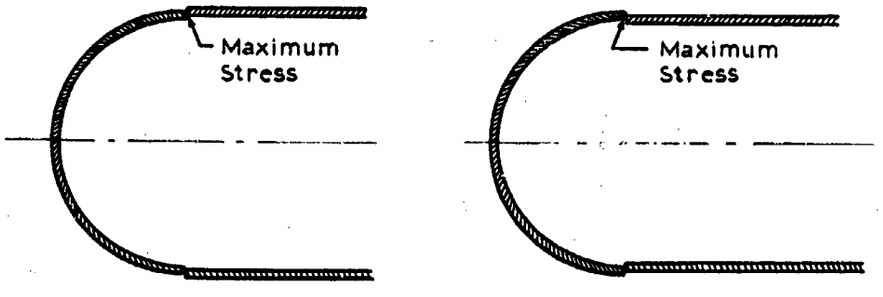

Positive Mismatch Negative Mismatch

Fig. 4-5

In areas away from the juncture the stress distributions are quite different in the positive and negative mismatch cases, as shown in Fig. 4-6. The antisymmetry exhibited by the cylinder-cylinder case is entirely absent.

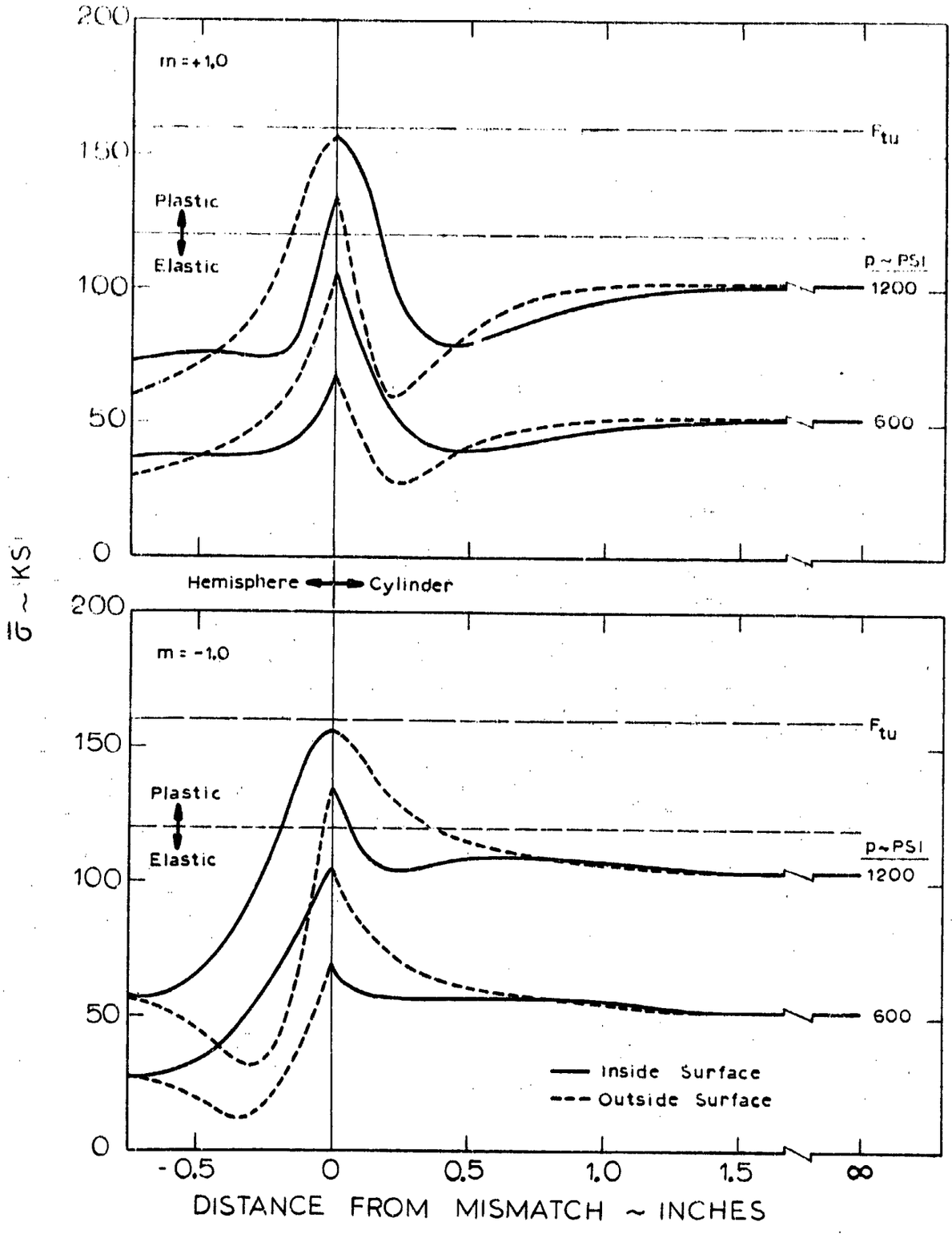

Fig. 4-6 Positive and Negative Mismatch at Hemisphere-Cylinder Juncture, Uniform Thickness

In spite of this the maximum stress is identical for both the positive and negative mismatch cases. No nonlinear behavior was found at the juncture; but at some distance away from the juncture nonlinearity is the rule. From the point of view of maximum stress the nonlinear behavior is of no consequence: the critical point in the shell is always either the point of mismatch, or the "pure" membrane (no bending) part of the cylinder.

4.2 Weld Lands

The weld land configurations investigated for the hemisphere-cylinder juncture are identical to those used at the cylinder-cylinder juncture described in Section 3.2. The comments made in connection with the cylinder-cylinder all apply in kind, with the only differences being in degree. As in the case of uniform thickness positive and negative mismatches (Fig. 4-5) were investigated, with no evidence of any differences between the two types of mismatch.

A typical example of stress distributions for positive and negative mismatch is shown in Fig. 4-7. An interesting point is illustrated by the figure: In the elastic region there is, in the negative mismatch case, a slight "overshoot" compared to the membrane stress in areas remote from the discontinuity. (See the lower part of Fig. 4-7, curve marked 800 psi.) As the pressure is increased this "overshoot" tends to disappear, and it does not seem to play a part in the collapse mechanism. The shell will still fail at the mismatch point, if the mismatch is large enough, or in membrane areas at the load p_m, if the mismatch is small. Even so, this points out that negative mismatch apparently is even less desirable than positive mismatch.

4.3 Design Graphs

The design graphs for mismatch at the juncture of a hemisphere and a cylinder, which are presented in Section 6, were produced in the same manner as the ones for cylinder-cylinder mismatch. Thus the discussion in Section 3.3 applies. One thing should be pointed out: The hemisphere-

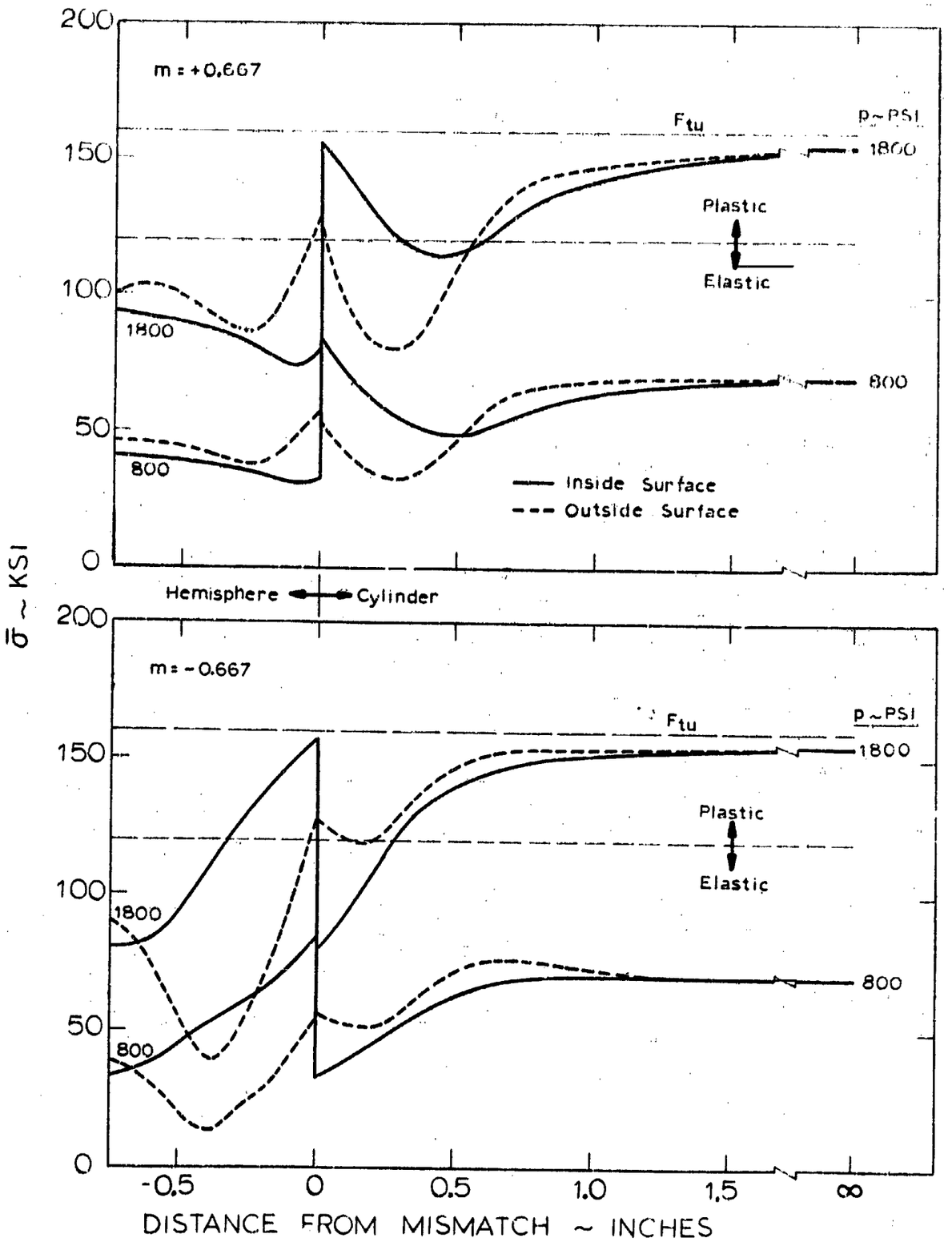

Fig. 4-7 Positive and Negative Mismatch at Hemisphere-Cylinder Juncture, $\tau = 1.5$, $L^* = 3$

cylinder curves marked $m = 1$ may be used for the cylinder-cylinder case as an approximation for $m \approx 1.4$. (This is based on the discussion of equivalent stress factors in Section 4.1.) $m = 1.4$ may appear an impossibility, but when it is considered that the effect of the mismatch is to introduce a line moment into the pressure vessel, it will be realized that all the design curves given here are approximately valid for externally applied line moments, regardless of the source of such moments. For instance, a situation such as the one shown in Fig. 4-8 may be analyzed using the accompanying design graphs. The figure shows a pressure vessel

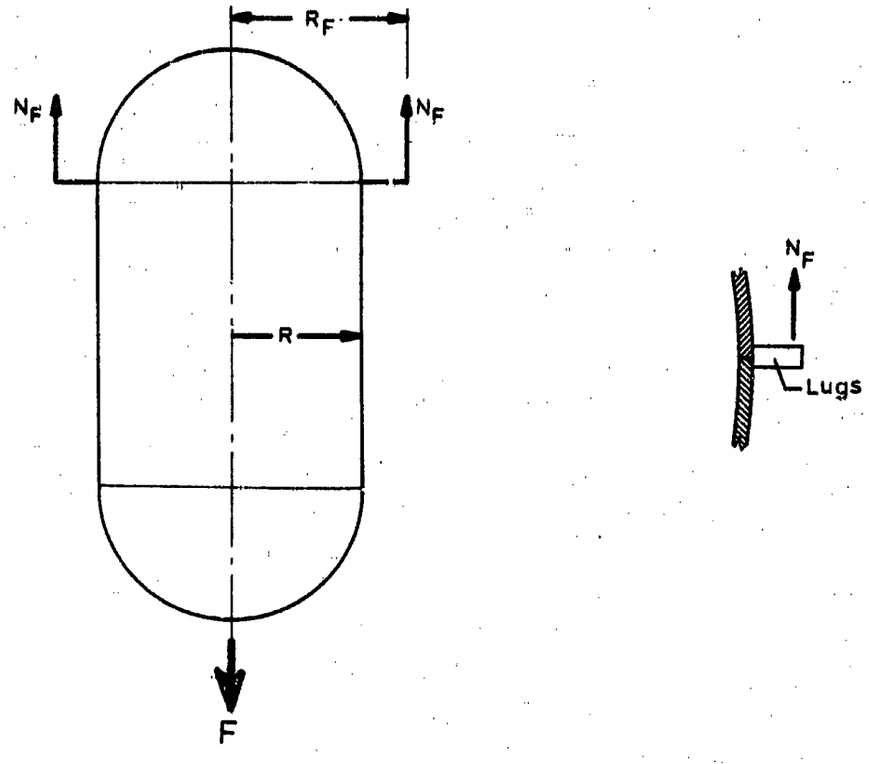

Fig. 4-8

supported by circumferential lugs spaced close enough so that the reaction to the axial inertial load may be considered uniform around the circumference. (If the reaction is not uniform, the use of peak values

will be slightly conservative.) The equivalent mismatch is now calculated:

Inertia load reaction: $N_F = \frac{F}{2\pi R_F}$ (a)

Pressure stress resultant: $N_\varphi = \frac{pR}{2}$ (b)

Total axial stress resultant: $N_x = N_F + N_\varphi$ (c)

Hoop stress resultant: $N_\theta = \frac{1}{4} pR$ (d)

Moment: $M_F = N_F(R_F - R)$ (e)

Then the maximum meridional stress is, assuming uniform thickness

$$\sigma_\varphi = \frac{N_x}{t} + \frac{1}{2} \frac{6M_F}{t^2}$$

Comparing this with the similar expression for stress caused by a mismatch moment, it is found that the moment parameter is

$$m_F = \frac{M_F}{tN_x}$$

$$= \frac{R_F - R}{t} \frac{1}{1 + \frac{N_\varphi}{N_F}}$$

$$= \frac{R_F - R}{t} \frac{1}{1 + \pi \frac{pR\,R_F}{F}} \qquad (f)$$

The stress resultant ratio is

$$n = \frac{N_\theta}{N_x}$$

$$= \frac{3}{2} \frac{1}{1 + \frac{F}{\pi pR\,R_F}} \qquad (g)$$

Using the two values (f) and (g) the equivalent m may be found from Fig. 2-2. Entering the appropriate design chart (remembering that p_m is a function of n, see Eq. 2.13) the strength of the pressure vessel supported in this way may be found.

Residual stresses may be calculated using the graph prepared for the cylinder-cylinder mismatch configuration. Spot checks were made and are shown in Fig. 4-9. There is a tendency for the shorter weld land configurations, and the negative mismatches to have smaller residual stresses than shown by the graphs (these are the points below the lines), but the tendency is not very strong, and a further delving into the finer points of that problem cannot be easily justified.

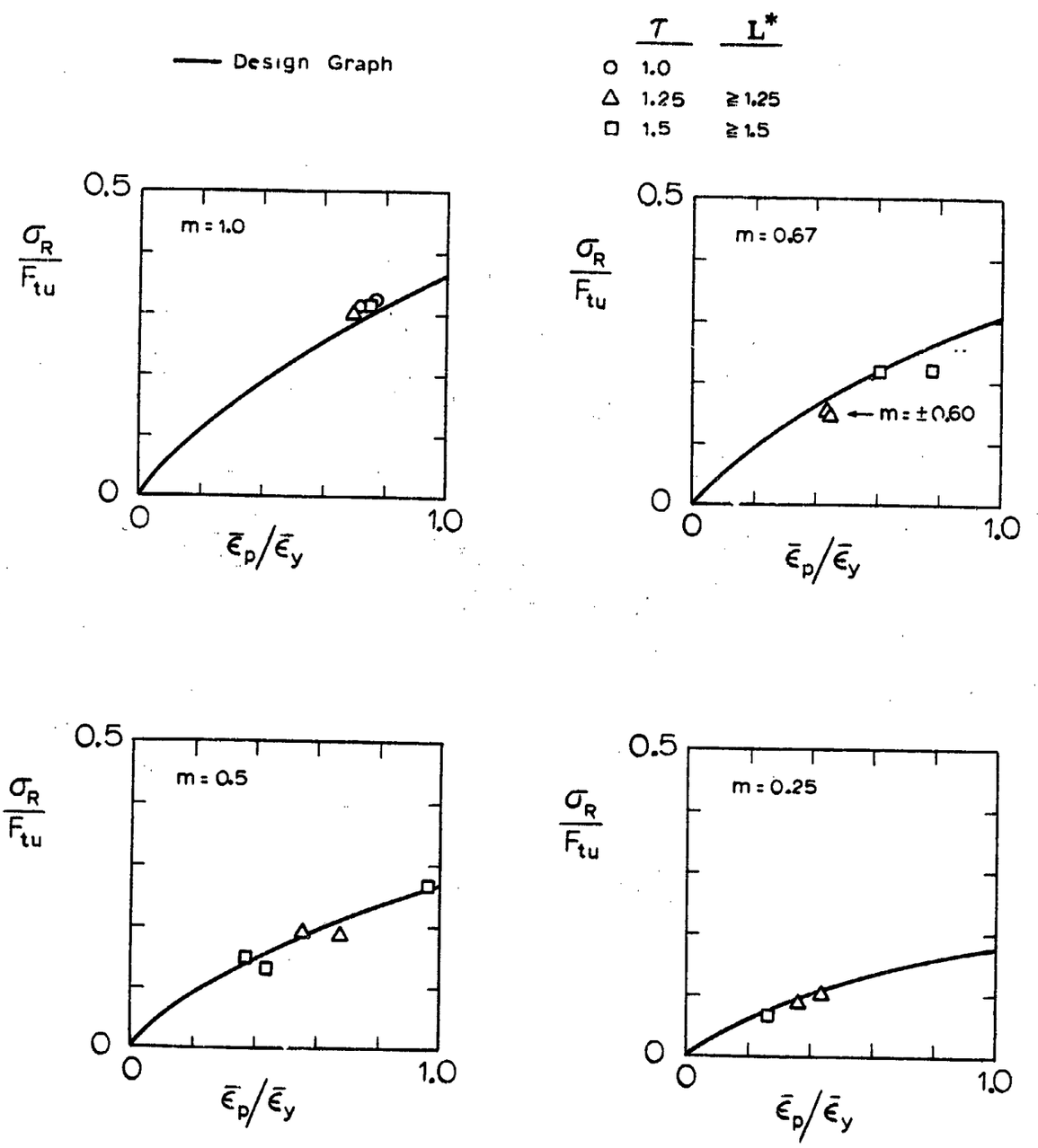

Fig. 4-9 Residual Stresses in Hemisphere-Cylinder Junctures

Section 5

FAILURE CRITERIA

5.1 Static Failure

Consider the stress-strain curve of the material used here, titanium 6Al-4V. Whether in the annealed or the heat treated (STA) condition, this material has a practically horizontal progression after the relatively low strain $\bar{\epsilon}/\bar{\epsilon}_y \approx 2$ has been reached:

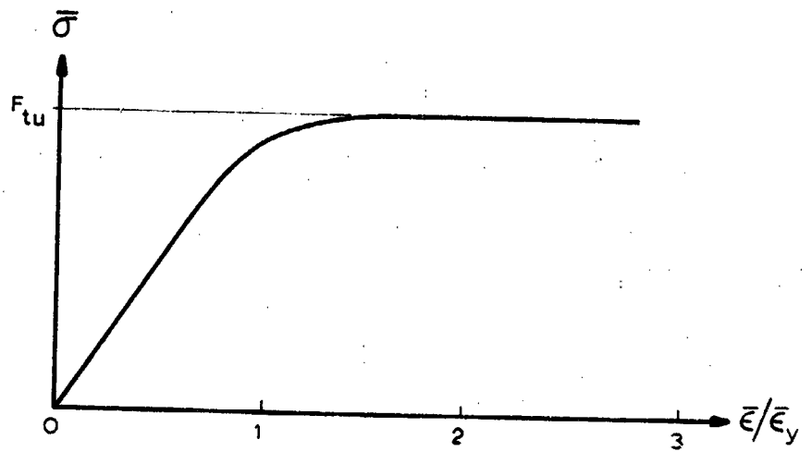

Fig. 5-1

At this point the material is rather unstable and a very slight increase in stress will cause a large increase in strain and the shell will collapse.

The curves of pressure versus strain (Section 6) for this material used in mismatched weld lands is quite similar to the curve above for the larger mismatch values, but for smaller mismatches the horizontal, or near horizontal, part is sometimes modified and delayed to larger strain values:

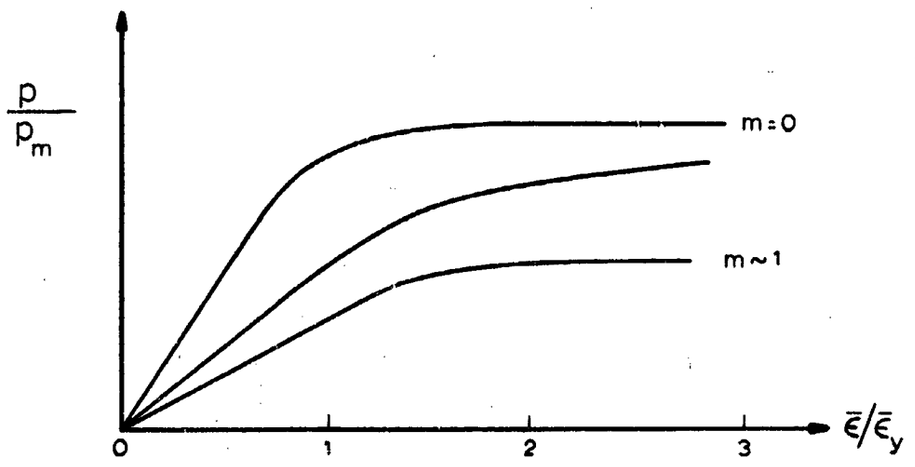

Fig. 5-2

Thus, for intermediate values of m the geometry-material combination is somewhat more stable than the material itself, and additional pressure can be sustained at higher strain values than $\bar{\epsilon}/\bar{\epsilon}_y \approx 2$. However, the material cannot withstand more than a particular measure of strain. From coupon tests (see Fig. 7-8) the uniaxial ultimate strain is of the order 3-5 percent.

The normalized strain may be expressed as

$$\frac{\bar{\epsilon}}{\bar{\epsilon}_y} = \epsilon_1 \frac{E}{F_{tu}} \tag{5.1}$$

where ϵ_1 is the uniaxial (coupon) strain. Taking the values of Fig. 7-8 this equation gives the following values:

Coupon Series "S": $2.61 \leq \left(\frac{\bar{\varepsilon}}{\varepsilon_y}\right)_{ult} \leq 2.64$

Coupon Series "C": $3.80 \leq \left(\frac{\bar{\varepsilon}}{\varepsilon_y}\right)_{ult} \leq 4.03$

From these results it is recommended that the following criterion be used as a failure criterion for pressure vessels fabricated from titanium 6Al-4V:

$$\left(\frac{\bar{\varepsilon}}{\varepsilon_y}\right)_{ult} = 2.6 \qquad (5.2)$$

This corresponds to the criterion of [1]. Note that this is for virgin material; in an natural welds a lower figure may have to be used.

Static testing to failure load on pressure vessels with mismatch was not a part of the present program. Agreement between theoretical results and tests below the failure load, but in the plastic region, was very good (see Section 8), which tends to back up the failure criterion.

In Table 5.1 are shown some particulars for the test specimens, including failure pressures after a relatively small number of pressure cycles into the plastic region, and calculated failure pressures. The predicted failure pressures are based on the geometry of the test specimens as fabricated, with ultimate strength values of 170,000 psi for the cylindrical test specimens (Tita "A", "B", "C", "D") and 160,000 for the hemisphere-cylinder test specimens (Tita "E", "F"). The predicted failure modes were, on the whole, realized in the tests. (If failure occurs in the mismatch it is a "meridional", if in the membrane away from the weld land it is "hoop" mode.) It is interesting to note that the accuracy of prediction is quite closely correlated with the amount of mismatch. Plotting the ratio of actual to predicted ultimate pressures

Table 5.1

BASIC TEST DATA

Test Specimen	τ	L^*	m	Tested		Predicted		Ratio Tested to Predicted p_{ult}
				p_{ult}	Mode	p_{ult}	Mode	
Tita A	1	--	1	1580	Merid.	1340	Merid.	1.18
Tita B	1.5	6	1	> 2000	Note 1	1900	Merid.	> 1.05
Tita C	1.5	3	0.5	2100	Hoop	1960	Hoop	1.07
Tita D	1.25	3	0.5	1800	Note 2	1920	(Hoop)	0.94
Tita E	1.5	1.5	-0.67	1940	Note 3	1760	(Merid.)	1.10
Tita F	1.20	3	1	1600	Merid.	1200	Merid.	1.33

Note 1: Not tested to failure.

Note 2: Estimated meridional failure pressure is 1960 psi. Failure started in the hoop mode and progressed meridionally in the mismatch.

Note 3: Estimated hoop failure pressure is 1850 psi. Failure started in hoop tension.

results in the following figure (only specimens with estimated meridional failure are plotted, for obvious reasons):

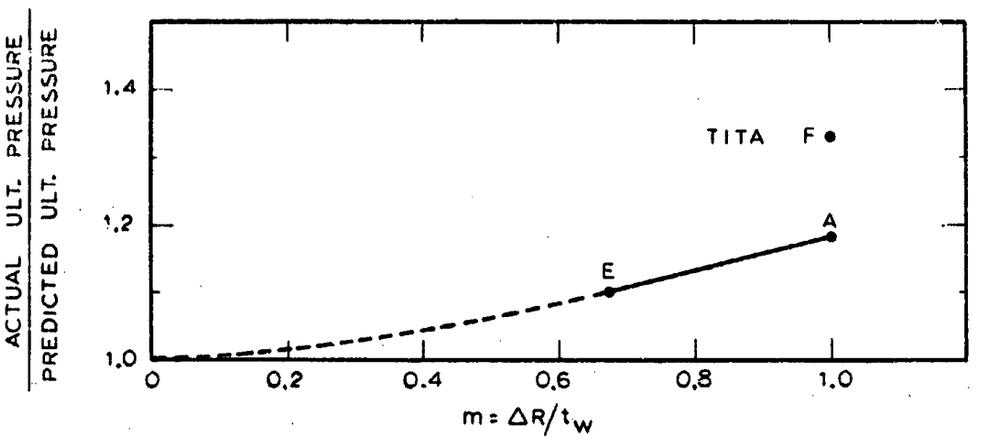

Fig. 5-3 Shake-Down Effect

The term shake-down effect is used here based on the observation, during tests, that creep effects are apparently resulting in improved strength of the mismatch area due to cycling (see Section 8). Thus, for pressure vessels which have experienced pressures up to 90 or 95 percent of the ultimate pressure predicted by the use of the criterion (4.2), a strengthening according to Fig. 5-3 may occur.

An alternate way to handle the discrepancy between the predicted and actual collapse pressures after shake-down, would be to find the value of m, which, when used to predict collapse, will yield the actual results. This was done and the results are shown in Fig. 5-4. It appears that by setting $m = 0.75\ \Delta R/t_w$ and using this reduced (or actual) mismatch in connection with the design graphs, an accurate prediction of ultimate pressure after shake-down will be realized.

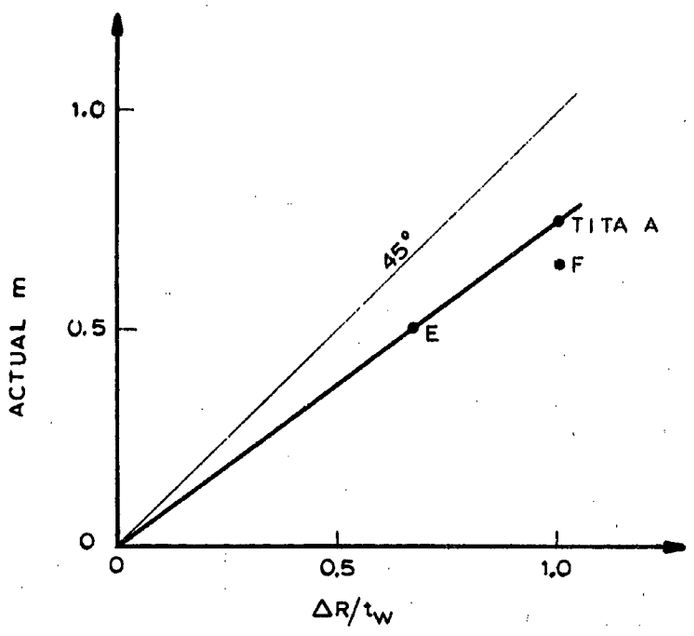

Fig. 5-4 Actual m at Collapse

5.2 Low-Cycle Fatigue

In Ref. [1] there is a discussion of the type of repeated loading considered here; i.e., pressure cycling between zero and a sufficiently large pressure to cause plastic deformations in the discontinuity area and/or in the membrane parts of the shell. A derivation of equations for predicting low-cycle fatigue based on the work of Manson [4] and Mattavi [7] was made, and a "best estimate" curve based on this equation is reproduced in Fig. 5-5. Also shown in the figure are results from the cycling tests obtained in the present test program.

The test program was, among other things, designed to provide verification (or improvement) of the curve in Fig. 5-5 in the region 10-100 cycles. To that end the following cycling sequence was devised:

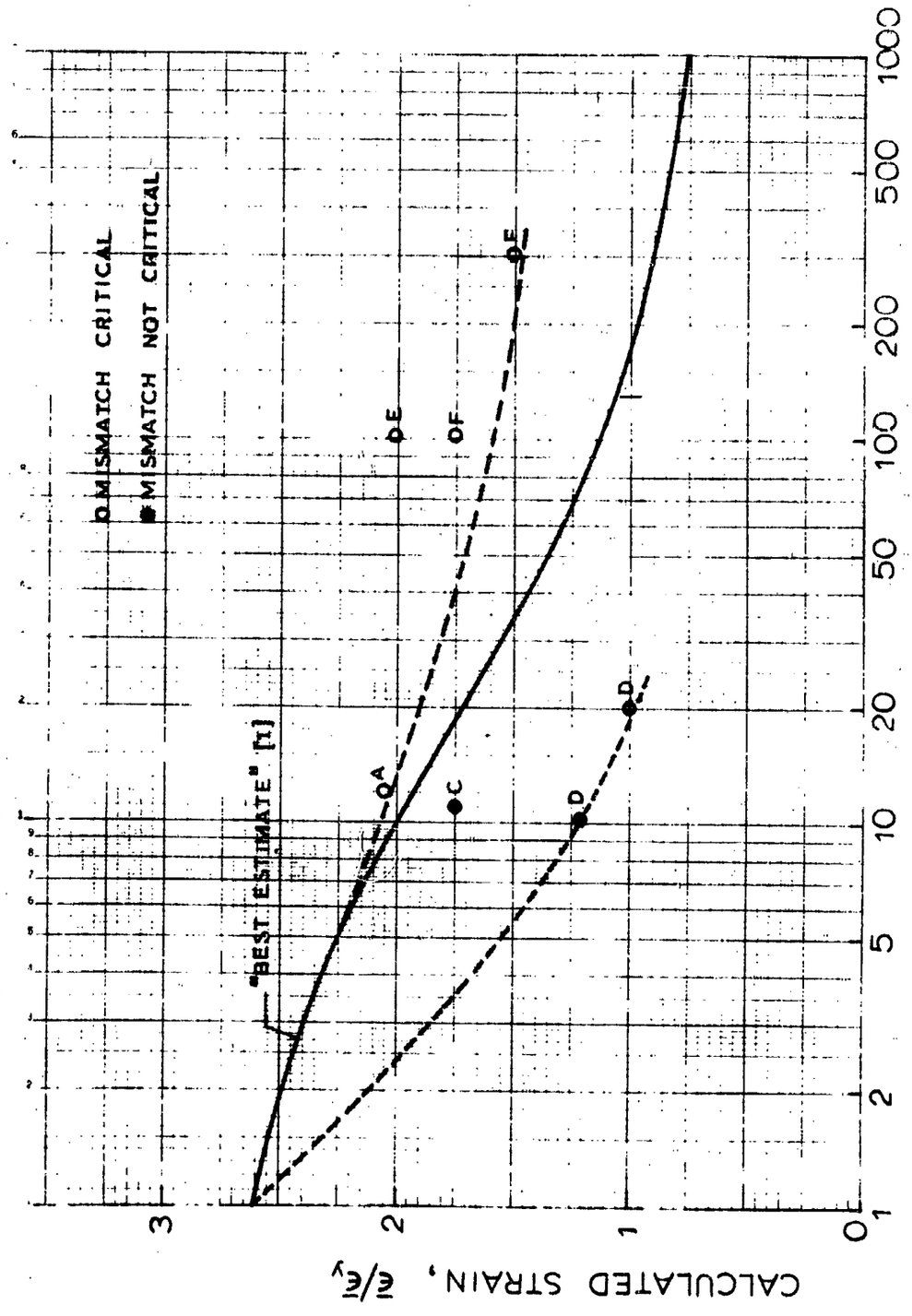

Fig. 5-5 Failure Criteria for Cycle Loading

1. Bring the specimen up to a pressure p which causes yielding

2. Cycle x times between 0 and p psi

3. Increase pressure by Δp and cycle x times between 0 and $\Delta p + p$

4. Repeat Step 3 until failure occurs

The reason for this particular procedure was to reduce testing time and expense to manageable size and still get reasonably good data.

An unexpected phenomenon occurred during the testing: there was evidence of quite a considerable amount of creep during the cycling (see Section 8 and Appendix B for details). This confronts us with a very complicated problem which is beyond present analytical capabilities. (The effect of this creep appears to be beneficial as evidenced by the data of Table 5.1 and Figures 5-3 and 5-4.)

In preparing the test data in a form suitable for the plotting in Fig. 5-5 the test data were reduced in the manner indicated below.

If the pressure vessel is subjected to a number of pressure reversals, say n_1 reversals at the pressure p_1 at which pressure the nominal life is N_1 (see Fig. 5-6), then the life left in the material is $N_1 - n_1$ cycles

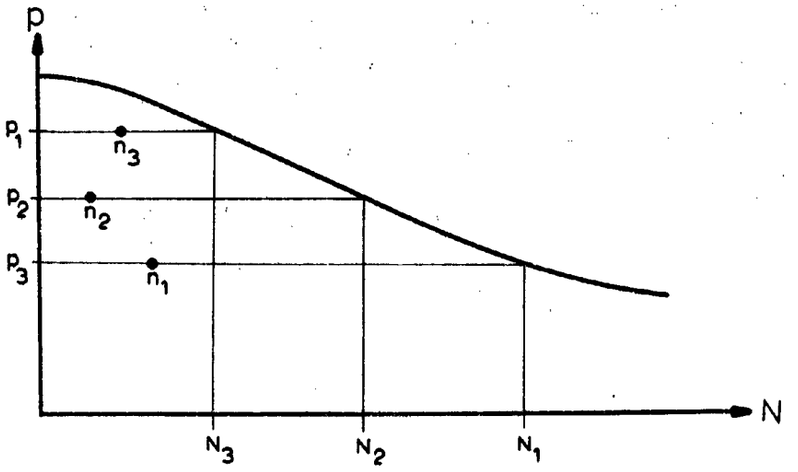

Fig. 5-6

at that pressure, and the fraction of life "used up" is n_1/N_1. Similarly, at another pressure level p_2 with n_2 pressure reversals the life "used up" is n_2/N_2, etc. By extending the process further and assuming that the damage caused at one pressure is applicable at all other pressures, one arrives at the following general solution: if a specimen is subjected to n_1 cycles at pressure p_1, n_2 cycles at pressure p_2 ... and n_n cycles at pressure p_n, then

$$\frac{n_1}{N_1} + \frac{n_2}{N_2} + \frac{n_3}{N_3} + \ldots + \frac{n_n}{N_n} = 1 \qquad (5.3)$$

This is known as Miner's Law [8]*

Multiply Eq. (5.3) by N_1. Then

$$N_1 = n_1 + \frac{N_1}{N_2} n_2 + \frac{N_1}{N_3} n_3 + \ldots + \frac{N_1}{N_n} n_n$$

or, since $\frac{N_1}{N_i} > 1$,

$$N_1 > n_1 + n_2 + n_3 + \ldots + n_n$$

Similarly

$$N_2 = \frac{N_2}{N_1} n_1 + n_2 + \frac{N_2}{N_3} n_3 + \ldots + \frac{N_2}{N_n} n_n$$

or $$N_2 > \frac{N_2}{N_1} n_1 + n_2 + n_3 + \ldots + n_n$$

*The discussion above is, however, taken from Pope [9], p. 104

In general

$$N_i = \frac{N_i}{N_1} n_1 + \frac{N_i}{N_2} n_2 + \ldots + n_i + \frac{N_i}{N_{i+1}} n_{i+1} + \ldots \frac{N_i}{N_n} n_n \qquad (5.4)$$

or

$$N_i > n_1 + n_{i+1} + \ldots + n_n \qquad (5.5)$$

Thus, Eq. (5.5) gives a lower bound for the fatigue life. Note that the higher "i" is, the more accurate Eq. (5.5) becomes.

The relation (5.5) was applied to data for test specimen Tita "A" from Table 7.4 (Page 7-24). Fig. 5-5 shows a plot of these data, compared with the "best estimate" of Fig. 5-4. (The values of p in the latter curve were found from Fig. 6-5, m = 1.) Note, for example, that at the point where the "best estimate" curve predicts 10 cycles the lower bound

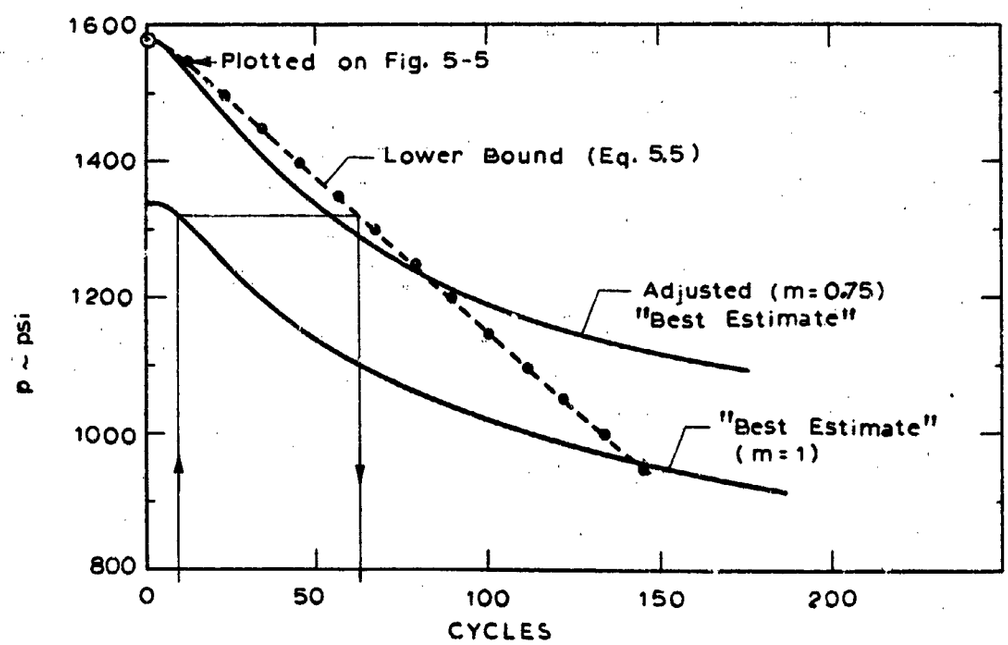

Fig. 5-7 Cyclic Data for Tita "A"

predicts more than 60 cycles. Thus, the "best estimate" curve seems quite conservative. Note, however, that the ultimate pressure of the test specimen is higher than the predicted; the test specimen seems to behave, close to the failure load, as if the actual mismatch is smaller than the geometric mismatch $\Delta R/t_w$, as shown in Fig. 5-4. Using the "actual" m from Fig. 5-4 an adjusted "best estimate" curve can be devised, as shown in Fig. 5-7. Note that even this adjusted curve is below the lower bound. The most accurate point on the lower bound curve is the failure point, the next most accurate is the point immediately below, 12 cycles at 1560 psi. This point corresponds to 9 cycles on the adjusted "best estimate", and is plotted on Fig. 5-5 as point "A".

The cyclic data for the other tests were treated in the same manner and the number of cycles at the load levels closest to the failure pressure plotted on Fig. 5-5. The results would have been quite encouraging, except for the anomalous behavior of test specimen "D". It should be noted, though, that the abscissa of Fig. 5-5 is the predicted strain; had the actual strain been used, the "D" points would have been higher. Note also, that test "D" (and "C"), being critical in hoop tension, rather than in bending at the mismatch, are not subject to the shake-down effect as much as the mismatch-critical shells.

The results of this exploratory work on low-cycle fatigue point out the need for further, and much more ambitious, work in the field.

Section 6

APPLICATIONS

This section summarizes the results obtained in the present investigations. The results are presented in the form of a series of graphs, which should enable the practical engineer to rapidly estimate elastic and plastic stresses in weld mismatches at the junctures of cylinders to cylinders, and hemispheres to hemispheres.

While designed expressively for the types of shells mentioned above, the design graphs may also be used to estimate, approximately, elastic and plastic stresses in other types of pressure vessel configurations.

6.1 Background Information

Pressure vessels are, typically, fabricated from segments of shells which are joined by welding (or other methods) to form the complete structure. During this process a mismatch is often introduced. To minimize the stress-raising effect of the mismatch, and to compensate for the lower mechanical properties in the weld, a weld land, i.e., a local thickening of the shell thickness is used, see Fig. 6-1.

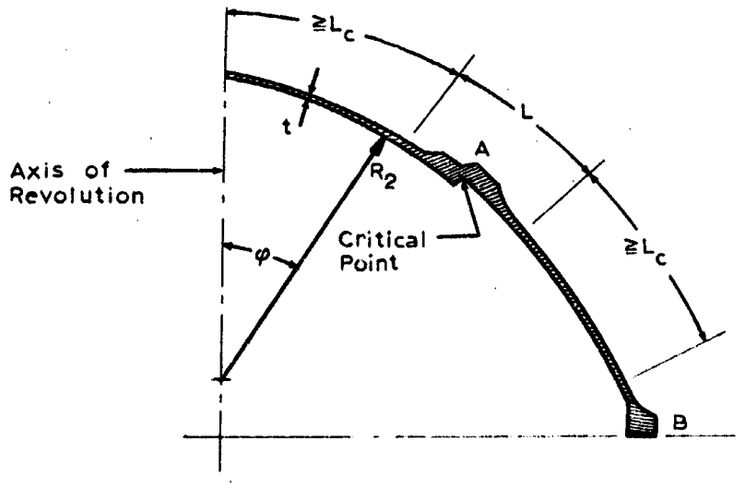

Fig. 6-1

The critical point, i.e., the point where failure is likely to occur, is the inside surface of the shell with the larger radius. (Theoretically, for uniform thickness shells, the outside surface of the smaller radius shell has almost the same stress, however, the existence of a weld fillet tends to alleviate this stress somewhat). The length of the weld land is L, including a rather long, tapered transition zone.

The analysis method used here is based on the nonlinear elastic and plastic theory for shells. Stresses include membrane and bending effects but exclude stress concentration due to sharp corners. The information contained here is applicable only to axisymmetric discontinuities in long, steep, thin shells. These terms will be discussed briefly.

Long Shell:

A shell element is considered long when there is no coupling between the discontinuity effects at A and B (see Fig. 6-1). This condition is satisfied when the meridional distance between A and B is approximately equal or greater than the characteristic length L_c of the shell. L_c is defined as the decay distance of discontinuity stresses. Linear theory predicts this distance to be approximately equal to $3\sqrt{R_2 t}$. However the results obtained by nonlinear theory [10] indicate that the characteristic lengths of shells vary with the amount of pressure. This relation is shown in Fig. 6-2. The pressure effect is a function of nonlinearity parameter ρ which is expressed by

$$\rho = \frac{p}{1.2\,E\left(\frac{t}{R_2}\right)^2} \qquad (\text{for } \nu = 0.3)$$

where

p = pressure (lb/in^2)
(negative pressure indicates external pressure)

E = modulus of elasticity (lb/in^2)

Observe that at $\rho = 0$, $L_c = 3\sqrt{R_2 t}$ which corresponds to the linear theory solution.

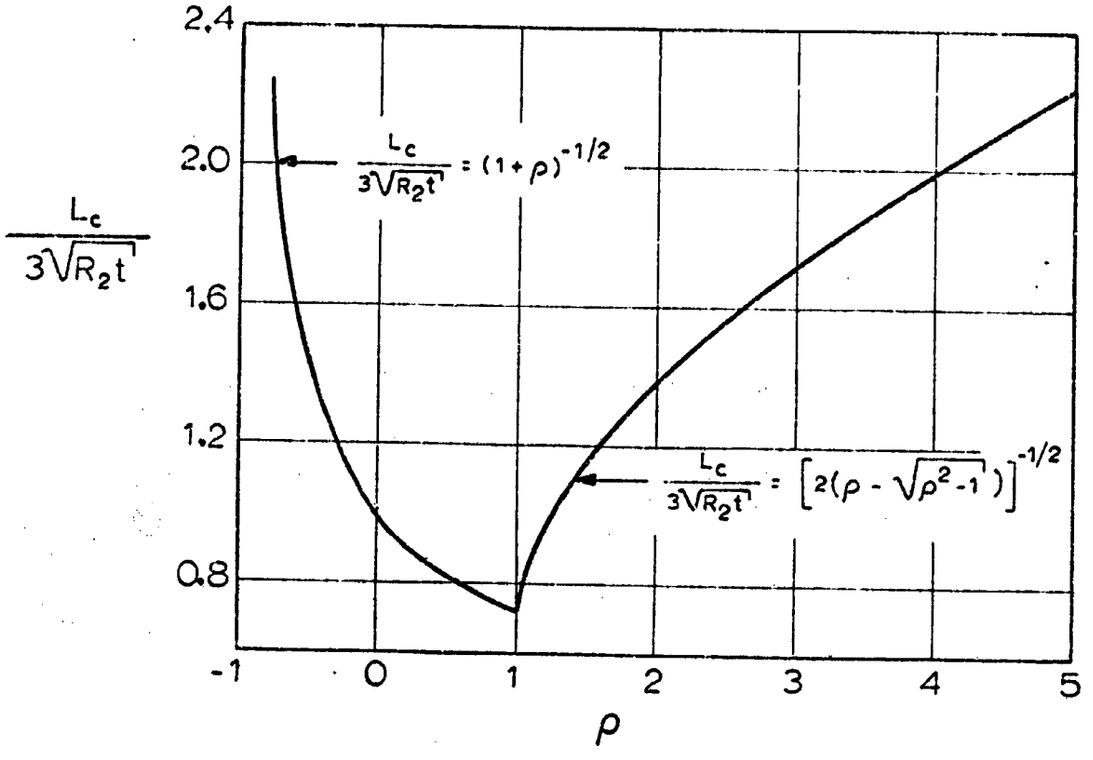

Fig. 6-2 Characteristic Lengths of Shells of Revolution

For practical use the limitation imposed by Fig. 6-2 may not be strictly adhered to. It is generally safe to consider shells "long", which have half the length indicated by Fig. 6-2.

Steep and Thin Shells

A shell element is considered sufficiently thin [11] when

$$1.8\sqrt{R_2/t_w} \geq 10$$

and sufficiently steep [11] when

$$1.8 \sin\varphi\sqrt{R_2/t_w} \geq 10$$

Axisymmetry

While the information given here is based on axisymmetric discontinuities, it can also be used for discontinuities extending only partially around the circumference, provided that this length is more than about five times the characteristic length L_c. For shorter distances, the present results are usually conservative, but sometimes slight underestimation may occur [12]. A particular case of lack of axisymmetry which is eminently suited to be treated by the present methods is shown in Fig. 6-3.

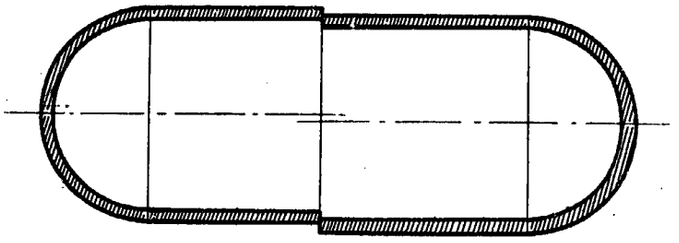

Fig. 6-3

6.1.2 Weld Land Geometry

The weld land configuration family for which the design graphs strictly apply is shown in Fig. 6-4. The geometric quantities defining this configuration are the length, thickness, and mismatch, expressed in nondimensional

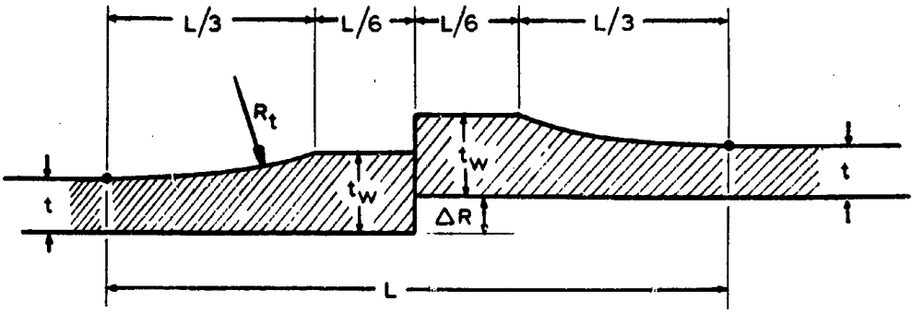

Fig. 6-3 Weld Land Configuration

parameters as follows:

$$\text{Length} \quad L^* = \frac{L}{\sqrt{Rt}} \quad , \quad 1.5 \leq L^* \leq \infty \tag{6.1}$$

$$\text{Thickness} \quad \tau = \frac{t_w}{t} \quad , \quad 1 \leq \tau \leq 1.5 \tag{6.2}$$

$$\text{Mismatch} \quad m = \frac{\Delta R}{t_w} \quad , \quad 0 \leq m \leq 1 \tag{6.3}$$

The main effect of the weld land length L^* is to modify the distribution of the mismatch moment between the two shells (when $L^* \to \infty$ each part receives one half of the moment, for $L^* < \infty$ more than one half of the mismatch moment goes to the larger radius, or outside shell). This effect is largely a "ring" effect, i.e., the added area, rather than the added thickness distribution, is the dominant factor. Thus, for weld land configurations with geometries deviating from the one shown in Fig. 6-3, the definition of the length L^* is changed to the following:

$$L^* = \frac{9}{5} \frac{A_w}{t(\tau-1)} \times \frac{1}{\sqrt{Rt}} \tag{6.4}$$

where A_w is the weld land area as defined in Fig. 6-4. This equation

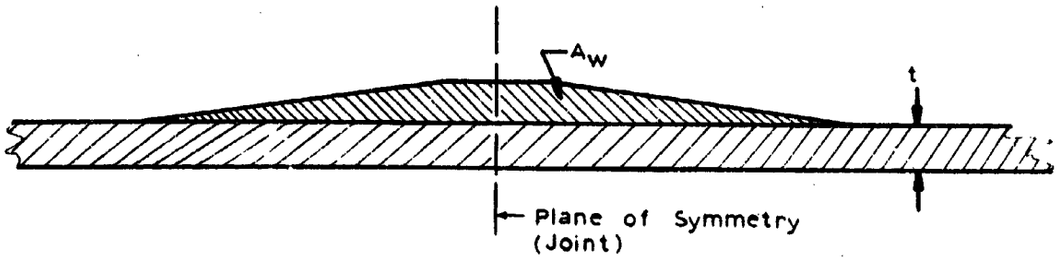

Fig. 6-4

becomes identical to Eq. (6.1) for the configuration shown in Fig. 6-3 when the transition is expressed as a second degree curve, and very nearly identical when the transition radius R_t (Fig. 6-3) is constant. For a triangular weld land

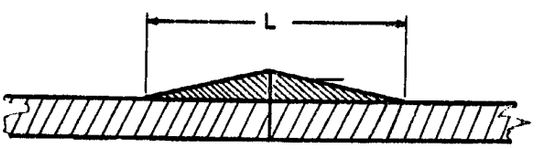

Eq. (6.4) reduces to $L^* = 0.9\, L/\sqrt{Rt}$, which is not very much different from Eq. (6.1) showing the relative insensitivity of this parameter to rather gross changes in the geometry.

6.1.3 Stresses and Strains

The stresses computed by the use of the design graphs are total effective stresses composed of membrane and discontinuity stresses. The total effective stress is defined as

$$\bar{\sigma} = \sqrt{\sigma_\varphi^2 + \sigma_\theta^2 - \sigma_\varphi \sigma_\theta} \tag{6.5}$$

where σ_φ and σ_θ are meridional and hoop stresses, respectively. This relationship is based on the energy of distortion theory used to predict the onset of plasticity effects. The theory states that yielding in a biaxial field will occur when the effective stress becomes equal to the uniaxial yield stress of the material.

The effective strain corresponding to the effective stress is

$$\bar{\epsilon} = \frac{2}{3}\sqrt{\epsilon_\varphi^2 + \epsilon_\theta^2 - \epsilon_\varphi \epsilon_\theta} \tag{6.6}$$

The design graphs are given in terms of pressure versus strain, and the stresses are then found as a function of the strain. Both the pressure

and the strain are in nondimensional form through the use of the following normalizing factors:

$$p_m = F_{tu} \frac{t_w}{R_2} \frac{2}{\sqrt{1 + n^2 - n}} \tag{6.7}$$

$$\bar{\epsilon}_y = \frac{2}{3}(1 + \nu) \frac{F_{tu}}{E} \tag{6.8}$$

p_m is the pressure at which a shell with a uniform thickness equal to t_w and no mismatch would collapse at the weld juncture.

The material is assumed to be titanium 6Al-4V, but any material, with a similar stress-strain curve, i.e., with a smooth transition between the elastic and plastic region, and with a practically horizontal plastic region (see the nondimensional stress-strain curves in Fig. 6-23) can be used.

6.2 Procedure to Obtain Stresses

The following procedure is suggested (and followed in the example problems in the following sections) to obtain stresses in weld lands with mismatch.

1. Obtain parameters required for the solution. These include the following:

   - o Dimensions of the shell - R_2, t, t_w, L (or A_w), ΔR
   - o Material properties - E, F_{tu} and $F_{P.L.}$ (in shell and weld), ν
   - o Internal pressure - p

2. Determine nonlinear parameter ρ

$$\rho = \frac{p}{1.2E\left(\frac{t}{R_2}\right)^2}$$

3. Check the applicability of the curves. The shell must satisfy the following criteria:

   - o <u>Long shell</u>: Fig. 6-2
   - o <u>Thin shell</u>: $1.8 \geq R_2/t_w$
   - o <u>Steep shell</u>: $1.8 \sin \varphi \; R_2/t_w \geq 10$

   The material stress-strain curve must satisfy, approximately, the following criteria:

$$1 < \frac{F_{PL}}{F_{tu}} \leq 0.70$$

4. Determine weld land geometrical parameters

$$\tau = t_w/t$$

$$L^* = \frac{L}{\sqrt{R_2 t}}$$

$$\left(\text{or } L^* = \frac{9}{5} \; \frac{A_w}{t(\tau-1)} \; \frac{L}{\sqrt{R_2 t}}\right)$$

$$m = \frac{\Delta R}{t_w}$$

5. Determine collapse pressure in the membrane area of the shell

$$p_m = F_{tu} \; \frac{t}{R_2} \; \frac{2}{\sqrt{1+n^2}-n}$$

$n = 2$ for cylinders

$n = 1$ for spheres

Use the appropriate material strength F_{tu}.

6. Determine juncture collapse pressure for no mismatch

$$p_m = F_{tu} \frac{t_w}{R_2} \frac{2}{\sqrt{1+n^2}-n}$$

$n = 2$ for cylinder-cylinder juncture

$n = \frac{3}{2}$ for hemisphere-cylinder juncture

Use F_{tu} for the weld.

7. Determine normalizing strain

$$\bar{\varepsilon}_y = \frac{2}{3}(1+\nu)\frac{F_{tu}}{E}$$

8. Find appropriate design graph for the τ and L^* values of Step. 5.

Key to the figures:

τ	L^*	Figure Number	
		Cylinder-Cylinder	Hemisphere-Cylinder
1	All	6-5	6-14
1.25	1.5	6-6	6-15
	3.0	6-7	6-16
	4.5	6-8	6-17
	6	6-9	6-18
	≥ 7	6-5	6-14
1.50	1.5	6-10	6-19
	3.0	6-11	6-20
	4.5	6-12	6-21
	6	6-13	6-22
	≥ 7	6-5	6-14

Enter the figure with p/p_m and m, and read strain $\bar{\varepsilon}/\bar{\varepsilon}_y$ (or enter with strain and m, and read pressure p/p_m). Interpolation

between charts for τ and L^* may be necessary, if so, use linear interpolation.

9. Enter Fig. 6-23 with strain $\bar{\varepsilon}/\bar{\varepsilon}_y$ and read stress $\bar{\sigma}/F_{tu}$ and residual strain $\bar{\varepsilon}_R/\bar{\varepsilon}_y$.

10. Enter Fig. 6-24 with m and $\bar{\varepsilon}_R/\bar{\varepsilon}_y$ and read residual stress $\bar{\sigma}_R/F_{tu}$.

Note that approximate solutions to other than the above junctures, or to external line loads in addition to internal pressure may be obtained by judicious application of the graphs. For example, the curves will be exact for mismatch in the joints "1" and "2" (see sketch) in a conical pressure vessel if the radius R_2 is used instead of the cylinder radius R.

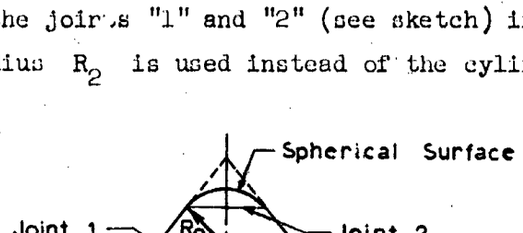

Joint 1 is analyzed by the use of the cylinder-cylinder curves and joint 2 by the use of the hemisphere-cylinder curves. Joint 3 may be analyzed approximately by finding the appropriate factor n at the juncture and then proceeding by the use of equivalent mismatch factors in a way similar to the one outlined in Section 4 for solving problems involving external support loads.

6.3 Example Problems

The following examples of direct use of the design graphs are given:

Example No. 1: Stresses in a cylinder-cylinder juncture with mismatch

Example No. 2: Stresses in a hemisphere-cylinder juncture with mismatch

6.3.1 Example Problem No. 1

Two cylindrical shell segments are welded together, with a weld land as shown. The structure is subjected to a pressure of 400 psi. The segments are made of titanium alloy Ti-6Al-4V.

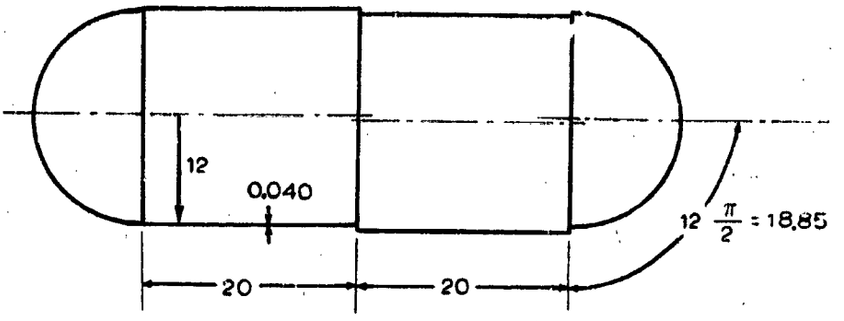

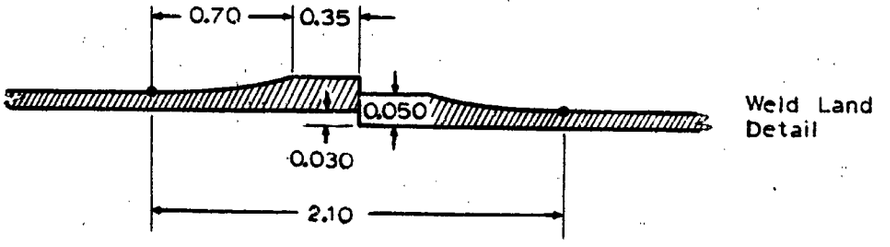

Determine

- Maximum stress at p = 400 psi
- Collapse pressure

Solution

1. Parameters required for the solution:

R_2 = 12 in.

t = 0.040 in.

t_w = 0.050 in.

L = 2.10 in.

ΔR = 0.030 in.

E = 17×10^6 psi

F_{tu} = 160,000 psi
F_{PL} = 120,000 psi
} in shell

F_{tu} = 120,000 psi
F_{PL} = 90,000 psi
} in weld

ν = 0.3

p = 400 psi

2. $$\rho = \frac{400}{(1.2)(17\times10^6)\left(\frac{0.04}{12}\right)^2} = 1.76$$

3. Applicability of curves

- Long shell

  From Fig. 6-2 $\dfrac{L_c}{3\sqrt{R_2 t}} = 1.30$

  $L_c = (1.30)(3)\sqrt{(12)(0.04)} = 2.70 \ll 20$

- Thin shell

  $(1.8)\sqrt{\dfrac{12}{0.05}} = 27.9 > 10$

- Steep shell

$$(1.8)(\sin 90^{\circ})\sqrt{\frac{17}{0.05}} = 27.9 > 10$$

- Stress-strain curve

$$\frac{F_{PL}}{F_{tu}} = \frac{120,000}{160,000} = 0.75 \quad \text{in shell}$$

$$\frac{F_{PL}}{F_{tu}} = \frac{90,000}{120,000} = 0.75 \quad \text{in weld}$$

The above results indicate that design curves are applicable.

4. Weld land parameters

$$\tau = \frac{0.05}{0.04} = 1.25$$

$$L^{*} = \frac{.10}{\sqrt{(12)(0.04)}} = 3.03 \text{ (use 3.00)}$$

$$m = \frac{0.030}{0.050} = 0.60$$

5. $p_m(\text{membrane}) = (160,000)\frac{0.04}{12}\frac{2}{\sqrt{1+4\text{-}2}} = 615$ psi

6. $p_m = (120,000)\frac{0.05}{12}\frac{2}{\sqrt{1+4\text{-}2}} = 577$ psi

(Smaller than $p_m(\text{membrane})$, hence weld land critical even with no mismatch.)

$$p/p_m = \frac{400}{577} = 0.693$$

7. $\bar{\epsilon}_y = \frac{2}{3}(1+0.3)\frac{120,000}{(17)(10^6)} = 0.00612$

8. $\tau = 1.25$, $L^{*} = 3 \rightarrow$ Fig. 6-7

From Fig. 6-7, with $p/p_m = 0.693$ and $m = 0.60$:

$\bar{\epsilon}/\bar{\epsilon}_y = 1.42$

9. From Fig. 6-23 with, $\bar{\varepsilon}/\bar{\varepsilon}_y = 1.42$:

$\bar{\sigma}/F_{tu} = 0.970$, $\sigma = (0.970)(120{,}000) = 116{,}400$ psi

$\bar{\varepsilon}_R/\bar{\varepsilon}_y = 0.45$

10. From Fig. 6-24, with $\bar{\varepsilon}_R/\bar{\varepsilon}_y = 0.45$ and m = 0.60:

$\bar{\sigma}_R/F_{tu} = 0.175, \bar{\sigma}_R = (0.175)(120{,}000) = 21{,}000$ psi

Step 8 is repeated for collapse pressure determination. Assume that maximum elongation for the weld material is 1.2%

8. (Repeat)

$$\bar{\varepsilon}/\bar{\varepsilon}_y = \frac{0.012}{0.00612} = 1.96$$

From Fig. 6-7 with $\bar{\varepsilon}/\bar{\varepsilon}_y = 1.96$ and m = 0.60:

$p/p_m = 0.760$

$p = (0.76)(577) = 438$ psi (collapse)

(See also Example Problem No. 2)

6.3.2 Example Problem No. 2

One of the spherical ends on the pressure vessel of Problem No. 1 has a mismatch of 0.040 inch. The weld land geometry is the same as in Problem No. 1.

Determine

- Maximum stress and number of cycles to failure at p = 400 psi
- Collapse pressure

Solution

1. Same as Problem No. 1, except $\Delta R = 0.040$.

2. Same as Problem No. 1

3. Same as Problem No. 1

4. Weld land parameters

$$\tau = \frac{0.05}{0.04} = 1.25$$

$$L^* = \frac{2.10}{\sqrt{(12)(0.04)}} = 3.03 \quad \text{(use 3.0)}$$

$$m = \frac{0.040}{0.050} = 0.80$$

5. Membrane p_m

- Cylinder: $p_m(\text{membrane}) = 160{,}000 \ \frac{0.04}{12} \ \frac{2}{\sqrt{144-1}} = 615$ psi
- Sphere: $p_m(\text{membrane}) = 160{,}000 \ \frac{0.04}{12} \ \frac{2}{\sqrt{144-1}} = 1067$ psi

6. $p_m = (120{,}000)\,\frac{0.05}{12}\,\frac{2}{\sqrt{1+2.25-1.5}} = 755$ psi

(Larger than p_m(membrane), hence weld land not critical for no mismatch)

$p/p_m = \frac{400}{755} = 0.530$

7. $\bar{\varepsilon}_y = \frac{2}{3}(1+0.3)\,\frac{120{,}000}{(17)(10^6)} = 0.00612$

8. $\tau = 1.25$, $L^* = 3$ → Fig. 6-16

From Fig. 6-16, with $p/p_m = 0.530$ and $m = 0.80$:

$\bar{\varepsilon}/\bar{\varepsilon}_y = 1.80$

9. From Fig. 6-23, with $\bar{\varepsilon}/\bar{\varepsilon}_y = 1.80$:

$\bar{\sigma}/F_{tu} = 0.990$, $\bar{\sigma} = (0.990)(120{,}000) = 118{,}800$

$\bar{\varepsilon}_R/\bar{\varepsilon}_y = 0.83$

10. From Fig. 6-24, with $\bar{\varepsilon}_R/\bar{\varepsilon}_y = 0.83$ and $m = 0.80$:

$\bar{\sigma}_R/F_{tu} \approx 0.295$, $\bar{\sigma}_R = (0.295)(120{,}000) = 35{,}400$ psi

Step 8 is repeated for collapse pressure determination. Assume that maximum elongation for the weld material is 1.2%.

8. (Repeat)

$\bar{\varepsilon}/\bar{\varepsilon}_y = \frac{0.012}{0.00612} = 1.96$

From Fig. 6-16 with $\bar{\varepsilon}/\bar{\varepsilon}_y = 1.96$ and $m = 0.80$:

$p/p_m = 0.54$, $p = (0.54)(755) = 408$ psi (collapse)

Compare this collapse pressure with that of Problem No. 1. The critical point in the pressure vessel is the hemisphere-cylinder juncture, and the pressure vessel will fail there at a pressure of about 408 psi.

The number of pressure cycles to cause failure at 400 psi can be predicted approximately by using the information in Section 5, as follows:

a. (Refer to page 5.5) m(actual) = (0.75)(0.80) = 0.60

b. From Fig. 6-16, with $p/p_m = 0.530$ and $m = 0.60$: $\bar{\varepsilon}/\bar{\varepsilon}_y = 1.30$

c. Calculate ratio of applied to ultimate strain. (See also step 8 Repeat)
   1.30/1.96 = 0.663

d. Calculate equivalent strain for use with Fig. 5-5:
   $\bar{\varepsilon}/\bar{\varepsilon}_y$ (Fig. 5-5) = (2.6)(0.663) = 1.72

e. Enter Fig. 5-5 with $\bar{\varepsilon}/\bar{\varepsilon}_y = 1.72$ and read cycles to failure from the top dashed curve:
   Cycles to Failure = 50 (at p = 400 psi)

Note: This is a tentative figure based on the results of the particular test series described in Section 5-5. Large deviations may be expected from this figure, and the above procedure is only included here as a suggestion for possible application of the results of Section 5.

6.4 Design Graphs

The following design graphs solve elastic and plastic problems associated with weld lands with mismatch in cylinder-cylinder and hemisphere-cylinder junctures. It is suggested that before using them at least Section 6.2, and preferably the whole of Section 6 be consulted.

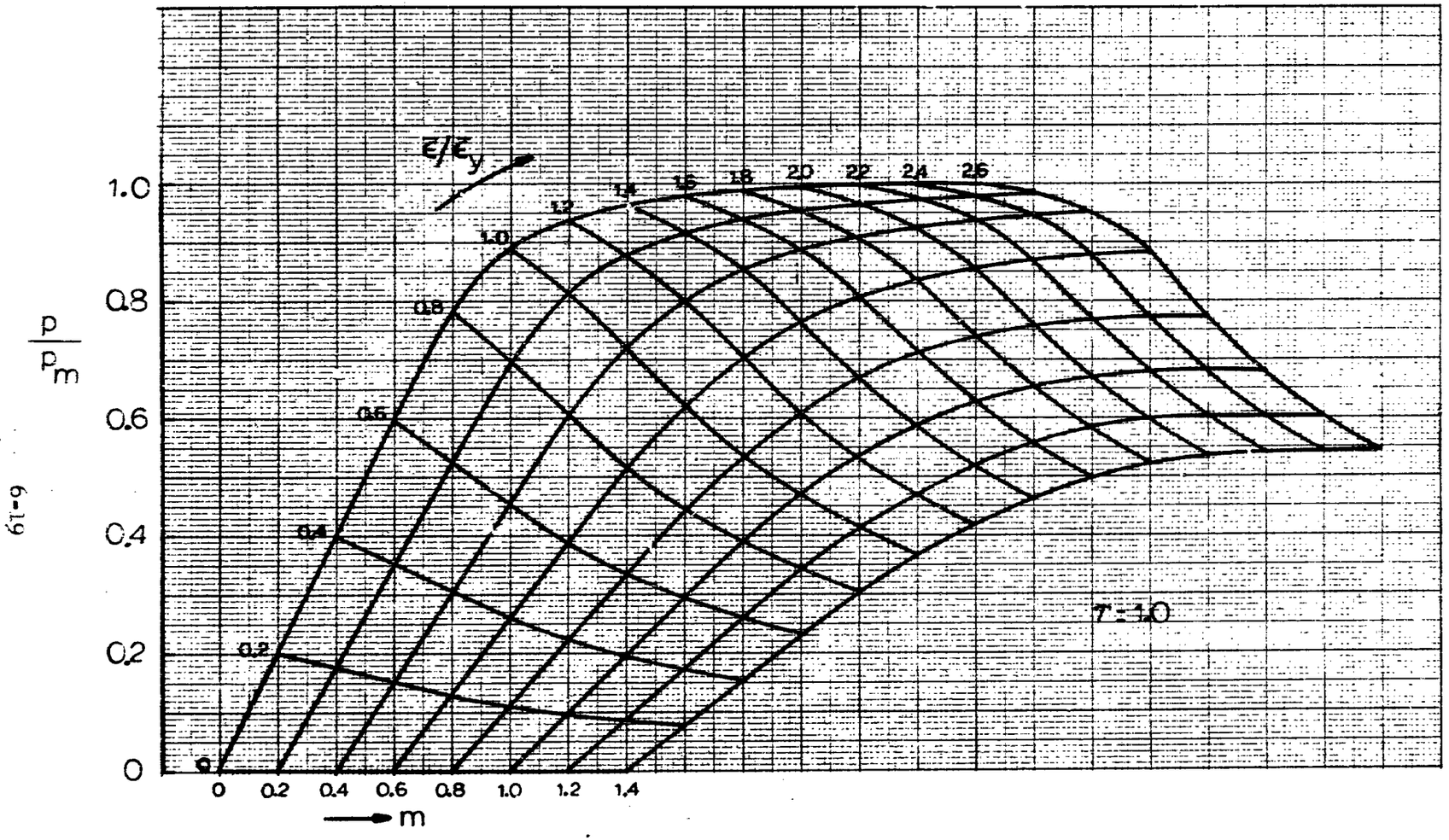

Fig. 6-5 Cylinder-Cylinder Juncture with Mismatch. Uniform Thickness.

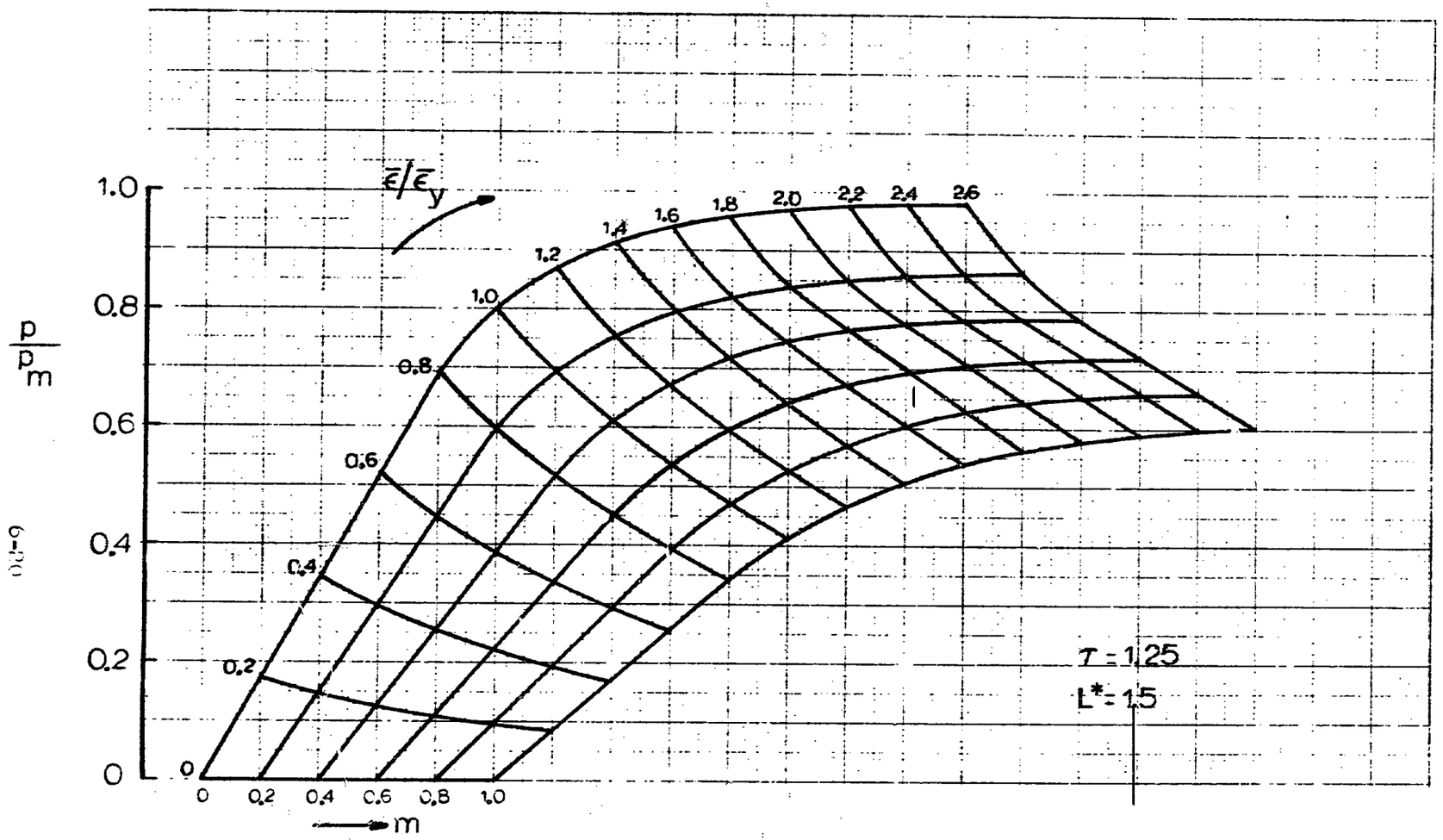

Fig. 6-6 Cylinder-Cylinder Juncture with Mismatch. Weld Land, $\tau = 1.25$, $L^* = 1.5$.

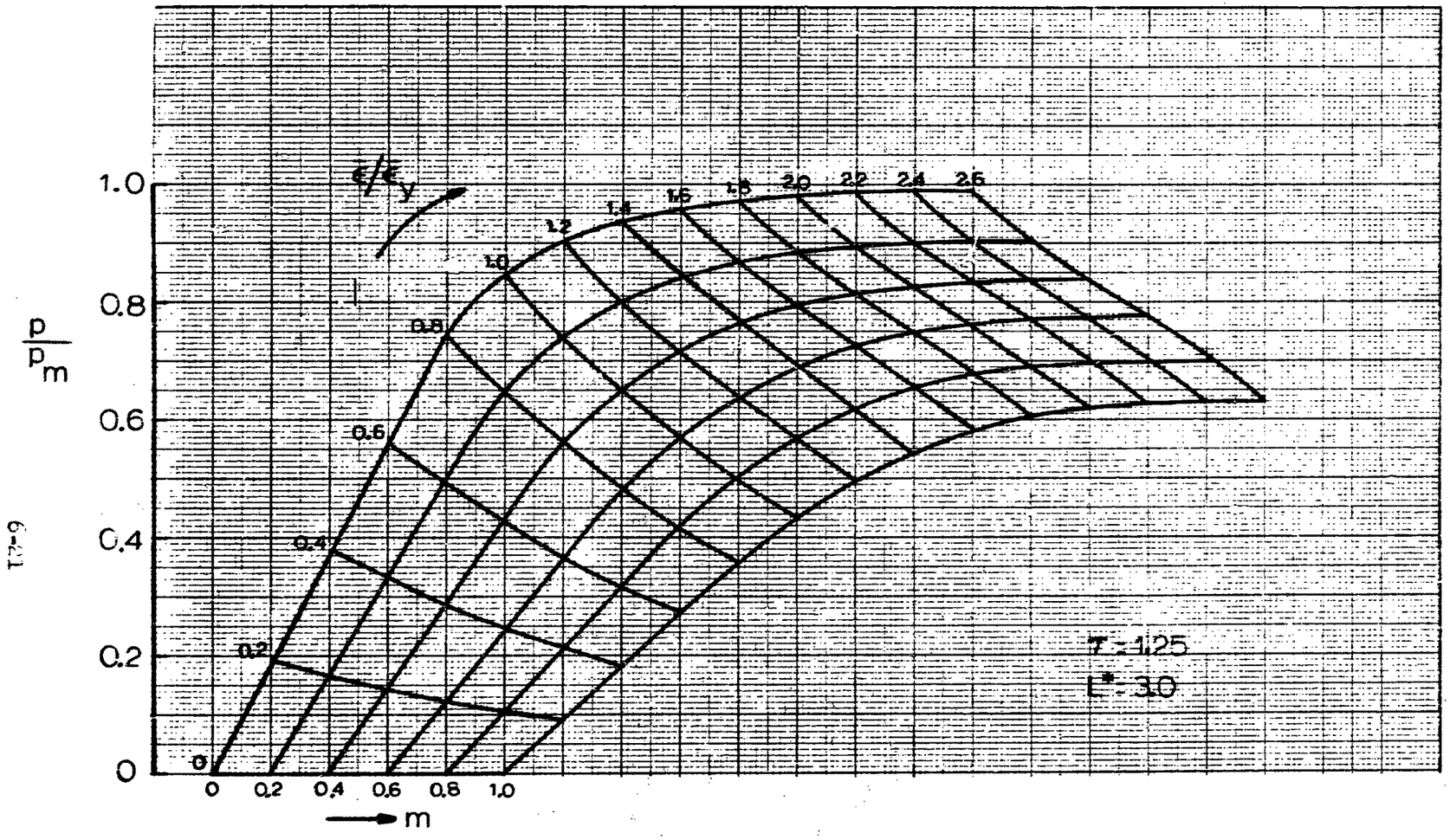

Fig. 6-7 Cylinder-Cylinder Juncture with Mismatch. Weld Land, $\tau = 1.25$, $L^* = 3.0$.

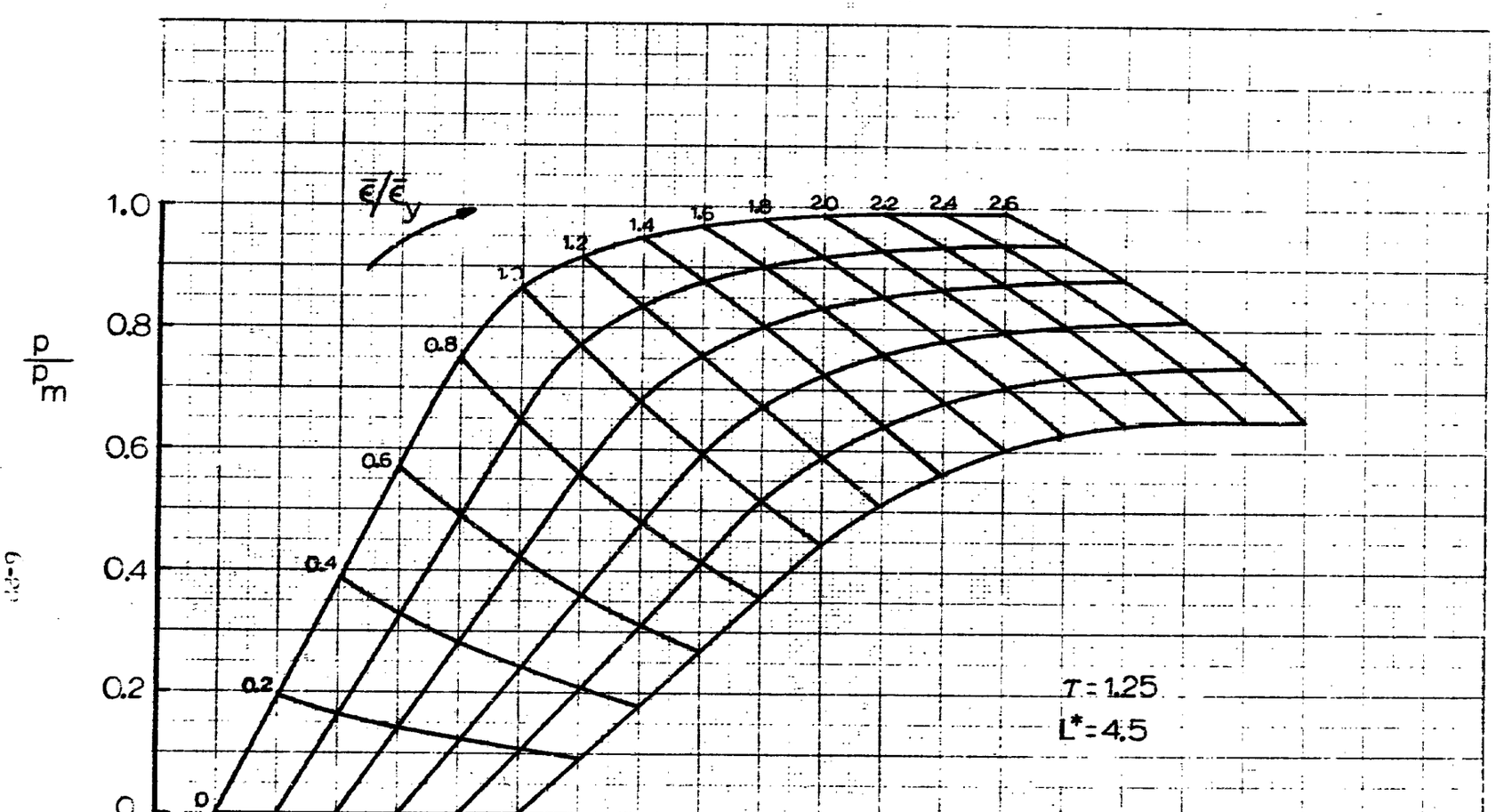

Fig. 6-8 Cylinder-Cylinder Juncture with Mismatch. Weld Land, $\tau = 1.25$, $L^* = 4.5$.

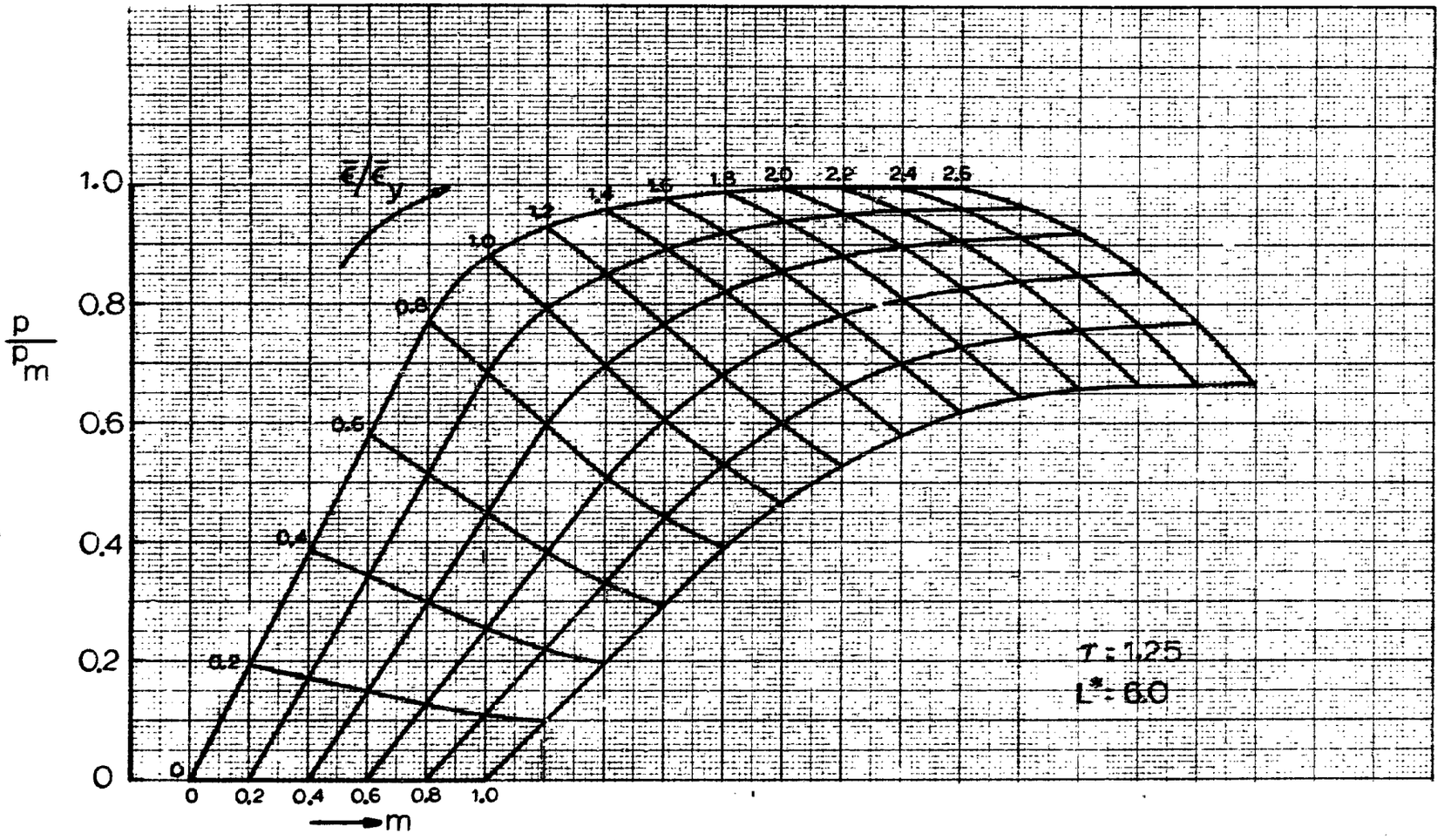

Fig. 6-9 Cylinder-Cylinder Juncture with Mismatch. Weld Land, $\tau = 1.25$, $L^* = 6.0$.

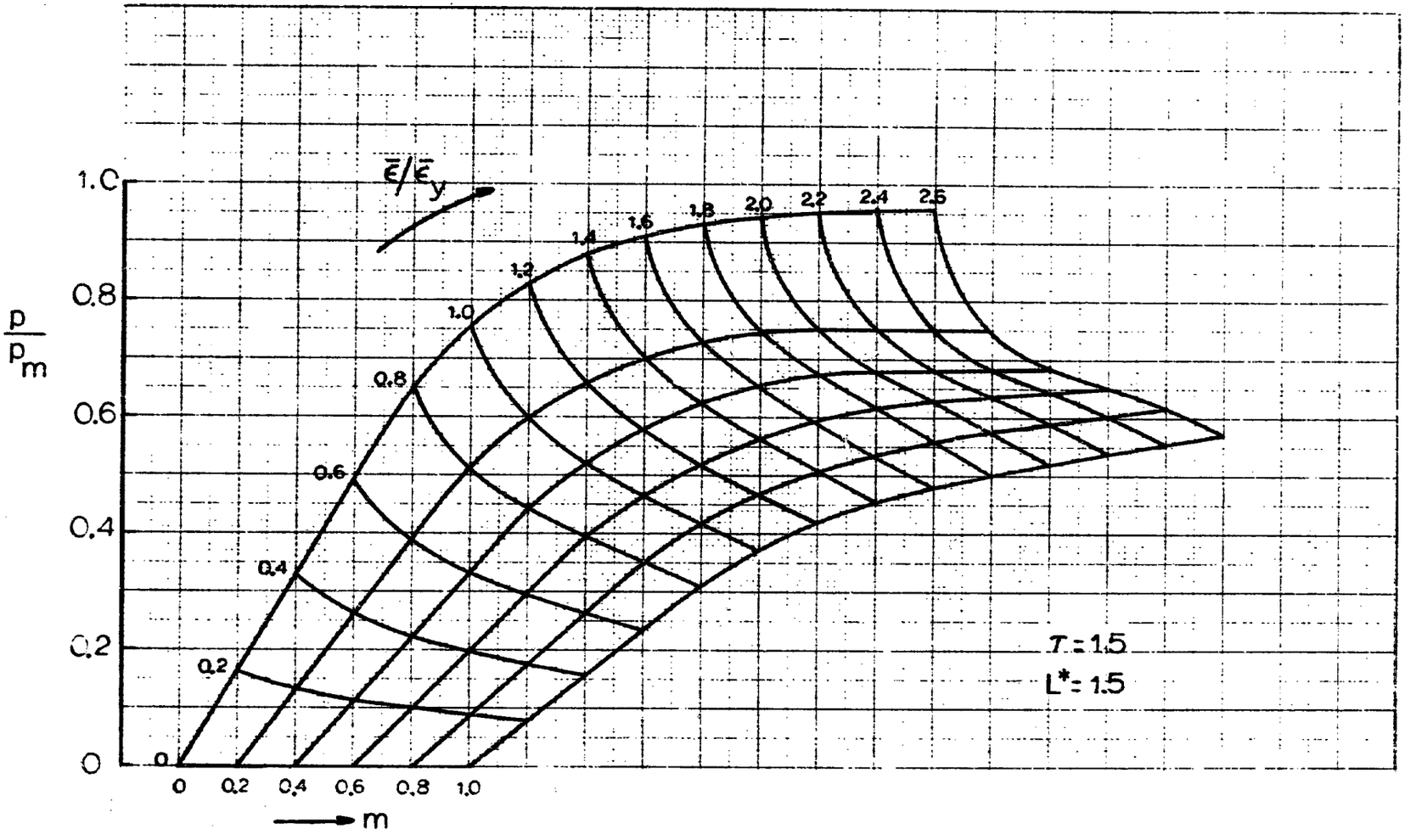

Fig. 6-10 Cylinder-Cylinder Juncture with Mismatch. Weld Land, $\tau = 1.5$, $L^* = 1.5$

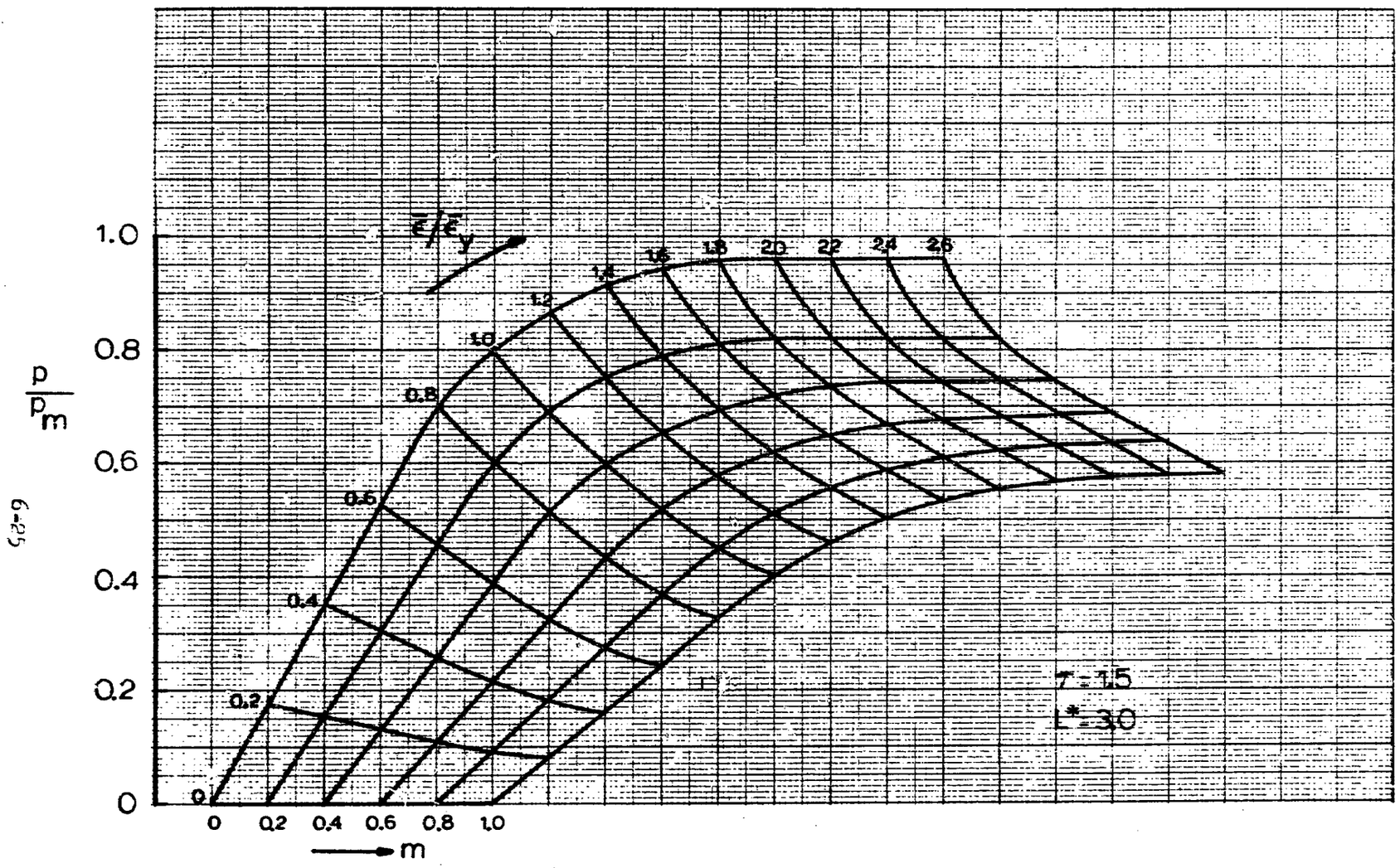

Fig. 6-11 Cylinder-Cylinder Juncture with Mismatch. Weld Land, $\tau = 1.5$, $L^* = 3.0$.

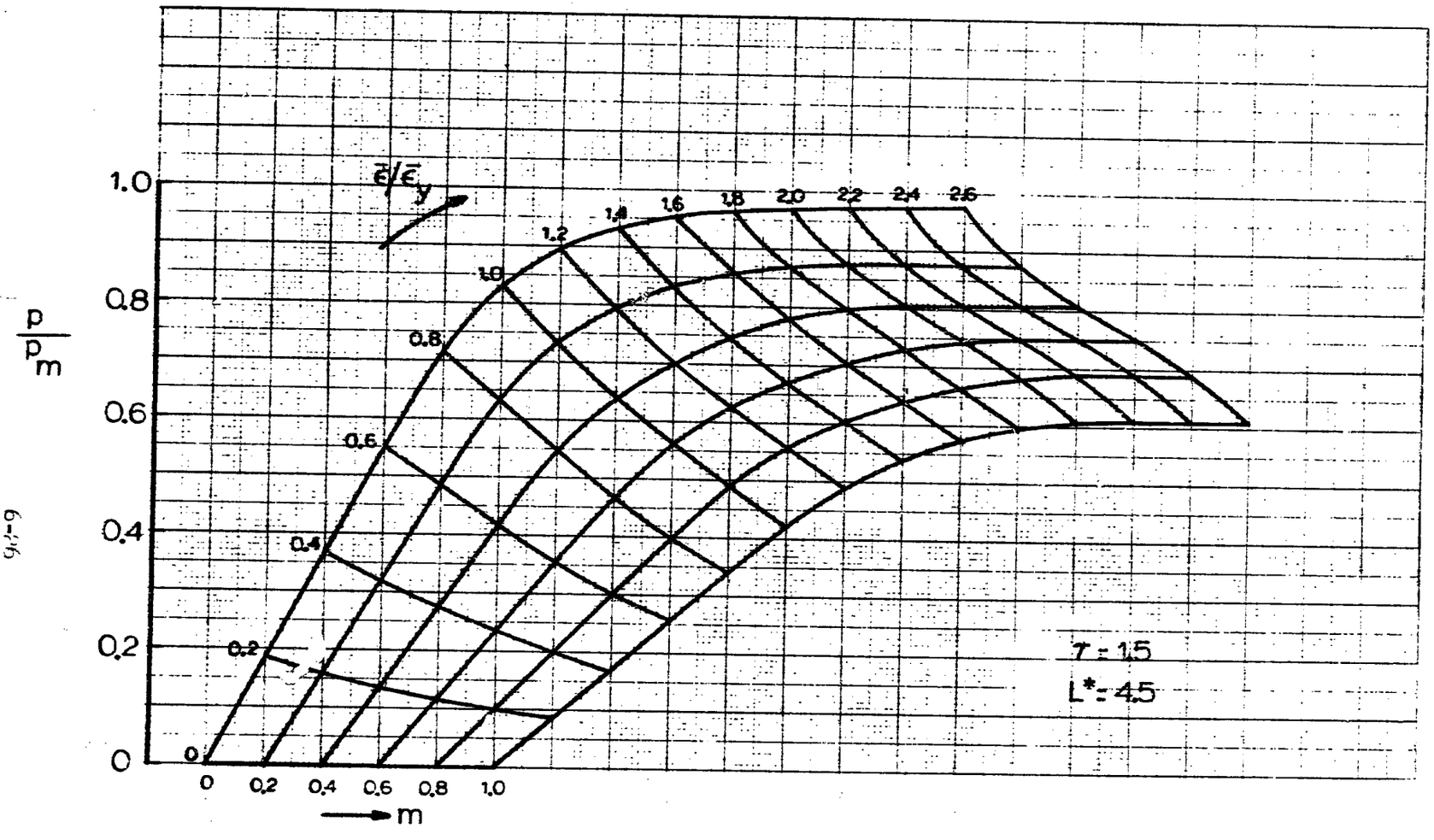

Fig. 6-12 Cylinder-Cylinder Juncture with Mismatch. Weld Land, $\tau = 1.5$, $L^* = 4.5$.

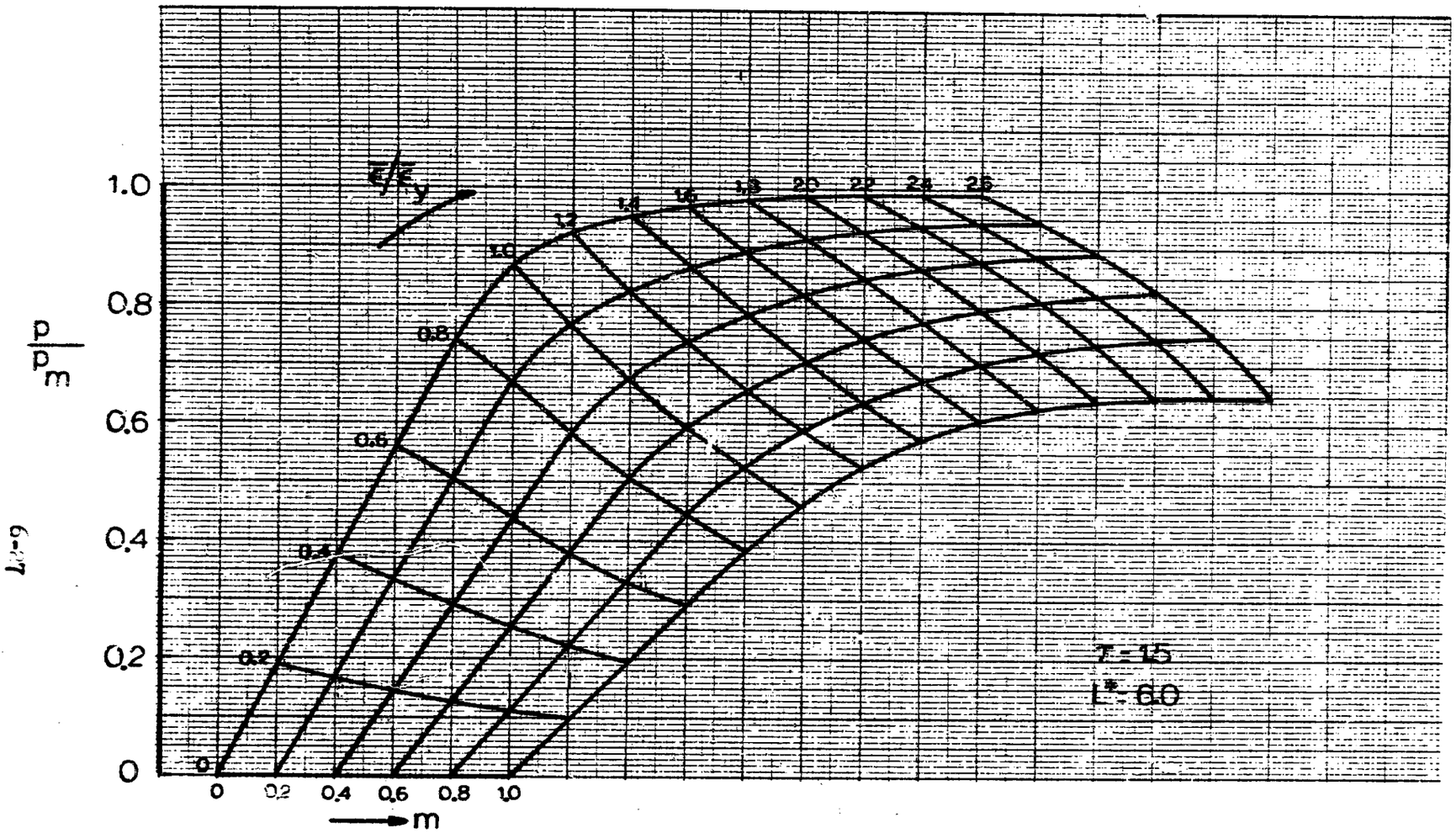

Fig. 6-13 Cylinder-Cylinder Juncture with Mismatch. Weld Land, $\tau = 1.5$, $L^* = 6.0$.

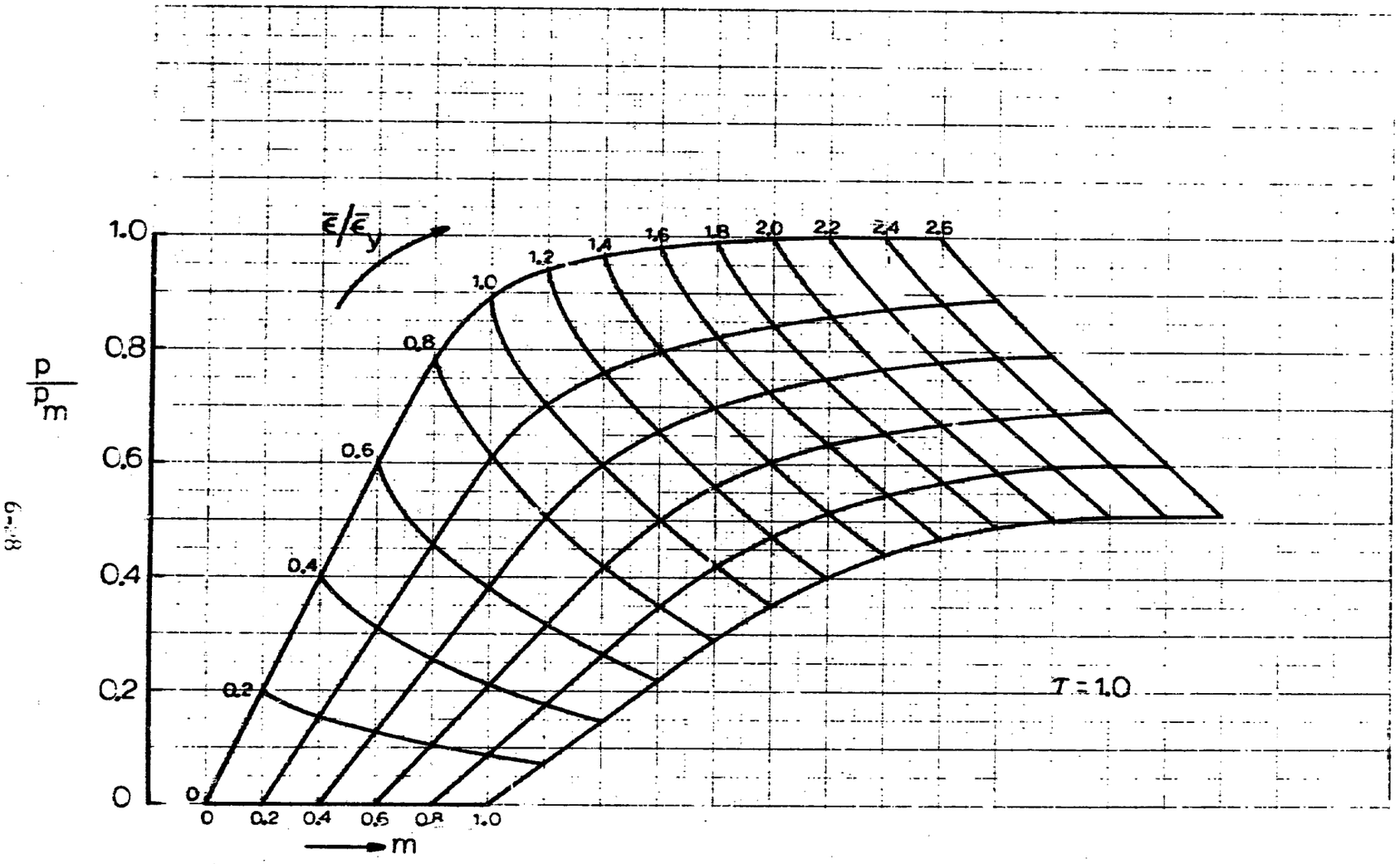

Fig. 6-14 Hemisphere-Cylinder Juncture with Mismatch. Uniform Thickness.

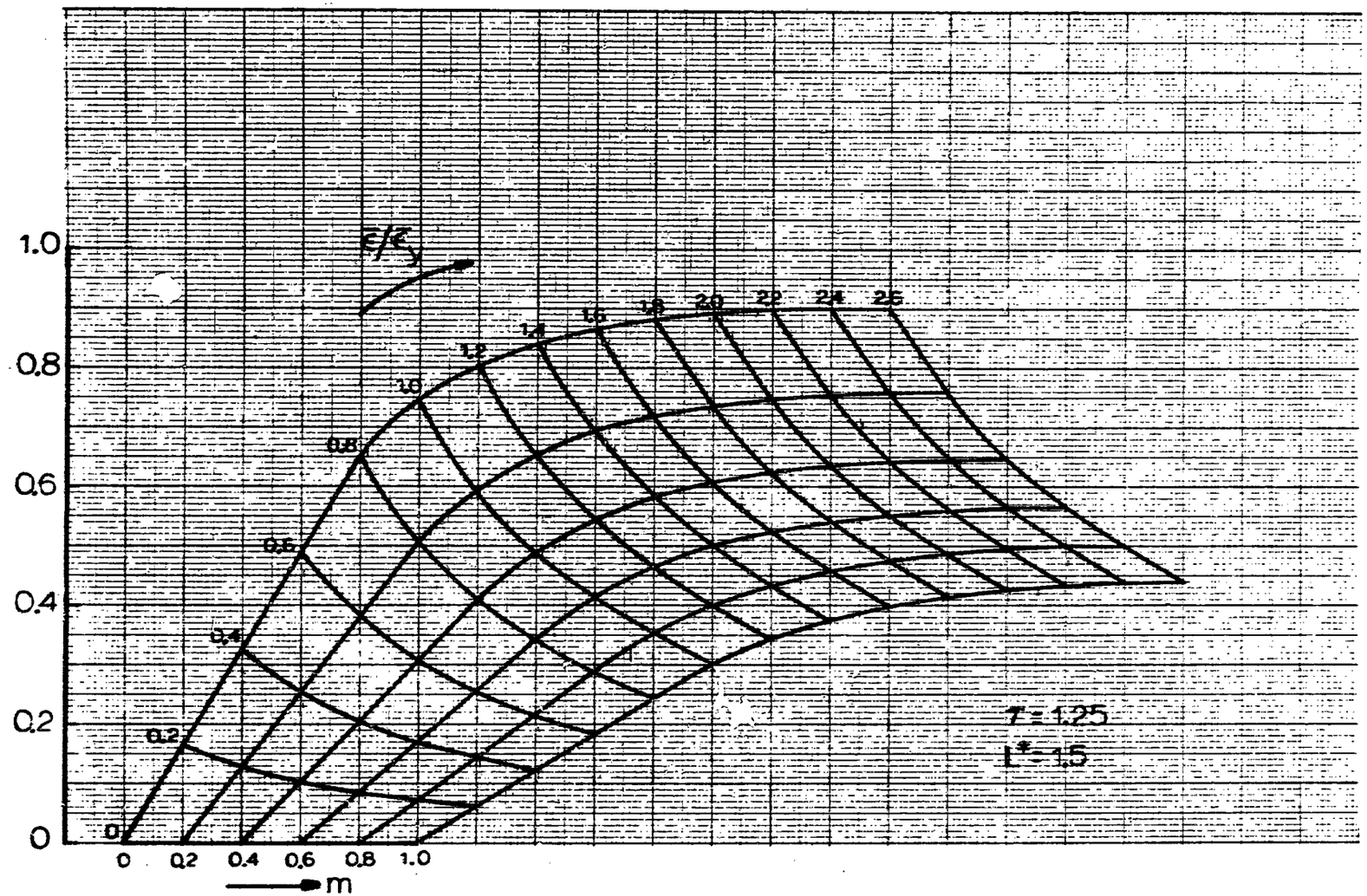

Fig. 6-15 Hemisphere-Cylinder Juncture with Mismatch. Weld Land, $\tau = 1.25$, $L^* = 1.5$.

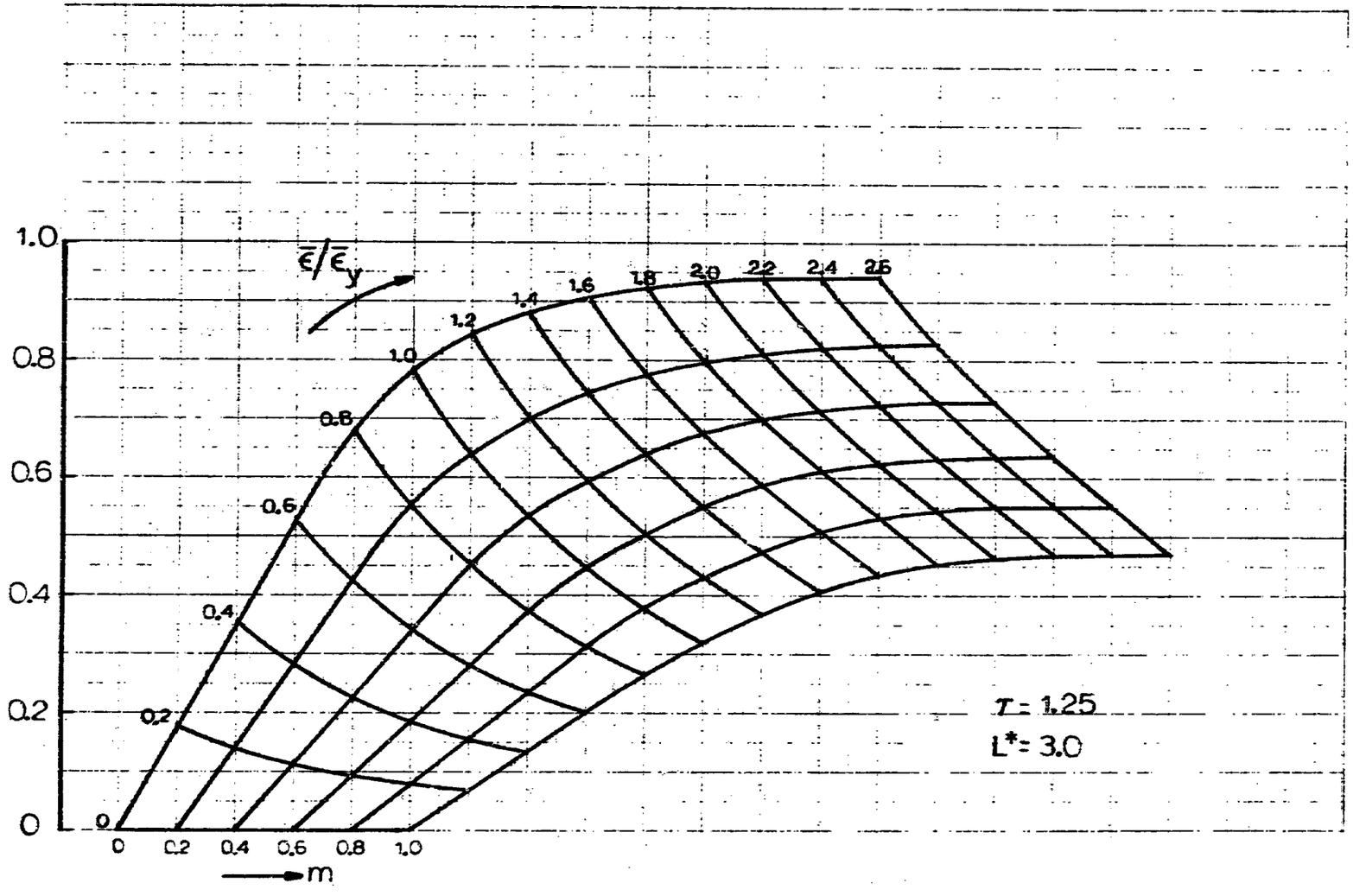

Fig. 6-16 Hemisphere-Cylinder Juncture with Mismatch. Weld Land, $\tau = 1.25$, $L^* = 3.0$.

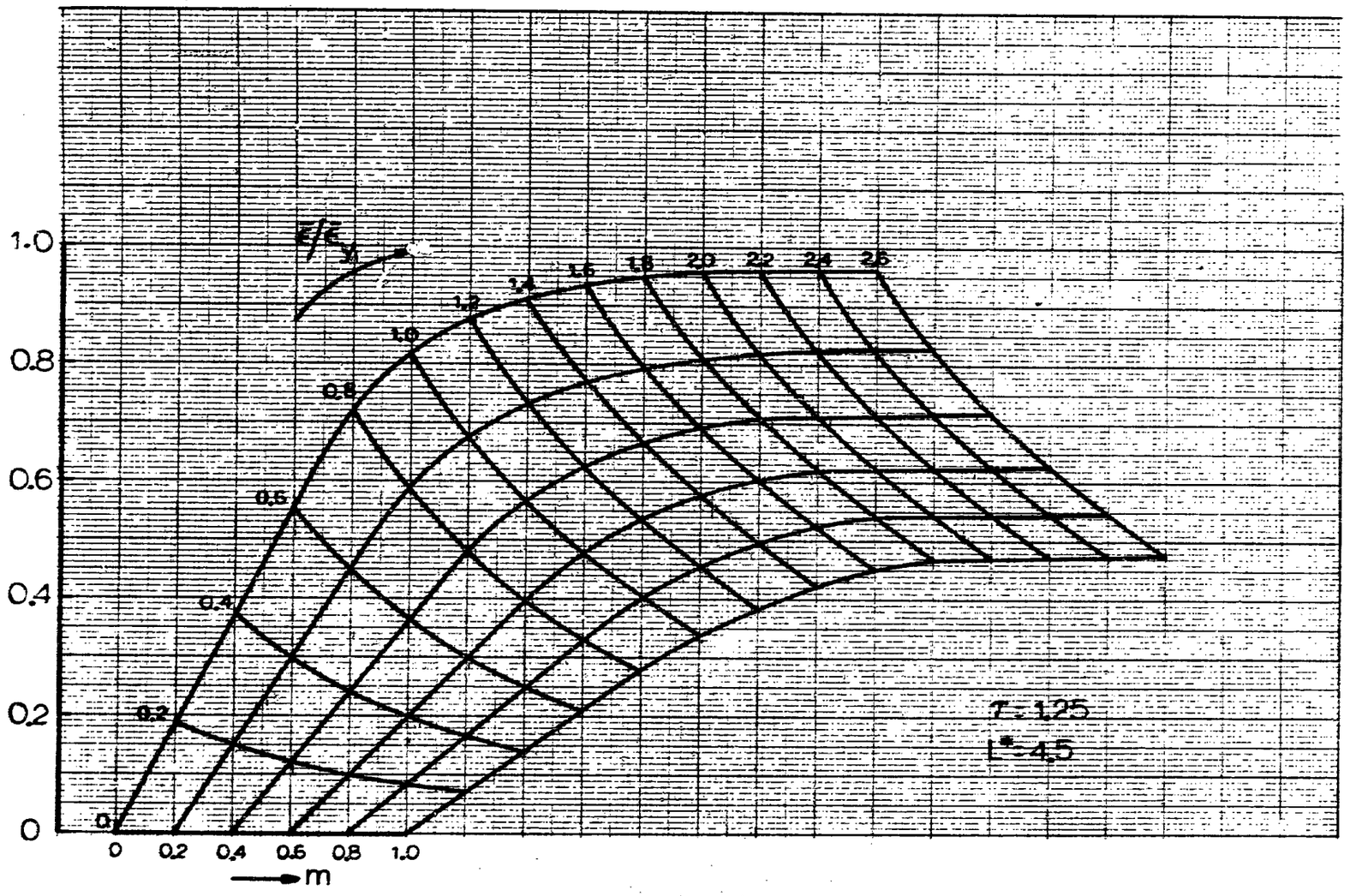

Fig. 6-17 Hemisphere-Cylinder Juncture with Mismatch. Weld Land, $\tau = 1.25$, $L^* = 4.5$.

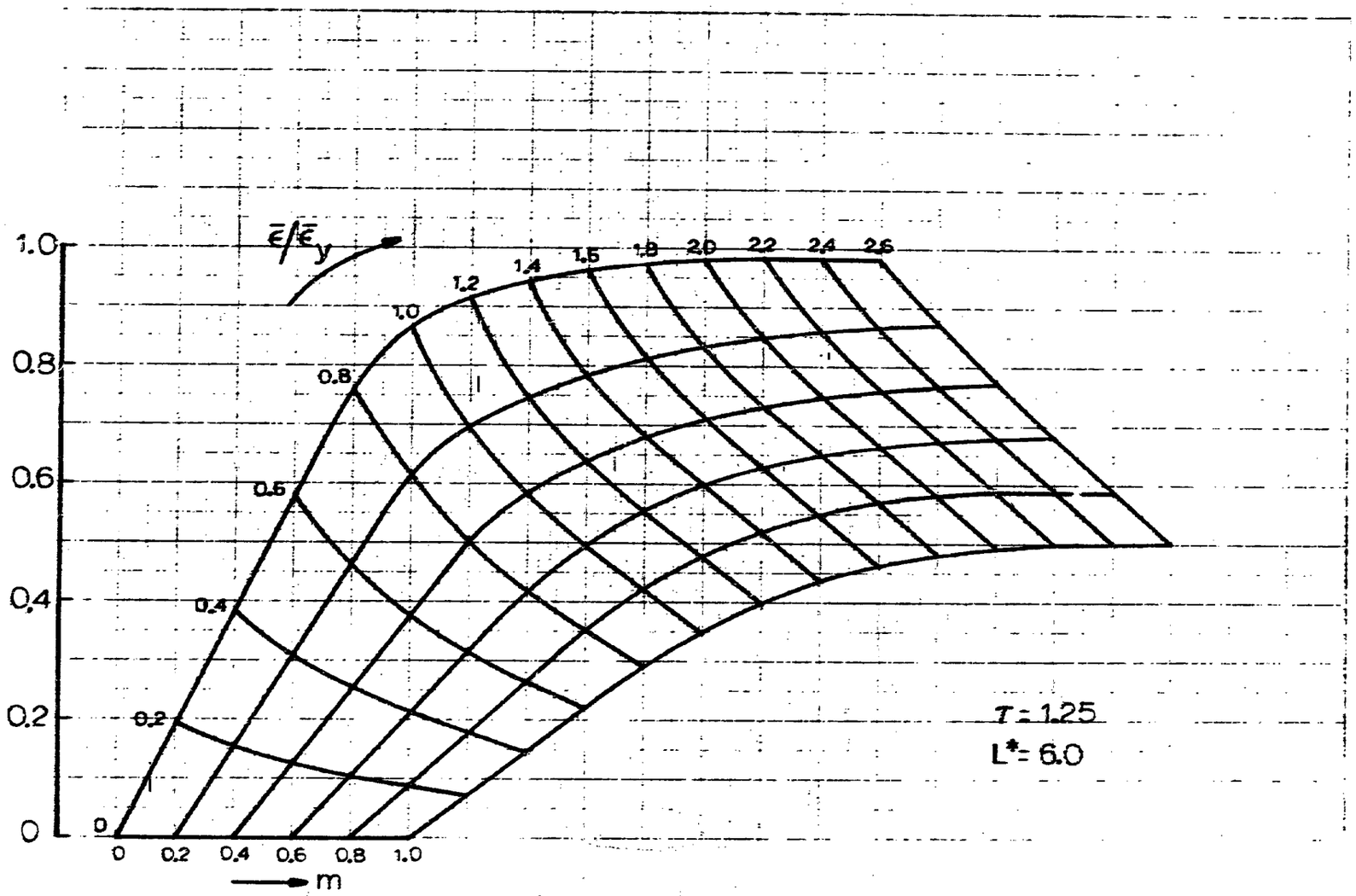

Fig. 6-18 Hemisphere-Cylinder Juncture with Mismatch. Weld Land, $\tau = 1.25$, $L^* = 6.0$.

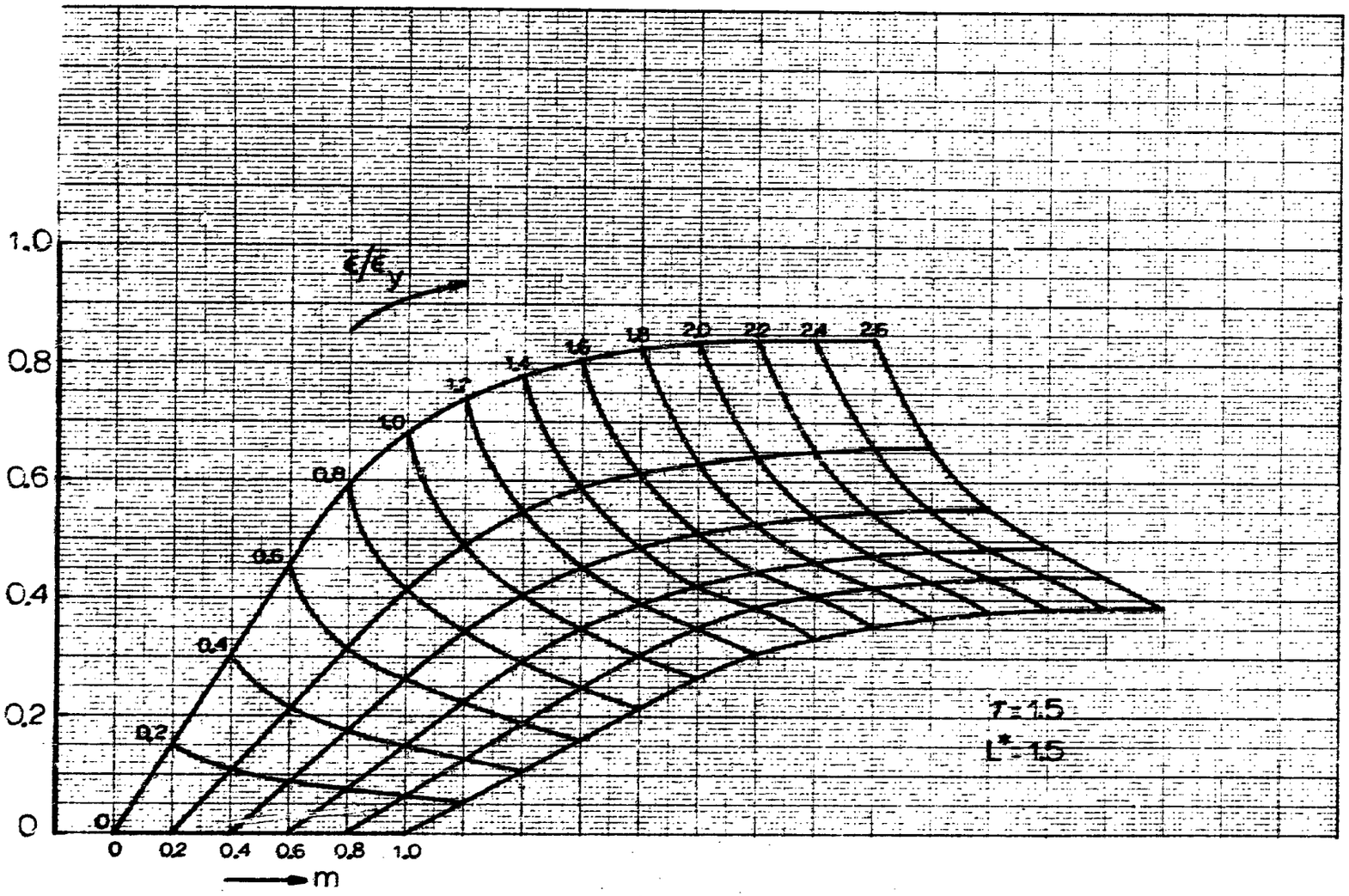

Fig. 6-19 Hemisphere-Cylinder Juncture with Mismatch. Weld Land, $\tau = 1.5$, $L^* = 1.5$.

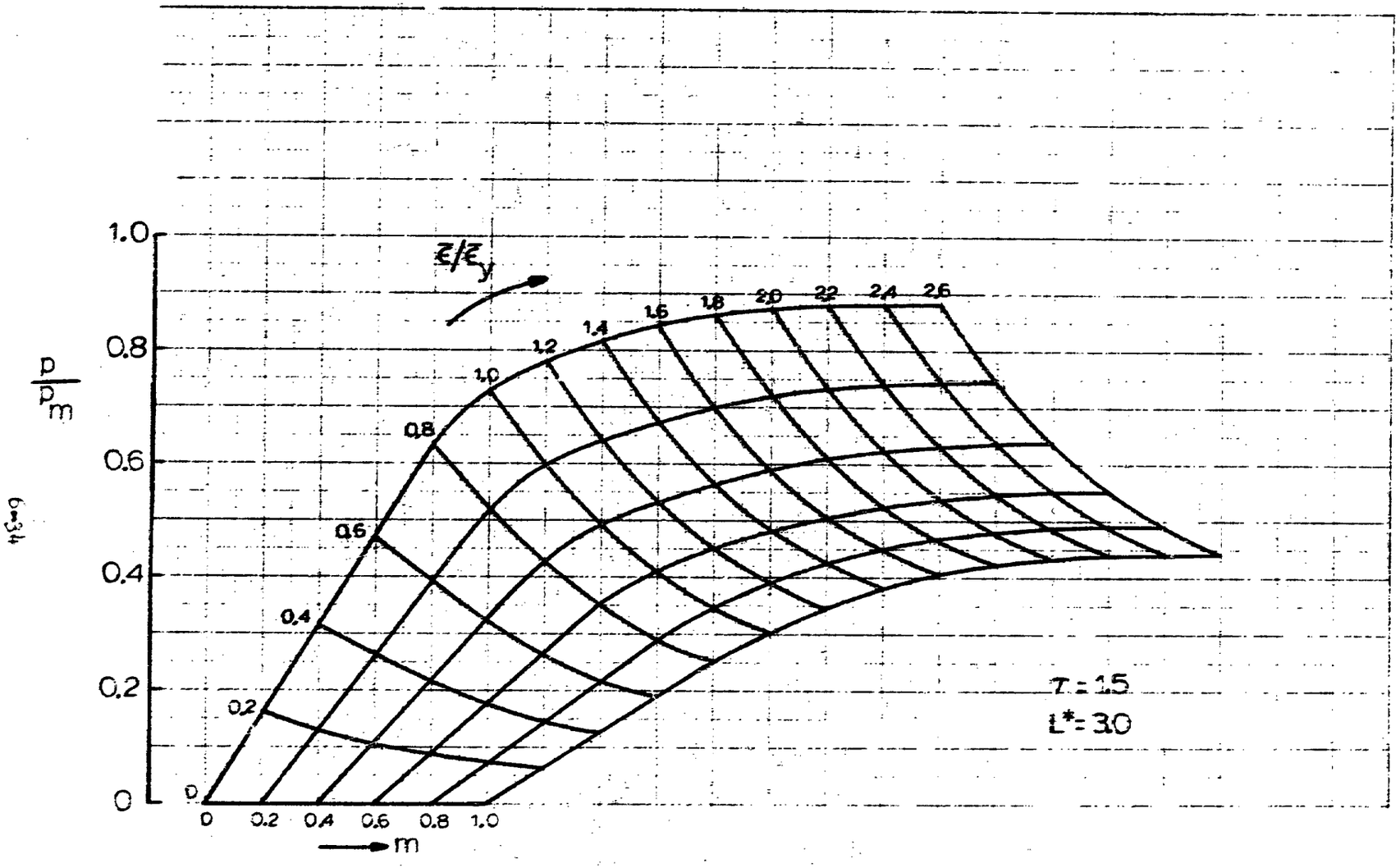

Fig. 6-20 Hemisphere-Cylinder Juncture with Mismatch. Weld Land, $\tau = 1.5$, $L^* = 3.0$.

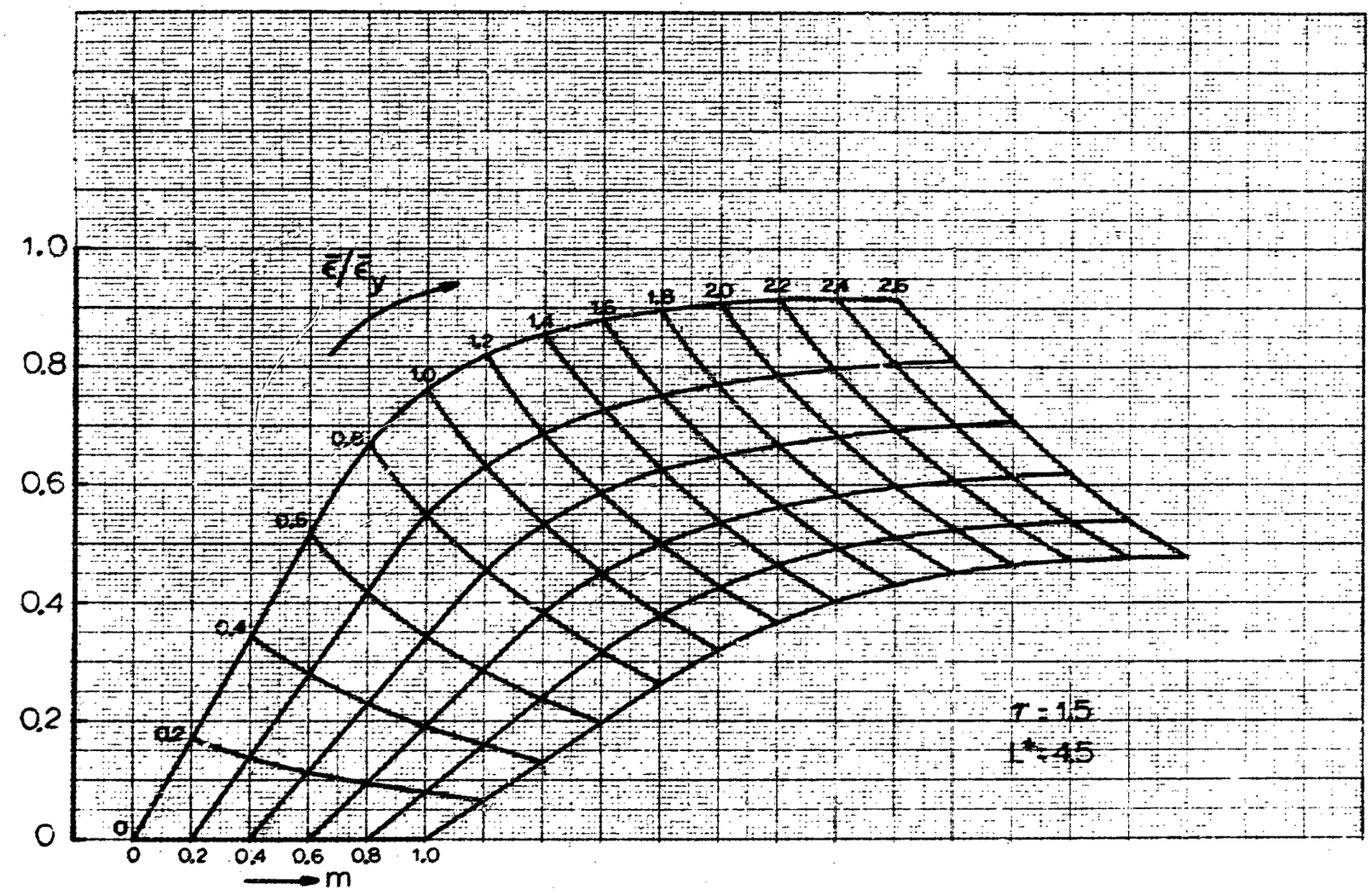

Fig. 6-21 Hemisphere-Cylinder Juncture with Mismatch. Weld Land, $\tau = 1.5$, $L^* = 4.5$.

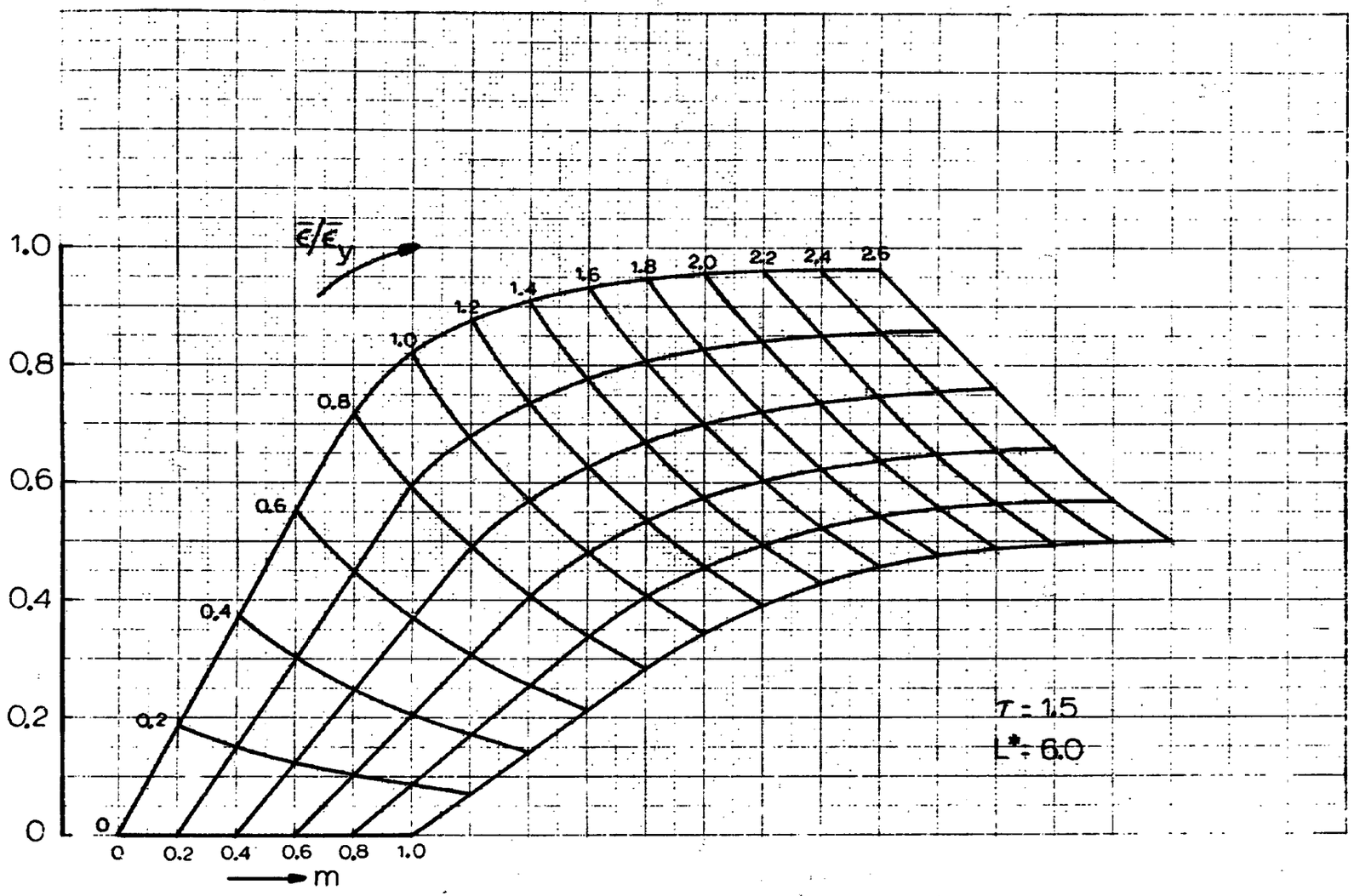

Fig. 6-22 Hemisphere-Cylinder Juncture with Mismatch. Weld Land, $\tau = 1.5$, $L^* = 6.0$.

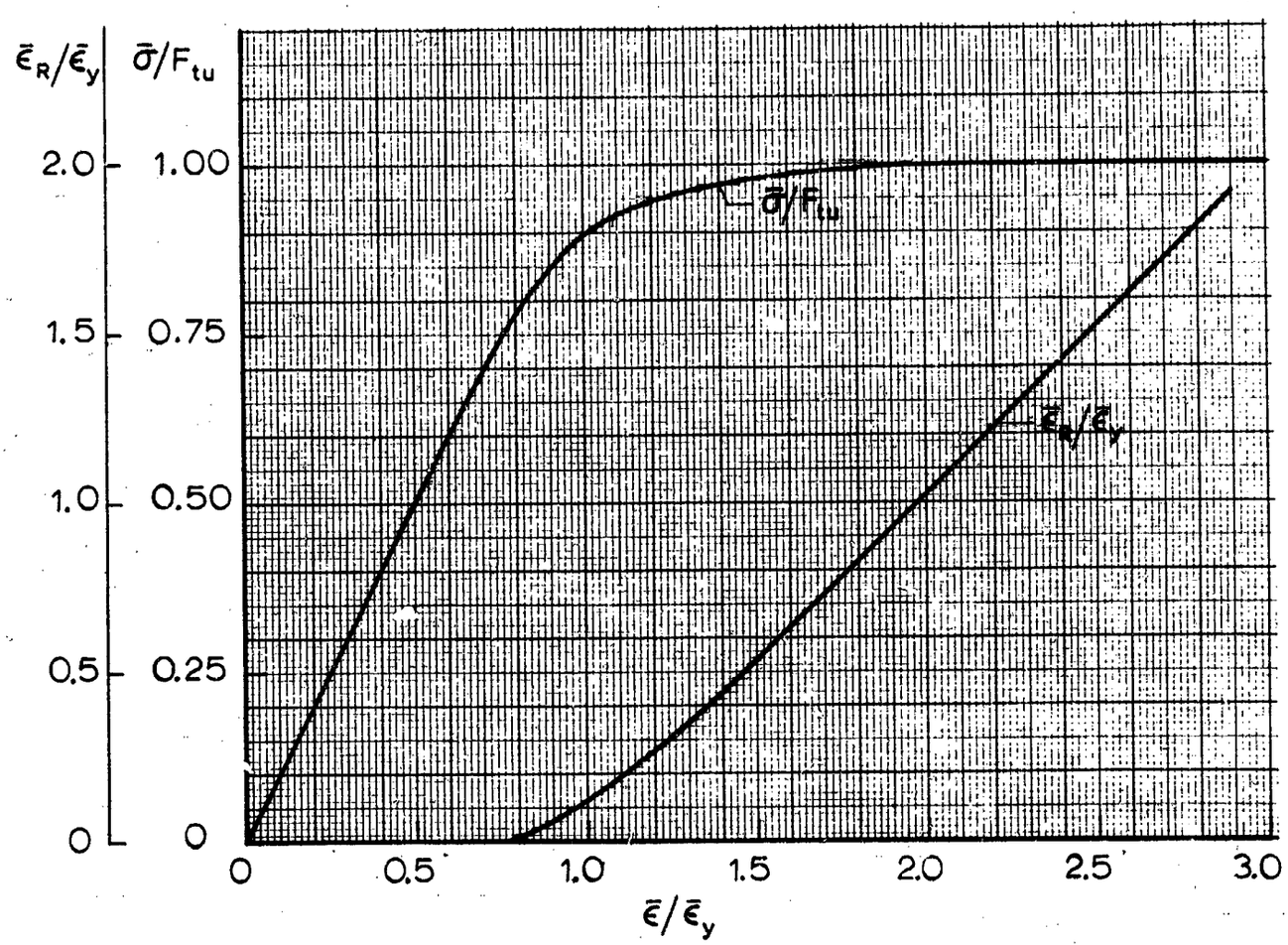

Fig. 6-23 Stress-Strain Relations

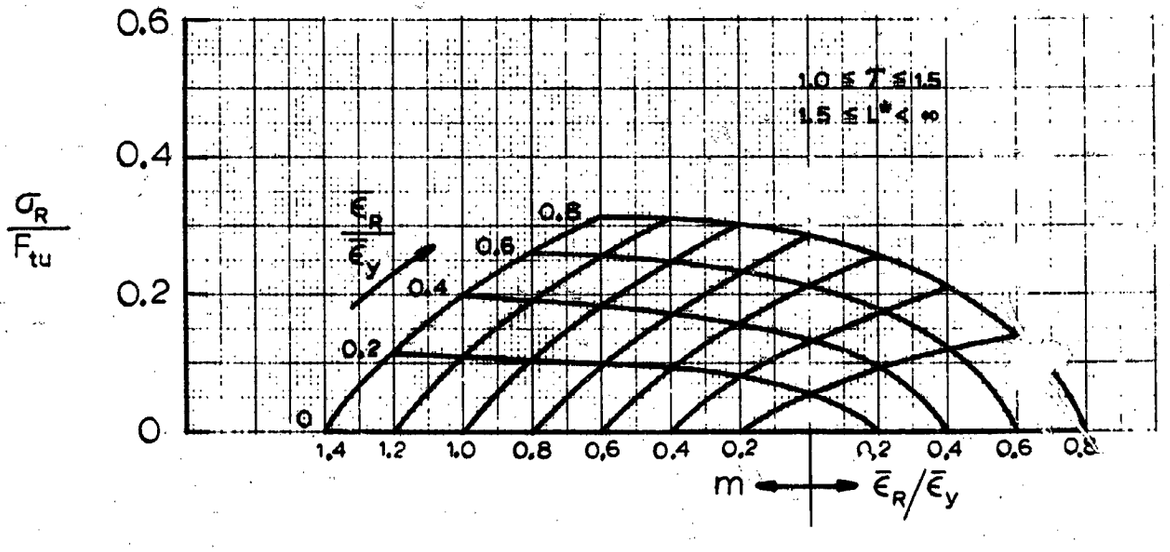

Fig. 6-24 Residual Stress in Shell Junctures with Mismatch

Section 7

EXPERIMENTAL PROGRAM

7.1 Introduction

Six titanium specimens having simulated weld land mismatches were pressurized for purposes of comparison with theoretically predicted behavior and to experimentally develop low-cycle fatigue data. In each case, extensive strain gage data was taken in the vicinity of the mismatch. Cycling of the pressure in the plastic range of the material was performed on all specimens, and strain data on cycles repeated to the same pressure was obtained. Five of the six specimens were pressurized to failure.

Four of the specimens (Tita "A" through "D") simulated mismatches between two nominally identical cylinders. Tita "E" and "F" each represented a ~~mismatch~~ between a cylinder and a sphere, both having nominally the same diameter.

The stress gradients in the vicinity of such mismatches are very steep, so that it was clear from the start that exact numerical correlation with theory, at any given strain gage site and pressure, would be impossible. The ten strain gages used on each specimen were therefore arranged along a meridian so as to show the characteristic peaks and gradients near the mismatch. Even for this to be successful, the geometry of the mismatch had to be clean and well defined. The mismatch was therefore obtained by careful machining of a thicker blank, rather than by actual welding.

Section 7 is divided into the following subsections:

7.2 Description of the Specimens and Their Manufacture.

7.3 Instrumentation and Test Details.

7.4 Data Processing and Presentation.

Five photographs of the tested specimens are located in Section 9, at the end of this report. All strain data tables are presented in Appendix B.

7.2 Description of the Specimens and Their Manufacture

7.2.1 Material

All specimens were made of 6Al-4V titanium. The blanks for both the cylinder-cylinder specimens and the cylinder-hemisphere specimens were forged by the Viking Forge and Steel Company, Albany, California, and received ultrasonic inspection to a 3/64" standard flat bottom hole. The chemical analysis supplied by Viking Forge shows the following chemical composition:

Aluminum	6.00 %
Vanadium	3.88
Nitrogen	0.009
Oxygen	0.13
Hydrogen	0.0011
Iron	0.135
Carbon	0.021
Titanium to 100%	

In the annealed, forged and stress relieved condition, Viking reports a 0.2 percent offset yield strength of 128.6 ksi, fourteen percent maximum elongation and an ultimate strength ranging fr m 142.5 to 170.0 ksi.

The cylinder-cylinder specimens (Tita "A" through "D") were machined from forged rings having an O.D. of 10.25 inches, a wall thickness of 0.5 inches, and a length of 9.75 inches. The extra length was used to provide material for test coup ns (machined from the blank after heat treat). The cylinder-hemisphere specimens were machined from solid forged cylindrical billets, and coupons were taken from the corners of these billets. The solid billets were rough-machined to an outline approximately 0.5 inches thick and containing the finished desired cross-section of the specimen.

7.2.2 Solution Treatment and Aging

The six units (all having an approximate uniform thickness of 0.5 inches) were then solution treated and aged. This consists of a soak at

1700°F for one hour followed by a water quench (solution treatment), then aging for four hours at 950°F.

7.2.3 Finish Machining

The final machining was done in four stages on all specimens. In stage #1, approximately 0.1 inches of material was removed from the inner surface of the blank. In stage #2, about the same amount was removed from the outside surface. In stage #3, the inside was finished to the final dimensions (requiring the removal of about 0.1 inches more of material thickness). A close-fitting hard-wood mandrel was then inserted inside the specimen, and in stage #4, the outside surface was finished to the final dimensions. Figures 7-1 through 7-6 show the cross-sections of revolution of the six specimens. The dimensions given in these figures were machining goals, and are not necessarily the finished dimensions, though the difference between these two was quite small. Tables 7.1, 7.2 and 7.3 list the results of thickness mappings done on Tita "A", Tita "E" and Tita "F", respectively. As can be seen from these tables, the circumferential variation in thickness is usually less than plus/minus 0.001 inches.

The successive removal of material first from the inner then outer surfaces was intended to minimize ovalizing and circumferential thickness variation which can occur due to residual stresses. The removal of material from one surface (in stage #1) inevitably causes ovalizing of the unmachined surface. But this ovalness is machined away in stage #2. While stage #2 is in process the once true surface of stage #1 is becoming ovalized, but to a much lesser extent. This ovalness is eliminated in stage #3 which in turn may leave an ovalness of even lesser order to be machined away in stage #4. Each time a surface is machined, it ends up true at the expense of the other surface. But the less material there is left, the less residual stress there is to cause further ovalizing. For once, the Law of Diminishing Returns works in our favor. Final "out-of-roundness" was never move then 0.005 inches, compared to figures ten to twelve times larger in a previous similar test program [1] where the inner-outer technique was not used. Circumferential thickness variations were also far better than in the previous program, for obvious reasons.

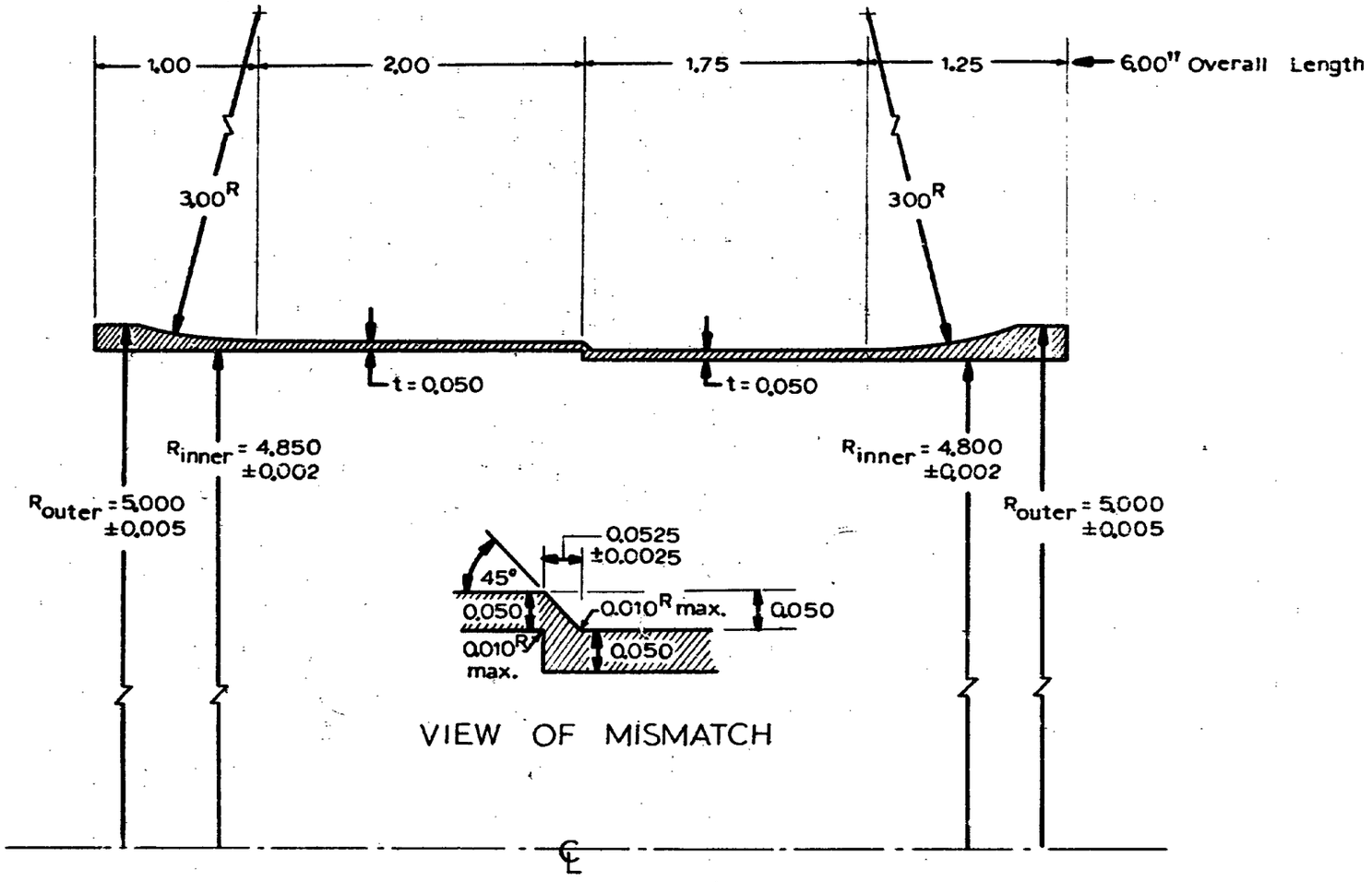

Fig. 7-1 Tita "A" Nominal Geometry (Closures Not Shown)

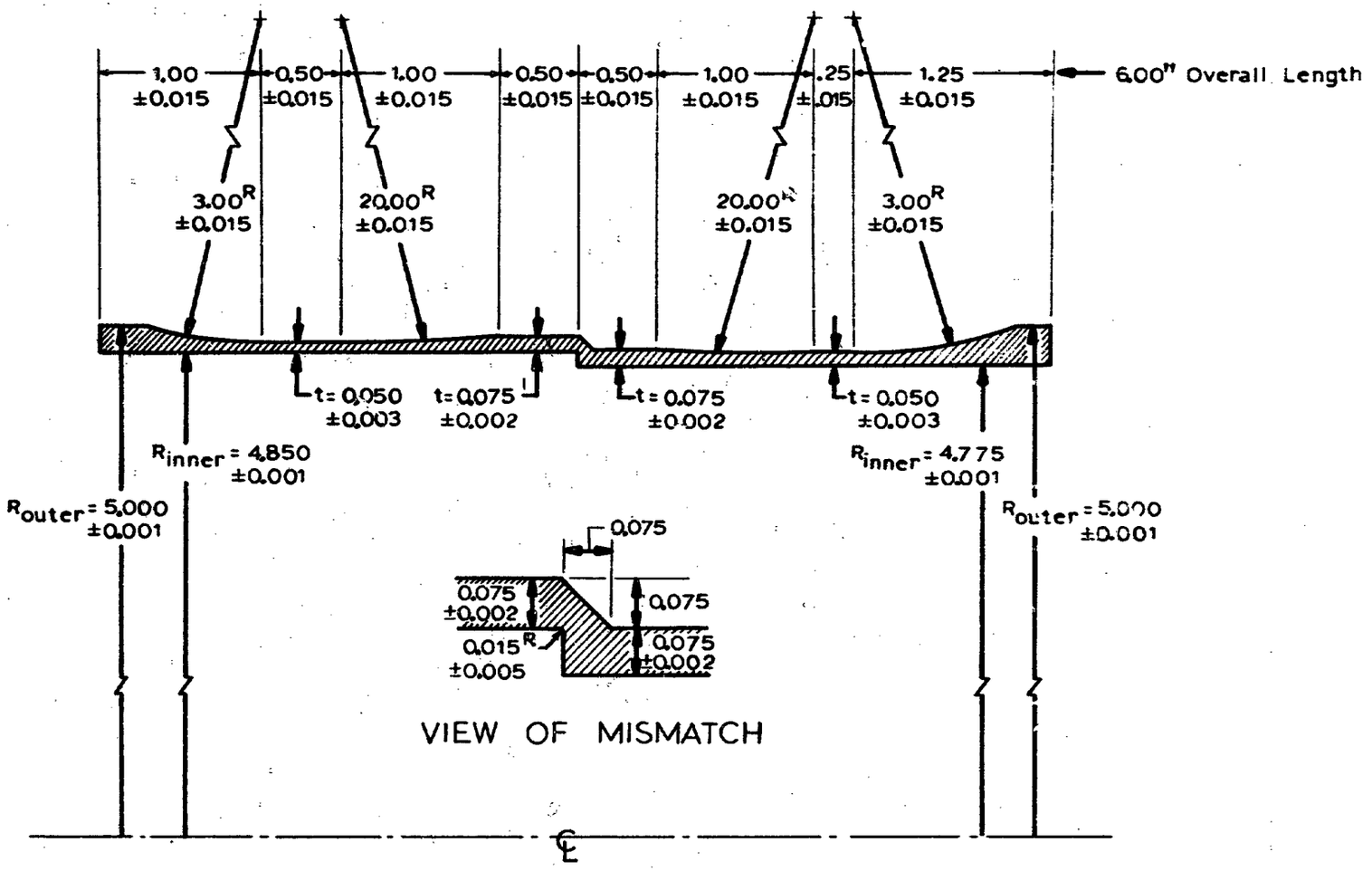

Fig. 7-2 Tita "B" Nominal Geometry (Closures Not Shown)

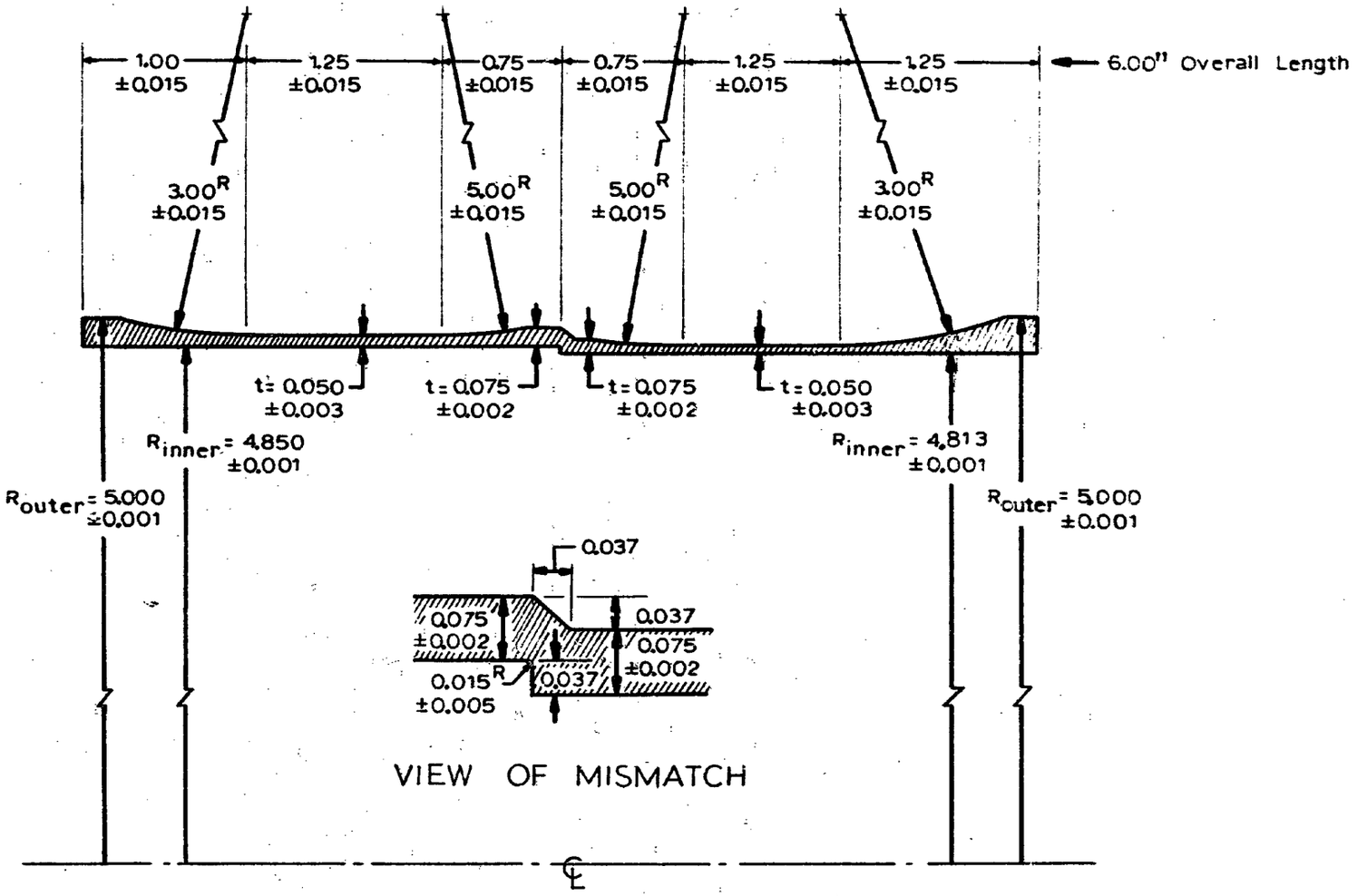

Fig. 7-3 Tita "C" Nominal Geometry (Closures Not Shown)

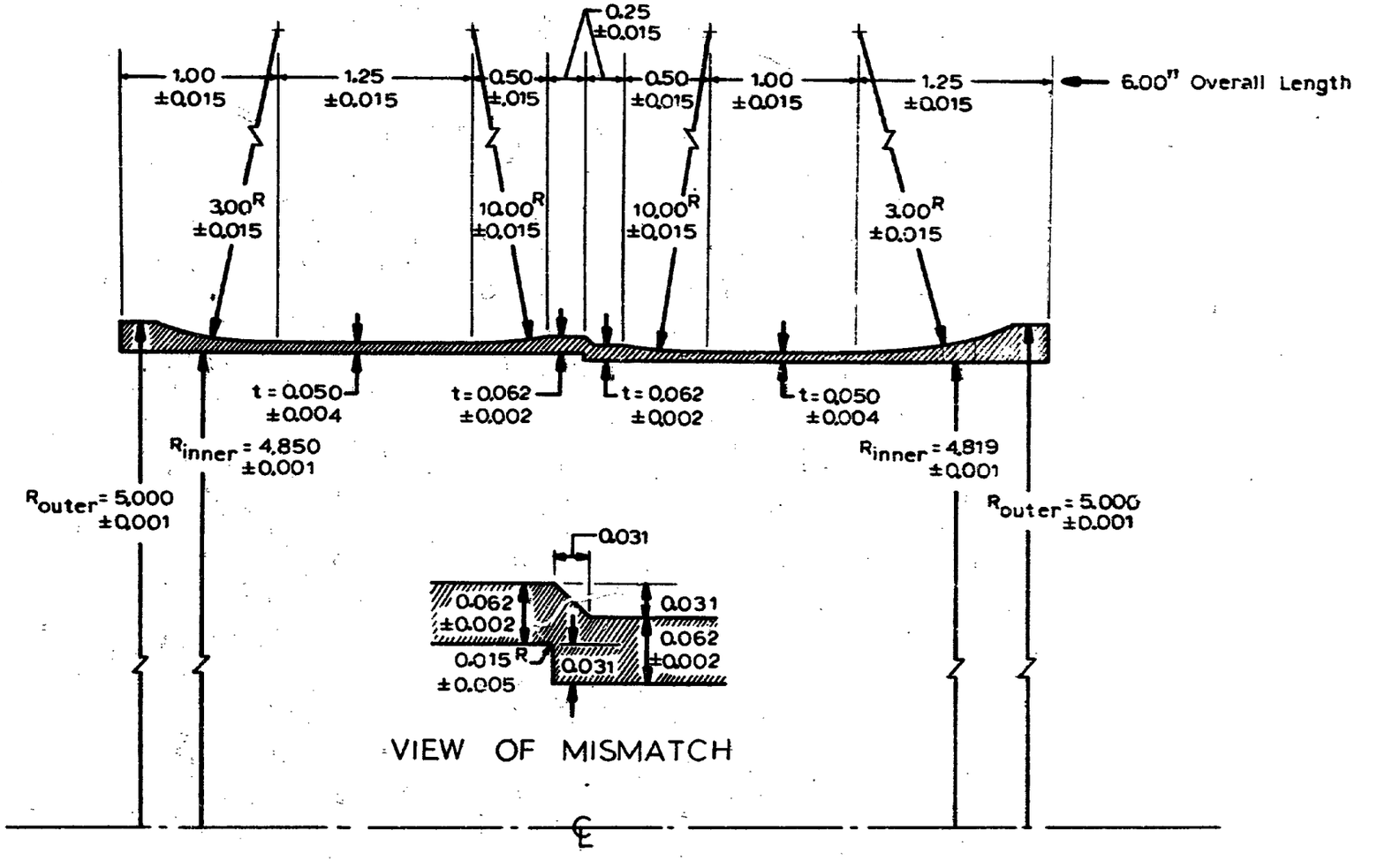

Fig. 7-4 Tita "D" Nominal Geometry (Closures Not Shown)

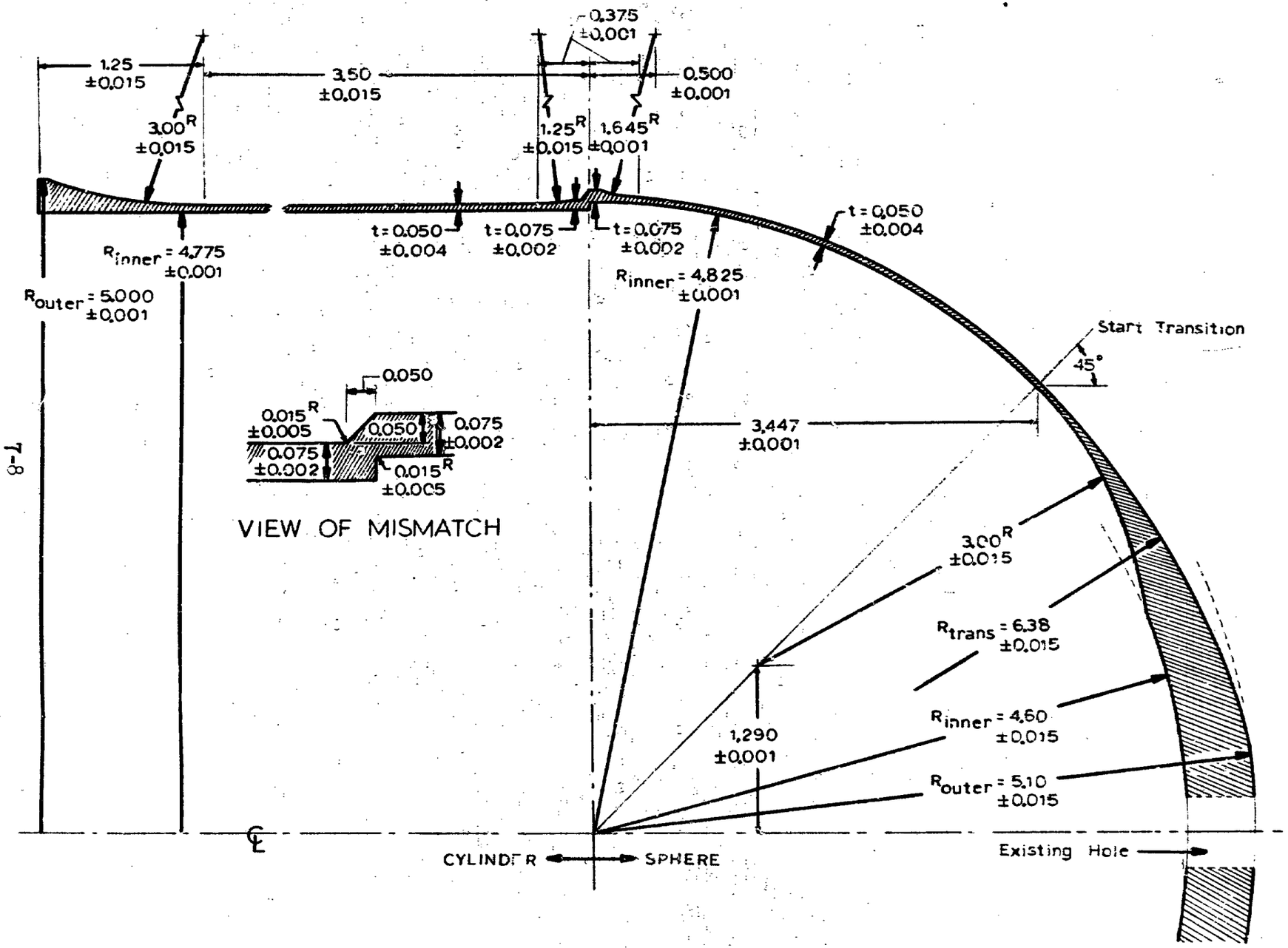
0.375 ±0.001
1.25 ±0.015
3.50 ±0.015
0.500 ±0.001
3.00R ±0.015
1.25R ±0.015
1.645R ±0.001
t = 0.050 ±0.004
t = 0.075 ±0.002
t = 0.075 ±0.002
t = 0.050 ±0.004
Rinner = 4.775 ±0.001
Router = 5.000 ±0.001
Rinner = 4.825 ±0.001
Start Transition
45°
0.050
0.015R ±0.005
0.050
0.075 ±0.002
0.075 ±0.002
0.015R ±0.005
VIEW OF MISMATCH
3.447 ±0.001
3.00R ±0.015
Rtrans = 6.38 ±0.015
Rinner = 4.60 ±0.015
Router = 5.10 ±0.015
1.290 ±0.001
CYLINDER
SPHERE
Existing Hole

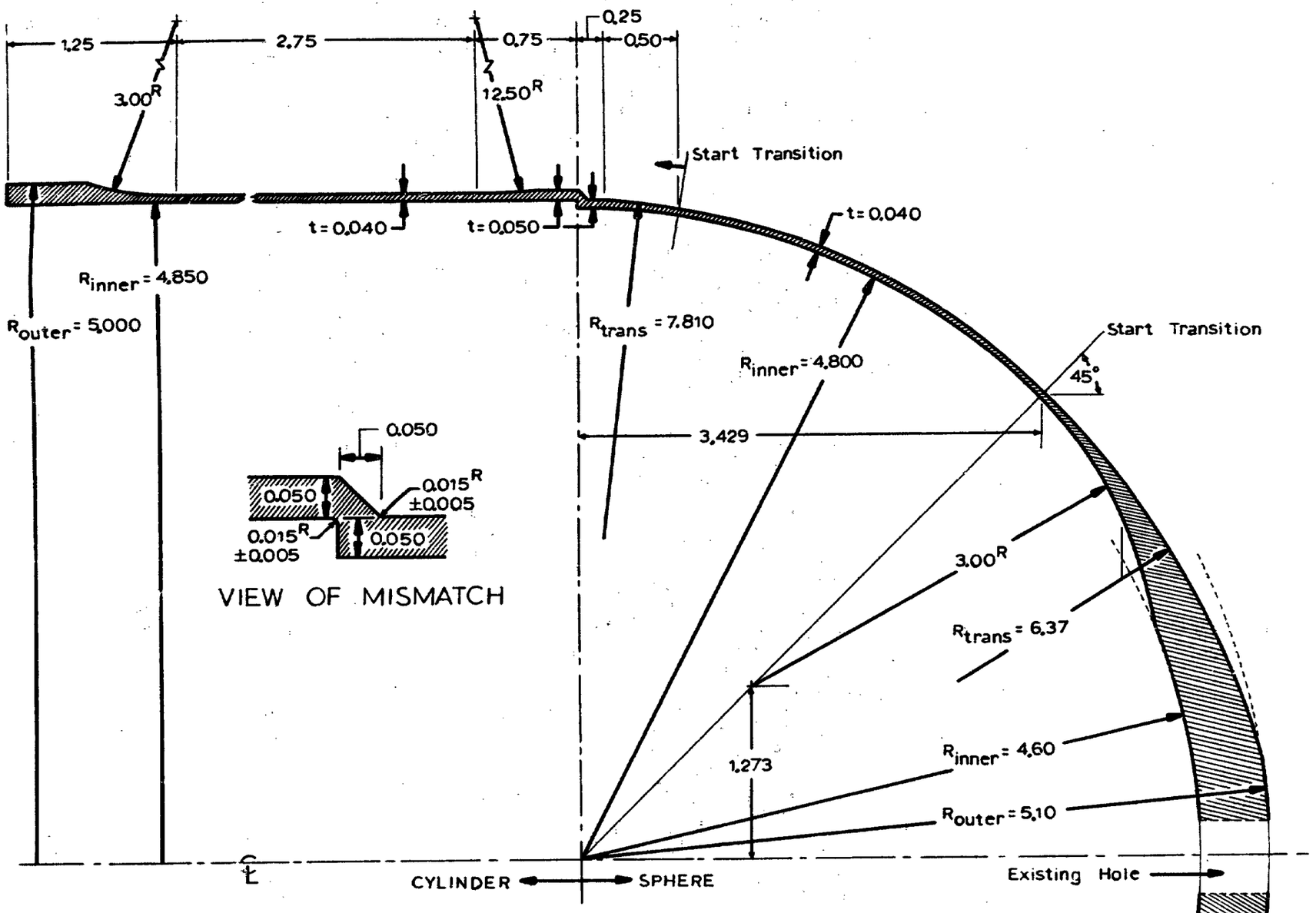

Fig. 7-6 Tita "F" Nominal Geometry (One Closure Not Shown)

Table 7.1

THICKNESS MEASUREMENTS - TITA "A"

Inches (Circumferentially) from Strain Gaged Zone →	-9.7	-5.8	-1.9	0.0	+1.9	+5.8	+9.7	+13.6	+17.5
Inches (Longitudinally) from Mismatch (Vertical Surface) ↓									
-1.05	.0526	.0520	.0527	.0522	.0517	.0525	.0512	.0523	.0526
-.80	.0526	.0518	.0527	.0522	.0520	.0515	.0512	.0522	.0523
-.55	.0520	.0522	.0523	.0522	.0520	.0520	.0512	.0520	.0520
-.30	.0500	.0522	.0522	.0522	.0512	.0513	.0512	.0517	.0520
+.25	.0503	.0500	.0505	.0492	.0493	.0503	.0492	.0503	.0500
+.50	.0503	.0503	.0505	.0492	.0497	.0498	.0502	.0512	.0503
+.75	.0508	.0502	.0507	.0492	.0497	.0497	.0500	.0507	.0505
+1.00	.0505	.0501	.0502	.0492	.0497	.0497	.0508	.0501	.0500

Table 7.2

THICKNESS MEASUREMENTS - TITA "E"

Inches (Circumferentially) from Strain Gaged Zone → / Inches (Longitudinally) from Mismatch (Vertical Surface) ↓	-9.7	-5.8	-1.9	0.0	+1.9	+5.8	+0.7	+13.6	+17.5
1.00	.0428	.0416	.0415	.0407	.0410	.0415	.0417	.0425	.0425
.750	.0428	.0420	.0412	.0410	.0410	.0417	.0424	.0425	.0430
.500	.0425	.0420	.0412	.0405	.0412	.0417	.0420	.0427	.0430
.250	.0422	.0420	.0407	.0402	.0414	.0407	.0410	.0432	.0420
.050	.0750	.0750	.0750	.0740	.0750	.0750	.0750	.0760	.0765
.250	.0520	.0533	.0517	.0512	.0525	.0535	.0540	.0565	.0553
.500	.0455	.0502	.0463	.0460	.0455	.0450	.0463	.0454	.0450
.750	.0490	.0486	.0478	.0472	.0488	.0495	.0488	.0500	.0490
1.00	.0498	.0490	.0488	.0485	.0488	.0500	.0500	.0502	.0492

Table 7.3

THICKNESS MEASUREMENTS - TITA "F"

Inches (Circumferentially) from Strain Gaged Zone →	-9.7	-5.8	-1.9	0.0	+1.9	+5.8	+0.7	+13.(	+17.5
Inches (Longitudinally) from Mismatch (Vertical Surface) ↓									
1.000	.0425	.0428	.0428	.0422	.0430	.0423	.0437	.0445	.0432
.750	.0432	.0428	.0423	.0420	.0424	.0422	.0434	.0439	.0425
.500	.0432	.0430	.0422	.0417	.0420	.0418	.0440	.0438	.0430
.250	.0505	.0502	.0497	.0497	.0497	.0508	.0515	.0505	.0504
.150	.0500	.0507	.0500	.0500	.0503	.0514	.0514	.0514	.0506
.500	.0502	.0489	.0483	.0480	.0495	.0504	.0501	.0501	.0495
.750	.0442	.0436	.0435	.0435	.0450	.0452	.0448	.0457	.0441
1.000	.0432	.0430	.0432	.0430	.0432	.0443	.0442	.0440	.0433

7.2.4 Test Coupons

Seven test coupons were taken from the rough-machined blanks after solution treatment and aging. Those taken from Tita "E" are labelled S-1, S-2 and S-3. Those taken from Tita "A" are marked "C-1" through "C-4". The outline of the test coupons is shown in Fig. 7-7. An accurately retraced stress-strain curve for specimen S-2 is shown in Fig. 7-8. This figure also includes a table summarizing the principal test results for all the specimens.

Tests on these coupons were run on a screw-driven universal testing machine at a strain rate of approximately .005 percent (strain) per minute. Strain was measured by means of two back-to-back foil gages installed at the specimen's minimum cross-section. These gages were .062 inches square, and were wired to read the average axial strain.

7.2.5 Closure Hemispheres

Three additional solid billets were machined to form closure hemispheres. These hemispheres had a varying thickness, being 0.5 inches thick at the crown and tapering gradually and smoothly to the same thickness as that of the piece to which it was welded. After a test, the hemispheres were sawn off and their open end remachined to the proper thickness and flatness for rewelding to the next test specimen. A 9/16 inch hole at the crown of these hemispheres served to allow pressurization and passage of electrical conductors for use on the two internal strain gages.

The welding of the closure to the test specimen was done by means of an electron beam welder. For this operation, the closure was mounted onto a jig which made it possible to rotate the assembly about its axis inside the welding chamber. A weld land of at least .150 inch thickness

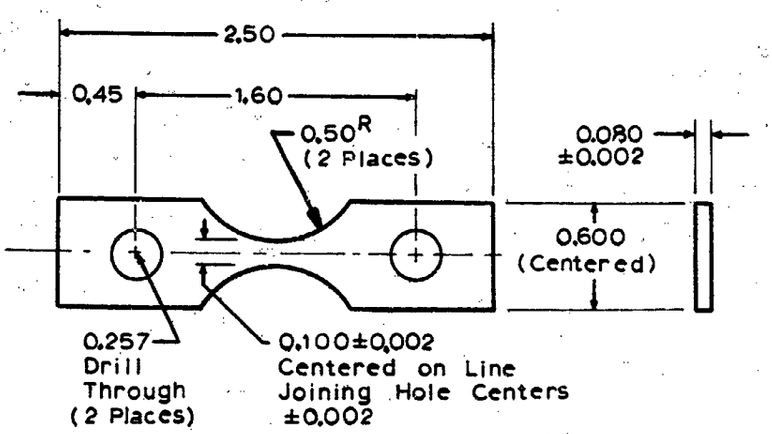

Fig. 7-7 Test Coupon Outline

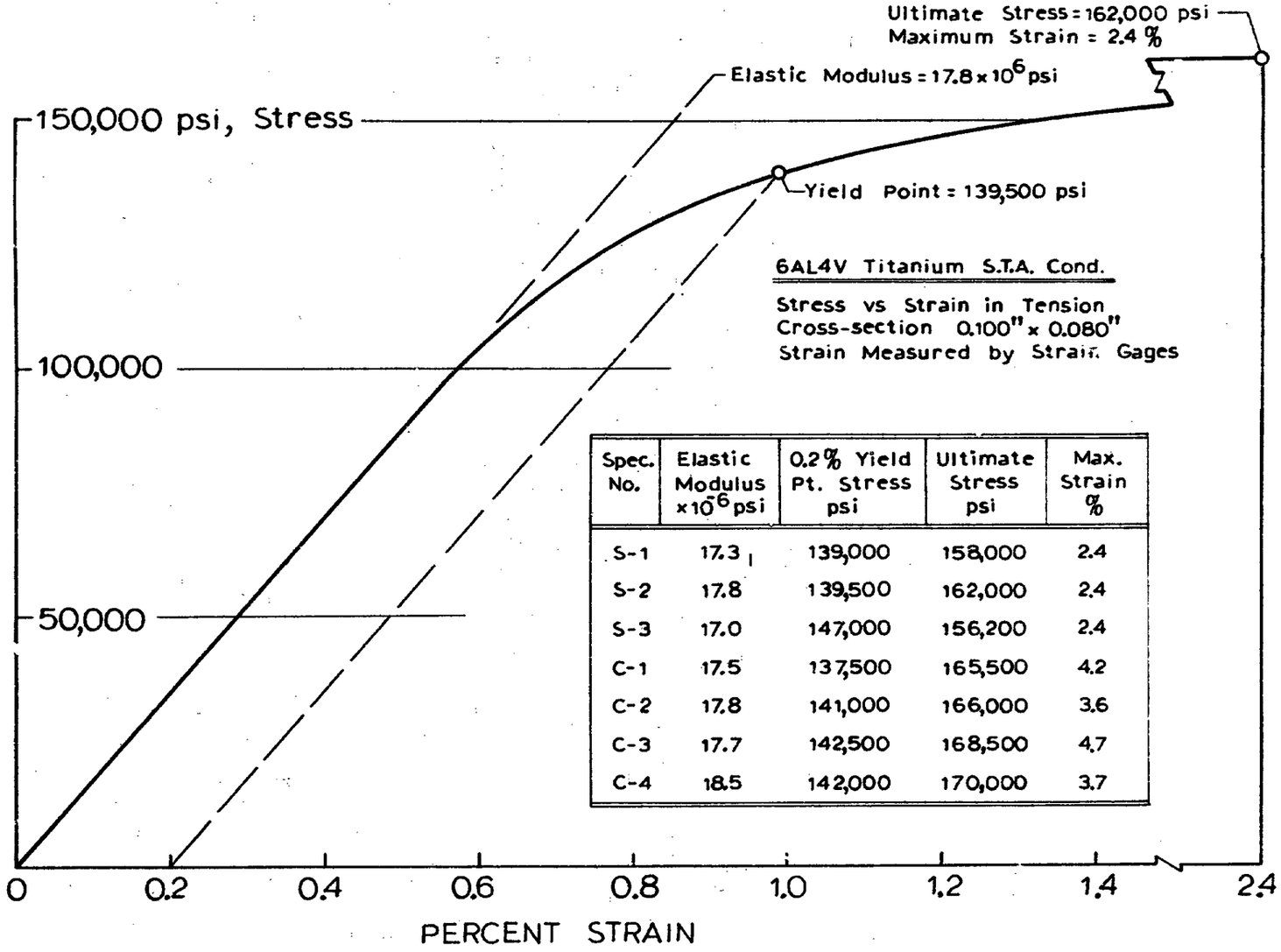

6AL4V Titanium S.T.A. Cond.

Stress vs Strain in Tension
Cross-section 0.100" x 0.080"
Strain Measured by Strain Gages

Spec. No.	Elastic Modulus $\times 10^{-6}$ psi	0.2% Yield Pt. Stress psi	Ultimate Stress psi	Max. Strain %
S-1	17.3	139,000	158,000	2.4
S-2	17.8	139,500	162,000	2.4
S-3	17.0	147,000	156,200	2.4
C-1	17.5	137,500	165,500	4.2
C-2	17.8	141,000	166,000	3.6
C-3	17.7	142,500	168,500	4.7
C-4	18.5	142,000	170,000	3.7

Fig. 7-8 Test Coupon Stress-Strain Curve

was provided on each specimen, and no difficulties were encountered in the welding of these thicker portions. The saw cut following the test was made to fall at the center of the weld.

7.3 Instrumentation and Test Details

7.3.1 Strain Gages and Their Recording

Ten strain gages were installed on each specimen, two of which were installed on the inside surface.

The numbering system and relative locations of the strain gages is the same in all tests, and is shown in Figs. 7-9 and 7-11. It will be noted in these figures that the exact distance from one gage to the next varies from one test to the other, and this is because the variations in geometry made these changes advisable.

These figures also supply the actual thicknesses measured in the vicinity of the strain gage sites, and gives the widths of the simulated weld lands, weld land transitions, and weld beads, as well as the actual mismatch or offset in each case.

Note also that from Tita "E" to Tita "F" there is a reversal in the direction of the gage numbering (from left to right). This was done to preserve the relative positions of the gages and because the larger diametered member was of more interest from the standpoint of strain measurement.

While these diagrams are essentially to scale, a few dimensions were distorted to avoid the need for a fold-out sheet. All distorted dimensions are marked by an asterisk.

Where a transverse (circumferential) gage is shown coupled with a longitudinal gage, a T-rosette was used, with their elements about 0.10 inches apart (in the circumferential direction only).

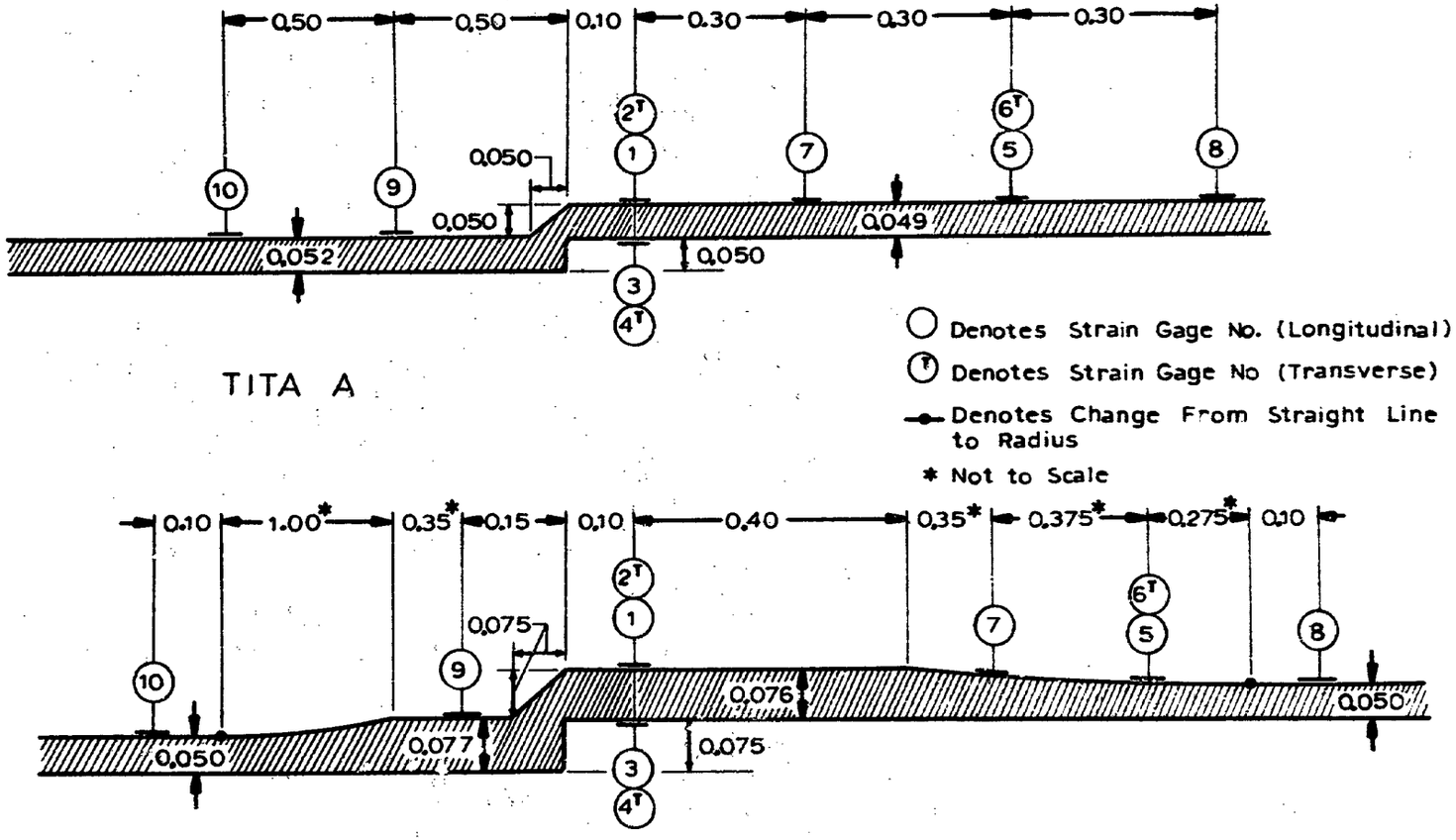

Fig. 7-9 Geometry at Mismatch, and Gage Locations for Tita "A" and Tita "B"

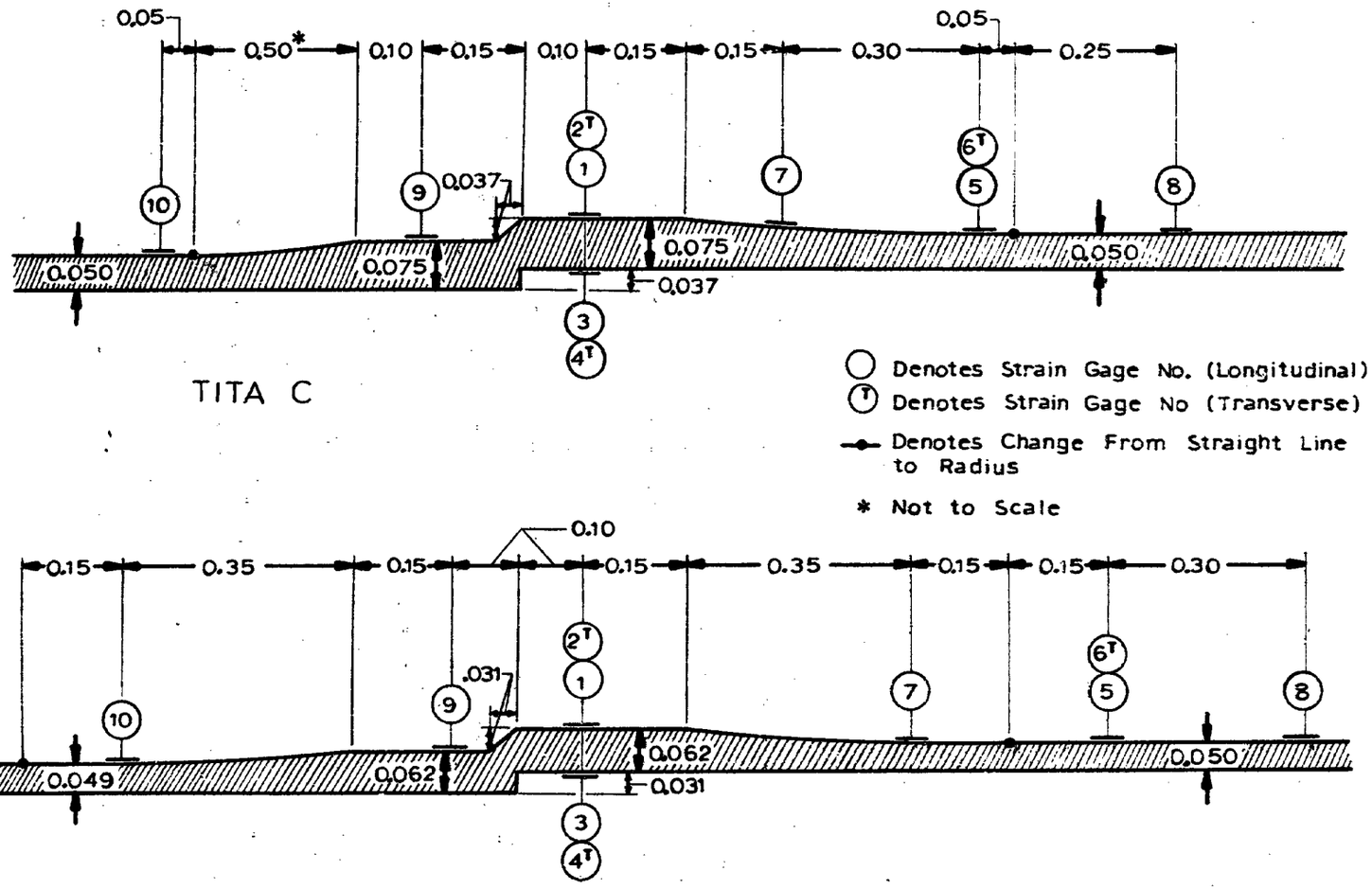

Fig. 7-10 Geometry at Mismatch, and Gage Locations for Tita "C" and Tita "D"

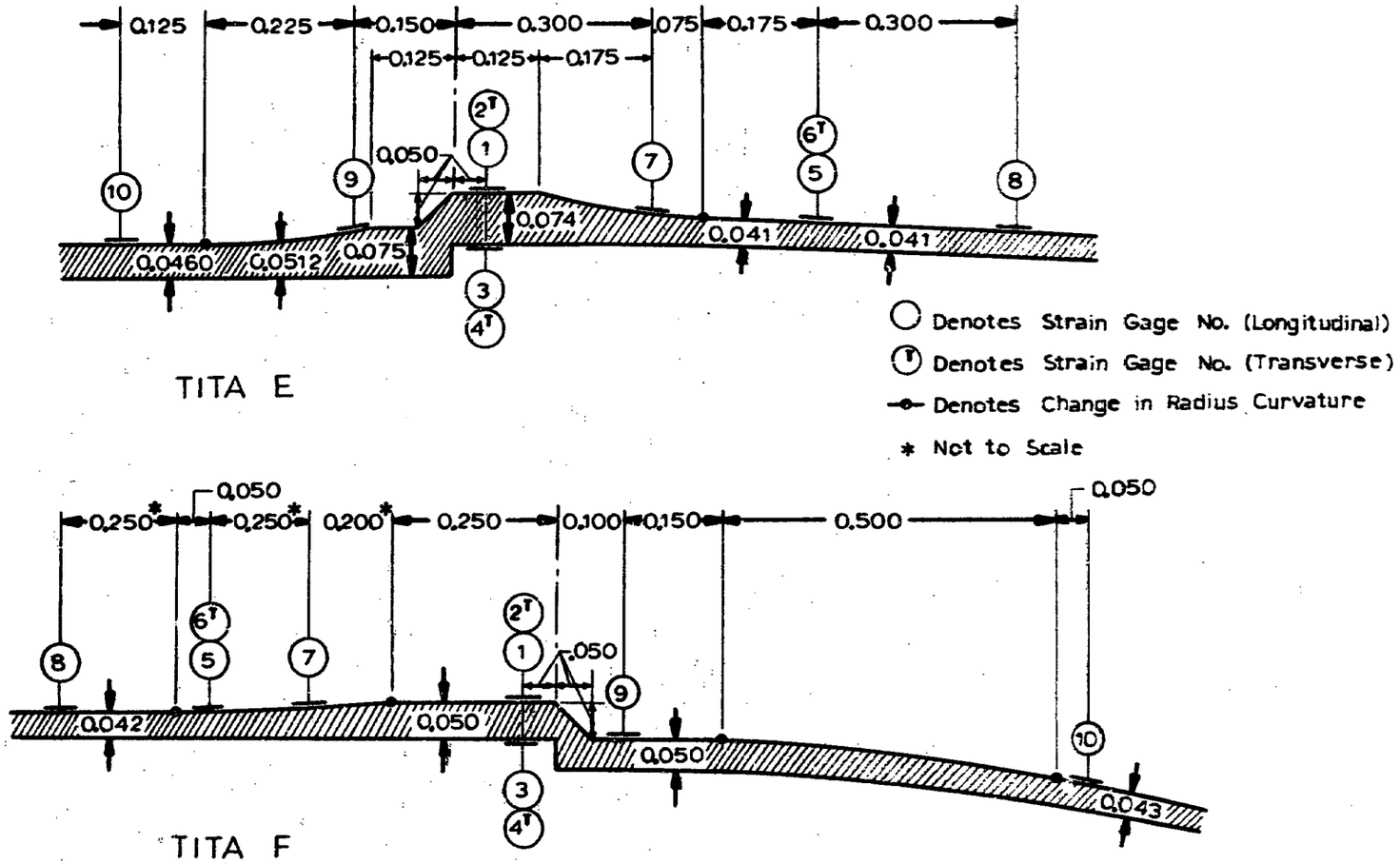

Fig. 7-11 Geometry at Mismatch, and Gage Locations for Tita "E" and Tita "F"

Gages used were epoxy-backed constantan foil, having six parts per million per degree F temperature compensation and 1/16 inch gage length, whether rosette or single element. The surface of the titanium was first degreased with successive acetone swabbings. A quick wipe with a dilute etchant (1.5% HF, 30% HNO_3, 68.5% H_2) was followed by swabbing with an ammoniated neutralizer. The cement used for bonding the gages was William T. Bean's epoxy "RTC Fix-Mix" which requires an hour's cure at 140°F.

The gages were shunt calibrated, with the usual corrections applied for lead resistance and for any shunt resistors needed to balance the bridge.

The strain gage signals, along with that of the pressure transducer, were measured and recorded by a Hewlett Packard 2445 Series Data Acquisition System (DAS). The DAS consists of a cross-bar scanner which selects the gage to be read, an integrating digital voltmeter (reading to one microvolt accuracy), and two recording devices in parallel: One, a printer which puts the data in digital form on a tape for test monitoring purposes, and two, a perforated tape punch so that the data can be processed on a computer.

To obtain strain data in engineering units, the DC bridge voltage is set at approximately two. The exact voltage is set with a finely adjustable control to produce the desired number of digital counts upon application of a precision calibration shunt to the gage.

The largest source of inaccuracy in the system is the manufacturer's stated precision of the gage factor (plus/minus half a percent). The resolution and repeatability of the system is one microstrain. This fact is made amply evident from the strain tables which are discussed further on.

The external array of gages is visible in Fig. 9-2 which shows Tita "B" after test.

7.3.2 Pressure Measurement

Pressure was measured by two independent devices in parallel with the pressure line into the specimen. One of these was a Teledyne Model 206-SA strain gage bridge pressure transducer with a range from zero to

2000 psi, and the other was a Heise precision dial gage with the same range and a resolution of 2.5 psi. The Teledyne gage was connected to the above mentioned DAS, and the bridge excitation was adjusted to produce one count per psi of pressure.

7.3.3 Pressurization Device

Hydraulic pressure was obtained from an electrically driven hydraulic power supply, and controlled by a Research Inc. "Servac" unit which in turn controlled a Moog Series 73 servovalve with a two gpm capacity.

A ramp voltage generator also capable of holding a constant voltage at any desired level, was used to supply a command voltage to the Servac, thus assuring smooth pressure increase with no overshoot at the pressure plateaus.

7.3.4 Test Procedure - Preliminary

Prior to gaging, the specimen thickness was systematically mapped (see Tables 7.1 through 7.3). The strain gage array (falling entirely on one generator) was placed in the thinnest region.

Thickness mapping was done with a sheet metal micrometer having a vernier scale reading to .0001 inches, but on curved and non-rectilinear profiles the accuracy of the measurement is more probably plus/minus .0005 inches because of uncertainty as to the micrometer alignment and placement.

After closure welding, strain gage installation, and connection to the hydraulic power supply, all air was bled from the system through a T-fitting right at the specimen connection, and the specimen was installed inside a section of thick-walled pipe for personnel protection.

Pressure was applied in a series of steps, with the pressure increase between the plateaus being smooth and gradual (about 100 psi per minute). The plateaus (on the pressure vs. time record) were set at nominally 100 psi increments (50 psi for Tita "A"). Strain and pressure readings were taken at these plateaus while the pressure was being held

constant. After reaching the third (ascending) plateau and taking readings at this level, the pressure was returned to zero, at which time a full data scan was again taken. On the next cycle, the first (lowest) plateau was set at the level of the second plateau of the previous cycle, so that the highest plateau of each cycle was one pressure increment higher than the highest pressure of the previous cycle. Each cycle thus consisted of taking strain readings at three pressures, followed by a reading at the return to zero. The pressure increments between each reading (on each cycle) were nominally equal. The reason for this loading pattern was to identify the onset of yielding and will be more apparent after reading the section on Data Processing (Section 7.4).

7.3.5 Repeated Cycling

In this test program (as opposed to the work described in Ref. 1), the cycling of pressure to a given maximum pressure was repeated, in some cases up to 100 times, as a means of investigating low-cycle fatigue characteristics. The repeated cycling procedure was not initiated until the several strain gages on the specimen indicated that significant plastic behavior had occurred.

Once the repeated cycling was initiated, strain readings were no longer taken at every cycle. The general rule followed was to take readings at three pressure steps (as described above) and upon return to zero pressure for the first, fifth and tenth cycle of a group of repeated cycles, all having nominally the same peak pressure. The readings being taken at three pressure steps is an essential part of the computer data processing, but on cycles where no data was "read" (or taken), the specimen was brought smoothly up to the peak pressure, then returned to zero pressure. Such a cycle (with no readings) took approximately one minute - slightly less at the lower pressures, slightly more at the higher ones.

The strain data tables (Appendix B) show a left-most column headed "reading". This word was chosen to avoid a terminology confusion with the word "cycle". In this case, they are in fact synonymous, but the distinction is made because once the repeated cycling procedure is

initiated, the reading number no longer corresponds to the true cycle number (experienced by the specimen). This is, of course, because "readings" were not being taken at every cycle.

To assist the reader in keeping track of true cycles and their corresponding reading numbers, and to provide an immediate aperçu of the low-cycle fatigue program for any given specimen, a "Cycling Chronology" (Tables 7.4 through 7.9) is supplied for each test specimen. Since these relate to procedure they will be discussed here.

7.3.6 Cycling Chronologies

The first column of these tables (7.4 through 7.9) gives the "reading" number which appears in the strain gage data tables (Appendix B). The computer prints these serially, and it would have required elaborate programming (for each specimen) to get it to print the true cycle number (henceforth, just "cycle").

The second column supplies the corresponding cycle number, which is the number of cycles actually experienced by the specimen. Parentheses are used throughout the table to distinguish cycle number from reading number. The number in parenthesis is the cycle number in every case.

The third column supplies the peak pressure to which the specimen was repeatedly cycled - for that group of cycles. Each such group is represented by a single line in the table.

For some groups, additional data readings were taken at some of the intermediate repetions within the group. The reading numbers and their corresponding cycle numbers (in parenthesis) are given in the fourth column for these intermediate readings.

The column at right gives the total number of cycles for that group. The cumulative subtotal (for any line) of cycles in this column corresponds to the highest cycle number cited in the second column (for that line).

Table 7.4

TITA "A"

CYCLING CHRONOLOGY

READING(S) LABELLED: (on strain data tables)	CORRESPONDING TRUE TO CYCLE NUMBER(S)	MAXIMUM PRESS. (OF GROUP) P.S.I.	STRAIN MEASUREMENTS ALSO MADE AT READINGS (CYCLES) LABELLED	NUMBER OF CYCLES AT MAX. PRESS. SHOWN AT LEFT
1 thru 12	(1 thru 12)	950	*1	12
13 thru 17	(13 thru 23)	1000	14(14), 15(16), 16(18)	11
18 thru 21	(24 thru 34)	1050	19(25), 20(29)	11
22 thru 25	(35 thru 45)	1100	23(36), 24(40)	11
26 thru 29	(46 thru 56)	1150	27(47), 28(51)	11
30 thru 33	(57 thru 67)	1200	31(58), 32(62)	11
34 thru 37	(68 thru 78)	1250	35(69), 36(73)	11
38 thru 41	(79 thru 89)	1300	39(80), 40(84)	11
42 thru 45	(90 thru 100)	1350	43(91), 44(95)	11
46 thru 49	(101 thru 111)	1400	47(102), 48(106)	11
50 thru 53	(112 thru 122)	1450	51(113), 52(117)	11
54 thru 57	(123 thru 133)	1500	55(124), 56(128)	11
No Data *2	(134 thru 144)	1550	(135), (139)	11
" "	(145)	1580		

*1. In this elastic range, strain measurements were made at 50 psi increments from 300 to 950 psi, with a return to zero after each set of "3-step readings".

*2. Cycles 134 through 145 were performed on the following day. Strain data had drifted badly overnight and no good zero strain datum remained, so no strain measurements were taken during this set of cycles, hence no reading numbers.

Failure was in longitudinal tension (due to bending). Failure line followed center of mismatch all the way around the specimen.

Table 7.5

TITA "B"

CYCLING CHRONOLOGY

READING(S) LABELLED: (on strain data tables)	CORRESPONDING TRUE TO CYCLE NUMBER(S)	MAXIMUM PRESS. (OF GROUP) P.S.I.	STRAIN MEASUREMENTS ALSO MADE AT READINGS (CYCLES) LABELLED	NUMBER OF CYCLES AT MAX. PRESS. SHOWN AT LEFT
1	*1	1300	*2	1
2		1400	*3	1
3, 4 & 9		1500		7
10, 14 & 19		1600		10
20, 24 & 29		1700		10
30, 34 & 39		1800		10
40, 44 & 49		1900		10
50, 54 & 59		2000		10
60		2000 *4		1

*1. Tape punch malfunctioned resulting in no computer processing of data. Printed tapes are submitted as data instead, with true cycle number added to data by hand (see text).

*2. Strain measurements made at 100 psi (nominal) increments from 100 to 1200 psi, with no return to zero pressure between measurements.

*3. Strain measurements made at 1200 and 1300 psi with no return to zero between measurements.

*4. 2000 psi pressure was held for 80 minutes and strain measurements were made at 5 minute intervals. Specimen was not taken to failure.

Table 7.6

TITA "C"

CYCLING CHRONOLOGY

READING(S) LABELLED: (on strain data tables)	CORRESPONDING TRUE TO CYCLE NUMBER(S)	MAXIMUM PRESS. (OF GROUP) P.S.I.	STRAIN MEASUREMENTS ALSO MADE AT READINGS (CYCLES) LABELLED	NUMBER CYCLES AT MAX. PRESS. SHOWN AT LEFT
1, 2 & 3	(1, 2 & 3)	*1		3
4 thru 6	(4 thru 13)	1500	5(8)	10
7 thru 9	(14 thru 23)	1600	8(18)	10
10 thru 12	(24 thru 33)	1700	11(28)	10
13 thru 15	(34 thru 43)	1800	14(38)	10
16 thru 18	(44 thru 53)	1900	17(48)	10
19 thru 21	(54 thru 63)	2000	20(58)	10
22	(64)	2100 *2		

*1. 1200, 1300 and 1400 psi, respectively.

*2. Specimen failed at 2100 psi immediately following the scanning of data at this pressure.

Failure was in circumferential tension.

Table 7.7

TITA "D"

CYCLING CHRONOLOGY

READING(S) LABELLED: (on strain data tables)	CORRESPONDING TRUE TO CYCLE NUMBER(S)	MAXIMUM PRESS. (OF GROUP) P.S.I.	STRAIN MEASUREMENTS ALSO MADE AT READINGS (CYCLES) LABELLED	NUMBER OF CYCLES AT MAX. PRESS. SHOWN AT LEFT
1 thru 5	(1 thru 5)	1600	*1	5
6 thru 8	(6 thru 15)	1700	7(10)	10
9 thru 11	(16 thru 25)	1800 *2	10(20)	10

*1. 1000 to 1600 in 100 psi increments (return to zero after each increment).

*2. Specimen failed immediately after the scanning of data at this pressure.

Failure was in circumferential tension.

Table 7.8

TITA "E"

CYCLING CHRONOLOGY

READING(S) LABELLED: (on strain data tables)	CORRESPONDING TRUE TO CYCLE NUMBER(S)	MAXIMUM PRESS. (OF GROUP) P.S.I.	STRAIN MEASUREMENTS ALSO MADE AT READINGS (CYCLES) LABELLED	NUMBER OF CYCLES AT MAX. PRESS. SHOWN AT LEFT
1 thru 3	(1 thru 10)	1600	2(5)	10
4 thru 6	(11 thru 20)	1700	5(15)	10
7 thru 9	(21 thru 30)	1800	8(25)	10
10 thru 25	(31 thru 130)	1900 *1	11(35), 12(40) 13(45), 14(50) 15(55), 16(60) 17(65), 18(70) 19(75), 20(80) 21(90), 22(100) 23(110), 24(120) 25(130)	100

*1. Tita "E" failed on true cycle number (131) during which the goal was to attain 2000 psi. The specimen failed at 1940 psi, and no strain data was obtained on cycle 131.

Failure was in circumferential tension.

Table 7.9

TITA "F"

CYCLING CHRONOLOGY

READING(S) LABELLED: (on strain data tables)	CORRESPONDING TRUE TO CYCLE NUMBER(S)	MAXIMUM PRESS. (OF GROUP) P.S.I.	STRAIN MEASUREMENTS ALSO MADE AT READINGS (CYCLES) LABELLED	NUMBER OF CYCLES AT MAX. PRESS. SHOWN AT LEFT
1	(1)	1200		1
2 thru 4	(2 thru 10)	1300	3(5)	9
5 thru 19	(11 thru 210)	1400	6(15), 7(20), 8(30), 9(40), 10(50), 11(60), 12(70), 13(90), 14(100), 15(110), 16(120) 17(130), 18(150), 19(210)	200
20 thru 25	(211 thru 310)	1500	21(230), 22(240) 23(250), 24(260) 25(310)	100
26	311	1600 *1		1

*1. Specimen failed immediately upon completion of taking data on true cycle number 311. Pressure was already decreasing preparatory to taking a "return to zero" reading when failure occurred.

Failure was in longitudinal tension (due to bending). Failure line followed center of mismatch all the way around the specimen.

For Tita "B", the tape-punch malfunctioned, and it was not possible to process the data by computer. The printed tapes were edited and pasted onto the data sheets to provide the reader with the raw data (which is quite close - numerically - the normally computer processed data). Since the blocks of data had to be labelled, the correct cycle was marked on each group of readings, and so the "reading vs. cycle" distinction needed in the other tests is superfluous.

7.4 Data Processing and Presentation

7.4.1 General Goals and the Approach

The basic purpose of the loading sequence and data processing was to recognize and emphasize the onset of yielding, and to make it possible to differentiate between nonlinear elastic behavior and nonlinearity due to plastic stress. The key to this lies in being able to measure strain at exactly the same pressures on successive loading cycles, where each cycle progresses to some pressure level higher than the preceding cycle. The problem was to take measurements at exactly the same pressure, for purposes of comparing strain. The solution was to take strain readings at several pressures on each cycle, and to set these pressures so that their values overlapped and gradually increased from one cycle to the next. If the increment of pressure between successive strain measurements (on the same cycle) were not too large, it would then be possible to interpolate to some "exact" pressure value for each cycle. Because of the overlapping of actual pressures in the data taking on successive cycles, there could be overlapping, or more correctly, coincidence, of the interpolated "exact" pressure values from one cycle to the next.

7.4.2 The Data Interpolation Technique

Although this data processing is called the "Data Interpolation Technique", it should be pointed out that in some cases the data is in

fact, extrapolated. The calculation process is handled by a Tymshare computer. The punched tape from the data acquisition system is "read-in" at the Tymshare console, which then prints out the strain tables presented in Appendix B, after additional test parameter information has been supplied. The difference between interpolation or extrapolation is merely one of sign, which is handled automatically by the computer program. So that the reader is not forced to refer to the perhaps less accessible appendix, a sample set of data is included here for easy reference (Table 7.10).

7.4.3 The Strain Data Tables

The first strain column in these tables (for each strain gage) is headed by a "zero", which of course refers to pressure. Values listed in this column are the residual strains accumulated from previous cycling. Attention is drawn to the fact that a zero pressure value listed for the reading numbered "n" was a value obtained upon return to zero (pressure) immediately following the set of readings (at pressure) labelled "n - 1". This is of some significance where extra cycles (with no strain readings) are added between the readings labelled "n - 1" and "n". For the reader who skips, the above reference to extra cycles (with no strain readings) will be clearer if Sections 7.3.5 and 7.3.6 are reviewed more carefully.

The first reading in this zero pressure column is always zero, which is the initial zero strain datum. Other zero values in this column (if they occur) do in fact mean that the strain returned to its initial zero value. As at other pressures, it was necessary to extrapolate to zero pressure. The system never completely dumps all pressure, and "return-to-zero" pressure readings are inevitably taken at some pressure value slightly above zero. In this case, the extrapolation is based on the slope of the pressure-strain line to the lowest pressure at which strain readings were taken.

The single zeros in all columns except the first column signify that no data was taken at that pressure and on that cycle. With the acute hindsight so commonly found after all the work is done, it is

Table 7.10 SAMPLE: STRAIN GAGE 1 READINGS FOR TITA A

READING	INTERNAL PRESSURE PSI						
	0	300	350	400	450	500	550
	MICROSTRAIN						
1	0	-1163	-1339	-1513	0	0	0
2	-32	0	-1339	-1512	-1682	0	0
3	-28	0	0	-1514	-1682	-1849	0
4	-14	0	0	0	-1683	-1850	-2012
5	-18	0	0	0	0	-1850	-2014
6	-16	0	0	0	0	0	-2015
7	-16	0	0	0	0	0	0
8	-20	0	0	0	0	0	0
9	-11	0	0	0	0	0	0
10	-74	0	0	0	0	0	0
11	-15	0	0	0	0	0	0
12	-14	0	0	0	0	0	0
13	-8	0	0	0	0	0	0
14	-24	0	0	0	0	0	0
15	-37	0	0	0	0	0	0
16	-40	0	0	0	0	0	0
17	-43	0	0	0	0	0	0
18	-69	0	0	0	0	0	0
19	-70	0	0	0	0	0	0
20		0	0	0	0	0	0
21	-83	0	0	0	0	0	0
22	-100	0	0	0	0	0	0
23	-117	0	0	0	0	0	0
24	-126	0	0	0	0	0	0
25	-153	0	0	0	0	0	0
26	-172	0	0	0	0	0	0
27	-199	0	0	0	0	0	0
28	-226	0	0	0	0	0	0
29	-257	0	0	0	0	0	0
30	-283	0	0	0	0	0	0
31	-334	0	0	0	0	0	0
32	-367	0	0	0	0	0	0
33	-424	0	0	0	0	0	0
34	-504	0	0	0	0	0	0
35	-612	0	0	0	0	0	0
36		0	0	0	0	0	0
37	-725	0	0	0	0	0	0
38	-793	0	0	0	0	0	0
39	-888	0	0	0	0	0	0
40	-942	0	0	0	0	0	0
41		0	0	0	0	0	0
42	-1159	0	0	0	0	0	0
43	-1286	0	0	0	0	0	0
44	-1369	0	0	0	0	0	0
45	-1547	0	0	0	0	0	0
46	-1702	0	0	0	0	0	0
47	-1854	0	0	0	0	0	0
48	-1948	0	0	0	0	0	0
49	-2174	0	0	0	0	0	0
50	-2341	0	0	0	0	0	0
51	-2534	0	0	0	0	0	0
52	-2667	0	0	0	0	0	0
53	-2943	0	0	0	0	0	0
54	-3175	0	0	0	0	0	0
55	-3369	0	0	0	0	0	0
56	-3613	0	0	0	0	0	0
57	-3923	0	0	0	0	0	0

realized that getting the computer to print a star (or other symbol) in place of these "no-measurement zeros" would have been an improvement over the present arrangement.

The non-zero values listed in the tables are strain in units of microstrain (one microstrain is one micro-inch per inch of strain), and positive values are for tensile strain.

It will be noted that when the pressure increment was 100 (or 50) psi, the first pressure listed in any table is not 100 (or 50) psi, but some multiple of this value higher. Readings were not taken at very low pressures because they would not have added useful data to an already voluminous listing. The reason is then strictly economic.

For Tita "A" for which the data is a matrix of 57 rows by 26 columns, some of the printed pages have been omitted. This was done wherever the entire page consisted of "no-measurement zeros".

A very thorough discussion of the data interpolation technique (which was at that time called "Data Normalization") is found in Section 6.4 of Reference 1.

7.4.4 Special Data Handling - Tita "B"

As mentioned above, the tape punch malfunctioned during the test on Tita "B", so that the data interpolation procedure (by computer) could not be performed. The data was not lost, however, since it was available in its "raw" form on the printed tapes.

These printed tapes are the only data supplied for Tita "B", but a careful study of these tapes will show that strain readings were taken at pressure values so close to the nominal 100 psi increments that the interpolation correction required sould have been quite small in most sets.

Each "scan" consists of eleven pieces of data, the first of which (labelled "p") is the pressure. The next ten values, proceeding upward

from the "p" value are the ten strain gages in their proper numerical order. The value of "p" is in actual psi, but each of the ten strain readings must be multiplied by five to give the answer in units of microstrain. The cycle number (for each scan) has been written in by hand just above the pressure value for that scan. As already explained, no distinction is necessary between "reading" and "cycle" number for Tita "B" data.

Because it made the finished pages easier to read, all the zero pressure readings (labelled "RTZ" for "return to zero") are found on the first two pages, with the exception of the RTZ's* for cycles 1, 59 and 60. The reasons for these exceptions will be immediately evident.

The records of cycle #1 show that pressure was raised in 100 psi increments up to 1300, and readings were taken at each increment. The "RTZ" for cycle #1 is the center block of data of the fourth (Tita "B") page of data, and it shows that 290 microstrain (tensile) strain still remains on gage #3 (58 x 5 = 290).

Cycle #2, on the same page, went to 1400 psi with readings at 1200, 1300 and 1400, followed by an RTZ (at the lower right-hand corner). The RTZ for cycle #2 was taken at 30 psi vs. 48 psi for cycle #1, and the reading for gage #3 still (coincidentally) shows a reading of 290 microstrain. Reference to the gage #3 reading at 1400 psi shows 1300 counts or 6500 microstrain. The slope to 1400 psi of the strain vs. pressure curve (assuming linearity) is then 4.65 microstrain per psi. To obtain the true permanent strain (if any), this slope (or extrapolation factor) must be applied to the "RTZ" pressures of cycles #1 and #2. For cycle #1, this produces 67 microstrain (290-223) and cycle #2, 150 microstrain (290-140). These two values are then the true permanent set following cycles #1 and #2, respectively.

The systematic pattern of repetitive cycles starts on page 5 (of the Tita "B" data). The three stepped pressure readings for each cycle

*RTZ = Return to Zero

appear side by side (across the page) and each page has this data for three cycles, the first, fifth and tenth cycle of each group of repeated cycles, where each cycle of each group is identical in pressure levels and readings.

This continues to cycle #59 (with a peak pressure of 2000 psi) on the tenth page of the Tita "B" data.

On cycle #60, the data for which starts on the eleventh page, with the RTZ strain values for cycle #59, the pressure was raised to 2000 psi and held there for 80 minutes, and readings were taken at five minute intervals to monitor the creep (change in strain with time, while under load). The reading at 40 minutes was inadvertently not taken. The RTZ for cycle #60 is shown beside the RTZ for cycle #59 for easier comparison (i.e., just before the "0 minutes at pressure" reading).

7.4.5 Other Irregularities in the Strain Tables

For Tita "E" and Tita "F," the printed raw data tapes have been pasted together for the first cycle only, in order to provide a view of the pressure-strain relationship in the elastic range. For Tita "E", strain measurements for cycle #1 were taken at 100 psi increments up to 1300 psi, and for Tita "F" in the same increments up to 900. Thereafter, measurements were taken in the usual pattern for the rest of the first cycle, i.e., at 1400, 1500 and 1600 psi for Tita "E", and 1000, 1100 and 1200 psi for Tita "F". The data for these measurements appear in the regular form and are labelled "Reading #1".

Occasionally, throughout the data, an irregularity appears in a strain value. This takes the form of a number that does not fall into the general pattern. This happens when electrical noise is present in the phone lines of the Tymshare computer. If it happens more than twice in a printed page, the usual procedure was to have the computer re-do that page, but since it happens at least once a page most of the time, the re-doing of pages would have gotten out of hand if total perfection was essential. Since these occurences are usually obvious and since so much of the data overlaps itself, it was felt that these occasional errors should be overlooked.

7.4.6 Onset of Yielding

There are two ways to recognize the onset of yielding from the strain tables. The first is non-repeatability of strain at any given pressure. The writer feels that plus/minus five microstrain non-repeatability is a suitable criterion because it is distinctly greater than the resolution of the instrumentation system and the subsequent processing procedure. If most gages will repeat to within a total span of four microstrain at three different pressurizations, it is reasonable to claim a resolution of plus/minus two microstrain. This claim can, of course, only be made with the knowledge that the system is inherently very stable and the test set-up basically free from typical disturbances such as fluctuating "ambient" temperature, large sources of electrical noise, etc. In addition, the integrating voltmeter is a very stable device, electrical shielding was used on all leads and a "guard system" is incorporated in the scanner. The absolute strain readings may not be accurate to plus/minus two microstrain, but certainly the relative measurements (on any one gage) have this accuracy on repeatability. This accuracy (of the strain gage) begins to deteriorate after very large strain excursions (over 2500 microstrain or 0.25 percent strain), but the resolution allowance is multiplied by 2.5 for the criterion, and the criterion is usually applied before 2500 microstrain is attained.

The second sign of plastic strain is the build-up of residual strain upon return to zero pressure (after each cycle). Here, the writer feels the discrepancy or resolution allowance should be increased to plus/minus ten microstrain. The reason for the larger allowance is two-fold: First, the extrapolation to zero operation uses a less reliable "correction slope" than those used at the higher pressure increments. Secondly, strains upon return to zero pressure have been found (on other testing programs) to be less repeatable than strains at some well defined load. This may be because the stresses that induce a given strain at the higher loads are large enough to overcome certain friction mechanisms that play a role in the strain magnitude, whereas at zero load/pressure levels the stress drops below a threshhold level, and friction prevents the last deformations to from being "cleanly terminated". The gravity supports of the specimen itself may be significant in this respect. At high pressures,

the force of the specimen's own weight at its support points is negligible compared to the force sustained by any comparable cross-section area under tension due to the pressure.

It should also be emphasized (for the benefit of the reader who may feel he is only concerned with the experimental aspects of this report), that a nonlinear pressure-strain relation at any gage is not necessarily an indication of plastic stress. The structure is inherently nonlinear in the elastic range. This is discussed more fully in the analytical portion of this report.

Another caution which should be mentioned is that a strain gage can give the indication of plastic strain (as defined above) even though plastic stress has not occurred at the site of the gage itself. If plastic strain has occurred in the vicinity of a gage (but not at the gage), it will cause stress redistributions which break the normal pressure-strain pattern for the gage (and thus have the appearance of plastic strain). Furthermore, the plastically strained region will not return to its zero strain datum (upon return to zero pressure), so that adjacent regions must "balance" out the resulting geometrical anomaly. Any gage in the zone where the anomaly is "being balanced" will then show a residual strain. This explains why some "plastic strain occurrence" is evident at relatively low strain levels in some gages. The extent to which this occurs at a gage is of course a function of how near it is to a region under plastic strain and how severe the plastic strain is in that region.

Section 8

COMPARISON BETWEEN THEORY AND TEST

A series of analyses using the computer program EPSOR [?] was carried out for each one of the six test specimens used in the experimental program. These analyses were made using the nominal data for the test specimens. In all cases, except for Tita F, the measured geometry of the test specimens was so close*) to the nominal dimensions that it was not considered warranted to re-analyze the specimens using the exact thickness.

The objective of the tests was to check, for a variety of geometrical configurations, some of the details of the analytical predictions, and to explore low-cycle fatigue, which is not within the state of the art of current analytical methods.

8.1 Static Failure

No tests on static failure, i.e., a one-load cycle to failure, was made. All test specimens were cycled between zero and high pressures into the plastic region before failure occurred. This cycling appears to have had the effect of a "shake-down": the effective mismatch seems to become less than the nominal mismatch after cycling. This aspect is discussed in Section 5.1.

The following conclusions as to the static failure prediction can be made from the tests:

- The predicted mode of failure (meridional or hoop) was realized in the tests. Thus, the effect of mismatch in combination with the various weld land geometries is accurately predicted by the design graphs in Section 6.

*) Within one or two percent in the discontinuity region. See Section 7 for details of the test specimens.

- Shake-down effects caused by cycling pressure loads into the high plastic region causes predicted failure pressures to be progressively conservative as the mismatch is increased. The shake-down effects do, however, require material strain capabilities of the order 2.5% or higher. Actual welded material may have much lower ultimate strain which would tend to cancel out the beneficial effects of cycling.

8.2 Low-Cycle Fatigue

The cycling to which the test specimens were subjected did not constitute a low-cycle fatigue test in the classical sense. In classical low-cycle fatigue a mechanical hysteresis hoop develops due to the accumulation of plastic strain at both the low and the high end of the load cycle. ~~In the present case,~~ however, no plastic strains were developed at the low (i.e., zero pressure) point of the load cycle.*) The cycling was characterized by a first loading into the plastic range, followed by a number of elastic reloadings to the same pressure level, as shown below.

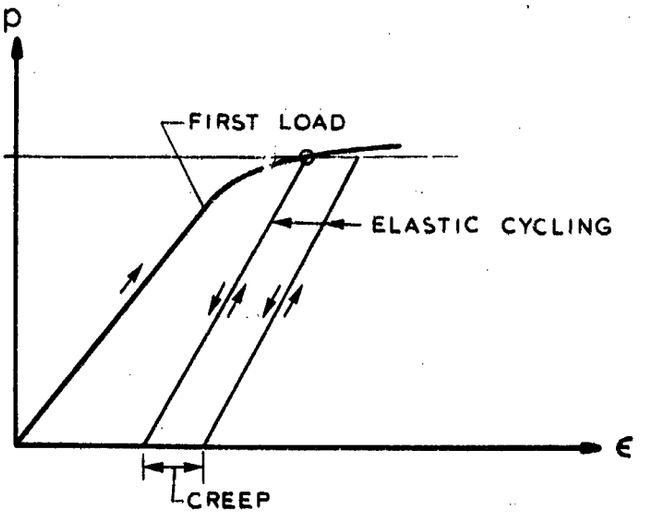

*) Appendix A shows that to develop plastic strain at the low end would require a mismatch factor of 5.7.

During the elastic cycling a certain amount of creep took place, as shown in the figures for the individual test specimens in Section 8.3. The creep, which seems to be independent of the cycling, is part of a complicated interaction of material properties and geometric changes which takes place in the high plastic region. This interaction which is beneficial in that it "smoothes out" the geometry, and detrimental in that it "uses up" strain, is beyond the capabilities of present analytical methods. However, an effort to interpret the test data has been made in Section 5.2. The data presented in Fig. 5-5 should be quite conservative for the type of material investigated here (Ti 6Al-4V STA), but caution for application to other materials, such as the actual weld material, is warranted.

Fractographic examination of the failed specimens suggests a rather tough material behavior where failure occurred by local large plastic flow. In the specimens that failed meridionally (i.e., in the mismatch) large rotations of the shell on each side of the mismatch were observed. This plastic deformation most likely preceded the completion of the primary fracture, and occurred in a manner consistent with analytical predictions.

A further insight into the actual failure mechanism could, in all probability, be gained from a SEM (Scanning Electron Microscope) analysis of the failed specimens. Such an analysis was not budgeted in the present investigation and could therefore not be performed.

8.3 Strain Distributions

The most direct, and most critical, way of comparing the theoretical to the experimental data is to compare the strain distribution. In the present case this kind of comparison presents some degree of uncertainty due to the nature of the problem, but the mass of data and the repeatability of agreement tend to diminish this uncertainty. However, the following points should be made:

- The strain gages could not be positioned at the point of maximum strain, i.e., at the mismatch.

- o In the area of interest the strains are varying very rapidly (sometimes doubling in 0.1 inch of surface length) making the accurate determination of the position of the strain gage relative to the mismatch critical.

- o The analysis used points (stations) spaced about .05 inch in the discontinuity area. Thus, in general no exact correspondence between analysis stations and strain gage stations exist. Rather than interpolate between analysis stations, analysis stations on either side of the strain gage stations have been plotted in the comparison figures.

As is evident from the figures of this section, there exists a high degree of correlation between the tests and the analysis. This correlation is both qualitative and quantitative and includes both the elastic and the plastic regions. Comparison between residual strains was not done due to the presence of creep in the tested articles. However, the very close agreement of test and analytical data of total strains, as shown in the accompanying graphs, would indicate a similarly close agreement for one-load residual strains.

It is thought that a study of the accompanying figures will be more fruitful than a lengthy discussion. Therefore, only a few comments will be made on these figures.

TITA A (Figures 8-1 through 8-3)

Fig. 8-1 shows strain distributions along a meridional generatrix. The agreement between the theoretical (curves) and tested (points) data is very good. Note that a displacement of only 0.05 inches, or less, would be required to cause an exact agreement. The strain units used in this, and following, graphs is microstrain.*

*10,000 microstrains = 1 percent strain

Fig. 8-2 shows strain versus pressure plots for three strain gage locations (inside and outside surface close to the discontinuity, and outside surface some distance away). Again, the agreement is very good. As cycling loads progress into the plastic region creep takes place as indicated by the double points.

Fig. 8-3 shows strain gage data for the one hour soak at 1500 psi, which was done for this specimen. There is a tendency for the material-geometry configuration to stabilize at a constant strain at the end of the time period. Unloading after the soak takes place elastically.

TITA B (Figures 8-4 and 8-5)

Tita B has the longest weld land of all the specimens. Agreement between test and theory is excellent, both in the elastic and the plastic region. Note again (Fig. 8-5) the presence of creep during cycling. Note also that the slope of the curve with creep is the same as the theoretical, no-creep, curve. This specimen experienced an 80 minutes soak at 2000 psi. As in the case of Tita A the specimen seemed to stabilize at a constant strain of the end of this period.

TITA C (Figures 8-6 and 8-7)

This test specimen has a predicted failure in the hoop mode, at 1960 psi. It failed at 2100 psi, in the hoop mode, as predicted. This is a medium long weld land with $L^* = 3$.

TITA D (Figures 8-8 and 8-10)

This test specimen is similar to Tita C, but has only half as much weld land thickness increase. This is the only specimen that failed at a lower load than predicted:

Actual failure: 1800 psi
Predicted hoop failure in membrane: 1920 psi
Predicted meridional failure in discontinuity: 1960 psi

It is not clear why this specimen should fail at this comparably low load. The measured strain distribution agrees almost exactly with predictions, but at 1500 psi there is a very sudden increase in hoop strains. (Possibly the heat treat of this specimen is faulty.)

TITA E (Figures 8-11 and 8-12)

This specimen, which tests a hemisphere-cylinder juncture, has the shortest of all weld lands, and therefore the worst one from an analysis point of view. However, as can be seen from the figures, the agreement between test and theory is excellent. Note the predicted nonlinearity at station S=0.156, which is very nicely reproduced by strain gage 9.

TITA F (Figures 8-13 and 8-14)

The analysis for this configuration (a hemisphere-cylinder joint) was performed on a model with 0.05 inch membrane thickness, and 0.0625 inch weld land thickness, rather than the test specimen average figures of 0.042 and 0.050, respectively. To compensate for this the pressures in the analysis were multiplied by the factor 0.85, which is the ratio of membrane thickness. The values arrived at in this ~~way should be~~ almost exact. The analytical figures show very good agreement with the test. The usual creep is also present.

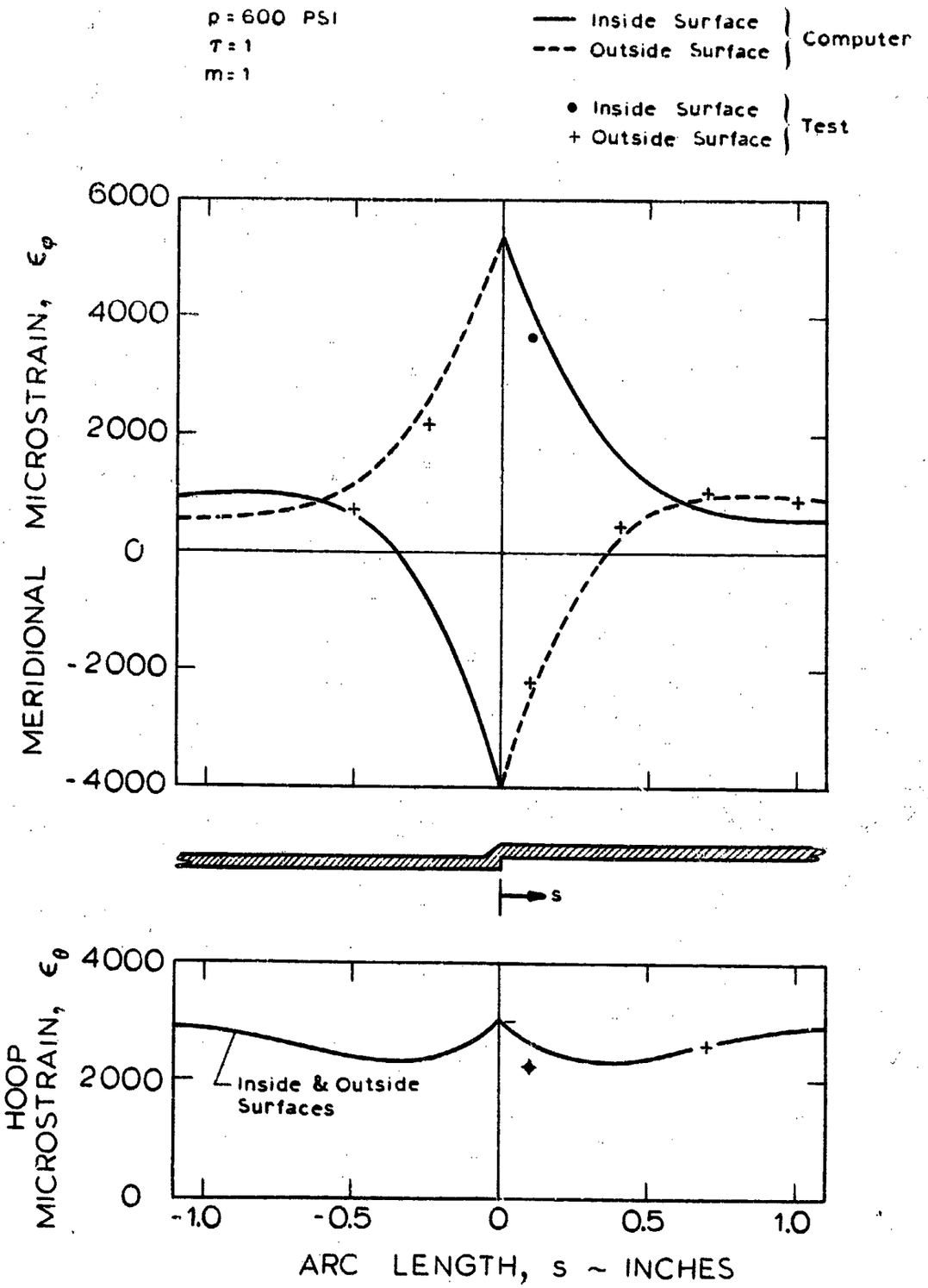

Fig. 8-1 Strain Distribution, Tita A

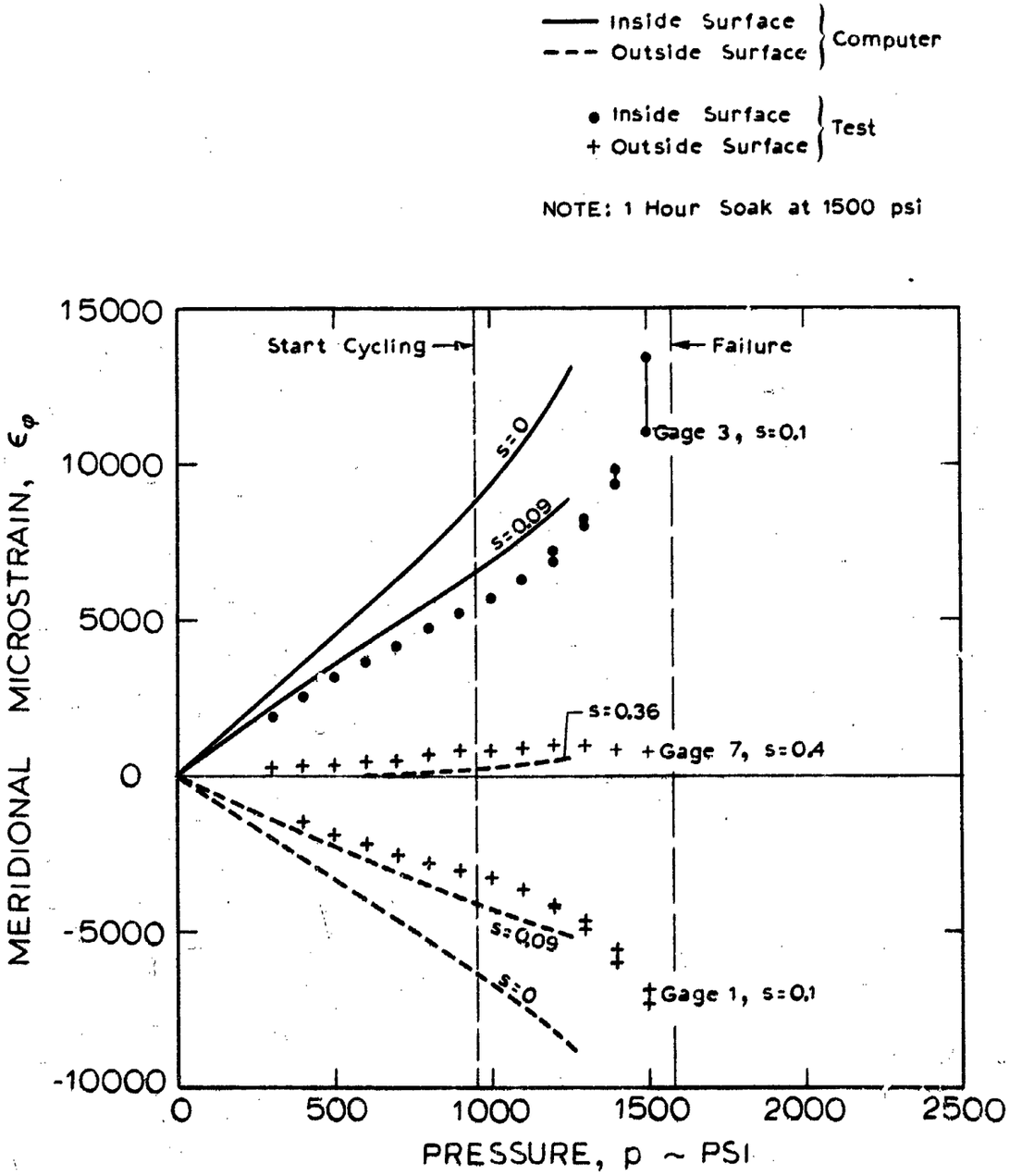

Fig. 8-2 Strain Versus Pressure, Tita A

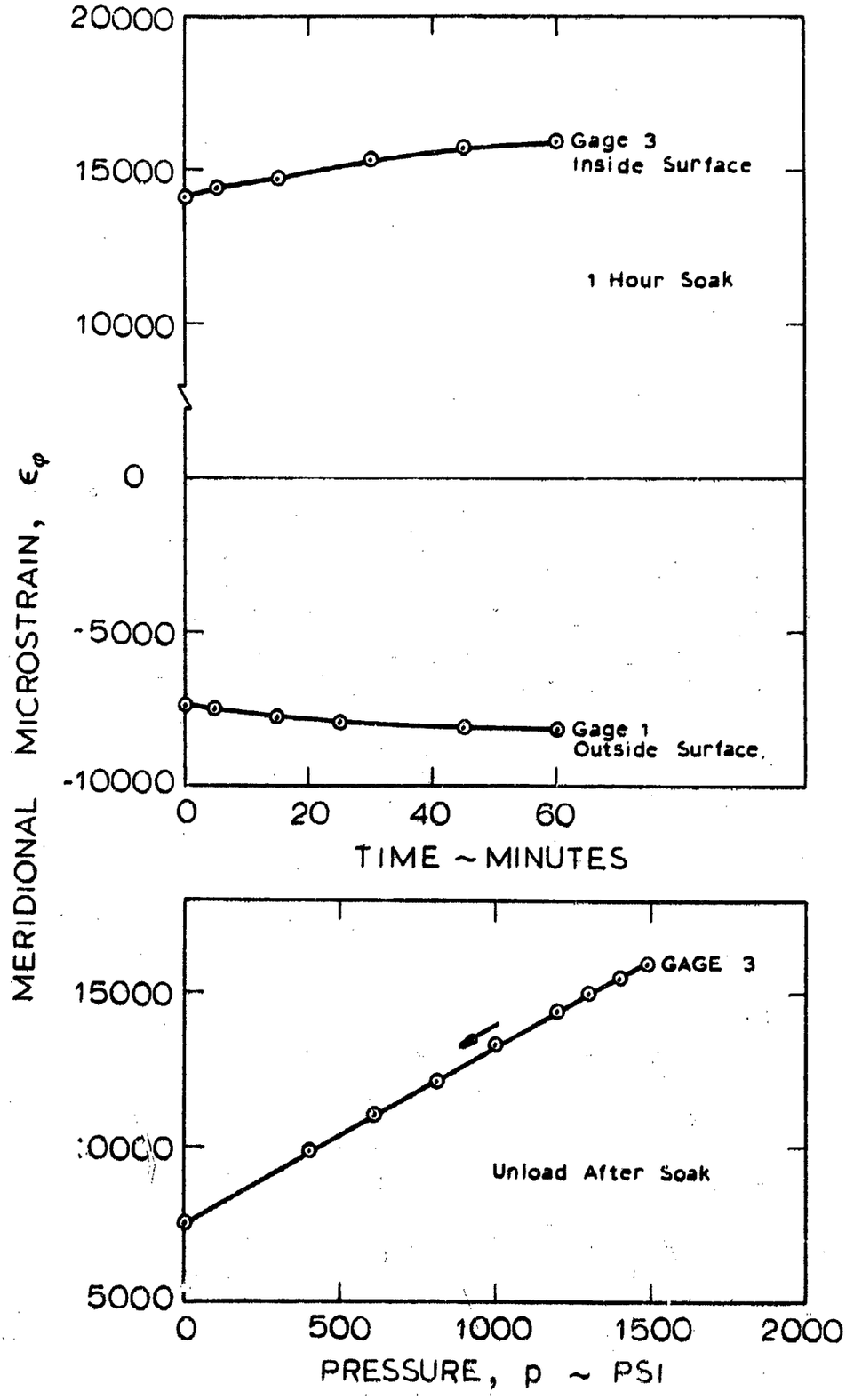

Fig. 8-3 Soak at 1500 psi for One Hour, Tita A

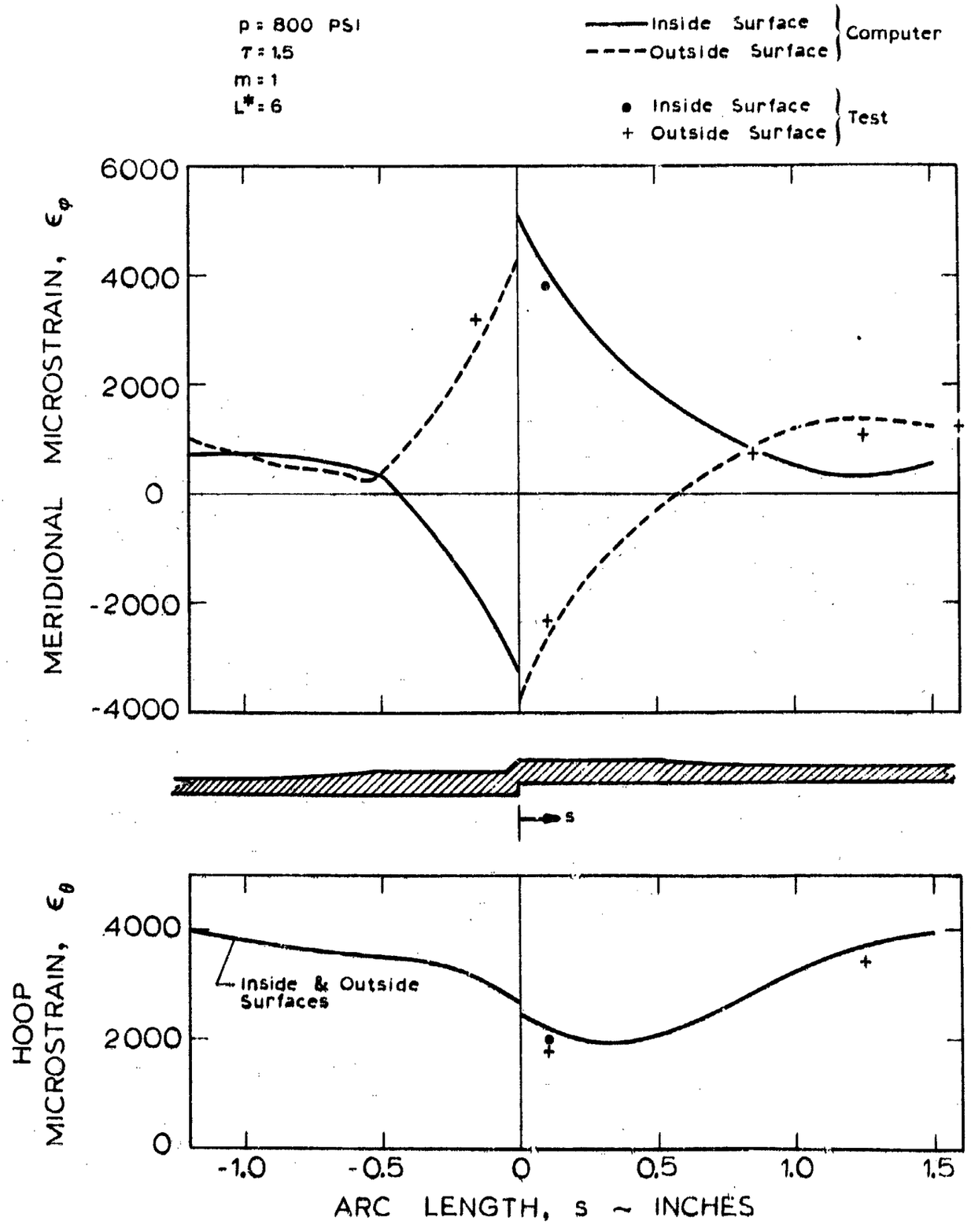

Fig. 8-4 Strain Distribution, Tita B

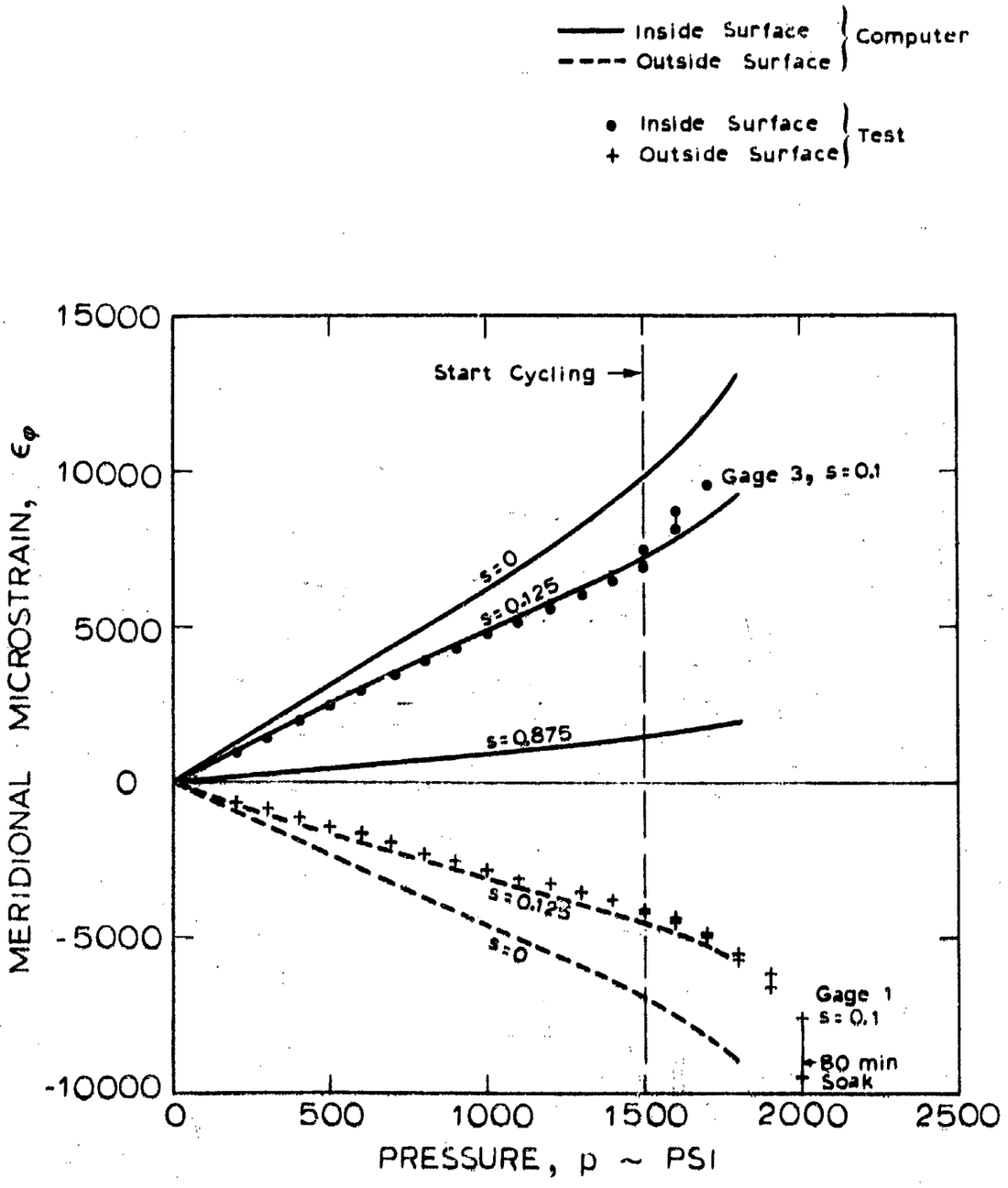

Fig. 8-5 Strain Versus Pressure, Tita B

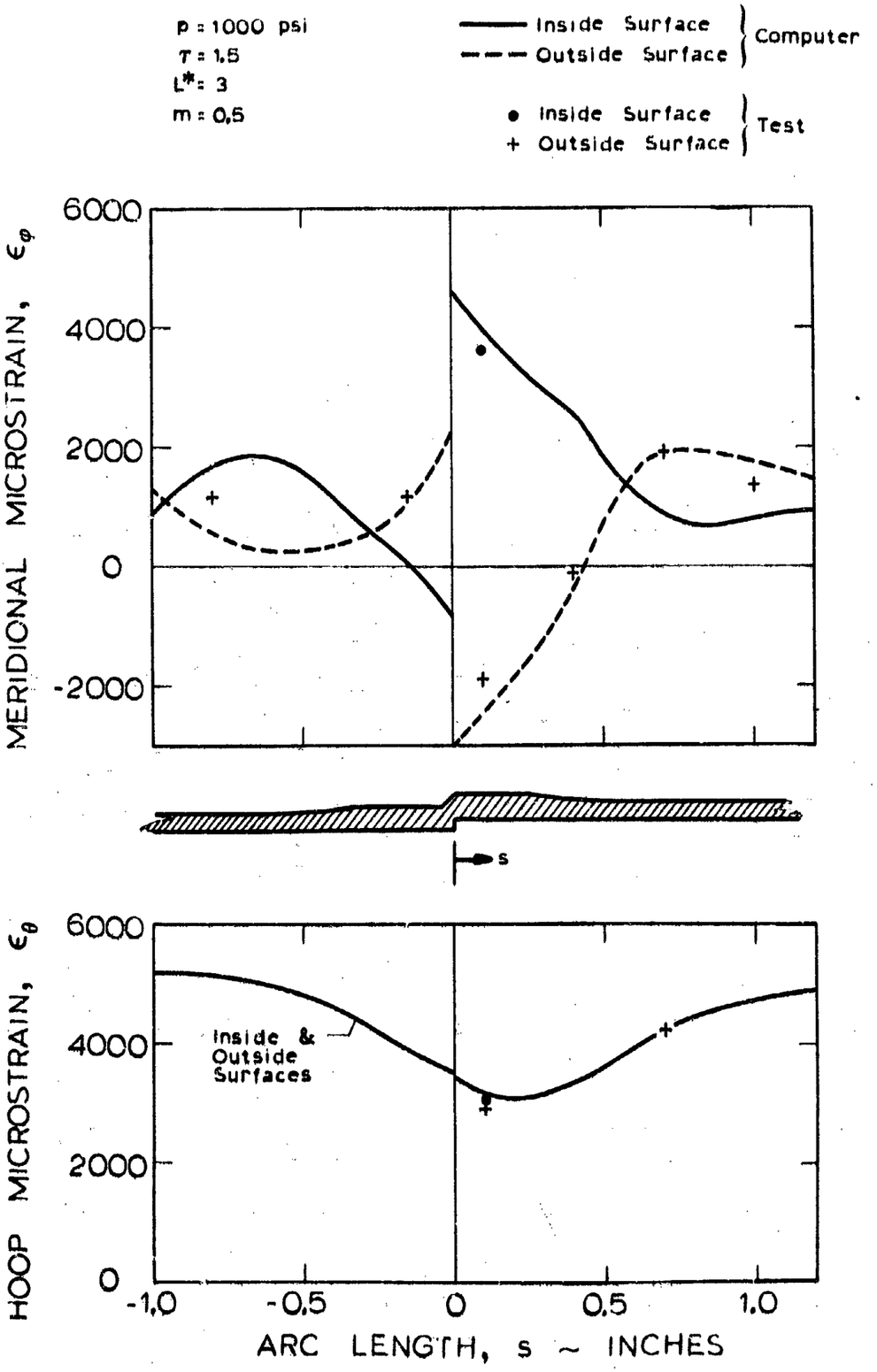

Fig. 8-6 Strain Distribution, Tita C

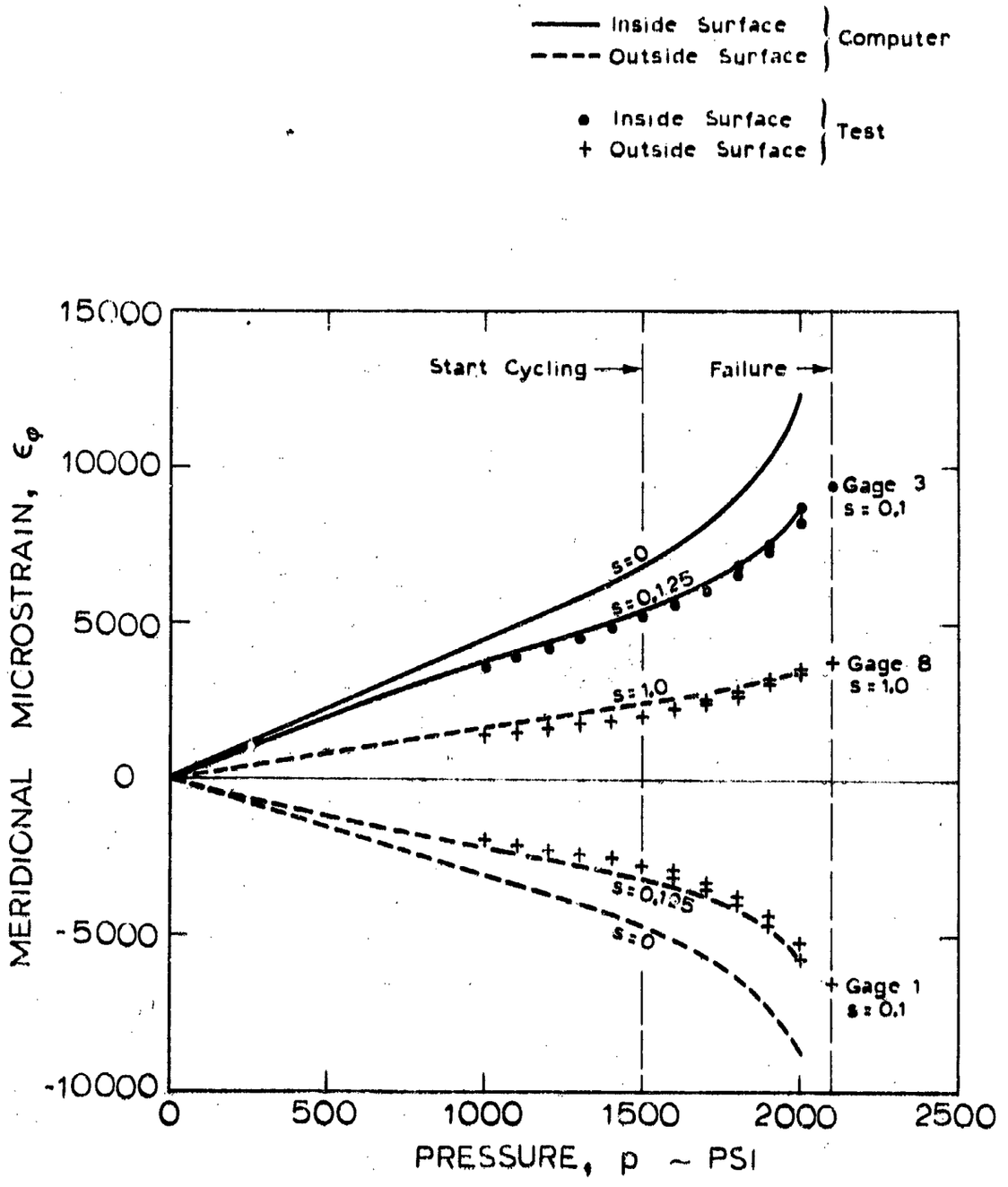

Fig. 8-7 Strain Versus Pressure, Tita C

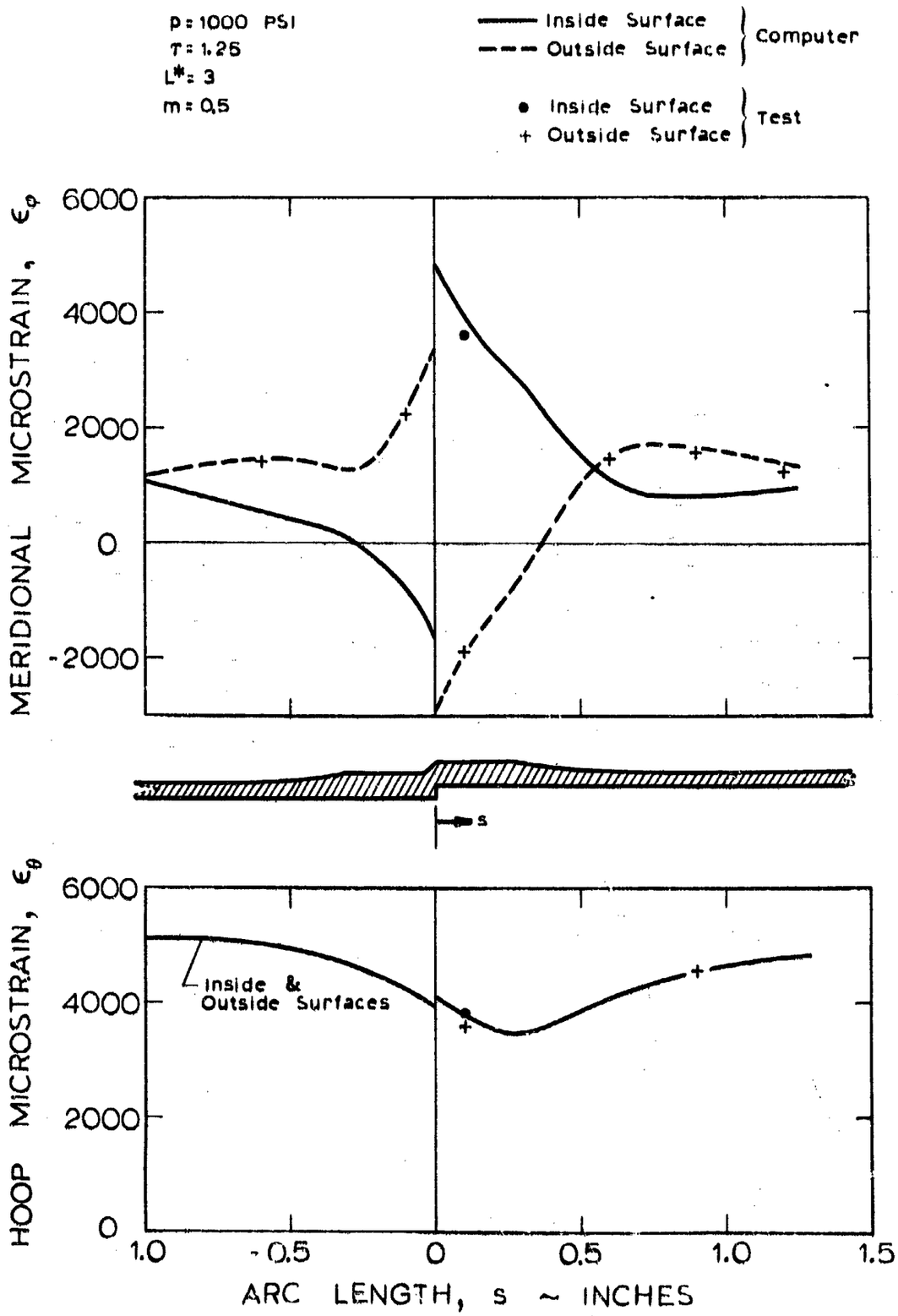

Fig. 8-8 Strain Distribution, Tita D

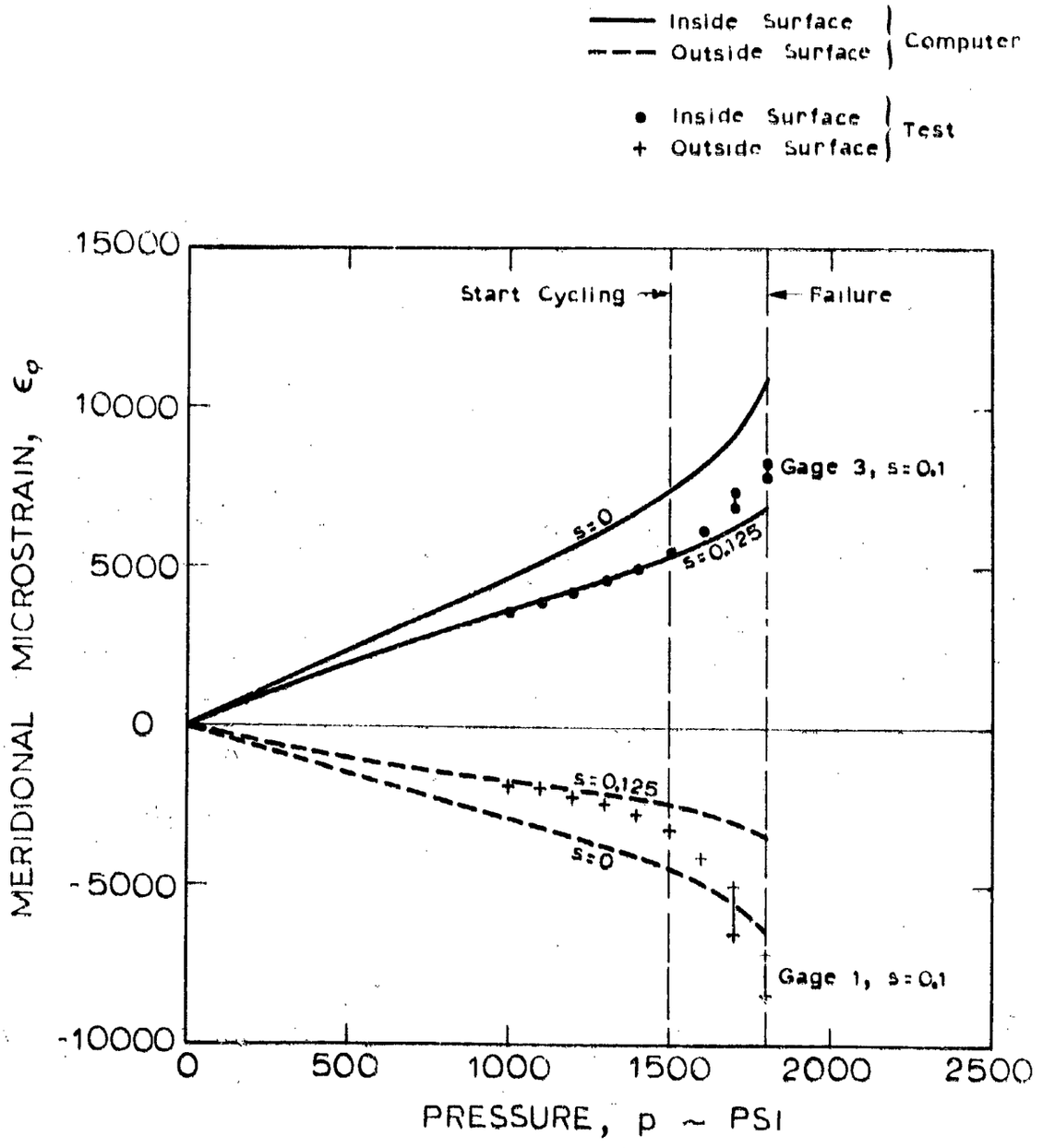

Fig. 8-9 Strain Versus Pressure, Tita D

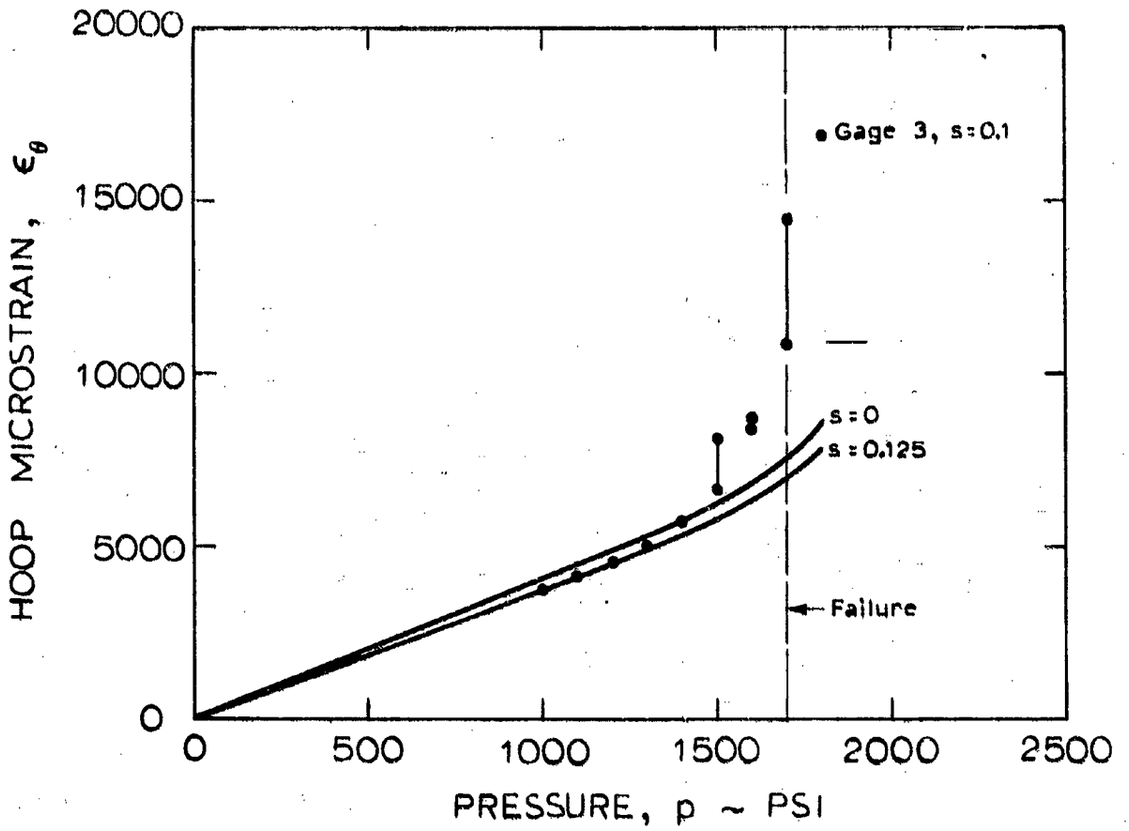

Fig. 8-10 Hoop Strain Versus Pressure, Tita D

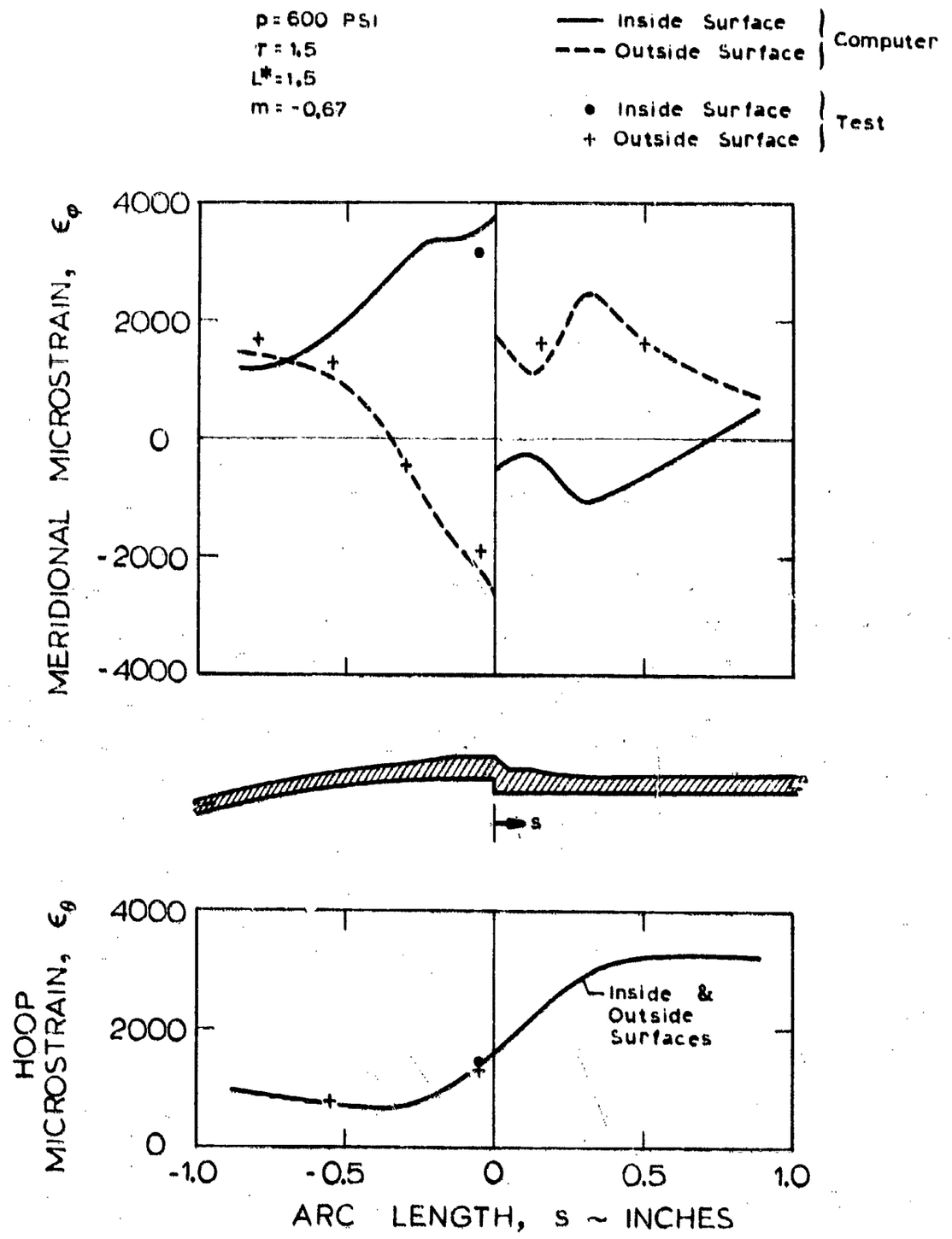

Fig. 8-11 Strain Distribution, Tita E

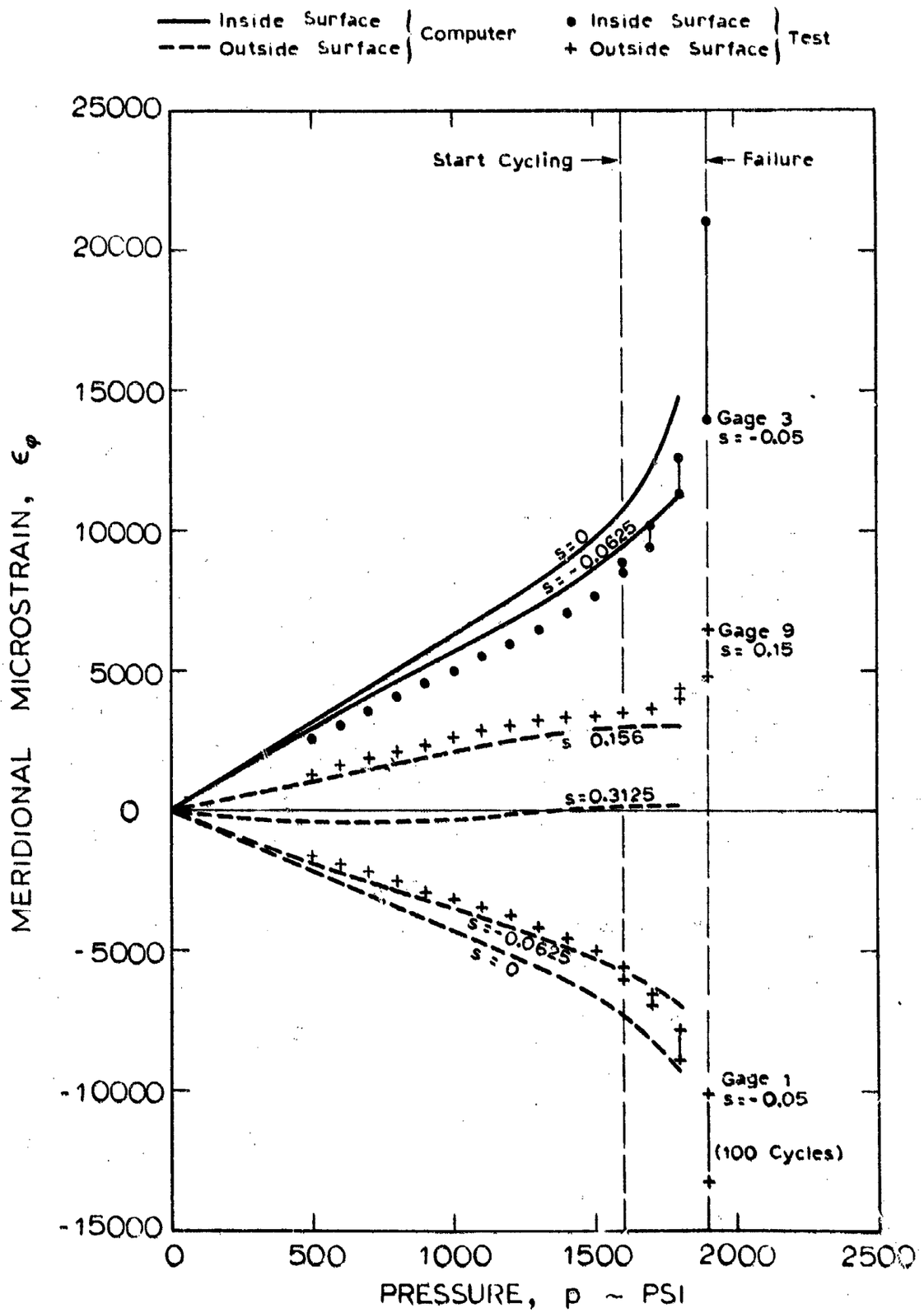

Fig. 8-12 Strain Versus Pressure, Tita E

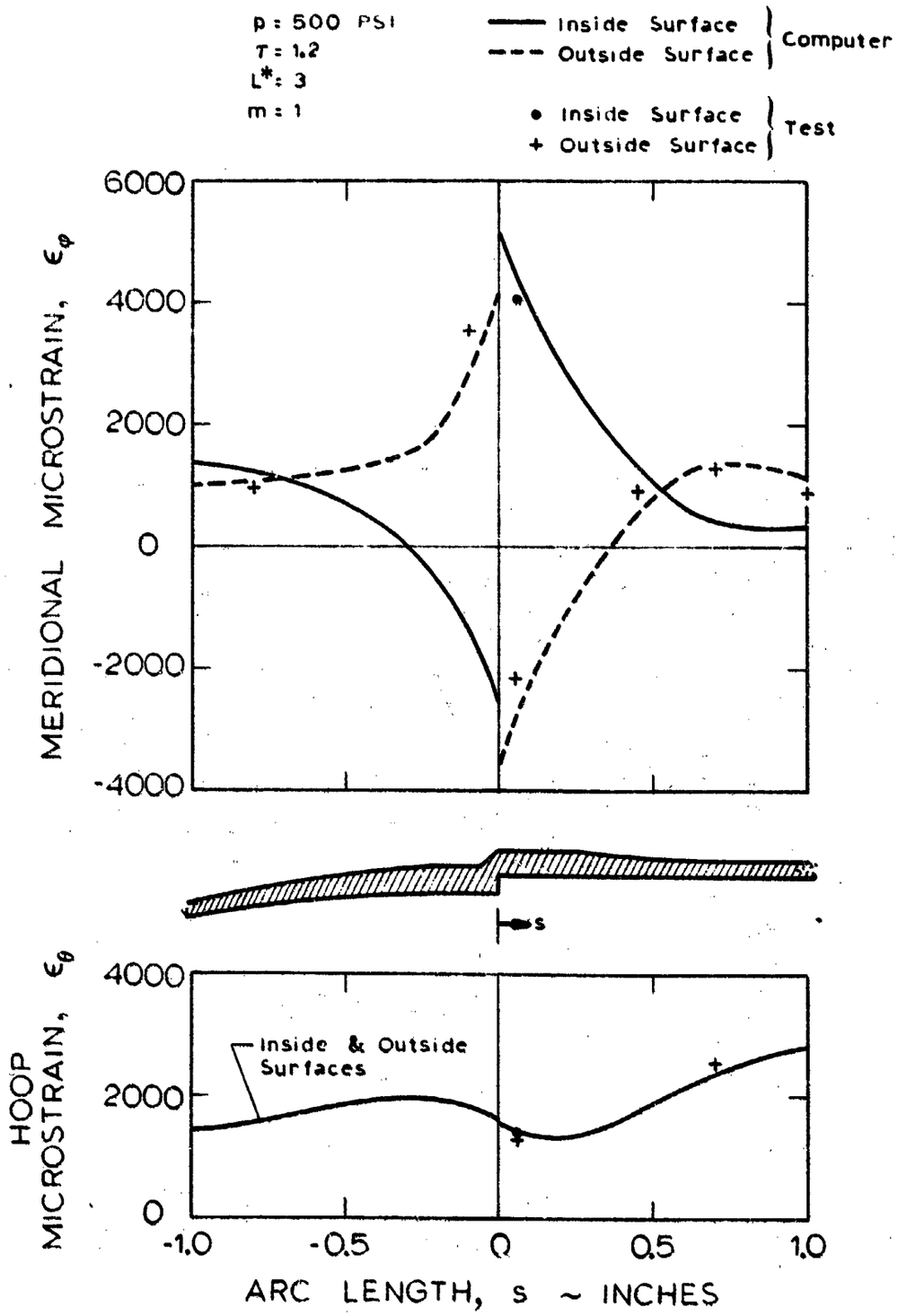

Fig. 8-13 Strain Distribution, Tita F

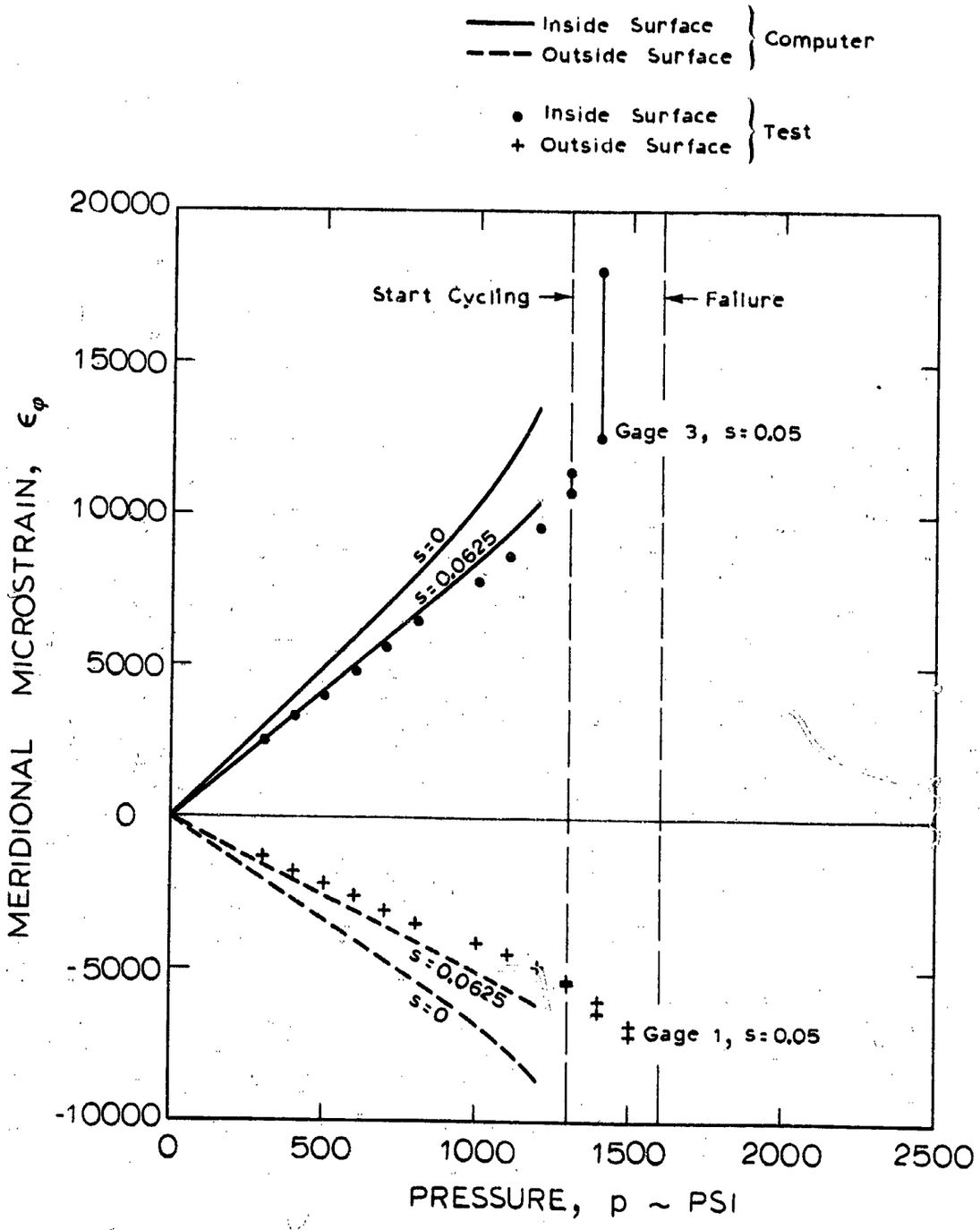

Fig. 8-14 Strain Versus Pressure, Tita F

Section 9

TEST SPECIMEN PHOTOGRAPHS

Photographs of specimens "B" through "F" are included in this section. No photograph of Tita "A" is supplied because it failed in the same manner as Tita "F", that is to say, due to a longitudinal tension (due to bending). In such cases, the line of failure runs right along the mismatch.

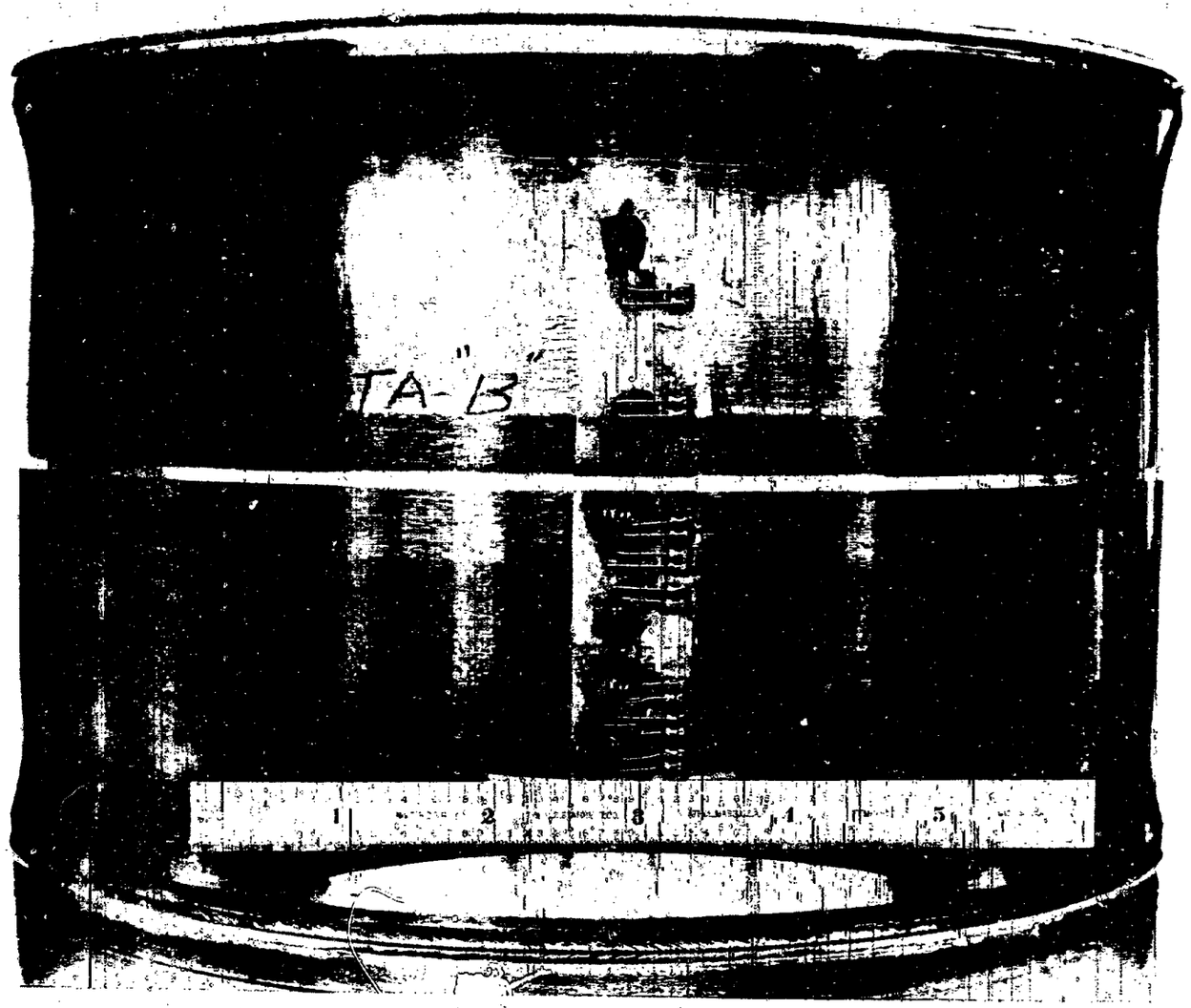

Fig. 9-1 Tita "B" After Test
(Note Strain Gages)

Fig. 9-2 Tita "C" After Test

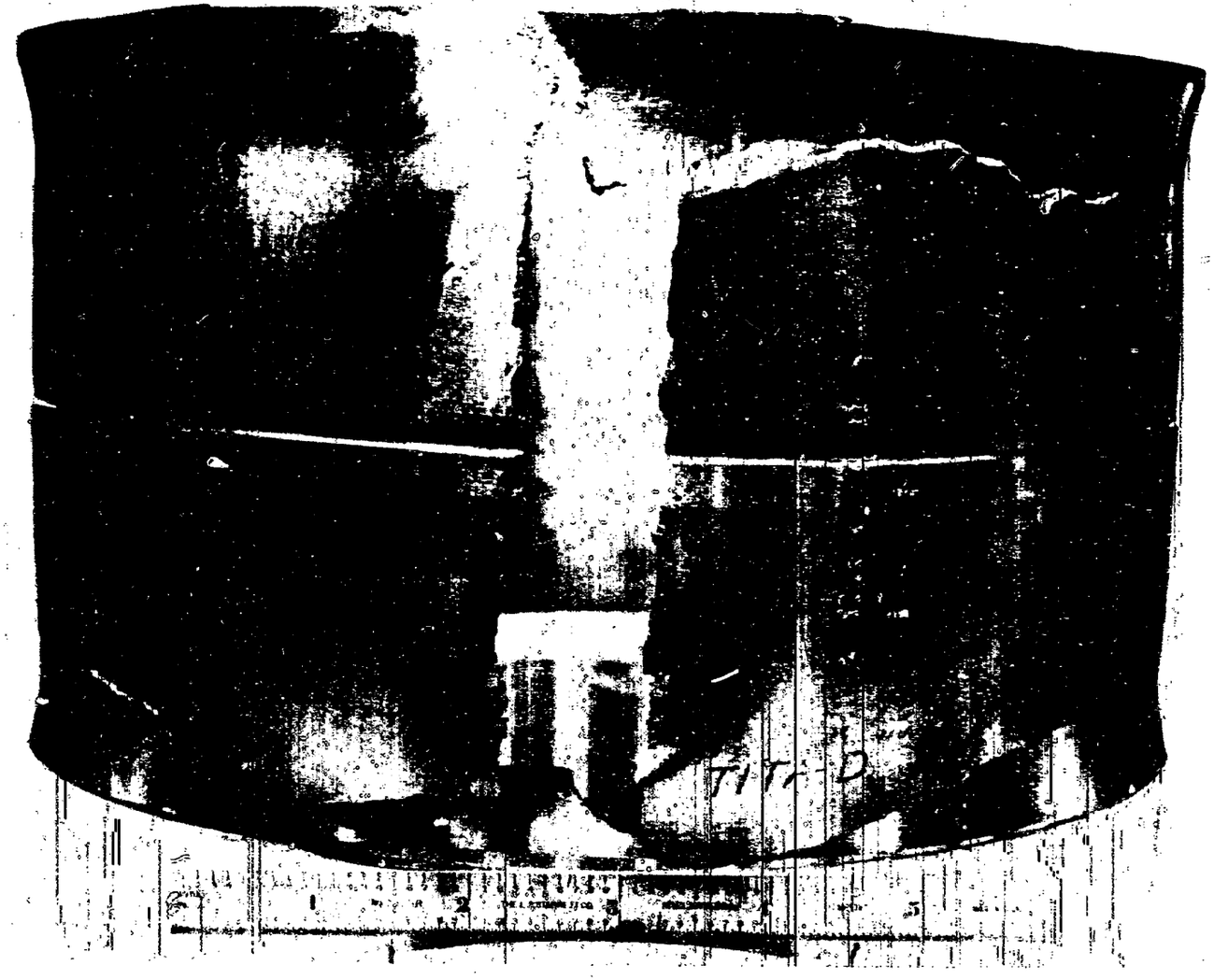

Fig. 9-3 Tita "D" After Test

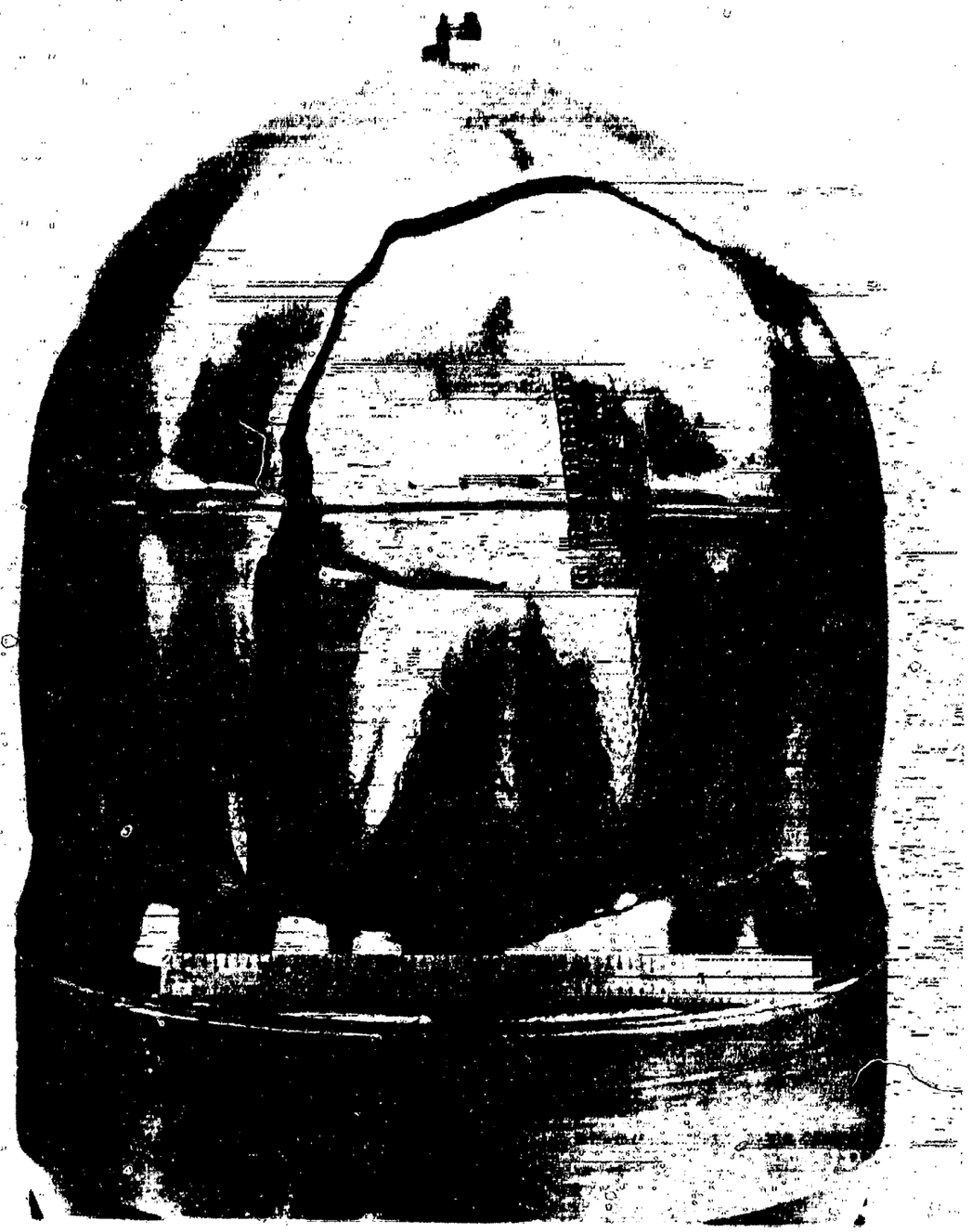

Fig. 9-4 Tita "E" After Test

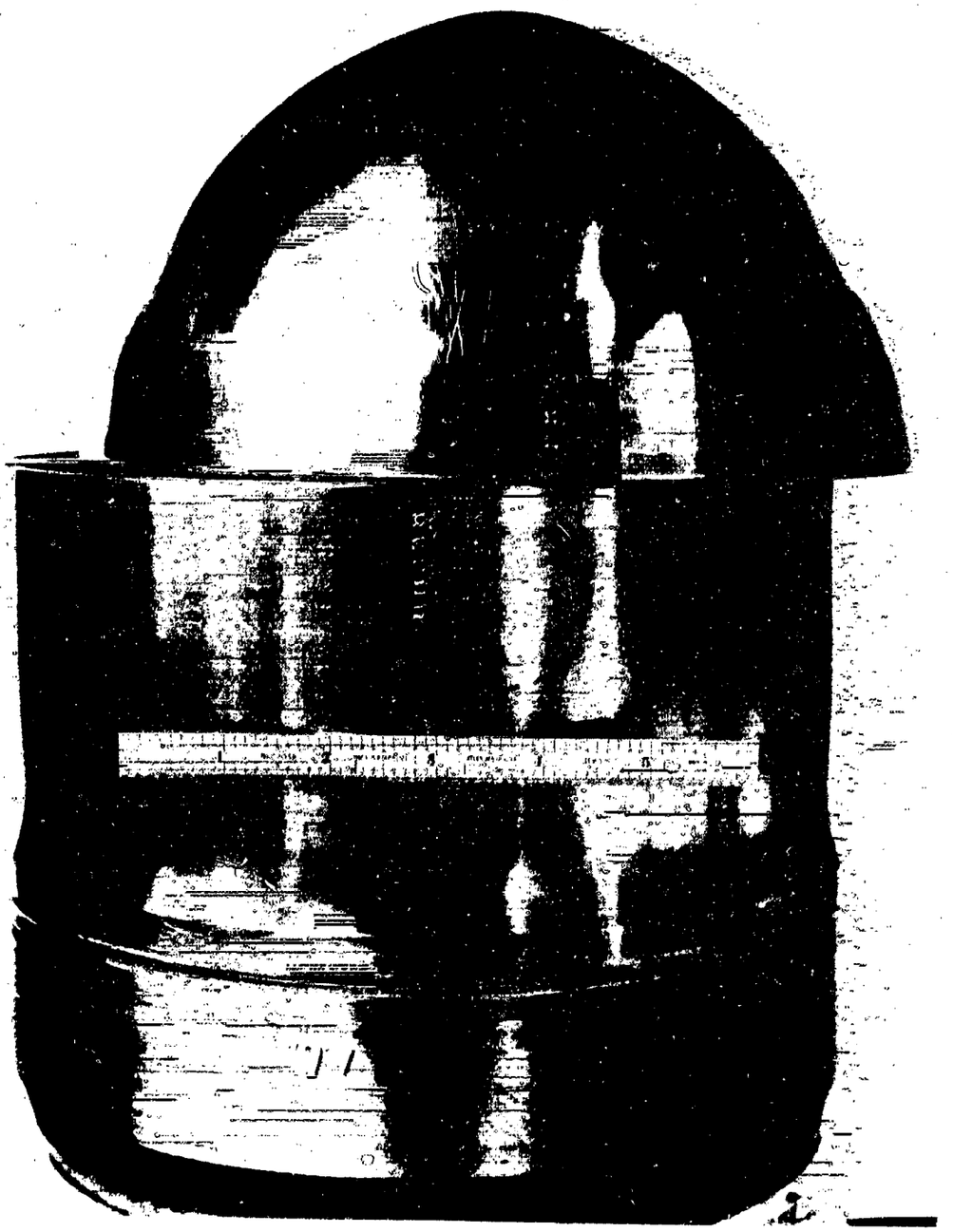

Fig. 9-5 Tita "F" After Test

Section 10

REFERENCES

1. J. Skogh, A.M.C. Holmes, "Elastic and Plastic Stresses at Weld Shrinkages and Other Discontinuities in Pressure Vessels", Lockheed Missiles & Space Company Report LMSC-4-05-69-7, October 1969 (Contract NAS9-8303), NASA Report CR-107071, October 1969.

2. P. Stern, "Stresses and Displacements in Elastic/Plastic Shells of Revolution with Temperature-Dependent Properties", Lockheed Missiles & Space Company Report LMSC-6-90-62-123, January 1966.

3. S. Timoshenko, S. Woinowsky-Krieger, Theory of Plates and Shells, McGraw-Hill, New York, 1959.

4. S. S. Manson, Thermal Stress and Low-Cycle Fatigue, McGraw-Hill, New York, 1966.

5. P. T. Bizon, "Elastic Stresses at a Mismatched Circumferential Joint in a Pressurized Cylinder Including Thickness Changes and Meridional Load Coupling", NASA TN D-3609, September 1966.

6. G. R. Evans, M. Kural, J. Skogh, "Shells with Discontinuities: Stress and Strength", An Annotated Bibliography, Lockheed Missiles & Space Company Literature Search LS 69-4, September 1969.

7. J. L. Mattavi, "Low-Cycle Fatigue Behavior under Biaxial Strain Distribution", Journal of Basic Engineering, March 1969, pp. 23-31.

8. M. A. Miner, "Cumulative Damage in Fatigue", Journal of Applied Mechanics, Vol. 12, 1945, No. 3, p. A159.

9. J. A. Pope, ed., Metal Fatigue, Chapman & Hall, Ltd., London, 1959.

10. E. Reissner, "On Axisymmetrical Deformation of Thin Shells of Revolution", Proceedings of Symposium on Applied Mathematics, Vol. III, McGraw-Hill, 1950, pp. 27-52.

11. C. R. Steele, "Juncture of Shells of Revolution", Journal of Spacecraft and Rockets, Vol. 3, No. 6, June 1966.

12. R. H. Johns, "Theoretical Elastic Mismatch Stresses", NASA TN D-3294, 1966.

APPENDIX A

COLLAPSE DUE TO DISCONTINUITY IN CYLINDRICAL PRESSURE VESSEL

For a thin cylinder, shown in Fig. A1, with a discontinuity ΔR in the nominal radius R, with interval pressure p, away from the discontinuity the stresses are

$$N_\varphi = \frac{pR}{2t} \qquad N_\theta = \frac{pR}{t} \tag{A1}$$

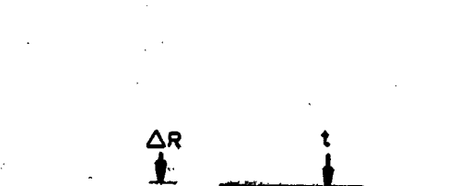

Fig. A1

Due to the asymmetry, at the discontinuity there is an additional bending moment

$$M_\varphi = \left(\frac{pR}{2t}\right) \frac{\Delta R}{2} \tag{A2}$$

while the axial stress resultant remains the same

$$N_\varphi = \left(\frac{pR}{2t}\right) \tag{A3}$$

and the circumferential displacement, which gives the circumferential strain, remains the same

$$\varepsilon_\theta = \left(\frac{pR}{2Et}\right)(2-\nu) \tag{A4}$$

Since the additional stress decreases with the distance from the discontinuity, the collapse will occur when the pressure exceeds the value giving the maximum M_φ and N_φ that the shell wall can sustain. Since M_φ and N_φ and the hoop strain are known (Eqs. A2-A4) the collapse pressure can be determined without solving the detailed equations for the behavior away from the discontinuity.

Before yielding occurs, the stresses across the shell wall at the discontinuity are

$$\sigma_\varphi = \frac{pR}{2t}\left[1 + \left(\frac{2z}{t}\right)\frac{3\Delta R}{t}\right]$$

$$\sigma_\theta = \frac{pR}{2t}\left[2 + \nu\left(\frac{2z}{t}\right)\frac{3\Delta R}{t}\right] \tag{A5}$$

so for large magnitudes of the discontinuity $\frac{3\Delta R}{t} > \frac{1}{1-\nu}$ the first yielding is in axial tension at the pressure

$$\frac{pR}{2t} = \frac{\sigma_Y}{1 + 3\Delta R/t} \tag{A6}$$

if the Tresca yield surface in Fig. A2 is assumed.

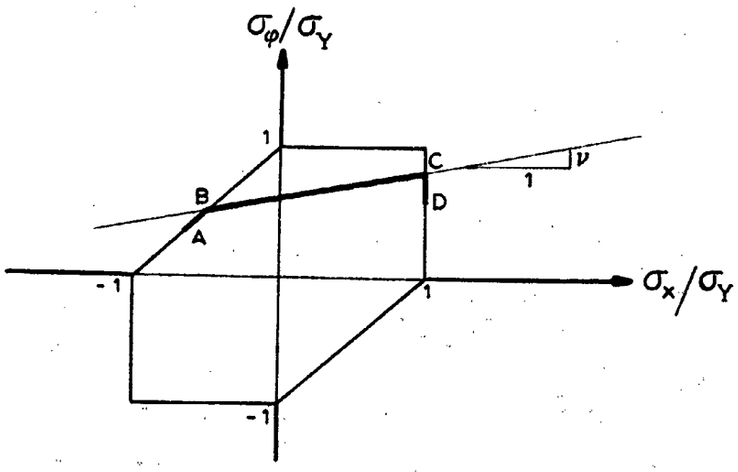

Fig. A2

After yielding occurs, in the portion of the wall cross-section that is still elastic we have

$$\sigma_\theta = Ee_\theta + \nu\sigma_\varphi$$

$$= \frac{pR}{2t}(2-\nu) + \nu\sigma_\varphi \qquad \text{(A7)}$$

which gives the line BC in Fig. A2. Thus the stress across the cross-section has the distribution shown in Fig. A3a. The stress at point B

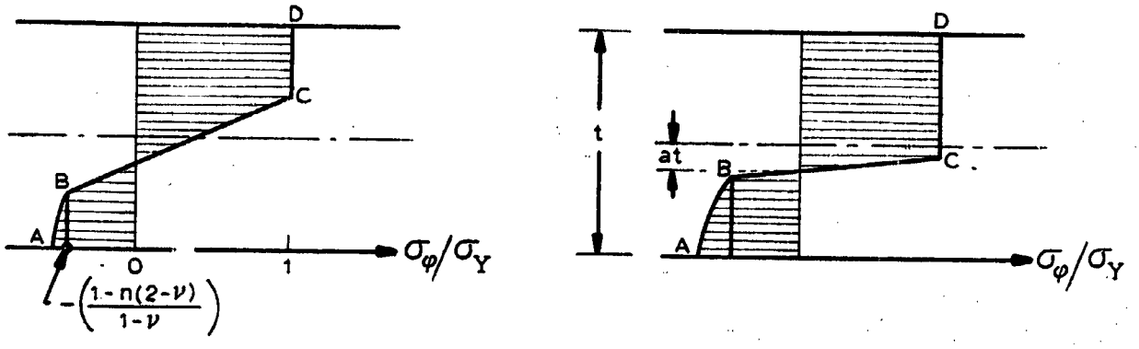

(a) Before Collapse (b) Just After Collapse

Fig. A3 - Axial Stress after Yielding

is obtained from the intersection of the two known lines in Fig. A2 and is

$$\left(\frac{\sigma_\varphi}{\sigma_Y}\right)_B = -\frac{1-\bar{n}(2-\nu)}{1-\nu} \tag{A8}$$

where

$$\bar{n} = \frac{pR}{2t\sigma_Y}$$

The distribution of stress between points A and B depends on the flow law. For a simple solution, which should give a lower bound on the collapse pressure, we take the stress between A and B to be equal to the stress at B. The collapse pressure is reached when the elastic portion of the cross-section B-C shrinks to zero; then the cross-section can sustain no further increase in pressure.

If the points B and C approach a point a distance ta from the mid-surface at collapse, then the condition (3) gives

$$\bar{n} = \left(\frac{1}{2} + a\right) - \left(\frac{1}{2} - a\right)\left(\frac{1 - (2-\nu)\bar{n}}{1-\nu}\right)$$

which gives

$$a = \frac{\nu}{2(2-\nu)} \tag{A9}$$

The conditions on the resultant moment (A2) gives

$$\bar{n}\,\frac{\Delta R}{t} = \left(\frac{1}{4} - a^2\right)\left[\frac{(2-\nu)(1-\bar{n})}{1-\nu}\right]$$

Solving for n gives the result

$$\bar{n} = \frac{1}{1 + \frac{\Delta R}{t}(2-\nu)} \tag{A10}$$

The previously discussed (see Section 3.1) simpler (uniaxial) yield surface, which gives for yield in compression $\sigma_\varphi = -\sigma_Y$, gave the result

$$\bar{n} = \frac{(\beta^2 + 9)^{1/2} - \beta}{3} \tag{A11}$$

where

$$\beta = 3\Delta R/t$$

which should give an upper bound since the material is actually much weaker.

The computer program, using a von Mises yield condition, as shown in Fig. 3-6 fails to converge at a pressure only slightly higher than that given by Eq. (A10). Thus this very simple formula accurately gives the collapse pressure.

Thus at the collapse pressure, the axial stress is

$$\frac{\sigma_\varphi}{\sigma_Y} = \begin{cases} 1 & -ta < z < t/2 \\ -\dfrac{1 - \bar{n}(2-\nu)}{1-\nu} & \dfrac{t}{2} < z < -ta \end{cases}$$

To find the residual stress when the shell is unloaded, add the linear solution

$$\frac{\sigma_\varphi}{\sigma_Y} \begin{cases} -(1+\nu)\dfrac{\Delta R}{t}\bar{n} & \text{at } z = \dfrac{t}{2} \quad (D) \\ \dfrac{(2-\nu)^2 + \nu}{2-\nu}\dfrac{\Delta R}{t}\bar{n} & \text{at } z = -at^+ \quad (C) \\ -\dfrac{(2-\nu)^2 - 3\nu(1-\nu)}{(1-\nu)(2-\nu)}\dfrac{\Delta R}{t}\bar{n} & \text{at } z = -at^- \quad (B) \\ \dfrac{(1-2\nu)}{1-\nu}\dfrac{\Delta R}{t}\bar{n} & \text{at } z = -t/2 \quad (A) \end{cases}$$

where $\bar{n}$ is given by (A10). The expression for the stress at (D) is approximate. A similar computation gives the circumferential residual stress.

$$\frac{\sigma_\theta}{\sigma_Y} \begin{cases} -\dfrac{(1+\nu)(2+3\nu\,\frac{\Delta R}{t})}{1+3\,\frac{\Delta R}{t}}\;\frac{\Delta R}{t}\,\bar{n} & \text{at (D)} \\ \dfrac{\nu[(2-\nu)^2+3\nu]}{2-\nu}\;\frac{\Delta R}{t}\,\bar{n} & \text{at (C)} \\ -\left[2\nu+\nu\,\frac{\Delta R}{t}\left(2-\nu-\frac{3\nu}{2\nu}\right)\right]\frac{\bar{n}}{1-\nu} & \text{at (B)} \end{cases}$$

The residual hoop stress at (A) cannot be determined by this type of an analysis, but would require a plastic flow analysis.

If the yield surface is the same in tension and compression as in Fig. A2, then the residual stresses do not violate the yield condition, except for a very severe discontinuity. This additional yielding as the pressure is decreased begins at point C, but only when the discontinuity is

$$\frac{\Delta R}{t} \geq \frac{2-\nu}{\nu}$$

$$= 5.7 \text{ for } \nu = 0.3$$

Thus any type of reversed yielding, which would be extremely serious for cyclic loading, does not generally occur.

APPENDIX B

STRAIN GAGE DATA

NOTE: The data of Appendix B are bound in a separate volume with limited distribution